Nuclear magnetic resonance studies of paramagnetic relaxation enhancement at high magnetic fields : methods and applications

Rami Nasser Din

THÈSE

Pour obtenir le grade de

DOCTEUR DE L'UNIVERSITÉ GRENOBLE ALPES

École doctorale : PHYS - Physique
Spécialité : Physique des matériaux
Unité de recherche : LNCMI - Laboratoire National des Champs Magnétiques Intenses

Etudes par résonance magnétique nucléaire de l'augmentation de la contribution paramagnétique de la relaxation dans les champs magnétiques intenses : méthodes et applications

Nuclear magnetic resonance studies of paramagnetic relaxation enhancement at high magnetic fields: methods and applications

Présentée par :

Rami NASSER DIN

Direction de thèse :

Mladen HORVATIC DIRECTEUR DE RECHERCHE, CNRS DELEGATION ALPES	Directeur de thèse
Steffen KRAMER INGENIEUR DE RECHERCHE, CNRS DELEGATION ALPES	Co-encadrant de thèse

Rapporteurs :

CHRISTOPHE GOZE-BAC
DIRECTEUR DE RECHERCHE, CNRS DELEGATION OCCITANIE EST
ALESSANDRO LASCIALFARI
FULL PROFESSOR, UNIVERSITA DEGLI STUDI DI PAVIA

Thèse soutenue publiquement le **14 décembre 2023**, devant le jury composé de :

CHRISTOPHE GOZE-BAC DIRECTEUR DE RECHERCHE, CNRS DELEGATION OCCITANIE EST	Rapporteur
ALESSANDRO LASCIALFARI FULL PROFESSOR, UNIVERSITA DEGLI STUDI DI PAVIA	Rapporteur
FRANCK BALESTRO PROFESSEUR DES UNIVERSITES, UNIVERSITE GRENOBLE ALPES	Président
GISELA GUTHAUSEN SENIOR SCIENTIST, KARLSRUHER INSTITUT FÜR TECHNOLOGIE	Examinatrice
MASOOMA IBRAHIM DOCTEURE EN SCIENCES HDR, KARLSRUHER INSTITUT FÜR TECHNOLOGIE	Examinatrice
HANNES KUHNE DOCTEUR EN SCIENCES, HELMHOLTZ-ZENTRUM DRESDEN-ROSSENDORF	Examinateur

Invités :

STEFFEN KRAMER
INGENIEUR DE RECHERCHE, CNRS DELEGATION ALPES

Acknowledgment

The success of this thesis is the outcome of collective efforts. The efforts of those who provided me unfailing support, restless motivation, in addition to fruitful scientific discussions. Without all of you, this road would have been a hundred times more difficult. That's why I'd like to start by thanking my supervisor Steffen Kramer (also member of thesis jury) for allowing me to discover the NMR from scratch, and for being patient with me and giving me all the time I needed. You have always been a great role model for me. I admire how you treat everyone with warmth and kindness. You teached me to separate work and personal life by always telling me : "When you go home, forget about work". Thank you for always supporting me through my ups and downs. You, Sylvie and Violaine have been my second family in Grenoble. I would need another thesis to express my gratitude towards you and your family. Thank you again for the quality time we spent together inside/outside the laboratory. I hope that next year, we will be able to celebrate your HDR together.

I would also like to acknowledge the support by the French National Research Agency in the framework of the "Investissements d'avenir" program (ANR-15-IDEX-02), which financed my thesis. During my thesis, I traveled to Karlsruhe several times to carry out experiments. The city embraced me with open arms, and I met some of the most exceptional people who made my stay unforgettable. Their warmth and kindness were so great that I will always cherish the memories of my time spent there. I couldn't have made it without the financial support of the EMFL at KIT. It was made possible by the EU project "Isabel" (Horizon 2020, grant agreement no. 871106), which funded my stay in Karlsruhe. I would like to thank both Annie POWELL and Gisela GUTHAUSEN (also member of thesis jury) and their groups members for the scientific discussions and to the quality time spent in Karlsruhe. Special thanks to Masooma IBRAHIM (also member of thesis jury) and Aiswarya VENU for helping me with the chemistry part of my thesis and for the good food at Karlsruhe. I would also like to thank Philip WURM and Klaus ZICK for the technical support while performing PRE studies at the Bruker site. I would like to express my gratitude to the IBS NMR team: Bernhard BRUTSCHER, Adrien FAVIER, and Alicia VALLET, for their technical support during the PRE studies at their site. I hereby acknowledge the financial support of IR INFRANALYTICS FR2054 for this research. Moreover, I thank again Bernhard BRUTSCHER along with Michel BARDET for their input as members of the CSI, which helped me improve my work.

I just wanted to take a moment to express my heartfelt gratitude to my supervisor, Mladen HORVATIC (also member of thesis jury). He's been such an amazing mentor, always offering honest feedback, engaging in scientific discussions, and sharing valuable insights that helped me improve my work.

I would like to thank Christophe GOZE-BAC and Alessandro LASCIALFARI for agreeing to review this manuscript as well as Franck BALESTRO for being the president of the thesis Jury, and Hannes KÜHNE for his contributions as member of the jury.

these were incredible three years at LNCMI! I have been given the joy of interacting with so many wonderful people. I just wanted to take a moment to express my sincere gratitude to all the members of the LNCMI laboratory for making my time here incredibly enjoyable.Your positive attitude and friendly demeanor have made all the difference. Thank you so much! Special thanks to Amélie PIC, Alexandra GASPARANI, Natacha HUBERT, and Dominique VITIELLO from the administration team for their availability and kindness. I extend my deepest gratitude to Ivan BRESLAVETZ, the unsung hero in the COMSOL dimension. Your technical support was my secret weapon, turning the challenging task of navigating COMSOL into a shared adventure filled with laughter. In addition, I thank Kevin PAILLOT for the technical support concerning the properties of the resistive magnets and the shared moments inside/outside the laboratory. Moreover, I thank both Christian BULALA and Jürgen SPITZNAGEL from the LNCMI workshop for the mechanical support, and Ghenadie NOVITCHI for the chemical support.

During these three years at LNCMI, I was a part of different teams: NMR, Instrumentation, and Action Climat. Participating in NMR and Instrumentation group meetings has been an invaluable helpful experience for me. Through presenting my work and listening to others, I have learned to appreciate and value the contributions of my colleagues. It has motivated me to work harder on myself to learn and improve as a researcher. My experience with the Action Climat team has allowed me to gain a deeper understanding of the imminent threat posed by climate change. I now recognize that it is our collective responsibility to take action in addressing this issue, as well as other environmental concerns. I hope that one day, I will be able to leverage this experience to benefit my home country, Lebanon.

I thank as well, the PhD students from the laboratory: Nathan AUBERGIER, Ivan MOHELSKY, Louanne VERYAT, Florian LE-MARDELE, Maria-Sara RAJU, Samy LALLOZ, Himanshu HIMANSHU, Anne MISSIAEN, Nouâmane Cherkaoui, and Jeremy SARRADE for all the great moments during the coffee breaks or around a beer outside the laboratory. Your unwavering support has made this journey much smoother and enjoyable. I feel blessed to have had such amazing companions on this road, and I will always cherish our time together.

I would also like to thank all those who shared their lunch with me followed by a coffee in the canteen: Marc-Henri JULIEN, Hadrien MAYAFFRE, Ranjith KUMAR, David LEBOEUF, Robert PANKOW, Luc RONAYETTE, Benjamin VINCENT (also for the football days), Xavier CHAUD, Romain RAISON, Teddy CHDID, Elias GHNATIOUS, François DEBRAY, Jung-Bin SONG, Ilya SHEIKIN, Loic SORIANO, Yanan LI and all the others... with your conversations, I enjoyed my lunch even more. I'll cherish the memory of Marilyne DRUART who generously gave me her canteen card so that I could enjoy extra meals there even after my contract ended. It was such a nice gesture that I'll always remember. Thank you so much for your kindness!

Yuriy KRUPKO, thank you for always reminding me that I'm also Ukrainian as well as Lebanese and for sharing conversations about Ukrainian culture and office jokes. As you read this, you might say when will you get your stuff and finally leave us or Clermont? Well, don't worry, I will. Thanks also to Milan ORLITA and his group for the most enjoyable coffee breaks at work. I would also like to express my gratitude to Albin DE MUER for giving me the opportunity to give practical work at the IUT. It was a very pleasant experience that I thoroughly enjoyed.

To my friends in Grenoble: Chafic, Idriss, Ahmad AL IBRAHIM, Ghida, Issam, Hsein KODEIH, Nour MKHEIL, Perla, Rafi, Soha, Ghadi, Abbas, Imad, Sirar, Rakan, Carmen, Khaldoun, Amani, Nour EL HOUSSEIN, Anna, Khodr, Elie ASSAF, Cherryl, Jenny, Tony, Hala, Joanna, Rand, Sally, Hani, Hsein,

Nour ZEAITIR, thank you for your encouragement during these years and for the moments spent beside the river, BBQ at parc d'amour, Chamonix, Playing card at IDRISS place, the nights at Rakan's place, for the trips we did together, and many other funny moments. Christia thank you for being part of my details and all your love. I would like to thank also: Elias CORREA, Mona NASSER DIN and her family, Nazih, Ihsan, Abed, Gaby, Hadi, Samar, Marwa, Khaled, Yorgo, Joseph KFOURY, Ghida FAYAD, George KFOURY, George NASSAR, Elie KFOURY, Rony, Rima, Rita for always being there, despite the distance! Despite this distance, many of you were able to attend my thesis defence, and I will never forget this. Thanks for coming, organizing my thesis defense, and making this day unforgettable.

I'd like to finish by thanking my family without whom none of this would be possible. Your love and hard work have made me who I am today, and I owe everything to you.

Contents

Résumé

La résonance magnétique nucléaire (RMN) est une technique analytique largement utilisée dans des domaines de recherche tels que la chimie, la physique et la biomédecine. L'imagerie par résonance magnétique (IRM) est l'une de ses applications les plus importantes, tant pour les investigations médicales que techniques. Dans ce contexte, l'augmentation de la contribution paramagnétique á la relaxation (PRE) constitue un domaine de recherche important, notamment avec l'utilisation croissante de champs magnétiques élevés dans l'IRM. PRE change le contraste de l'image IRM en accélérant la relaxation du spin nucléaire typiquement protoniques dans l'eau via leurs interactions magnétiques avec les spins électroniques des composés paramagnétiques ajoutés. Par conséquent, les composés présentant une PRE sont utilisés comme agents de contraste en IRM. La PRE dépend de la concentration des composés paramagnétiques dans le solvant. Le PRE d'un composé à un champ donné est mesuré par sa relaxivité, définie comme l'amélioration du taux de relaxation du proton de l'eau normalisé par sa concentration. Malgré les nombreuses années de recherche sur la PRE, des questions intéressantes subsistent concernant ces mécanismes microscopiques.

Dans ce contexte, il est important de mesurer la dépendance au champ du PRE jusqu'au champ magnétique le plus élevé possible. Cependant, la plupart des études PRE aboutissent à des fréquences inférieures à 800 MHz ($18,8$ T). Cette gamme de fréquences peut être étendue au-delà de la limite actuelle des aimants supraconducteurs de $28,2$ T en utilisant des aimants résistifs.

La disponibilité d'aimants résistifs au laboratoire LNCMI de Grenoble ouvre la voie à des études PRE jusqu'à 37 T. Cependant, la qualité limitée du champ des aimants résistifs, l'inhomogénéité du champ et les fluctuations font des expériences RMN un défi technique. Pour cette raison, au cours de cette thèse, nous avons travaillé de manière approfondie sur le développement d'instruments et de méthodes RMN pour surmonter l'inconvénient des aimants résistifs, notamment une canne RMN à large bande jusqu'à $1,4$ GHz pour un volume d'échantillon de microlitres, des mesures RMN à scan unique et des routines d'analyse de données personnalisées.

La validité de ces méthodes a été confirmée par la réalisation d'études PRE sur des échantillons de sels de chlorure de lanthanide qui ont fait l'objet de recherches approfondies depuis les premiers jours de la RMN. Leur comportement PRE est connu, ce qui en fait d'eux des échantillons de référence idéaux pour la comparaison entre les études PRE réalisées sur des aimants supraconducteurs et résistifs. Ces études PRE fournissent des informations sur la qualité des données des aimants résistifs et l'identification d'erreurs systématiques potentielles. En plus, l'extension de la gamme de champs dans les études PRE jusqu'à $1,4$ GHz de ces complexes de lanthanides relativement simples devrait fournir des informations importantes pour l'analyse de composés plus complexes.

De plus, la tendance vers de futures applications IRM à haut champ nécessite le développement de nouveaux agents de contraste efficaces en raison de la relaxivité réduite des composés PRE conventionnels à base de Gd (III) aux champs élevés. L'une des stratégies consiste à étudier d'autres complexes à base de lanthanides. Par conséquent, de nouveaux complexes à base de lanthanides tels que les polyoxométalates paramagnétiques (PM-POM) ont été synthétisés et étudiés sur une large gamme de fréquences allant de 20

MHz à $1,4$ GHz en utilisant des aimants permanents et supraconducteurs commerciaux et une RMN non standard dans les aimants résistifs pour les fréquences supérieures à 800 MHz. Ils indiquent que ces composés sont des candidats potentiels comme agents de contraste, notamment dans les champs magnétiques élevés.

Abstract

Nuclear Magnetic Resonance (NMR) is an analytical technique widely used in research fields such as chemistry, physics, and biomedicine. One of its most prominent applications is Magnetic Resonance Imaging (MRI) for both, medical and technical investigations. In this context, Paramagnetic Relaxation Enhancement (PRE) is an important research area, particularly with the increasing use of high magnetic fields in MRI. PRE changes the MRI image contrast by speeding up the nuclear spin relaxation of typically proton spins in water via their magnetic interactions with electron spins of added paramagnetic compounds. Therefore, compounds exhibiting PRE are used as contrast agents in MRI. PRE depends on the concentration of the paramagnetic compounds in the solvent. The PRE of a compound at a given field is measured by its relaxivity, defined as the enhancement of the relaxation rate of the water proton normalized by its concentration. Despite many years of research on PRE, there are still interesting questions about the microscopic mechanisms.

In this context, it is important to measure the field dependence of PRE up to the highest possible magnetic field. However, most PRE studies end up at frequencies below 800 MHz (18.8 T). This frequency range can be extended beyond the current superconducting magnet limit of 28.2 T by employing resistive magnets.

The availability of resistive magnets at the LNCMI laboratory in Grenoble opens the way for PRE studies up to 37 T. However, the limited field quality of resistive magnets, field inhomogeneity and fluctuations make NMR experiments a technical challenge. For this reason, during this thesis, we extensively worked on the development of NMR instrumentation and methods to overcome the disadvantage of resistive magnets including a wideband NMR setup up to 1.4 GHz for microliter sample volume, single scan NMR, and tailored data analysis routines.

The validity of these methods was confirmed by performing PRE studies on samples of lanthanide chloride salts that have been extensively investigated since the early days of NMR. Their PRE behavior is known, which makes them ideal benchmark samples for the comparison between PRE studies performed on superconducting and resistive magnets. These PRE studies provide information on the quality of the resistive magnet data and the identification of potential systematic errors. In addition, the extension of the PRE field range up to 1.4 GHz of these relatively simple lanthanide complexes is expected to provide important information for the analysis of more complex compounds.

Moreover, the trend towards future high-field MRI applications requires the development of new, effective contrast agents due to the reduced relaxivity of conventional PRE compounds based on Gd(III) at high fields. One of the strategies is to investigate other lanthanide-based complexes. Therefore, new lanthanide-based complexes like paramagnetic polyoxometalates (PM-POMs) have been synthesized, and investigated over a wide range of frequencies from 20 MHz up to 1.4 GHz using commercial permanent and superconducting magnets, and non-standard NMR in the resistive magnets for frequencies above 800 MHz. They indicate that these compounds are potential candidates for contrast agents, especially at high magnetic fields.

Introduction

Nuclear magnetic resonance (NMR) is an analytical technique widely used in research fields such as chemistry, physics, and biomedicine. One of its most prominent applications is magnetic resonance imaging (MRI) for both, medical and technical investigations. MRI images map the spatial distribution of the density or the relaxation times of the monitored nucleus, mostly ^{1}H in H_2O. The sensitivity and spatial resolution of MRI images depend on the signal-to-noise ratio, which is almost proportional to the square of the magnetic field strength. For this reason, there is growing interest within the MRI community in using high-field instruments. In this context, paramagnetic relaxation enhancement (PRE) is nowadays an important research area. PRE speeds up nuclear spin relaxation by magnetic interactions with unpaired electron spins providing an improved contrast of the image [1]. Therefore, compounds exhibiting PRE are used as contrast agents (CAs). They are chemical compounds containing paramagnetic ions. Their effectiveness at a given field is measured by their relaxivities, defined as the enhancement of the relaxation rate of the water proton normalized by the concentration of the CA.

Most conventional CAs are based on Gd(III) ions. The decrease in their relaxivity at higher fields and recent information on their toxicity raised concerns about their future in MRI high-field applications. New lanthanide-based complexes like paramagnetic polyoxometalates (PM-POMs) have interesting magnetic properties, making them suitable as contrast agents at intermediate and high magnetic fields. In this context, the NMR team at the Grenoble site of the LNCMI in collaboration with Karlsruhe Institute of Technology (KIT) started an activity on PRE of NMR relaxivities of potential contrast agents over a wide range of frequencies from 20 up to 1400 MHz [2–6].

The studies revealed that the relaxation dispersion should always be measured from low to ultrahigh magnetic fields to understand the PRE of the compounds. Most of the PRE studies end up at frequencies below 800 MHz (18.8 T). However, the PRE study of lanthanide compounds requires the use of the highest fields available that exceed the limits of commercial NMR spectrometers operating with superconducting (SC) magnets. The availability of resistive magnets at the LNCMI laboratory in Grenoble opens the way for PRE studies up to 33 T (1.4 GHz) and beyond. In this context, there are two important questions: Is it possible to use resistive magnets in PRE studies despite their strong limitations in field *inhomogeneity* and *instability* compared to state-of-the-art SC magnets? What are the adapted instruments and methods to overcome these limitations in the resistive magnets?

The objective of this thesis is to experimentally investigate the above questions and to develop tailored solutions to overcome the limitations of the resistive magnets. Furthermore, extending the frequency range of PRE studies beyond 800 MHz gives valuable information into PRE relaxation mechanisms that can be used in PRE modeling. The thesis is composed of six chapters.

Chapter 1 describes the NMR theory with a focus on the situation in resistive magnets, where fluctuations and inhomogeneities generate off-resonant effects. At the end of this chapter, we list the pulse sequences used to extract the relaxation times of water molecules.

Chapter 2 presents the non-standard methods for processing the NMR data obtained in the resistive magnet.

Chapter 3, extensively focuses on instruments and methods to overcome the limited field quality of resistive magnets. First, starting from the properties of the resistive magnets, solutions are developed to reduce the broadening of the NMR lines due to field inhomogeneity. Second, the high-frequency GHz NMR probe was modeled and characterized. Finally, the impact of spatial inhomogeneity and temporal instability on the NMR experiments was studied.

The last three chapters are dedicated to the application of the methods in experimental PRE studies.

Chapter 4 describes the theory of paramagnetic relaxation enhancement with restriction to lanthanide ions.

Chapter 5 shows an application example of PRE between 20 MHz and 1.4 GHz on *new PM-POMs samples* synthesized by KIT.

Chapter 6 presents an application example of PRE on samples of $LnCl_3$ salts, in aqueous solution from 20 MHz to 1.4 GHz with Ln $\in \{$Gd, Dy, Ho, Er$\}$. As their PRE behavior has been extensively investigated since the early days of NMR, they are ideal benchmark samples for comparison between PRE studies performed on superconducting and resistive magnets. Moreover, the extension of the field range up to 1.4 GHz of these relatively simple Ln complexes is expected to provide information for the analysis of more complex compounds. This PRE study provides information on the quality of the resistive magnet data and the investigation of potential systematic errors.

Chapter 1: Some theoretical concepts of NMR

In this part, I will describe the physics behind NMR using both the classical and the quantum mechanics approach with focus on aspects that are relevant for NMR in resistive magnets. Details can be found in these books [1, 7–12].

1.1 Quantum mechanical description of nuclear magnetic moments

1.1.1 Zeeman energy levels

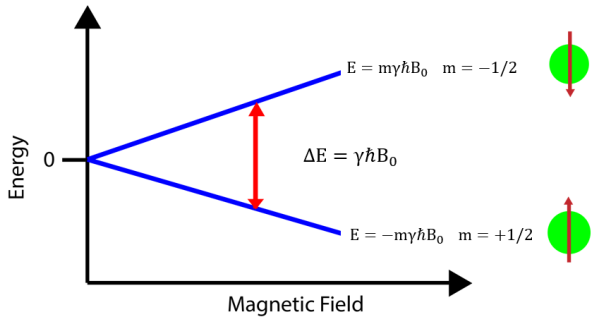

Figure 1.1: Splitting of nuclear energy levels in presence of a magnetic field for I = 1/2

In order to observe an NMR signal, we need to target an atomic nuclei that, in its ground state, has a non-zero spin angular momentum $\boldsymbol{I}$ and, hence, a dipolar magnetic moment $\boldsymbol{\mu}$. The relation between these two parameters is given by

$$\boldsymbol{\mu} = \gamma \boldsymbol{I}, \tag{1.1}$$

where γ is the gyromagnetic ratio, expressed in rad s^{-1} T^{-1} . For the proton ^{1}H, the gyromagnetic ratio is

$$\gamma = 2\pi \times 42.5774 \text{ MHz/T}. \tag{1.2}$$

The energy of a nuclear magnetic moment $\boldsymbol{\mu}$ in an external magnetic field $\boldsymbol{B}_0$ depends on the angle θ between them, and is given by the equation

$$E_m = -\boldsymbol{\mu} \cdot \boldsymbol{B}_0 = -\mu B_0 \cos\theta.$$

The lowest energy is obtained for $\theta = 0$, when the magnetic moment is parallel to the applied field. The highest energy occurs when the magnetic moment is opposed to the field.

One of fundamental postulates of quantum mechanics is that an angular momentum $\boldsymbol{I}$ is quantized into integer or half-integer values. In the magnetic field applied along the z-axis, I_z is quantized into $m_I = -I, -I+1, ..., I-1, I$, where I is the spin of the nucleus. The total number of these values is $2I+1$. For

a spin-half nucleus ($I = 1/2$), we have two possible values for $m_I : -1/2$ and $1/2$. For $I = 1$, we have 3 values for $m_I : -1, 0, 1$.

Under a magnetic field, the otherwise degenerated nuclear spin states split into $2I + 1$ energy levels called Zeeman levels, whose energy is proportional to the field

$$E(m_I) = -\gamma\hbar m_I B_0. \tag{1.3}$$

When we deal with a hydrogen nucleus ^{1}H ($I = 1/2$) in a magnetic field $\boldsymbol{B}_0$, the ground state splits into two levels as shown in figure 1.1. The energy difference between any two consecutive levels is $\Delta E = \gamma\hbar B_0$.

Up to this point, we have only considered a single spin and its magnetic moment. In the following, we consider that we are dealing with N spins in a volume V, where the magnetization $\boldsymbol{M}$ is the vector sum of all magnetic moments

$$\boldsymbol{M} = \frac{1}{V}\sum_{i=1}^{N}\boldsymbol{\mu}_i. \tag{1.4}$$

1.1.2 Boltzmann statistics and equilibrium magnetization

The spins populate different Zeeman levels with different probabilities for each of them. The probabilities are given by the Boltzmann statistics

$$P[E(m)]_{(T)} = \frac{e^{\frac{-E(m_I)}{k_B T}}}{\sum_{m_I=-I}^{I} e^{\frac{-E(m_I)}{k_B T}}}. \tag{1.5}$$

The population of an energy level for N identical nuclei is $NP[E(m)]_{(T)}$.

As seen from equation (1.3) and (1.5), the more populated energy levels have positive m_I (we consider γ positive), which corresponds to the magnetic moment parallel to the applied field. This gives rise to a finite magnetization in the sample.

In the absence of the static field B_0, the moments are randomly oriented because all orientations have the same energy. This means that there is no finite magnetization in the sample. After the application of the magnetic field, there is an energetic preference for the magnetic moments to be oriented parallel to the field (z-axis), as described above. This will lead, after a finite time, to the growth of the net magnetization vector along the z axis. As more moments adopt lower energy orientations, the magnetization grows, until it reaches a steady value. At this point we say that the system is at the equilibrium state. The magnetization at the equilibrium state for a sample of N nucleus and a volume V can be written

$$M_{eq} = \frac{1}{V}\sum_{i=1}^{N}\mu_i = \frac{1}{V}\sum_{m_I=I}^{m_I=-I} m_I\hbar\gamma NP[E(m_I)]_{(T)}. \tag{1.6}$$

All our experiments were performed at room temperature, where $\frac{\gamma\hbar B_0}{k_B T} << 1$. For this case the series expansion of equation (1.6) provides

$$M_{eq} = \frac{n\gamma^2\hbar^2 I(I+1)B_0}{3k_B T}. \tag{1.7}$$

The equation (1.7) gives us a lot of information about the magnetization, which is proportional to the volume density of the nuclei ($n = \frac{N}{V}$), the square of the gyromagnetic ratio of the studied nucleus and to the static magnetic field.

1.2 Classical treatment of NMR

1.2.1 Nuclear spin ensembles in spatially varying magnetic fields

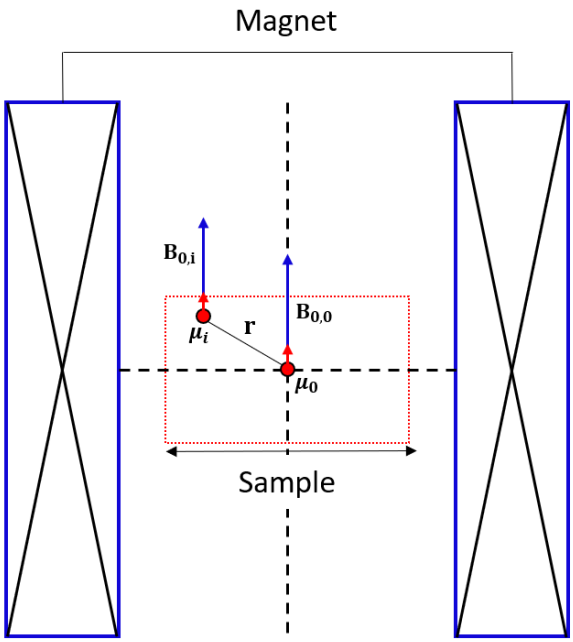

Figure 1.2: Illustration of a sample containing N spins of a nuclear magnetic moment $\boldsymbol{\mu}_i$ exposed to an external magnetic field $\boldsymbol{B}_0 = B_0(\boldsymbol{r})\boldsymbol{e}_z$.

So far, we have assumed that the spin ensemble is experiencing a uniform magnetic field $\boldsymbol{B}_0$. However, the strength of $\boldsymbol{B}_0$ can vary within the sample volume. To study the behavior of different sets of spins in different regions across the sample, we divide the sample into small and equally sized volume elements V_i, which we call voxels. It is important to note that within each voxel V_i, a local magnetization $\boldsymbol{M}_{eq,i}$ arises due to the alignment of the spins with the local field $\boldsymbol{B}_{0,i}$ represented by the equation (1.7). Since the variations of magnetization $\boldsymbol{M}_{eq,i}$ across the different V_i are very small (10^{-6}), we neglect the inhomogeneity effect of $\boldsymbol{B}_0(\boldsymbol{r})$ on the induced magnetization, i,e, $M_{eq,i} = M_{eq}$ at the equilibrium state.

This approach has been used to facilitate the exploration of variations in local magnetic field values across the sample, which provides a framework for studying the influence of inhomogeneity and fluctuations on an NMR experiment.

The magnetic field generated by a solenoid magnet is almost uniform in its center region. At the center, the field is oriented along the axis of the solenoid, which defines the z-axis of the field. However, as one moves away from the center, spatial variations in the magnetic field gradually increase. Moreover, the contribution

of the radial components remain negligible. Therefore, we can write

$$\boldsymbol{B}_0(\boldsymbol{r}) = B_0(\boldsymbol{r})\boldsymbol{e}_z, \tag{1.8}$$

1.2.2 Motion of free spins in a static magnetic field

Placed in a static field $\boldsymbol{B}_0(\boldsymbol{r})$, a torque $\boldsymbol{\Gamma}_i$ is exerted on $\boldsymbol{M}_i$

$$\boldsymbol{\Gamma}_i = \boldsymbol{M}_i \times \boldsymbol{B}_{0,i}. \tag{1.9}$$

The magnitude of $\boldsymbol{B}_{0,i}$ depends on the position of V_i relative to the center of the magnet $\boldsymbol{r}$ as shown in the figure 1.2. The equation of motion for the angular momentum is related to $\boldsymbol{\Gamma}_i$ by the following equation

$$\boldsymbol{\Gamma}_i = \frac{d\boldsymbol{I}}{dt}. \tag{1.10}$$

Using the equations (1.1), (1.9) and (1.10) leads to the law of the motion

$$\frac{d\boldsymbol{M}_i}{dt} = \gamma \boldsymbol{M}_i \times \boldsymbol{B}_{0,i}. \tag{1.11}$$

The solution of equation (1.11) is a precession of $\boldsymbol{M}_i$ around the magnetic field vector $\boldsymbol{B}_{0,i}$ with an angular frequency $\boldsymbol{\omega_{0,i}}$ known as the Larmor frequency and expressed by

$$\boldsymbol{\omega_{0,i}} = -\gamma \boldsymbol{B}_{0,i}. \tag{1.12}$$

We can write equation (1.11) in terms of angular frequencies by combining equations (1.11) and (1.12)

$$\frac{d\boldsymbol{M}_i}{dt} = \boldsymbol{\omega}_{0,i} \times \boldsymbol{M}_i. \tag{1.13}$$

Here, and in the following discussion, we refer to magnetic fields in units of angular frequency.

1.2.3 Perturbation of magnetization by radio frequency fields

NMR is a technique that makes the nuclear magnetization measurable. In order to achieve that, we will need to induce a perturbation of the magnetization to take it out from its equilibrium state. The general idea of this technique is to subject the sample, in presence of a static magnetic field $\boldsymbol{B}_0$ along the z-axis, to a time dependent oscillating field $\boldsymbol{B}_1(t)$ with a frequency ω_{rf} near the Larmor frequency ω_0. $\boldsymbol{B}_1(t)$ is applied in the transverse direction, that is in the (x,y) plane [13]. Depending on its frequency, it excites the magnetic moments of the corresponding nuclear spins.

$\boldsymbol{B}_1(t)$ is generated by passing an electrical current through a radio-frequency (RF) coil that englobes the sample. Due to imperfections in the coil geometry and other factors, the amplitude and direction of the magnetic field experienced by each voxel varies across the sample. Hence, $\boldsymbol{B}_1(\boldsymbol{r}, t)$ is a spatially varying magnetic field that is both space and time-dependent

$$\boldsymbol{B}_1(\boldsymbol{r}, t) = \quad \boldsymbol{B}_1(\boldsymbol{r}) \cos(\omega_{rf} t)\ . \tag{1.14}$$

We can write $\boldsymbol{B}_{1,i}(t)$ at each voxel i

$$\boldsymbol{B}_{1,i}(t) = (B_{1,x_i}\boldsymbol{e}_x + B_{1,y_i}\boldsymbol{e}_y + B_{1,z_i}\boldsymbol{e}_z)\cos(\omega_{rf}t) = -\frac{2\boldsymbol{\omega}_{1,i}(t)}{\gamma}, \tag{1.15}$$

where $\boldsymbol{\omega_{1,i}}(t) = (\omega_{1,x_i}\boldsymbol{e}_x + \omega_{1,y_i}\boldsymbol{e}_y + \omega_{1,z_i}\boldsymbol{e}_z)\cos(\omega_{rf}t)$.

Taking into consideration the static field $\boldsymbol{B}_{0,i}$ and the time dependent oscillating field $\boldsymbol{B}_{1,i}(t)$, the Bloch equation [14] at a voxel i is given by

$$\frac{d\boldsymbol{M_i}(t)}{dt} = (\boldsymbol{\omega}_{0,i} + 2\boldsymbol{\omega}_{1,i}(t)) \times \boldsymbol{M_i}(t). \tag{1.16}$$

In matrix notation

$$\frac{d\boldsymbol{M_i}(t)}{dt} = \left[\underline{\underline{\Omega_{0,i}}} + \underline{\underline{\Omega_{1,i}}}(t)\right] \boldsymbol{M_i}(t), \tag{1.17}$$

where

$$\underline{\underline{\Omega_{0,i}}} = \begin{pmatrix} 0 & -\omega_{0,i} & 0 \\ \omega_{0,i} & 0 & 0 \\ 0 & 0 & 0 \end{pmatrix} \quad \text{and} \quad \underline{\underline{\Omega_{1,i}}}(t) = \begin{pmatrix} 0 & -2\omega_{1,z_i}\cos(\omega_{rf}t) & 2\omega_{1,y_i}\cos(\omega_{rf}t) \\ 2\omega_{1,z_i}\cos(\omega_{rf}t) & 0 & -2\omega_{1,x_i}\cos(\omega_{rf}t) \\ -2\omega_{1,y_i}\cos(\omega_{rf}t) & 2\omega_{1,x_i}\cos(\omega_{rf}t) & 0 \end{pmatrix}.$$

For further consideration, it's convenient to transfer the system from the fixed laboratory frame into a rotating one. We choose the rotating frame such that it rotates at an angular frequency ω_{rf} and in the same sense as the Larmor frequency. The magnetization vector in the rotating frame is expressed by

$$\boldsymbol{M}_i(t) = \underline{\underline{U}}(t)\boldsymbol{M}'_i(t), \tag{1.18}$$

where the transformation matrix

$$\underline{\underline{U}}(t) = \begin{pmatrix} \cos(\omega_{rf}t) & -\sin(\omega_{rf}t) & 0 \\ \sin(\omega_{rf}t) & \cos(\omega_{rf}t) & 0 \\ 0 & 0 & 1 \end{pmatrix}. \tag{1.19}$$

Combining equations (1.16), (1.17) and (1.18) gives

$$\frac{d\boldsymbol{M}'_i(t)}{dt} = \left[\underline{\underline{U}}^{-1}(t)[\underline{\underline{\Omega_{0,i}}} + \underline{\underline{\Omega_{1,i}}}(t)]\underline{\underline{U}}(t) - \underline{\underline{U}}^{-1}(t)\frac{d}{dt}\underline{\underline{U}}(t)\right] \boldsymbol{M}'_i(t) \tag{1.20}$$

$$\frac{d\boldsymbol{M}'_i(t)}{dt} = \underline{\underline{\Omega}}'(t)\boldsymbol{M}'_i(t). \tag{1.21}$$

After applying the transformation, equation (1.20) can be written as

$$\frac{d\boldsymbol{M}'_i(t)}{dt} = [(\boldsymbol{\omega}_0 - \boldsymbol{\omega}_{rf}) + \boldsymbol{\omega}_{1,i}(t)]\, \boldsymbol{M}'_i(t), \tag{1.22}$$

where

$$\boldsymbol{\omega}_{rf} = \begin{pmatrix} 0 \\ 0 \\ \omega_{rf} \end{pmatrix}; \quad \boldsymbol{\omega}_{1,i}(t) = \begin{pmatrix} \omega_{1,x_i}\,(1 + \cos(2\omega_{rf}t)) + \omega_{1,y_i}\sin(2\omega_{rf}t) \\ \omega_{1,y_i}\,(1 + \cos(2\omega_{rf}t)) - \omega_{1,x_i}\sin(2\omega_{rf}t) \\ 2\omega_{1,z_i}\cos(\omega_{rf}t) \end{pmatrix}; \quad \boldsymbol{\omega}_0 = \begin{pmatrix} 0 \\ 0 \\ \boldsymbol{\omega}_{0,i} \end{pmatrix}.$$

We now neglect in the rotating frame all the time-dependent terms since they aren't contributing to the perturbation of the magnetization ("off-resonant" by $2\omega_{0,i}$ or $\omega_{0,i}$), which gives rise to a time-independent radio-frequency field

$$\boldsymbol{\omega}_{1,i} = \omega_{1,x_i}\boldsymbol{e}'_x + \omega_{1,y_i}\boldsymbol{e}'_y. \tag{1.23}$$

We therefore obtain

$$\frac{d\boldsymbol{M}'_i(t)}{dt} = \left(\omega_{1,x_i}\boldsymbol{e}_x + \omega_{1,y_i}\boldsymbol{e}_y + (\omega_{0,i} - \omega_{rf})\,\boldsymbol{e}_z\right) \times \boldsymbol{M}'_i(t) = \begin{pmatrix} 0 & -\Delta\omega_i & \omega_{1,y_i} \\ \Delta\omega_i & 0 & -\omega_{1,x_i} \\ -\omega_{1,y_i} & \omega_{1,x_i} & 0 \end{pmatrix} \boldsymbol{M}'_i(t), \tag{1.24}$$

where $\Delta\omega_i = \omega_{0,i} - \omega_{rf}$ is the deviation from the so-called "on-resonant" situation in which $\omega_{rf} = \omega_{0,i}$. The solution of this differential equation is the precession of the magnetization around the effective magnetic field vector represented in figure 1.3 (b)

$$\boldsymbol{\omega}_{eff,i} = \boldsymbol{\Delta\omega}_i + \boldsymbol{\omega}_{1,i},$$

with an amplitude

$$\omega_{eff,i} = \sqrt{\Delta\omega_i^2 + \omega_{1,x_i}^2 + \omega_{1,y_i}^2}\,. \tag{1.25}$$

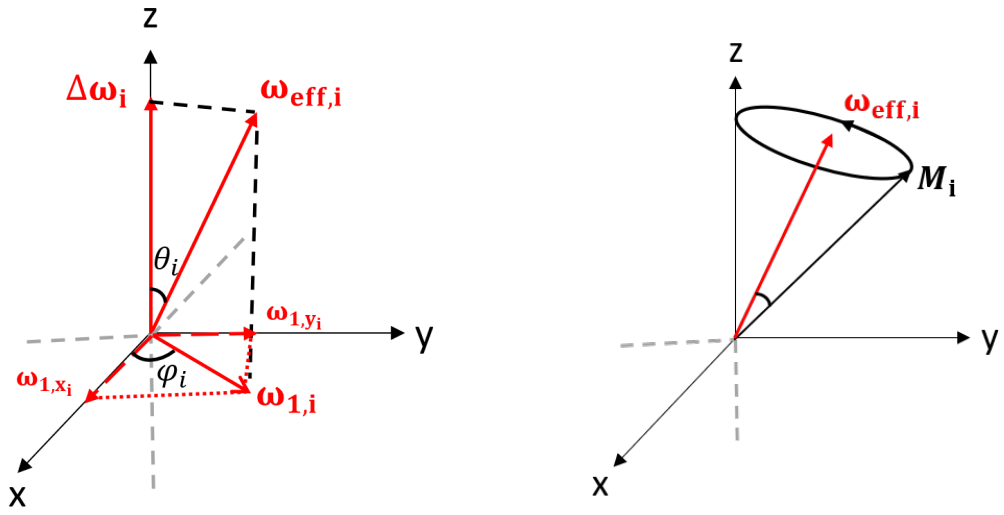

Figure 1.3: (a): In the rotating frame, the effective angular frequency $\boldsymbol{\omega}_{eff,i}$ is the vector sum of $\boldsymbol{\Delta\omega}_i$ and $\boldsymbol{\omega}_{1,i}$. This latter is the vector sum of ω_{1,x_i} and ω_{1,y_i}. The tilt angle θ_i is defined as the angle between $\boldsymbol{\omega}_{eff,i}$ and $\boldsymbol{\Delta\omega}_i$, and ϕ_i is the angle between $\boldsymbol{\omega}_{1,x_i}$ and $\boldsymbol{\omega}_{1,i}$. (b): Precession of the magnetization $\boldsymbol{M_i}$ after an NMR experiment in a magnetic field $\boldsymbol{\omega}_{eff,i}$.

Figure 1.3 illustrate the precession of $\boldsymbol{M}_i$ and $\boldsymbol{\omega}_{eff}$. We now define

$$\cos(\phi_i) = \frac{\omega_{1,x_i}}{\omega_{1,i}}; \quad \sin(\phi_i) = \frac{\omega_{1,y_i}}{\omega_{1,i}}; \quad \cos(\theta_i) = \frac{\Delta\omega_i}{\omega_{eff,i}}; \quad \sin(\theta_i) = \frac{\omega_{1,i}}{\omega_{eff,i}}; \quad \beta_i = \omega_{eff,i}t.$$

The expression of the magnetization at any time t in spherical coordinates for different initial conditions

1. $M_i(0) = M_{eq}\boldsymbol{e}_x$

$$M_i(t) \to M_{eq}\begin{pmatrix} \sin^2(\theta_i)\cos^2(\phi_i) + \left(\sin^2(\theta_i)\sin^2(\phi_i) + \cos^2(\theta_i)\right)\cos(\beta_i) \\ \sin(\theta_i)\cos(\phi_i)\sin(\phi_i)\left(\cos(\beta_i) - 1\right) - \cos(\theta_i)\cos(\phi_i)\sin(\beta_i) \\ \sin(\phi_i)\sin(\beta_i) + \cos(\theta_i)\sin(\theta_i)\left(\cos(\beta_i) - \cos^2(\phi_i) - \sin^2(\phi_i)\cos(\beta_i)\right) \end{pmatrix} \tag{1.26}$$

2. $M_i(0) = M_{eq}\boldsymbol{e}_y$

$$M_i(t) \to M_{eq}\begin{pmatrix} \sin(\theta_i)\cos(\phi_i)\sin(\phi_i)\left(\cos(\beta_{eff,i}) - 1\right) + \cos(\theta_i)\cos(\phi_i)\sin(\beta_i) \\ \sin^2(\phi_i) + \cos^2(\phi_i)\cos(\beta_i) \\ \cos(\theta_i)\cos(\phi_i)\sin(\phi_i)\left(1 - \cos(\beta_i)\right) + \sin(\theta_i)\cos(\phi_i)\sin(\beta_i) \end{pmatrix} \tag{1.27}$$

3. $M_i(0) = M_{eq}\boldsymbol{e}_z$

$$M_i(t) \to M_{eq}\begin{pmatrix} -\sin(\phi_i)\sin(\beta_i) + \cos(\theta_i)\sin(\theta_i)\cos^2(\phi_i)\left(\cos(\beta_i) - 1\right) \\ \cos(\theta_i)\cos(\phi_i)\sin(\phi_i)\left(1 - \cos(\beta_i)\right) - \sin(\theta_i)\cos(\phi_i)\sin(\beta_i) \\ \cos^2(\theta_i)\cos^2(\phi_i) + \cos^2(\theta_i)\sin^2(\phi_i)\cos(\beta_i) + \sin^2(\theta_i)\cos(\beta_i) \end{pmatrix} \tag{1.28}$$

1.2.4 Off-resonant effects on NMR pulses

In this section, we will discuss the "on-resonant" and the "off-resonant" effects in NMR. It is commonly known among the NMR community that the system is considered to be "on resonant" when the frequency of the applied magnetic field ω_{rf} is exactly at the Larmor frequency of the nuclei ω_0, i.e, $\Delta\omega = 0$. However, as the name indicates, the "off-resonant" case in NMR corresponds to a situation where ω_{rf} starts to deviate from the resonance frequency ω_0, i.e, $\Delta\omega \neq 0$.

For simplicity, we consider in this section that $\omega_{1,i}$ is along the -x axis, i.e. $\phi_i = 180°$. In addition, for this discussion from equation (1.28) we derive the explicit equations showing the variation of the magnetisation $\boldsymbol{M}_i(t)$ as a function of $x_i = \frac{\Delta\omega_i}{\omega_{1,i}}$ and $\beta_{nom,i} = \omega_{1,i}t$ the nominal pulse angle also called the resonant angle

$$\frac{M_i(t)}{M_{eq}} = \begin{pmatrix} \frac{x_i}{1+x_i^2}(\cos(\sqrt{1+x_i^2}\beta_{nom,i}) - 1) \\ \\ \frac{1}{\sqrt{1+x_i^2}}\sin(\sqrt{1+x_i^2}\beta_{nom,i}) \\ \\ \frac{1}{1+x_i^2}(x_i^2 + \cos(\sqrt{1+x_i^2}\beta_{nom,i})) \end{pmatrix}. \tag{1.29}$$

1. The first case to deal with, is when the transmitter frequency is exactly at the Larmor frequency $\omega_{rf} = \omega_{0,i}$, known by "on-resonant" pulse. In this case $\omega_{eff,i} = \omega_{1,i}$. The time dependance of the magnetization becomes

$$\boldsymbol{M_i}(t) = M_{eq}(\sin(\beta_{nom,i})\boldsymbol{e_y} + \cos(\beta_{nom,i})\boldsymbol{e_z}). \tag{1.30}$$

   As we can clearly see the equilibrium magnetization is now no longer parallel to the effective field, and so the magnetization will precess around $\boldsymbol{B_1}$ in the (y, z) plane. This will bring it towards the transversal plane, which is what we require.
   $\beta_{nom,i}$ refers to the pulse angle, through which we can control the amount of the rotation angle of the magnetization. The most commonly used angles in experiments are $\frac{\pi}{2}$ and π pulses. A $\frac{\pi}{2}$ pulse induces a rotation of the magnetization from the equilibrium position to the $+y$ axis. A π pulse inverts the magnetization to the $-z$ axis.

2. The second case we will deal with is the "off-resonant" one. Referring to the case we treated before ("on-resonant" $\boldsymbol{\Delta\omega_i} = 0$), we see that when $\boldsymbol{\Delta\omega_i}$ starts to become larger and comparable in size with the radio frequency field strength $\boldsymbol{\omega_{1,i}}$, the effective field $\boldsymbol{\omega}_{eff,i}$ begins to move from the direction $\boldsymbol{\omega}_{1,i}$ towards $\pm\boldsymbol{\Delta\omega_i}$, this will cause the magnetization to follow a more complex path.

The explicit equations for the nominal pulse angles $\frac{\pi}{2}$ and π can be obtained from equation (1.29) by replacing $\omega_{1,i}t$ respectively by $\frac{\pi}{2}$ and π. The simulations are shown in the figures 1.4 and 1.5. We will interpret the simulations of $\beta_{nom,i} = \frac{\pi}{2}$ and $\beta_{nom,i} = \pi$ impulse cases more deeply in the following of this section. We should note that both x and y components of the magnetization are detected in an NMR signal.

$\frac{\pi}{2}$ pulse case

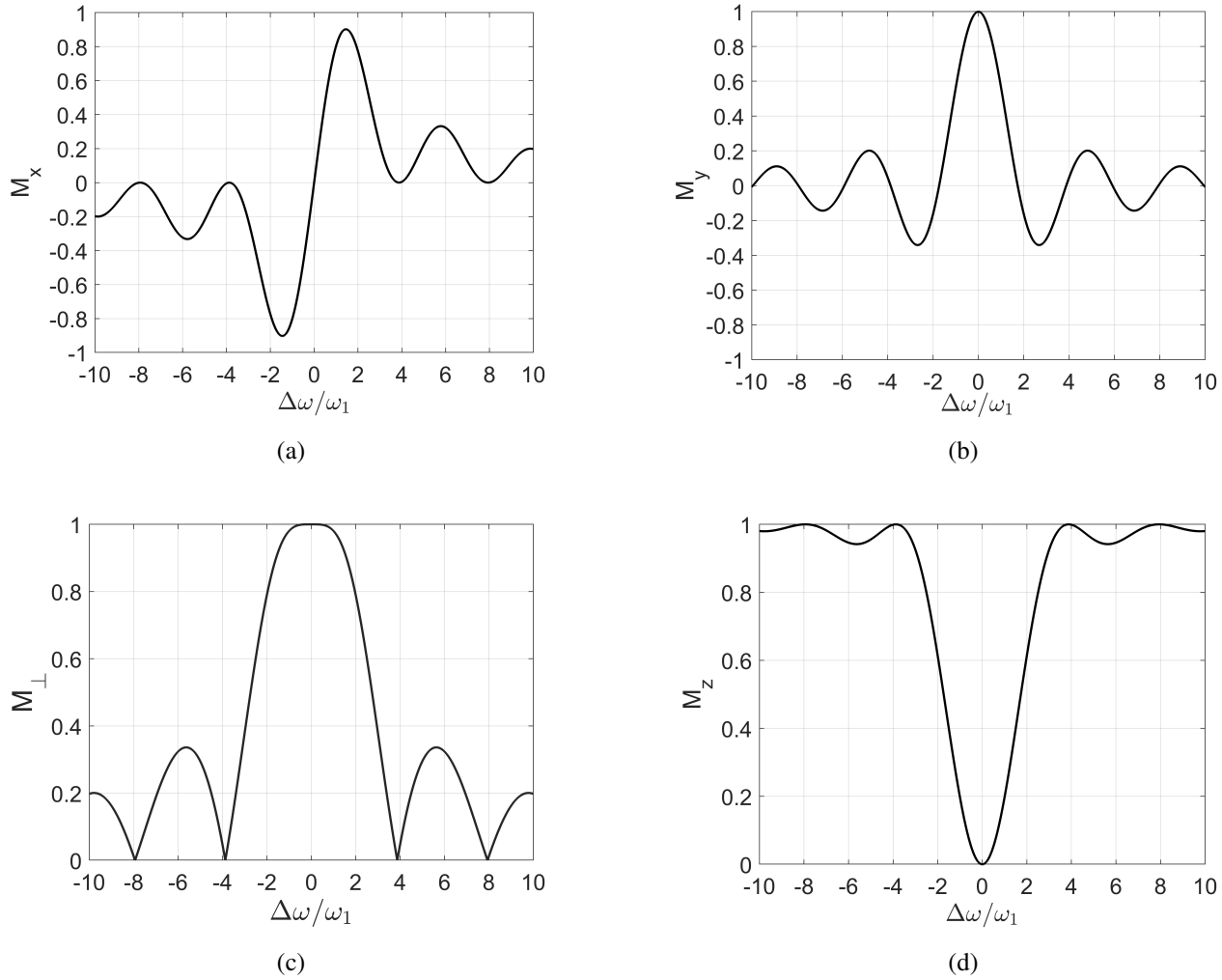

Figure 1.4: Magnetization M_x (a), M_y (b), $M_\perp$ (c) and M_z (d) under the influence of an off-resonance frequency for an on-resonant $\pi/2$ pulse angle.

Two things to note from figure 1.4

1. Firstly, we can notice that for $x_i = 0$ ("on-resonant"), the magnetization ends up along the y axis (Figure 1.4 (b)). For the "off-resonant" case, the vector starts to leave the transverse plane, the NMR signal observed after such a pulse will be weaker than that of the "on-resonant" case, because the magnitude of the transverse magnetization becomes smaller. As a result, the magnitude of the magnetization of the z axis starts to increase.

2. The second point to note is that the "off-resonant" pulses produce some x-magnetization which increases linearly and some z-magnetization which increases quadratically at the expense of the quadratic loss of the y-magnetization.

π pulse case

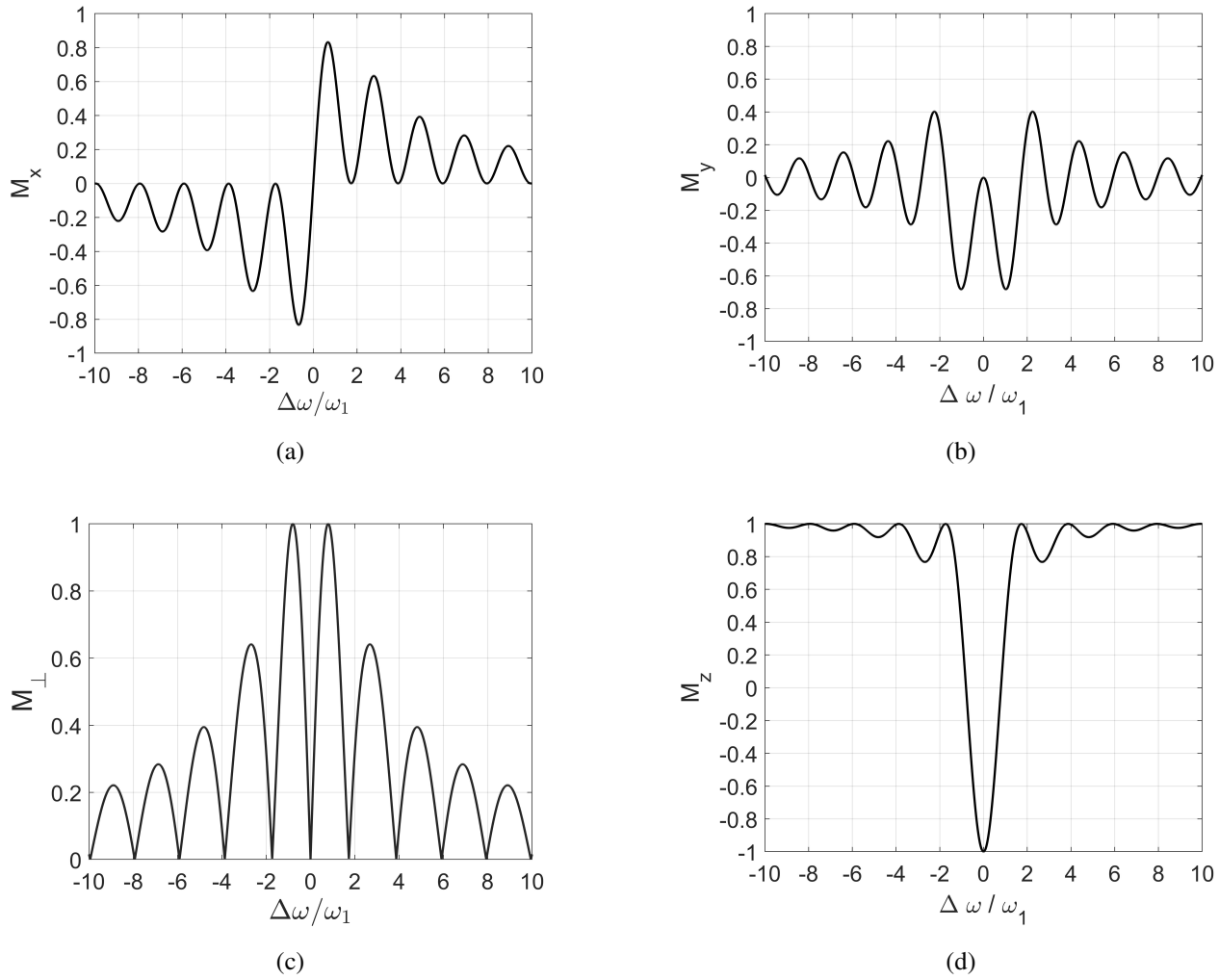

Figure 1.5: Magnetization M_x (a), M_y (b), $M_\perp$ (c) and M_z (d) under the influence of an off-resonance frequency for an on-resonant π pulse angle.

Three things to note from figure 1.5

1. Firstly, we can remark that for $x_i = 0$ ("on-resonant"), the magnetization ends up along the $-z$ axis (Figure 1.5 (c)). The NMR signal is zero since there is no finite transverse component of the magnetization available to induce such a signal. For the "off-resonant" cases, the magnetization starts to move away from -z axis to the transverse plane and an NMR signal begins to appear as the magnitude of the transverse magnetization components is no longer zero. For $\left|\frac{\Delta\omega}{\omega_1}\right| = 0.85$, the π pulse behaves like a $\frac{\pi}{2}$ pulse where $M_\perp = 1$.

2. The second point to note is that the "off-resonant" pulses produce some x-magnetization, which increases linearly and some y-magnetization which increases quadratically at the expense of the quadratic loss of the z-magnetization.

3. The third point to notice is that the NMR signal amplitude ($M_\perp$) after a π pulse is more sensitive to the variation of x_i than the $\frac{\pi}{2}$ pulse.

1.2.5 Magnetization dynamics under inhomogeneous $\boldsymbol{B}_0$ and $\boldsymbol{B}_1(t)$

In an NMR experiment, each set of spins positioned in a voxel "i" contributes to the NMR signal. The final signal is therefore the sum of the contributions from all the spin sets located in different voxels. The net magnetization across the sample

$$\boldsymbol{M}(t) = \sum_{i=1}^{N} \boldsymbol{M}_i(t). \tag{1.31}$$

The amplitude and phase of the NMR signal are determined by the net magnetization vector, which depends on the number of spins aligned with the external magnetic field. The amplitude is proportional to the net magnetization vector, while the phase is related to the angle between the net magnetization vector and the oscillating magnetic field $\boldsymbol{\omega}_{1,i}(\boldsymbol{r}, t)$.

Considering the contribution of all voxels i, we obtain the Bloch equation using equations (1.31) and (1.20), with a relaxation term $\underline{\underline{R}}$ that includes the effect of relaxation mechanisms on the return of magnetization to its equilibrium state

$$\frac{d\boldsymbol{M}(t)}{dt} = \sum_{i=1}^{N} \frac{d\boldsymbol{M}_i(t)}{dt} + \underline{\underline{R}}\boldsymbol{M}(t) + \frac{1}{T_1} M_{eq} \boldsymbol{e}_z$$

$$\frac{d\boldsymbol{M}(t)}{dt} = \sum_{i=1}^{N} \left[\underline{\underline{\Omega_{0,i}}} + \underline{\underline{\Omega_{1,i}}}(t)\right] \boldsymbol{M_i}(t) + \underline{\underline{R}}\boldsymbol{M}(t) + \frac{1}{T_1} M_{eq} \boldsymbol{e}_z, \tag{1.32}$$

where

$$\underline{\underline{R}} = \begin{pmatrix} -\frac{1}{T_2} & 0 & 0 \\ 0 & -\frac{1}{T_2} & 0 \\ 0 & 0 & -\frac{1}{T_1} \end{pmatrix} \tag{1.33}$$

T_2 is the relaxation time of the transverse magnetization and T_1 is the longitudinal relaxation time.

1.3 NMR pulse sequences

An NMR experiment uses a series of radio frequency pulses, called a pulse sequence, to determine T_1 and T_2 of a specific sample. During a pulse, $\boldsymbol{\omega}_1(\boldsymbol{r}, t_p)$ is activated for a certain time t_p. At the end of the pulse, $\boldsymbol{M}(t_p)$ is given by the equations (1.26), (1.27) or (1.28) based on the initial state of the magnetization before the pulse. Here, and in the following, we will treat the net magnetization such that the equilibrium state of the magnetization lies along the z-axis (equation (1.28)) and the relaxation term $\underline{\underline{R}}$ will be omitted.

We describe in this section the pulse sequences used throughout my thesis to calibrate the pulses and measure the longitudinal relaxation time T_1 and the transverse relaxation time T_2.

1.3.1 Definition of a pulse sequence

There are three steps in an NMR pulse sequence

1. Preparation or Excitation

   The excitation pulse (or a group of pulses) is applied to the sample to prepare a non-equilibrium initial state.

2. Evolution

   After the excitation pulse, the second step is the evolution of the magnetization in which we wait for a time interval to allow the spins to relax. In an NMR experiment, τ_i is the only parameter that varies during the experiment. Here we will use indexing to distinguish this parameter from other delays that might be present in the pulse sequence. This step may involve pulses or a group of pulses in addition to the time interval τ_i. Moreover, τ_i can be zero.

3. Detection

   The last step is the detection of the NMR signal. This step consists of applying a detection pulse or acquiring the NMR signal by detecting the magnetization in the transversal plane $\boldsymbol{M}_{\perp}$.

Following every pulse sequence, we wait an interval τ_{wait}, where the magnetization returns to its thermal equilibrium state M_{eq}. To assure this, the waiting interval τ_{wait} must be five times the spin-lattice relaxation time T_1 of the measured sample. During the detection, the magnetization is calculated using the equation (2.10) (from the following chapter 2) for each value of τ_i and then plotted as a function of it. The set of points for different value of τ_i are then fitted for each selected experiment configuration.

1.3.2 FID Experiment

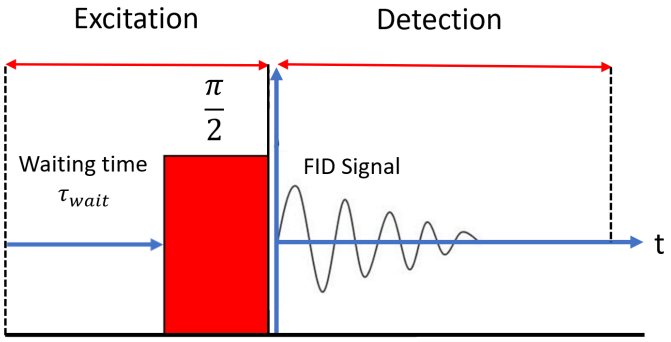

Figure 1.6: Example for a free induction decay (FID) pulse sequence.

An FID pulse sequence is composed of a waiting time τ_{wait}, the application of an excitation pulse $\frac{\pi}{2}$, and, finally, the detection. After such pulse, the magnetization ends up along the y axis (equation (1.30) for $\beta_{nom} = \frac{\pi}{2}$). The precession of the magnetization induces an oscillating electric current inside the detection coil, which decays with time. Therefore, the resulting signal after such a pulse is known as Free Induction Decay (FID). The schematic of the FID sequence is shown in figure 1.6.

1.3.3 Nutation Experiment

Calibrating RF pulses in NMR requires performing nutation experiments at each field, which is a crucial preliminary experiment [15]. The main objective of nutation experiments is to determine the pulse durations required to achieve a $\frac{\pi}{2}$ and π pulses. The method consists of performing consecutive FID experiments where the pulse angle $\beta = \omega_1 t_p$ is varied by changing the pulse length t_p. We use a rapidly relaxing sample (T_1 very small) to minimise the time interval τ_{wait} needed to wait between two successive FIDs. This approach reduces the experimental time required for pulse calibration.

At the end of the nutation experiment, we fit the y-component of the magnetization for different values of t_p by the equation(1.29) for the on-resonant case (equation (1.30))

$$M_\perp(t_p) = M_{eq} \sin(\omega_1 t_p) \tag{1.34}$$

We extract from the fit the pulse strength ω_1 and M_{eq}. In figure 1.7, we show an example of a nutation experiment performed on the resistive magnet at a magnetic field strength of 28 T ($f_0 = 1.2$ GHz) of a ^{1}H water reference sample containing $GdCl_3$ of a concentration $c = 60$ mMol/l, during which the y-component of the magnetization M_y was measured as a function of the pulse length t_p. Here we found $\omega_1 = 2\pi$ 85 krad s^{-1} ($f_1 = 85$ kHz) and $M_{eq} = 694$. Then we use the fit value of ω_1 to calculate $t_{\frac{\pi}{2}} = 2.95\ \mu s$ and $t_\pi = 5.9\ \mu s$.

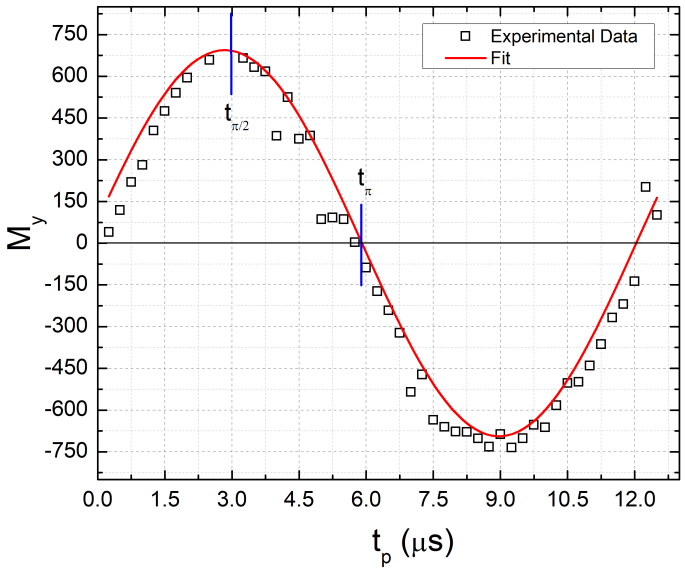

Figure 1.7: Example of a nutation experiment performed on the resistive magnet at a magnetic field strength of 28 T ($f_0 = 1.2$ GHz) of a ^{1}H water reference sample containing $GdCl_3$ of a concentration $c = 60$ mMol/l, during which the y-component of the magnetization M_y was measured as a function of the pulse length t_p. The symbols represent the experimental data, and the red line is the corresponding fit curve.

1.3.4 T_1 Experiment

The recovery process of the longitudinal component M_z after an excitation pulse back to its equilibrium value M_0 is known as longitudinal relaxation. T_1 is the longitudinal relaxation time needed for this return, expressed by

$$\frac{dM_z}{dt} = \frac{1}{T_1}(M_0 - M_z) \tag{1.35}$$

which has the solution

$$M_z(\tau_i) = M_{eq}\left(1 - C\exp\left(-\frac{\tau_i}{T_1}\right)\right) \tag{1.36}$$

where C represents the inversion rate of the RF pulses ($C = 2$ for a perfect inversion recovery sequence and $C = 1$ for a perfect saturation recovery sequence), τ_i the variable time interval, and M_{eq} the equilibrium magnetization state.

There are two popular sequences to measure the longitudinal relaxation time of the spins T_1: the inversion recovery (IR) (Section 1.3.4) and the progressive saturation recovery (PSR) (Section 1.3.4) [16–18]. Both pulse sequences consist of an excitation pulse or a series of excitation pulses, a magnetization evolution $\boldsymbol{M}(\tau_i)$, and an FID pulse for detection.

Inversion recovery (IR)

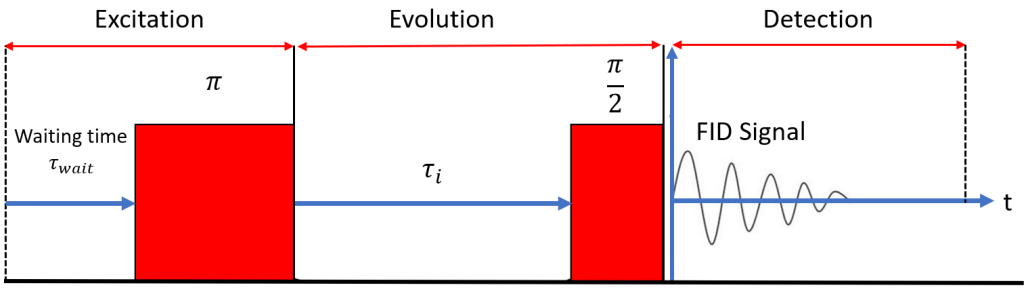

Figure 1.8: Example of an inversion-recovery (IR) pulse sequence

The excitation pulse is a π pulse, known as the "inversion pulse". It inverts the magnetization vector, and so, as a function of the time interval τ_i, the recovery goes from $-M_{eq}$ to M_{eq} accordingly to the equation (1.36) for $C = 2$. This process is called "inversion recovery", and is shown in figure 1.8.

Progressive saturation recovery (PSR)

The "saturation pulse" consists of a series of $\frac{\pi}{2}$ pulses, separated by a time interval $\tau_s \approx T_2^*$. It progressively saturates the magnetization vector ($M_z = 0$ and $M_\perp = 0$), and so, as a function of the time interval τ_i (with $\tau_s << \tau_i$), the recovery goes from zero to M_{eq} accordingly to the equation (1.36) for $C = 1$. This process is called "progressive saturation recovery" and is shown in figure 1.9. This method is very useful when T_1 is long since it is not necessary to wait for $5T_1$ between two consecutive pulse sequences.

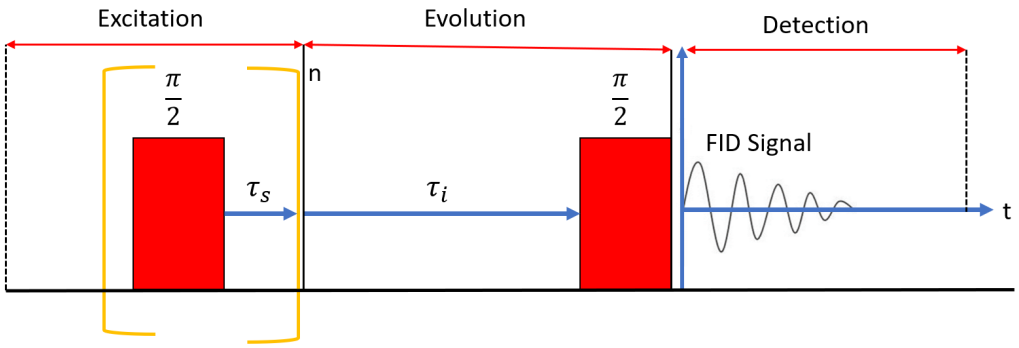

Figure 1.9: Example of the progressive saturation-recovery pulse (PSR) sequence. n is the number of $\frac{\pi}{2}$ pulses separated by a fixed time interval τ_s (a pulse train "comb").

Practical implementation of the sequence

For T_1 experiment, we need to generate a list of n time intervals τ_i for the pulse program. Typically n time intervals τ_i are chosen equidistant on a logarithmic scale

$$\tau_i = \tau_n . k^{(i-n)} \tag{1.37}$$

where k is the base of the logarithm, which is calculated based on the ratio between the last time interval τ_n and the first time interval τ_1

$$k = \left(\frac{\tau_n}{\tau_1}\right)^{\frac{1}{n-1}} \tag{1.38}$$

To ensure full recovery of magnetization M_{eq} at the end of the IR pulse sequence, we choose τ_n equal to $5T_1$. Furthermore, we choose τ_1 such that at the middle point $\tau_{\frac{n}{2}}$, the sign of M_z changes, i.e., for $M_z(\tau_{\frac{n}{2}}) = 0$ (see figure 1.10 (b)). For $n = 16$ measurements, we obtain $k = 1.3$. This approach ensures the experimental data coverage of M_z from $-M_{eq}$ to M_{eq} (figure 1.10 (b)) and saves experiment time. It is convenient, therefore, to plot the magnetization $M(\tau_i)$ as a function of $\log(\tau_i)$. Figure 1.10 shows an

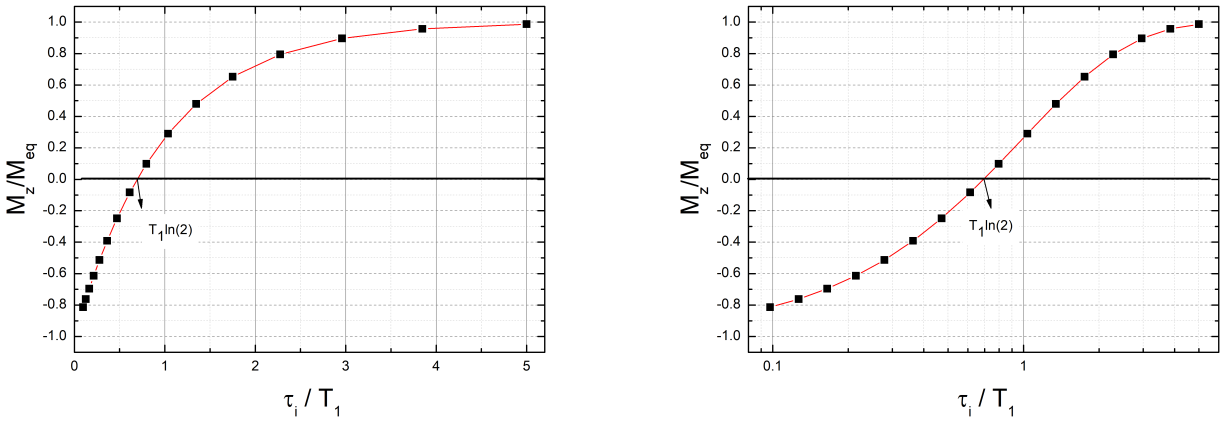

Figure 1.10: Example of the recovery curve of the magnetization after an IR pulse sequence in both (a) linear and (b) logarithmic time scales.

example of the recovery curve of the magnetization after an IR pulse sequence in both linear and logarithmic time scales. We obtain $M_z = 0$ for $\tau_{\frac{n}{2}} = T_1 \ln(2)$.

1.3.5 T_2 Experiment

The transverse relaxation time T_2 describes the decay of the transverse magnetization $M_\perp$ after its excitation. Following a radio frequency pulse, the magnetization vector initially lies in the transverse plane. However, due to magnetic field inhomogeneity, a decoherence of the spins occurs, and the transverse magnetization starts to decay. The relaxation process is expressed by

$$\frac{dM_\perp}{dt} = -\frac{M_\perp}{T_2} \tag{1.39}$$

which has an exponential decay as a solution

$$M_\perp(\tau) = M_\perp(0) \exp\left(\frac{-\tau_i}{T_2}\right) \tag{1.40}$$

However, the impact of the magnetic field inhomogeneity $\Delta\omega_{\text{inhom}}$, which causes additional spin decoherence and accelerates the decay of the transverse magnetization, must be taken into account. This means

$$\frac{1}{T_2^*} = \frac{1}{T_2} + \Delta\omega_{\text{inhom}} \tag{1.41}$$

where $\Delta\omega_{\text{inhom}}$ comes from the magnetic field inhomogeneity. The decoherence induced by this term is removed by the introduction of a train of refocusing π pulses at regular intervals during the evolution, which makes it possible to measure the decay of the transverse magnetization T_2 due to the spin-spin interactions within the sample.

There are several methods used to measure the transverse relaxation time of the spins T_2. The method used here is the Carr-Purcell-Meiboom-Gill (CPMG) sequence [19, 20].

CPMG sequence

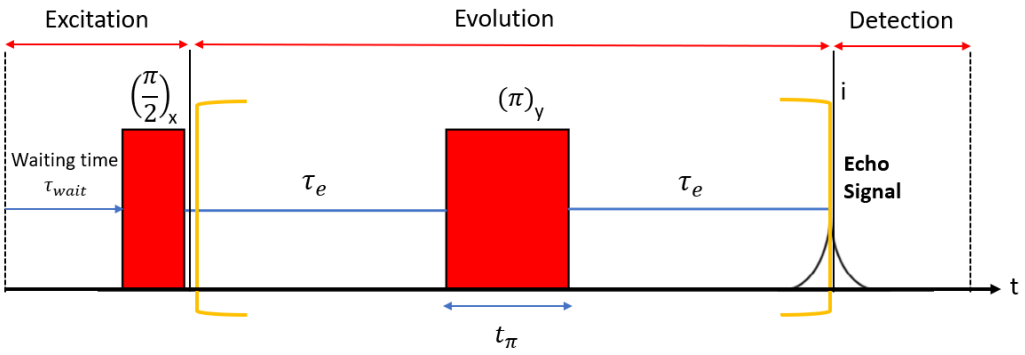

Figure 1.11: Example of the CPMG pulse sequence. i indicates the repetition rate of the refocusing pulses.

The CPMG sequence consists of an excitation pulse that flips the magnetization into the transverse plane, followed by a series of refocusing π pulses separated by a time interval of $2\tau_e$ and, finally, the detection.

After the $\frac{\pi}{2}$ pulse, initially, the spins precess in phase but due to the transverse relaxation $\frac{1}{T_2^*}$, it gradually dephases over time. The π pulses are applied then to refocus the magnetization at specific times, creating an echo signal that can be detected by NMR. Two methods were used to detect echoes

1. The first method involves a 2D experiment, in which a single echo signal is detected after repeated application of the evolution block (i times), as shown in figure 1.11. The value of i is consecutively selected from a list of n echoes. The echoes are then recorded at different time intervals

$$\tau_i = 2(\tau_e + t_\pi)i \tag{1.42}$$

   where τ_e is the echo time fixed and optimized so that the last time interval $\tau_{i,max} = 5T_2$. Two consecutive i are separated by the waiting time $\tau_{\text{wait}} = 5T_1$. The time consumed for this experiment will be

$$t_{\text{exp}} = \sum_{i=1}^{i=n} \tau_i + n\tau_{\text{wait}} \tag{1.43}$$

2. The second method shown in figure 1.12 involves a 1D experiment, wherein all the n echoes are detected in a single scan. In this case, τ_e is selected to satisfy $2(\tau_e + t_\pi)n > 5T_2$. This method is less time consuming than the first one with $t_{\text{exp}} = 2(\tau_e + t_\pi)n + \tau_{\text{wait}}$.

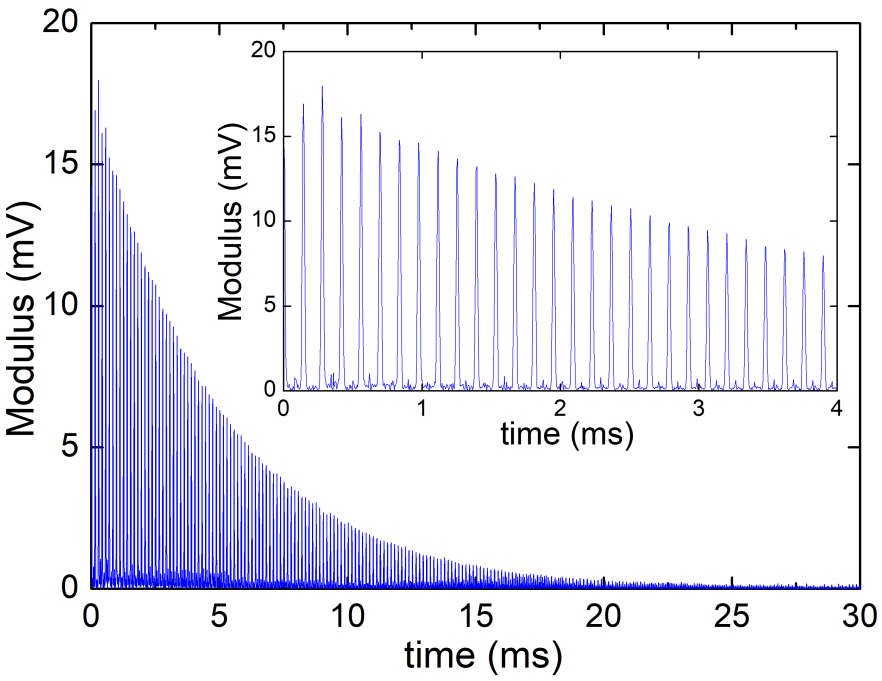

Figure 1.12: Example of CPMG (1D) experiment of ^1H NMR of an aqueous (9:1 D_2O : H_2O) solution of $GdCl_3$ for a concentration $c = 10$ mMol performed at $B_0 = 32.5$ T ($f_0 = 1382$ MHz) in the resistive magnets. All the echoes are recorded at the same time.

Chapter 2: Processing of NMR data obtained in resistive magnets

The NMR experiment does not directly provide the nuclear magnetization, nor the relaxation times, such as T_1 and T_2, which are essential for understanding the mechanisms of molecular relaxation. They are derived from the data processing procedure. Several commercial software applications exist to facilitate data processing. However, these software applications are not suitable for processing data in resistive magnets that have low field stability and inhomogeneity compared with superconducting magnets. Therefore, we developed special data analysis methods that allow efficient extraction of the relevant parameters from the NMR experiment.

In particular, special routines for baseline and frequency offset correction were developed, which will be the focus of this chapter, in addition to the standard processing methods found in NMR textbooks and articles, which we will briefly discuss.

2.1 NMR data analysis in a stable and homogeneous field

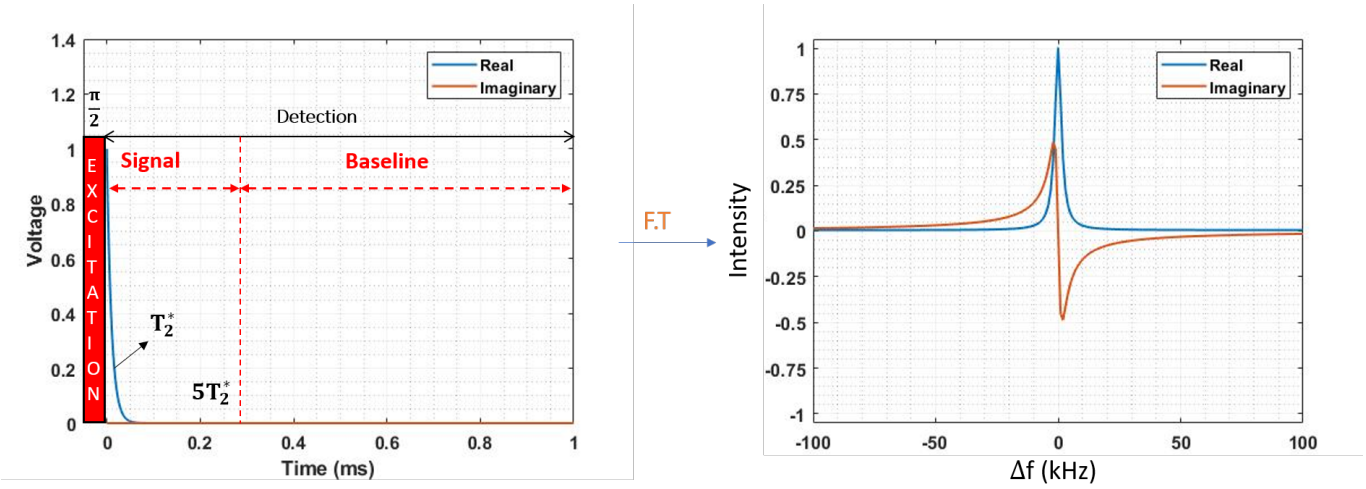

Figure 2.1: Simulation of an NMR FID for the ideal case: on-resonant case $\Delta f = 0$, $\phi_{elec} = 0$, and the baseline offset equals zero. Left:Time domain signal. Right: Frequency domain signal.

After the excitation, the NMR signal is recorded in presence of the static field $\boldsymbol{B}_0$. The data are recorded in the rotating frame of the excitation frequency f_{rf}: A quadrature detection method [21] is applied leading to the detection of both, M_x (real part) and M_y (imaginary part) components of the precessing magnetization (figure 2.1). These two signals are then used to build a complex time-domain signal

$$M_{\perp}(t) = M_x(t) + iM_y(t). \tag{2.1}$$

The transverse magnetization $M_\perp(t)$ decays with an exponential time constant T_2^*, which is typically due to the inhomogeneities of the local static magnetic field. $M_\perp(t)$ can be written

$$M_\perp(t) = M_{eq} \exp\left(\frac{-t}{T_2^*}\right) \exp(i\phi_{\text{elec}}) \exp(i(2\pi\Delta f)t), \tag{2.2}$$

where ϕ_{elec} is a constant phase induced by the probe electronic components of the NMR spectrometer. This phase is common to all measurements. $\Delta f = f_0 - f_{rf}$ is a frequency specific to each measurement and represents the deviation from the on-resonant situation ($f_{rf} = f_0$).

The Fourier transform of the $M_\perp(t)$ signal provides the NMR spectrum centered at Δf

$$I(f) = FT[M_\perp(t)] = \frac{1}{2\pi} \int_{-\infty}^{+\infty} M_\perp(t) \exp^{-i2\pi ft}\, dt \tag{2.3}$$

The Fourier transform then gives a spectrum at Δf, where the real part is a spectrum with an absorption mode of Lorentzian lineshape, and the imaginary part is a spectrum with a dispersion mode of Lorentzian shape, as shown in figure 2.1

$$M_\perp(t) \xrightarrow{\text{F.T}} I(f)$$

$$M_{eq} \exp\left(\frac{-t}{T_2^*}\right) \exp(i(2\pi\Delta f)t) \xrightarrow{\text{F.T}} \frac{M_{eq}}{2\pi} \left(\underbrace{\frac{1/T_2^*}{(1/T_2^*)^2 + 4\pi^2(f-\Delta f)^2}}_{\text{Real}} + i \underbrace{\frac{-2\pi(f-\Delta f)}{(1/T_2^*)^2 + 4\pi^2(f-\Delta f)^2}}_{\text{Imaginary}} \right) \tag{2.4}$$

For the ideal, on-resonant case, the real part is an even function centered at $\Delta f = 0$ with a maximum peak height at T_2^*, and with linewidth at half height equal to $I(\Delta f) = 1/\pi T_2^*$. It contains only positive values, with the integral resulting in $M_\perp(t = 0)$. For values far away from $\Delta f = 0$, the real part decays to zero with a power law f^{-2}. The imaginary part is an odd function also centered at $\Delta f = 0$. The resulting integral of the imaginary part is zero. For values far away from $\Delta f = 0$, the real part decays to zero with a power law f^{-1}. Figure 2.1 shows a simulation of an NMR signal for an ideal case and its corresponding spectrum in the frequency domain. The signal decays and reaches zero at $t > 5T_2^*$, where the baseline is defined.

2.1.1 First order phase correction

We use for the phase correction an integration method of the spectrum $I(f)$. The integral of the complex spectrum $I(f)$ is equal to

$$\int_{-\infty}^{+\infty} I(f)\, df = \boldsymbol{M}_\perp(t = 0) = M_{eq} \exp(i\phi) \tag{2.5}$$

$$\int_{-\infty}^{+\infty} I(f)\, df = \int_{-\infty}^{+\infty} \text{Real}[I(f)]\, df + i \int_{-\infty}^{+\infty} \text{Imag}[I(f)]\, df \tag{2.6}$$

Comparing the real and imaginary parts of the equations 2.5 and 2.5 provides two equations

$$M_{eq}\cos(\phi) = \int_{-\infty}^{+\infty} \text{Real}[I(f)]\,df \tag{2.7}$$

$$M_{eq}\sin(\phi) = \int_{-\infty}^{+\infty} \text{Imag}[I(f)]\,df \tag{2.8}$$

that allow the extraction of the corresponding phase

$$\phi = \arctan\left(\frac{\int_{-\infty}^{+\infty} \text{Imag}[I(f)]\,df}{\int_{-\infty}^{+\infty} \text{Real}[I(f)]\,df}\right) \tag{2.9}$$

The first-order phase correction is then applied by multiplication of the spectrum $I(f)$ by $\exp(-i\phi)$. For the phase corrected spectrum, the integral of the imaginary part of the spectrum is equal to zero.

2.1.2 NMR lineshape

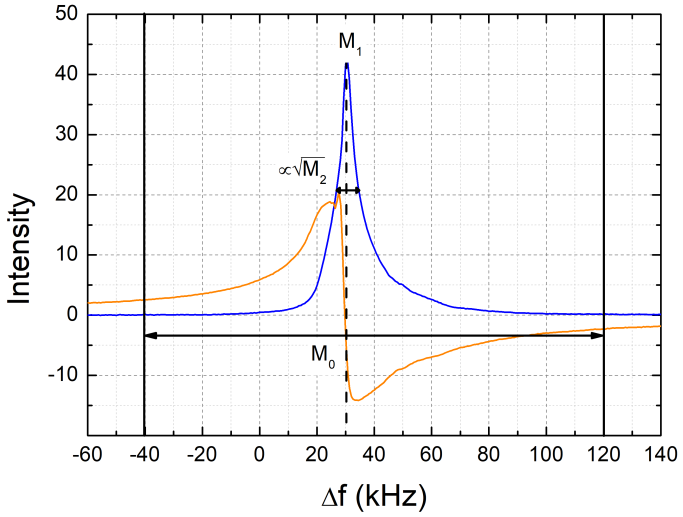

Figure 2.2: Example of ^1H NMR spectrum of an aqueous (H_2O) solution of $GdCl_3$ with a concentration c = 60 mMol/l at 24 T / 1020 MHz. The line shape deviates from a Lorentzian shape and is modeled by the moment equations. Details can be found in the text.

General NMR line shape often deviate from Lorentzian forms as can be seen in figure 2.2. The line shape of the NMR spectrum is then modeled by a model free approach as shown in figure 2.2 using moment equations

$$M_0 = \int I(f)df \quad , \quad M_1 = \frac{\int I(f)f\,df}{M_0} \quad , \quad M_2 = \frac{\int I(f)(f-M_1)^2 df}{M_0} \tag{2.10}$$

where M_0 represents the zero moment , M_1 the first moment, M_2 the second moment, $I(f)$ the signal intensity at each frequency f. The limits of the integrals (integration window size) for M_0, M_1, and M_2 are user-defined, which must be the same for all the measurements in the experiment.

Three main parameters are extracted from an NMR Spectrum

1. The integrated intensity of the spectrum M_0, which is related to the size of the transverse magnetization $M_\perp$ and is proportional to the number of spins in the sample.
2. The line position of the spectrum M_1 represents the offset frequency Δf with respect to the radio-frequency f_{rf}. In the example (figure 2.2), M_1 = 33 kHz.
3. The full width at half-height of the spectrum is proportional to $\sqrt{M_2}$ and represents the inhomogeneity of the magnetic field Δf_{inhom} and the relaxation mechanisms.

2.2 Processing of resistive magnet NMR data

In a typical NMR experiment in the resistive magnet all the cited parameters ϕ_{elec} + additional phases, baseline offset, and Δf deviate from the ideal case, so we have to apply different corrections to reduce their influence on the detected signal.

For this purpose a Matlab script was developed.

2.2.1 General description of the processing algorithm

The program carries out a systematic analysis of the experimental data as shown in the figure 2.3. It is divided into several phases

1. Importing the experimental data file (pulse program parameters , real and imaginary parts of the signals , experiment parameters). The data set can be a 1D file, as in the case of a simple FID experiment, or a 2D file, as in the case of a T_1, T_2, or nutation experiment. In the latter case, the experiment parameters include the delay list, each associated with its NMR signal.
2. Time domain corrections: Dead-time signal cutting and Baseline correction.
3. Frequency domain corrections: Field fluctuation and Phase correction.
4. Moment equations calculations: M_0, M_1, and M_2.
5. Export of the corrected spectra and the calculated parameters (M_0, M_1, and M_2) in two separate files.

The details of the program will be further detailed and discussed in the following sections.

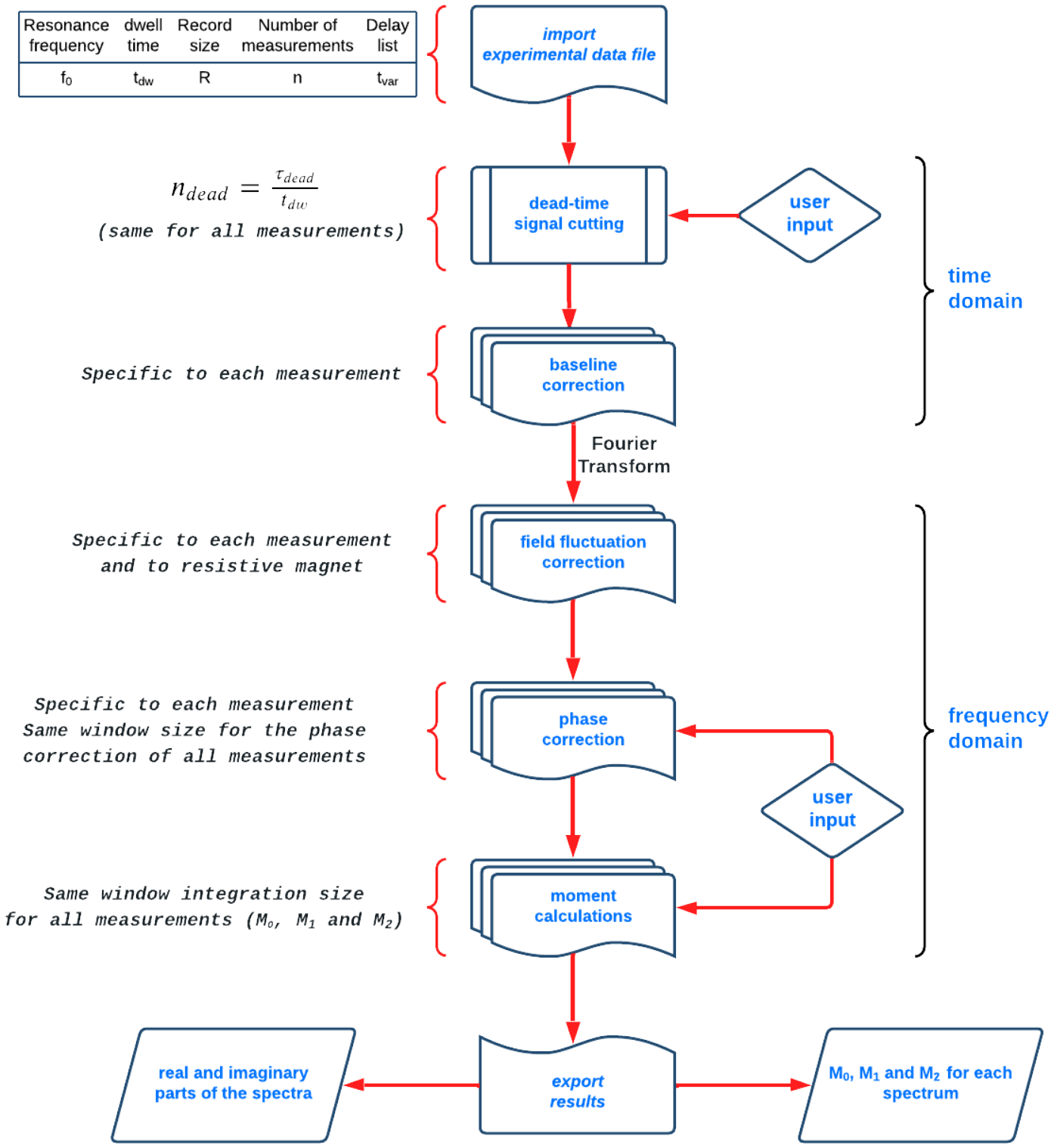

Figure 2.3: Main steps in the NMR data correction program. The corresponding program code is written in Matlab.

2.2.2 Time domain analysis

In the time domain, several problems arise, such as ringing noise and baseline offset. Several corrections must be applied to minimize their influence on the NMR signal before applying the Fourier transform. This will be the subject of this section.

Signal cutting

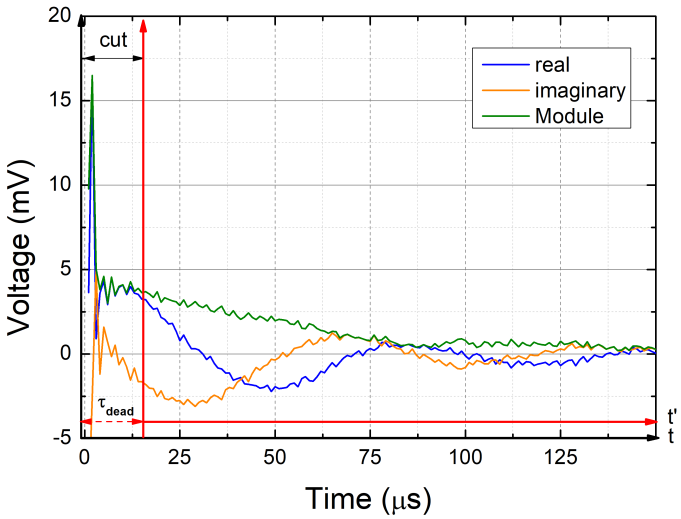

Figure 2.4: Signal cutting by few data points to take out the ringing noise induced by the amplifiers.

After the pulse, the amplifier that is used to increase the NMR signal intensity for recording is first saturated and then shows unwanted noise, as shown in figure 2.4. A part of this noise is an electronic noise linked to the recovery of the resonance circuit and the detection electronics from the strong RF pulse. Another part of this noise is an acoustic ringing or mechanical noise of some probe parts, mainly the NMR coil, due to the RF pulse, which produces mechanical oscillations picked up by the NMR coil [22] [23].

The method used here to eliminate the impact of the ringing noise on the NMR signal is to cut off the first few data points n×dwelltime, where n is the number of points chosen by the user [24]. This induces a dead time $\tau_{\text{dead}} = \text{n} \times \text{dwelltime}$. The dead time is removed from each measurement (common to all). The new acquisition time becomes $t' = t - \tau_{\text{dead}}$. By replacing $t = t' + \tau_{\text{dead}}$ in the equation 2.2, we obtain

$$M'_{\perp}(t') = M_{eq} \exp\left(\frac{-(t' + \tau_{\text{dead}})}{T_2^*}\right) \exp(i\phi_{\text{elec}}) \exp\left(i2\pi\Delta f(t_n)\,(t' + \tau_{\text{dead}})\right)$$

$$M'_{\perp}(t') = M_{eq} \exp(i\phi_{\text{elec}}) \exp\left(\frac{-\tau_{\text{dead}}}{T_2^*}\right) \exp\left(i2\pi\Delta f(t_n)\tau_{\text{dead}}\right) \exp\left(\frac{-t'}{T_2^*}\right) \exp\left(i2\pi\Delta f(t_n)t'\right) \quad (2.11)$$

Now, as the dead time subtracted from τ_{dead} is of the order of a few microseconds, whereas the $T_2^* >> \tau_{\text{dead}}$ is of the order of a millisecond, this leads to $\exp\left(\frac{-\tau_{\text{dead}}}{T_2^*}\right) \approx 1$. However, $\phi_n(t_n) = 2\pi\Delta f(t_n)\tau_{\text{dead}}$, the phase introduced by the dead time is specific to each measurement since $\Delta f(t_n) = f_{0,n}(t_n) - f_{rf}$ and is time dependant due to the fluctuations of the resistive magnet. Therefore, ϕ_n must be included in the phase correction step later on. Figure 2.4 shows the process of cutting the NMR signal to remove the initial data points affected by the ringing noise.

Baseline correction

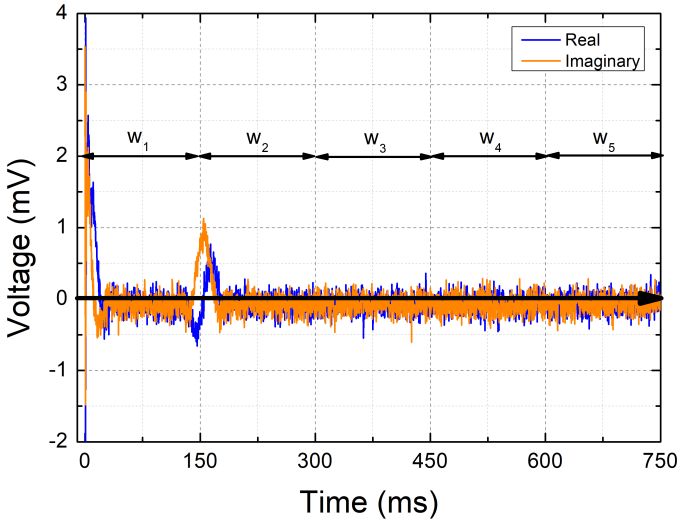

Figure 2.5: Baseline correction method by cutting the NMR signal into N equal windows w_i

As in the ideal case, the transverse magnetization detected should decrease to zero. However, the recorded signal may converge to a finite offset value, because of the electronics used for the amplification. The standard method assumes that the baseline offset is constant throughout the entire signal, which can be corrected by simply applying a zero-order baseline correction in the time domain. However, in our case and in particular in T_1 measurements, unwanted echoes due to imperfect pulses can arise in the NMR signal during the decay, and this varies from one measurement to another, which can affect the estimation of the baseline and lead to inaccurate baseline correction.

A new method has been developed to specifically treat these cases. It consists of

1. Dividing the NMR signal into N equal windows as shown in figure 2.5

$$w_j = \left\{ (j-1)\frac{R}{N}, j\frac{R}{N} \right\} \tag{2.12}$$

   where $\frac{R}{N}$ covers a sufficient number of data points, with a minimum requirement of at least 20% of R the record size of the NMR signal. N is selected and optimized by the user to achieve the desired accuracy and resolution for this specific analysis.

2. We calculate the average of the noise $\bar{w}_i$ at each window w_i

$$\bar{w}_j = \sum_{n=(j-1)\frac{R}{N}}^{n=j\frac{R}{N}} \frac{\left(M_x(n) + iM_y(n)\right) N}{R} \tag{2.13}$$

3. We find where the minimum of $\sqrt{\bar{w}_j^2}$ and then subtract the corresponding $\bar{w}_j$ value from the entire NMR signal.

The window size used is the same for all measurements. However, the minimum of $\sqrt{\bar{w}_j^2}$ depends on the measurement.

2.2.3 Frequency domain analysis

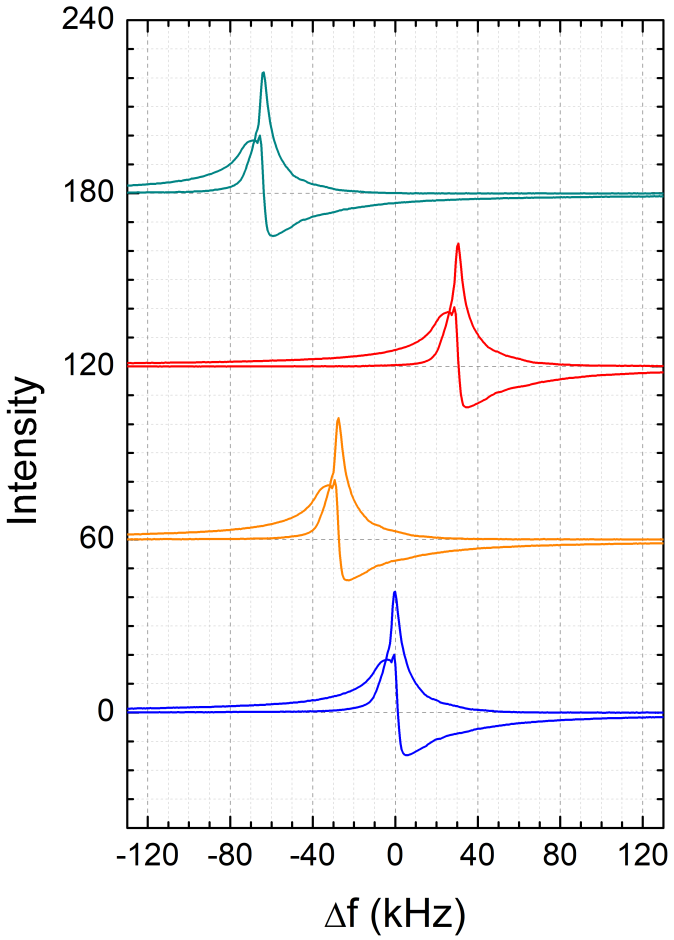

Figure 2.6: ^1H spectra for single scan measurements of an aqueous (H_2O) solution of $GdCl_3$ with a concentration c = 60 mMol/l at 24 T / 1020 MHz phased by a very large window. The four measurements were performed consecutively. The field fluctuations in the resistive magnets induces the detection at different off-resonant positions $\Delta f_n(t)$ from the radio-frequency f_{rf}.

In the frequency domain the ^{1}H spectra for the same sample appear at different positions Δf from one measurement to another during the same experiment due to field fluctuations of the resistive magnets as shown in figure 2.6. In order to obtain properly phased spectra, as shown in figure 2.6, and since we are applying collective data processing (over 100 of measurements for the field stability experiment), the user must define a very large window for the phase correction

1. To cover all the "off-resonant" positions Δf of the spectra for the phase correction. The size of the Δf can reach ± 100 kHz in some measurements.

2. To reduce the impact of window asymmetry on spectra phasing, a larger window size is used to compensate for this effect.

However, this method can still lead to phase correction errors because we are working with finite window size and asymmetric spectra. To avoid phase correction errors, we have developed a method specifically tailored to handle field fluctuations, which will be the subject of the next paragraph.

Field fluctuation correction

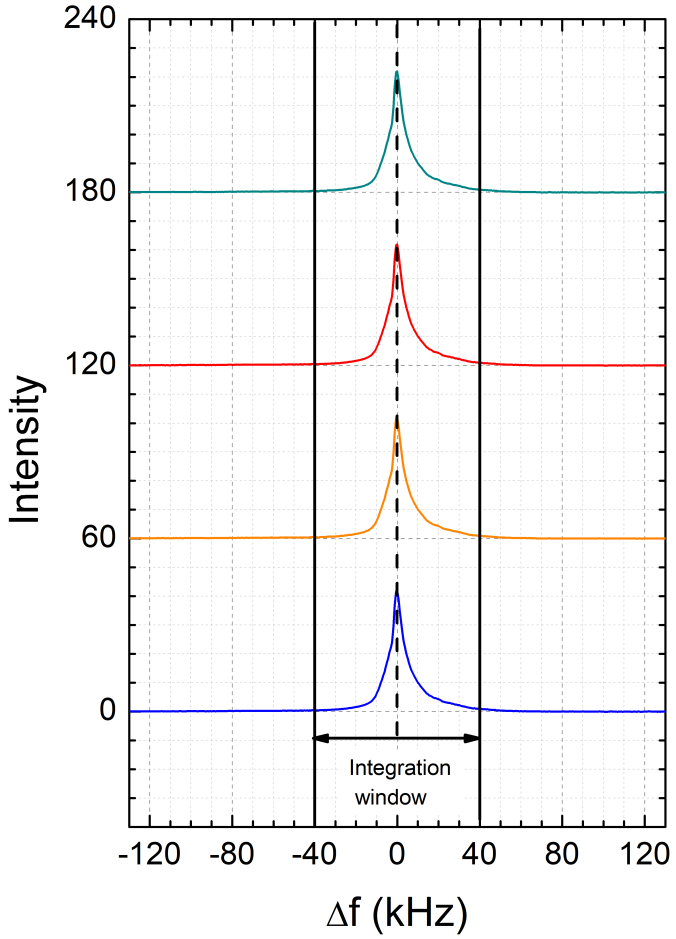

Figure 2.7: The spectra of the previous figure after the application of the correction of field fluctuations. The description of this figure follows the caption of figure 2.6. Details can be found in the text.

The core of this method is to recenter all the spectra at zero frequency offset. This generates a symmetrical window for the phase correction and allows to reduce the integration window size, which improves the signal-to-noise ratio for the moment calculation. To correct the frequency offset, we need to shift each spectrum by the associated $-\Delta f(t_n)$ (see figure 2.6). We decided to take the module of the spectrum to calculate $\Delta f(t_n)$ since it is independent of the phase, unlike the real and imaginary parts of the spectrum. We find $\Delta f(t_n)$ as the frequency that corresponds to the spectrum's maximum modulus.

Figure 2.7 shows the superposition of the spectral lines after the field fluctuation correction method was applied. The integration window is then selected to be seven times the line width at half height of the NMR spectra, which provides $99\ \%$ of M_{eq} for the above spectrum in figure 2.7. We can then apply the same integration window to calculate the first moment of the spectra for all measurements.

After correcting the frequency offset $\Delta f(t_n)$ specific to each NMR spectrum, the remaining step involves correcting their phases $\phi_{n,t}$. The total phase, specific to each measurement n, is derived from equations (2.2) and (2.11)

$$\phi_n = \phi_{\text{elec}} + \phi(t_n) = \phi_{\text{elec}} + 2\pi\Delta f(t_n)\tau_{\text{dead}}. \tag{2.14}$$

It is induced by the dead time specific to each measurement n and the constant phase introduced by the NMR spectrometer electronics ϕ_{elec}.

The value of ϕ_n for each measurement is calculated by replacing ϕ_{elec} by ϕ_n following the same procedure as explained in the section on phase correction (ideal case). After calculating the values of ϕ_n, the NMR signals $M'_{n,\perp}(t)$ (equation (2.11)) are multiplied by $\exp(-i\phi_{n,t_n})$ term to correct their phases.

Then, finally we can calculate the parameters M_0, M_1 and $\sqrt{M_2}$ from each NMR spectrum using the moment equations (2.10).

Chapter 3: Instruments and methods for NMR in resistive magnets

3.1 Constraints for NMR in resistive magnets

Figure 3.1: General view of the LNCMI Grenoble M9 resistive magnet: $B_{max} = 37$ T at $I = 4 \times 15000$ A. The height of the structure is approximately 2 m. The metal tubes are the water cooling: 300 l/s at $\Delta p = 20$ bar. The access to the magnet for user experiments is located in the floor above. Details can be found in the text and in references [25–27].

Most NMR experiments use superconducting magnets. The discovery of new superconducting materials (ceramic oxides) that maintain their superconductivity under intense magnetic fields opened the way to a new generation of highly homogeneous, high-field magnets, surpassing the magnetic field limits of the previous generation of commercial NMR superconducting magnets [28, 29]. The maximum achievable field strength of superconducting magnets stands at 28.2 T for commercial high resolution NMR magnets (Bruker) and 32 T for a non-commercial general purpose magnet (NHMFL in Tallahassee).

Nevertheless, resistive magnets continue to exceed these field limits. DC fields higher than 32 T are currently available at a few specialized high-field facilities that operate resistive magnets: Tallahassee (United States), Nijmegen (The Netherlands), Tsukuba (Japan), Hefei (China), and Grenoble (France).

The LNCMI laboratory (Laboratoire National des Champs Magnétiques Intenses) in Grenoble is one of these facilities. It enables researchers to carry out high-field experiments, such as NMR, in a DC magnetic field up to 37 T in a 34 mm bore resistive magnet shown in figure 3.1 [25–27]. The magnet allows a ramp rate of up to 5 T/min, which allows studies of field dependent phenomena. At full field, the magnet operates at 60000 A provided by four parallel power supplies, each operating at 15000 A and 400 V . It consumes a

total electrical power of 24 MW, which is evacuated by a water cooling operating at a flow rate of 300 l/s and a pressure difference of $\Delta p = 20$ bar.

Unfortunately, the spatial field homogeneity and field stability of this type of magnets does not meet the requirements of high resolution NMR experiments. NMR experiments in these magnets are therefore a technical challenge and need a tailored NMR approach [30, 31].

3.1.1 Architecture of LNCMI resistive magnets

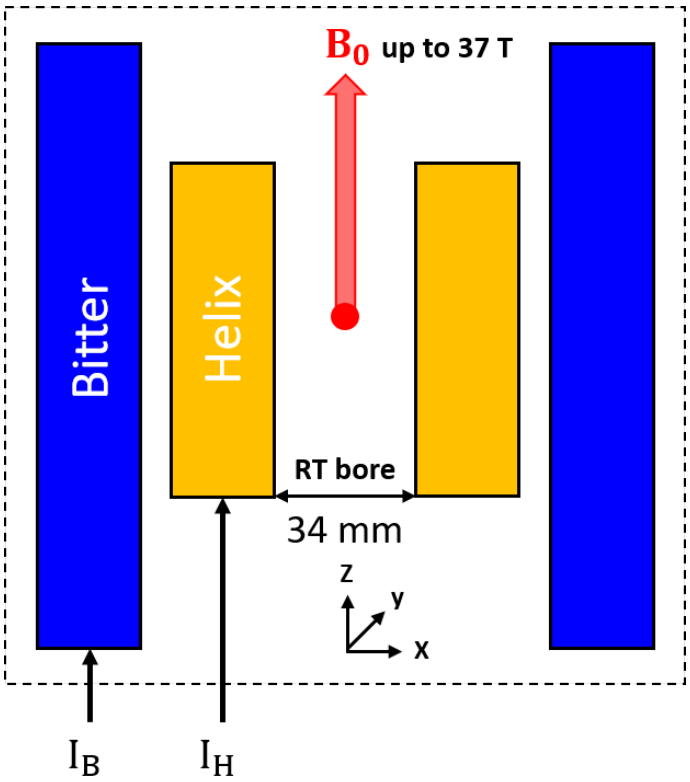

Figure 3.2: Schematic view of the high field LNCMI resistive magnet configuration. The magnet is composed of two sub-magnets (Helix + Bitter) that can be independently powered by two 12 MW power supplies, where $I_{H,B}$ are the current flowing in the magnet to produce the desired magnetic field. The figure is adapted from [27]. Details can be found in text.

A 24 MW LNCMI resistive magnet is composed of two sub-magnet as shown in figure 3.2: an inner magnet built from a Helix insert and an outer magnet built from two Bitter stacks that can be electrically powered in a separate way [25, 27]. Due to their different geometries, each sub-magnet contributes differently to the total magnetic field, with the poly Helix magnet capable of producing fields up to 26.5 T and the Bitter magnet up to 10.5 T. Therefore, the total magnetic field B_0 of the resistive magnet at its center is the superposition of B_H and B_B

$$B_0 = B_H + B_B,$$

where indexes B or H indicate the relevant parameter (here magnetic field) linked to the Helix and the Bitter magnet respectively. The magnetic field is proportional to the current $I_{H,B}$ and the equation can be

written as

$$B_0 = F_H I_H + F_B I_B, \tag{3.1}$$

where $F_{H,B}$ are the field factors of the two sub-magnets.

The total power consumption of the magnet can be expressed as the sum of the power consumed at each sub-magnet.

$$\begin{aligned} P &= P_H + P_B, \\ P &= R_H I_H^2 + R_B I_B^2, \end{aligned} \tag{3.2}$$

where $R_{H,B}$ are the resistance, and $I_{H,B}$ are the current flowing in the magnet to produce the desired magnetic field.

The LNCMI has developed a method for saving energy while performing experiments in the resistive magnet, wherein a minimum power P is found at each field B_0 [27]. This method is based on optimizing the current distribution pair (I_H,I_B) in the two sub-magnets in such a way that

$$\left.\frac{\delta P}{\delta I_H}\right|_{B=B_0} = 0 \Leftrightarrow \frac{I_H}{I_B} = \frac{F_H R_B}{F_B R_H}, \tag{3.3}$$

A detailed study [27] shows that an energy efficient operation is obtained by a field dependent current ratio

$$r_{HB} = \frac{I_H}{I_B}. \tag{3.4}$$

For fields below 24 T, $r_{HB} = 2$ is used. Above 24 T, r_{HB} linearly decreases with field down to $r_{HB} = 1$ at 37 T. More details on the LNCMI resistive magnet in Grenoble can be found in [25–27].

3.1.2 B_0 Field inhomogeneity

The LNCMI's resistive magnets have approximately a solenoidal configuration. The Biot-Savart law describes the magnetic field B_0 at a given point $\boldsymbol{r}$ as the integral of contributions from infinitesimally small current elements within the solenoid:

$$\boldsymbol{B}_0(\boldsymbol{r}) = \frac{\mu_0}{4\pi} \int\int\int_V \frac{\boldsymbol{J}(\boldsymbol{r'}) \times (\boldsymbol{r} - \boldsymbol{r'})}{|\boldsymbol{r} - \boldsymbol{r'}|^3}\, d^3 r', \tag{3.5}$$

$\boldsymbol{J}(\boldsymbol{r'})$ is the current density of the solenoid element located at $\boldsymbol{r'}$.

The formula shows that $\boldsymbol{B}_0(\boldsymbol{r})$ is determined by the current density distribution $\boldsymbol{J}(\boldsymbol{r'})$ within the conductor volume V. At a specific point located at $\boldsymbol{r}$, the magnetic field $\boldsymbol{B}_0(\boldsymbol{r})$ is dependent on the magnitude and direction of the current density $\boldsymbol{J}(\boldsymbol{r'})$ at all points in the conductor.

A second-order axisymmetric model in cylindrical coordinates is a suitable way of describing the field profile of a solenoid magnet oriented along the z-axis near the center located at $r = (x_0, y_0, z_0)$ [32]. This model gives the variation of the magnetic field magnitude

$$B_0(z, \rho) = B_0 \left(1 + G_{zz} \left(z^2 - \frac{1}{2}\rho^2\right)\right) \tag{3.6}$$

at a specific point, as a function of the relative distance from the center

$$z = z_i - z_0 \quad \text{and} \quad \rho = \sqrt{(x_i - x_0)^2 + (y_i - y_0)^2} \tag{3.7}$$

of the resistive magnet, where G_{zz} is the relative second order axial gradient coefficient.

We note from this formula (3.6) that the field variations in the radial direction are half of that in the axial direction.

The LNCMI resistive magnets is composed of two sub-magnet (Helix + Bitter) with different field factors and magnet geometries that are both centered at $(z_0, \rho_0) = (0, 0)$, therefore,

$$B_0(z, \rho) = B_H(z, \rho) + B_B(z, \rho), \tag{3.8}$$

where

$$B_H(z, \rho) = F_H I_H \left(1 + G_{zz,H} \left(z^2 - \frac{1}{2}\rho^2\right)\right), \tag{3.9}$$

and

$$B_B(z, \rho) = F_B I_B \left(1 + G_{zz,B} \left(z^2 - \frac{1}{2}\rho^2\right)\right). \tag{3.10}$$

Inserting equations (3.9) and (3.10) into the equation (3.8), and using equation (3.4) gives

$$B_0(z, \rho) = B_0 \left(1 + \left(\frac{F_H G_{zz,H} \cdot r_{HB}}{F_B + F_H \cdot r_{HB}} + \frac{F_B G_{zz,B}}{F_B + F_H \cdot r_{HB}}\right) \left(z^2 - \frac{1}{2}\rho^2\right)\right), \tag{3.11}$$

By comparing equation (3.11) with equation (3.6), we deduce the axial gradient of the resistive magnet

$$G_{zz} = \frac{F_H G_{zz,H} \cdot r_{HB}}{F_B + F_H \cdot r_{HB}} + \frac{F_B G_{zz,B}}{F_B + F_H \cdot r_{HB}}. \tag{3.12}$$

G_{zz} is field dependent due to the field dependency of r_{HB}. In table (3.1), we list the values of G_{zz} in units of ppm/mm^2 at the fields used in this thesis.

B_0 [T]	f_0 [MHz]	G_{zz} [ppm/mm^2]
19.2	820	-24.63
24	1020	-24.63
28.2	1200	-23.38
33	1400	-22.15

Table 3.1: Magnetic field dependence of the axial gradient coefficient G_{zz}.

In figure 3.3, we plot the field profile $\Delta B/B_0$ with $\Delta B = (B_0(z, \rho) - B_0)$ at the central axes of the LNCMI resistive magnet for $B_0 = 24$ T $\left(G_{zz} = -24.63 \text{ ppm/mm}^2\right)$.

It is worth noting that spatial field inhomogeneity is $100 - 1000$ times greater than in a commercial NMR superconducting magnet.

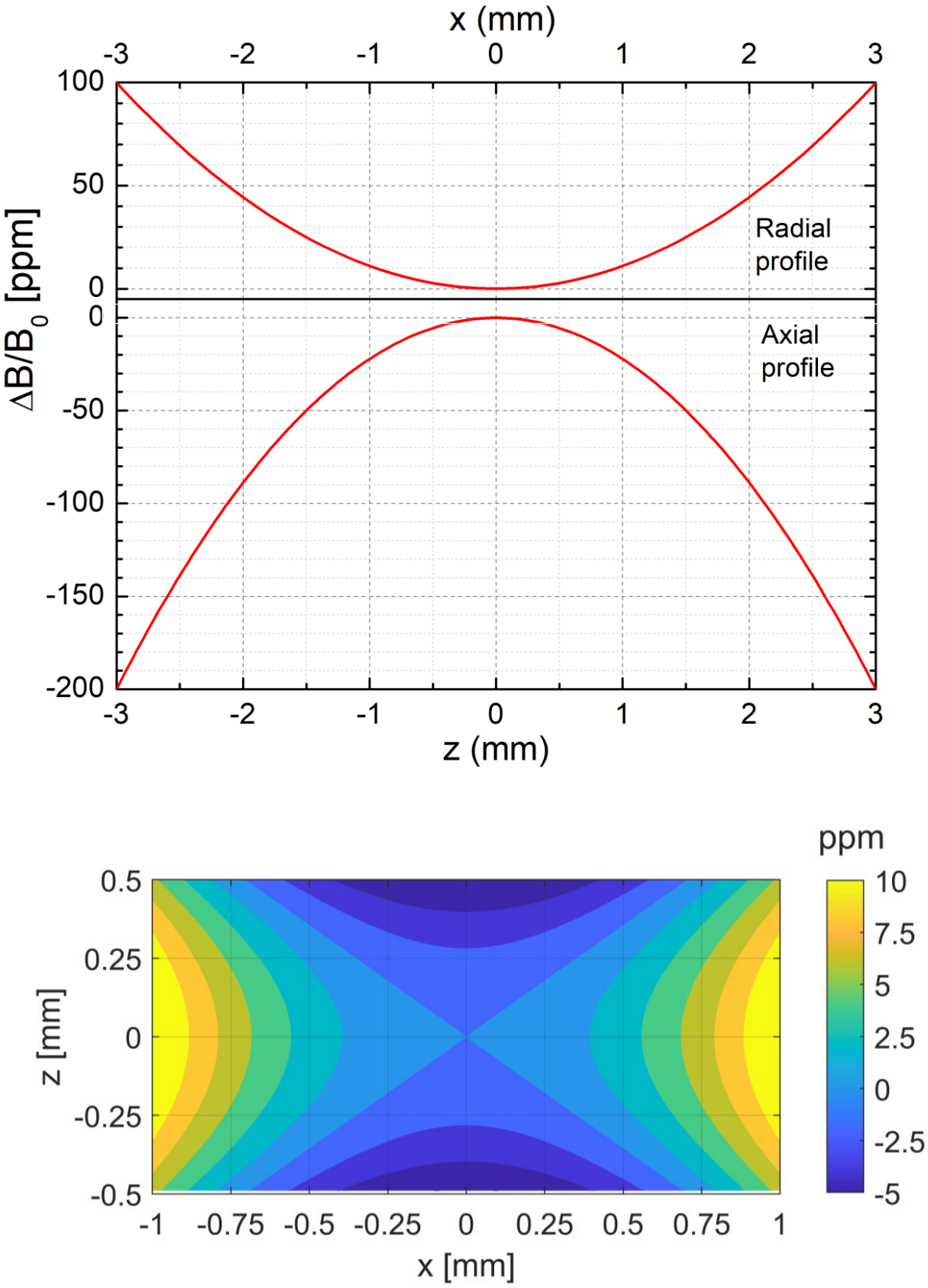

Figure 3.3: Top: Radial and axial magnetic field profile of the LNCMI M9 resistive magnet at the M9 site at 24 *T. Bottom: Contour plot of field distribution in the (x,z) plane of the magnet.*

3.1.3 NMR line shape in an inhomogeneous field

For NMR experiments, we use cylindrical samples with a diameter of $d = 1$ mm and lengths ranging from $l = 1$ to 2 mm. The samples are inserted in a capillary tube, where the axis of the cylinder is perpendicular to the magnetic field B_0 and positioned near its center.

According to equation (1.13) in chapter 1, the law of motion of the magnetization $M_i(z, \rho)$ at a given voxel V_i is

$$\frac{d\boldsymbol{M}_i(z,\rho)}{dt} = \boldsymbol{\omega}_{0,i}(z,\rho) \times \boldsymbol{M}(z,\rho). \tag{3.13}$$

In a magnetic field

$$\boldsymbol{B}_0(z,\rho) = B_0 \left(1 + Gzz\left(z^2 - \frac{1}{2}\rho^2\right)\right) \boldsymbol{e}_z, \tag{3.14}$$

the magnetization of each voxel V_i precesses with an angular frequency

$$\boldsymbol{\omega}_0(z,\rho) = -\gamma \boldsymbol{B}_0(z,\rho). \tag{3.15}$$

Transformation in the rotating frame with $\omega_{rf} = \omega_0$ gives

$$\boldsymbol{\Delta\omega}(z,\rho) = \omega_0(z=0,\rho=0)\Delta\omega_n(z,\rho)\ \boldsymbol{e}_z. \tag{3.16}$$

$\omega_0(z = 0, \rho = 0) = -\gamma B_0$ is the resonance frequency at the center of the magnet and

$$\Delta\omega_n(z,\rho) = Gzz\left(z^2 - \frac{1}{2}\rho^2\right) \tag{3.17}$$

is the field distribution over the voxels V_i normalized by the resonance frequency $\omega_0(z = 0, \rho = 0)$.

Assuming a homogeneous magnetization after a $\frac{\pi}{2}$ pulse for each voxel, the magnetization is

$$\boldsymbol{M}_i(z,\rho) = M_{eq,i}\ \boldsymbol{e}_y. \tag{3.18}$$

The spectrum intensity can be modeled by the histogram of $\boldsymbol{\Delta\omega}(z, \rho)$ on the sample volume as shown in figure 3.4. Figure 3.4 shows spectra simulations using voxel sizes of $0.01 \times 0.01 \times 0.01$ mm^3.

First, we present in figure 3.4 the influence of sample length at a constant field $B_0 = 24$ T ($G_{zz} = -24.63$ ppm/mm^3) on the NMR spectrum (the diameter of the sample is kept constant at $d = 1$ mm). Regardless of the sample length, we assume that the center of the sample coincides with the center of the magnet. All the spectra shown in this figure have a finite width and an asymmetric line shape due to the inequality of the axial and radial gradient coefficients. However, we can see that as the length of the sample increases, its volume increases and, as a result, the dispersion of $\boldsymbol{\Delta\omega}_n(z, \rho)$ is larger over the whole sample, resulting in a broader spectrum. The full width at half-maximum FWHM obtained for the simulated spectra are listed in table 3.2 (left).

Secondly, we present in figure 3.4 the influence of the field on the NMR spectrum for a sample of length $l = 1$ mm and diameter $d = 1$ mm, where the G_{zz} values used for this simulation are taken from the table (3.1). In contrast to the first case, here $\boldsymbol{\Delta\omega}_n(z, \rho)$ is constant and $\omega_0(z = 0, \rho = 0)$ varies. We can see in this figure that at higher fields, since $\omega_0(z = 0, \rho = 0)$ increases and G_{zz} values are close to each other, the NMR line becomes significantly broader. The full width at half-maximum FWHM obtained for the simulated spectra are listed in table 3.2 (right).

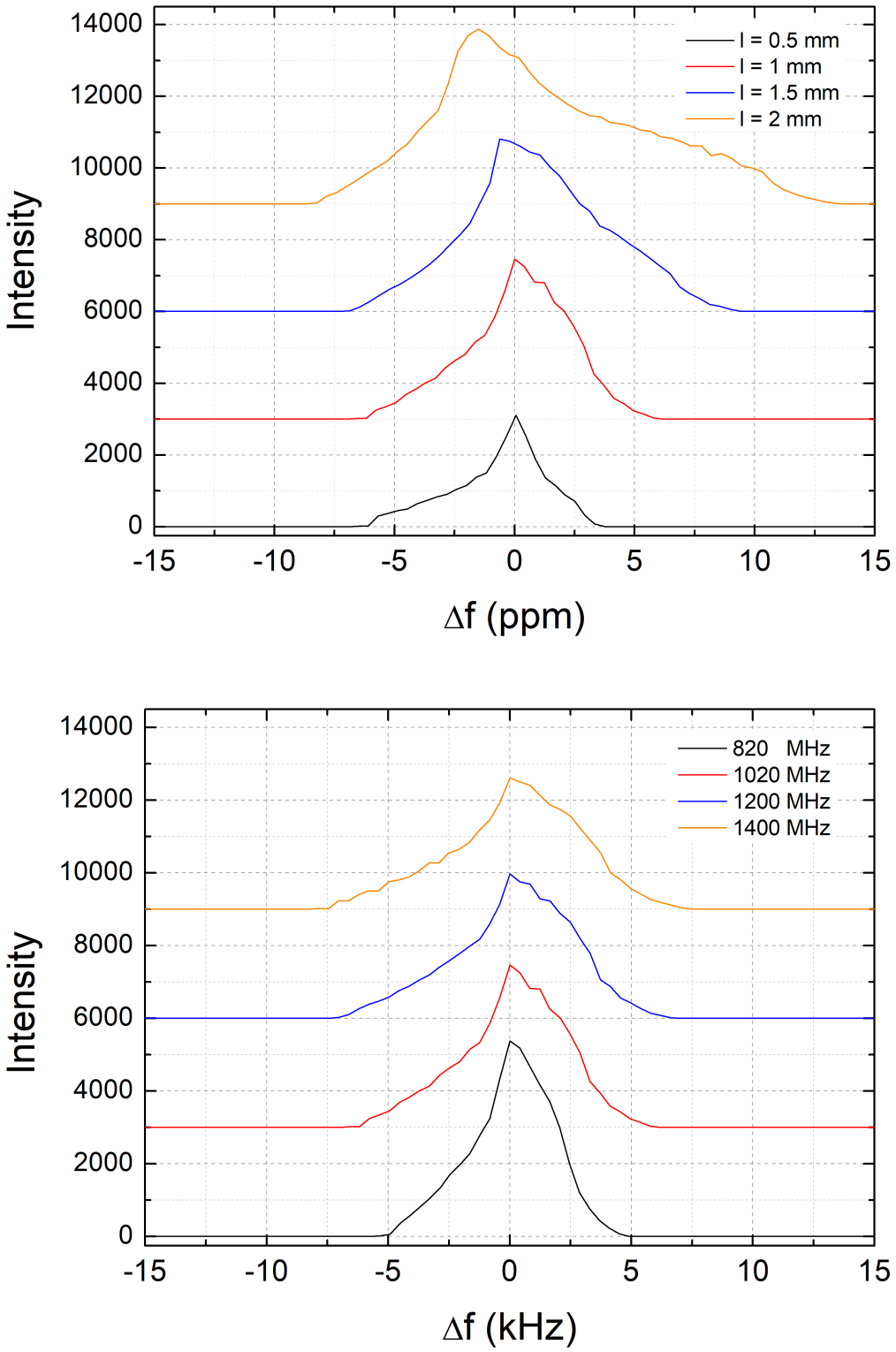

Figure 3.4: Top: Simulation of the broadening of ^1H NMR spectra at 24 T (1020 MHz) as a function of sample size for a cylindrical sample well centred in the magnet with fixed diameter d= 1 mm and varied lengths of l = 0.5, 1, 1.5, and 2 mm . Bottom: Simulation of the broadening of ^1H NMR spectra as a function of field strength for a cylindrical sample well centred in the magnet with length l = 1 mm and diameter d= 1 mm.

l [mm]	FWHM [kHz]	FWHM [ppm]
0.5	2.3	2.2
1	4.1	4.0
1.5	5.4	5.3
2	7.0	6.8

B_0 [T]	f_0 [MHz]	FWHM [kHz]	FWHM [ppm]
19.2	820	3.3	4.0
24	1020	4.1	4.0
28.2	1200	4.7	3.9
33	1400	5.1	3.6

Table 3.2: Left: Full width at half-maximum (FWHM) at 24 T of NMR spectra dependence with the different sample length l and fixed diameter $d = 1$ mm. Right: Full width at half-maximum for sample length $l = 1$ mm and diameter $d = 1$ mm of NMR spectra dependence with the different magnetic fields used in this thesis B_0.

3.2 Resolution enhancement in inhomogeneous fields

In this section, we present the solutions for improving the resolution of the NMR signal under inhomogeneous conditions encountered in resistive magnets. This method focuses on finding the optimum dimensions of a cylindrical sample for which the shape of the NMR line is symmetrical, and its broadening is minimal.

3.2.1 General considerations

For a first estimation of the NMR line broadening of a given cylindrical sample with a volume V, diameter d (along z) and length l (in the (x, y) plane), we use here a rule of thumb, derived from equation 3.14 and expressed as follows

$$\left|\frac{\Delta B}{B_0}(z = \frac{d}{2}, \rho = 0)\right| = G_{zz}\frac{d^2}{4} \tag{3.19}$$

for the axial contribution to the broadening, and

$$\left|\frac{\Delta B}{B_0}(z = 0, \rho = \frac{l}{2})\right| = \frac{1}{2}G_{zz}\frac{l^2}{4} \tag{3.20}$$

for the radial contribution to the broadening.

We can find an optimum d and l for which the NMR line shape is symmetrical for a well-centered sample, i.e., the axial contribution should be equal to the radial contribution

$$G_{zz}\frac{d^2}{4} = \frac{1}{2}G_{zz}\frac{l^2}{4}, \tag{3.21}$$

which gives

$$l = \sqrt{2}d. \tag{3.22}$$

Indeed, in the top panel of figure 3.4, we see that the $l = 1.5$ mm provides roughly the most symmetric spectrum, whereas longer samples produce frequency broadening.

Another important factor is to reduce the inhomogeneity of the magnetic field in the sample volume in order to obtain the narrowest possible NMR line during the experiments. Therefore, we show again in figure 3.5 (a) the axial and radial profile of the LNCMI M9 resistive magnet, where the NMR experiments were performed, together with typical NMR sample sizes.

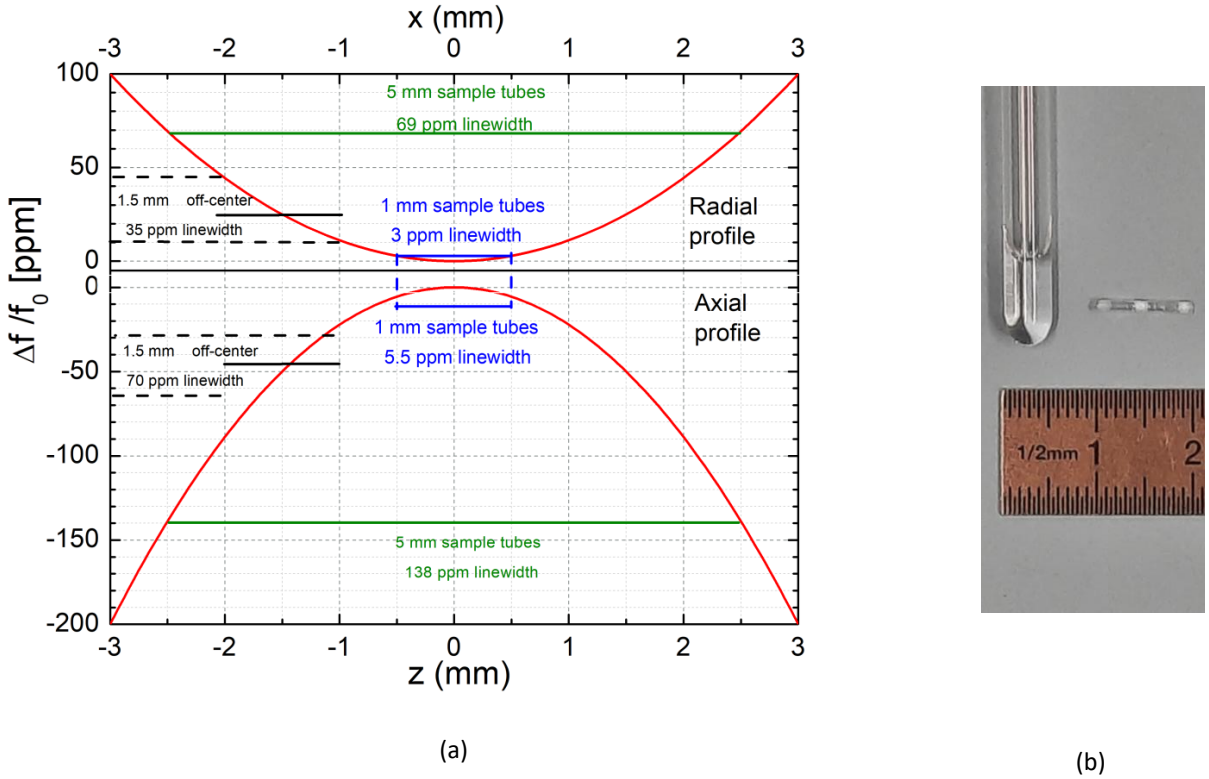

Figure 3.5: (a): Axial and radial magnetic field profile of LNCMI resistive magnet. (b): Comparison of sample sizes between the standard NMR samples used in the superconducting magnet and those used in the resistive magnet.

The 5 mm diameter sample tubes used for typical liquid-state NMR experiments in superconducting magnets are marked in green in the figure and, as we can see, their NMR spectra become very broad (138 ppm axially and 69 ppm radially) in the resistive magnet.

The only way to minimize this broadening effect is to switch to smaller samples (marked in blue in the figure), which cover less space in the magnetic field and experience a weaker field gradient. Therefore, we can reduce the broadening by a factor of $5^2 = 25$ by switching to μl samples. Figure 3.5 (b) highlights the difference in sample volume as we pass from NMR experiments on a superconducting magnet to a resistive magnet.

Moreover, each time we are displacing the sample out of the center, $\Delta f / f_0$ is increasing, thus broadening the NMR line of our sample. Therefore it's essential to have small samples *and* to properly center them inside the magnet. For a 1-1.5 μl sample precisely positioned at magnet center, the linewidth should stay below 15 ppm.

It is important to note, that the axial position of the sample can be modified during the experiments, unlike the radial position. This means that radial centering of the sample is part of the sample preparation, which becomes an important step before the experiments.

3.2.2 Preparation of μl NMR samples

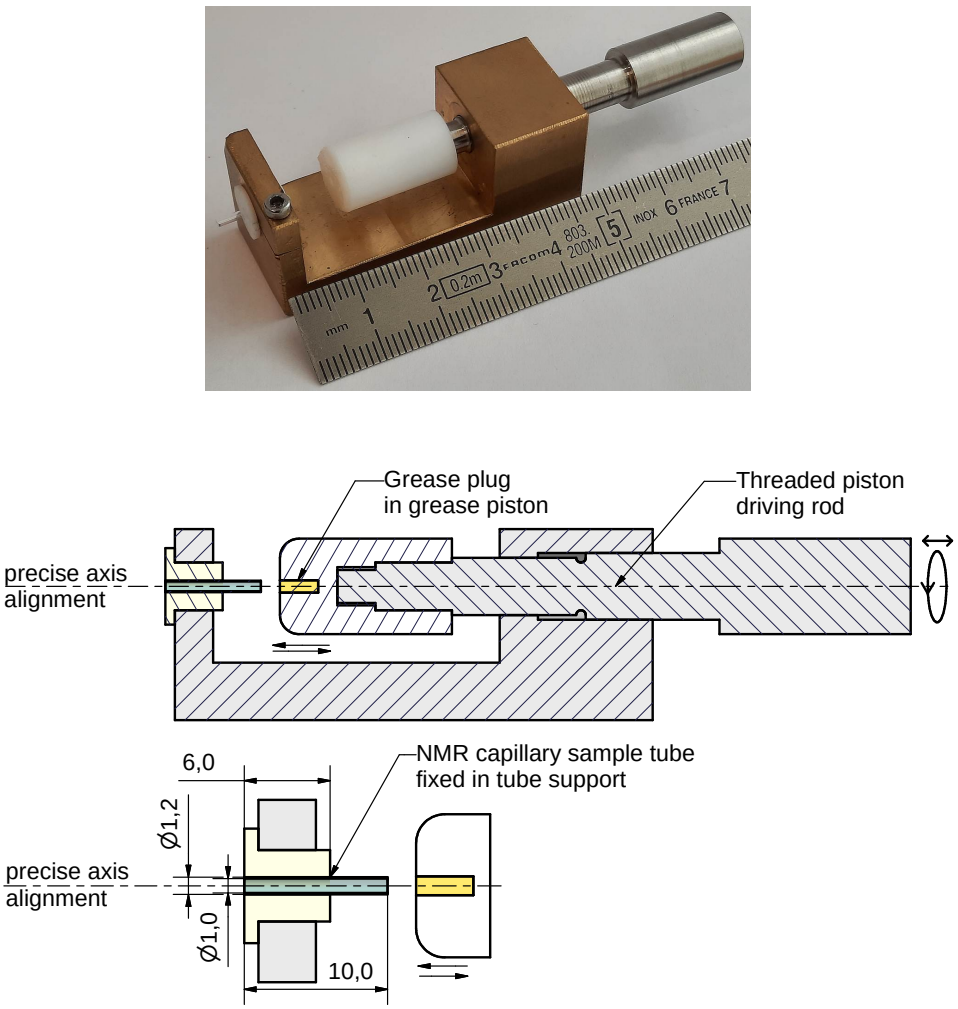

Figure 3.6: Top: Sample filling tool. Bottom: Detailed schematic of the filling tool.

To ensure a homogeneous magnetic field over the voxels V_i, the optimum sample size should be between 1-1.5 mm in length and with a diameter d = 1 mm equivalent to a volume of 1-1.5 μl and well centered in the magnet. Since we are dealing with liquid samples, we must fill them into capillary tubes. We choose to use capillary tubes with inner/outer diameters of 1/1.2 mm and a length of 10 mm.

Throughout the filling process, we had to overcome a number of technical challenges, which can be briefly stated as follows

1. Dealing with small sample volumes of 1-1.5 μl. The liquid sample insertion into the capillary tube was performed using a micropipette that can hold up to 10 μl of volume.

2. Inserting the 1 μl sample into small tubes of 10 mm length and 1 mm inner diameter and close them to prevent sample evaporation. We choose grease to close both capillary ends, where the grease should be proton free since we are doing ^{1}H NMR. Therefore, proton-free fluoropolymer grease (DAIFLOIL, Daikin Japan) was used.

3. Dealing with small amount of grease.

4. While axial centering is possible in situ, radial centering is not, which presents a significant challenge during the sample-filling process. We need to center a 1 mm long drop of length with a precision of less than 0.2 mm inside a 1 mm tube inner diameter. However due to the effect of air pressure when sealing the tubes, the sample will move during this process.

Therefore, a new tool shown in figure 3.6 was constructed to overcome these filling problems. It consists of a tube support, a grease piston, and a threaded piston driving rod to move the grease into the tube. The fabrication was done by the LNCMI workshop. The detailed schematic of the filling tool is shown in the bottom of the figure 3.6.

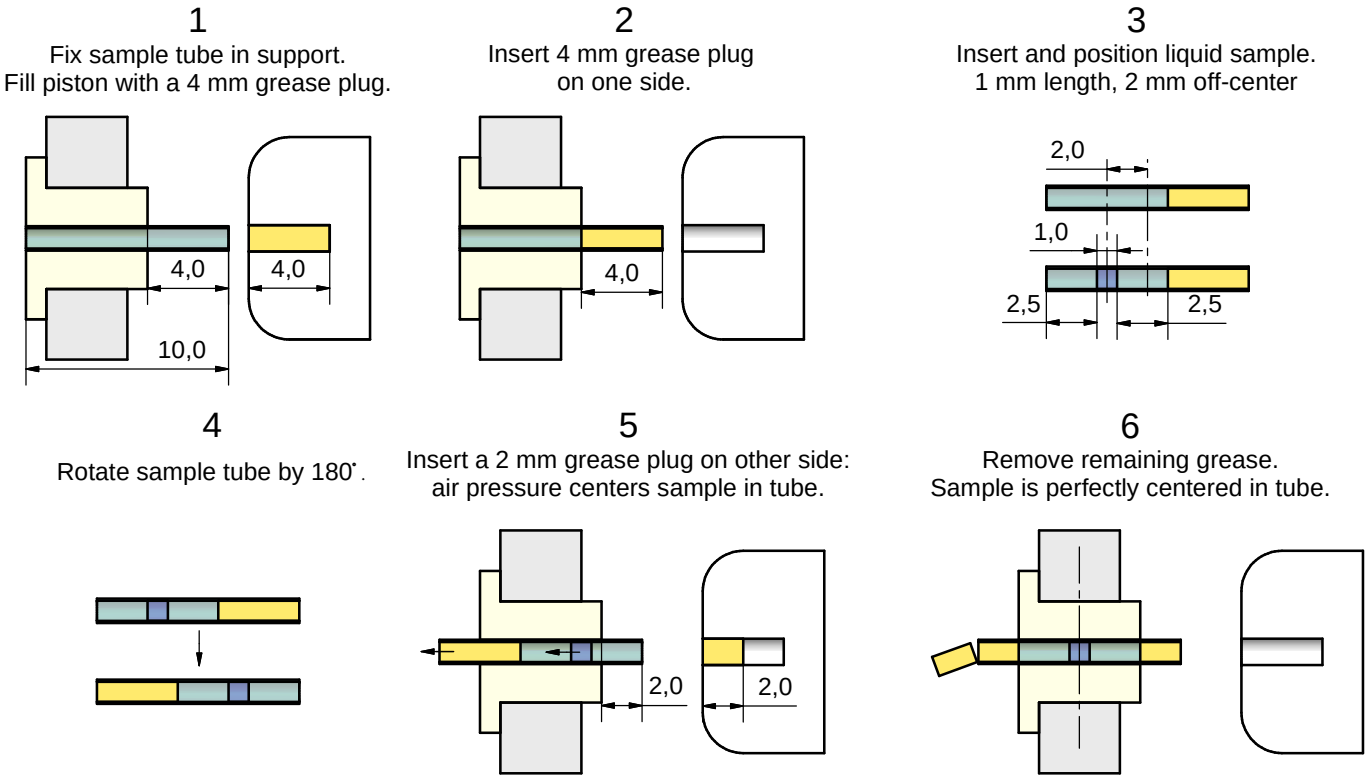

Figure 3.7: Steps of the procedure for filling the sample into the capillary tube for the resistive magnet NMR experiments.

The stepwise procedure of sample filling shown in the figure 3.7 is the following

1. We attach the tube to its support and fill 4 mm of grease in the grease piston.
2. We insert the grease into the first end of the capillary tube.
3. The fragility of the glass capillary tube makes it difficult to insert the 1 μl sample in the desired position. Indeed, placing the head of the micropipette at the specified position risks breaking the tube. To avoid that, precautions must be taken during the procedure. We insert the liquid sample of 1-1.5 μl inside the tube from the other end so that its position is 2 mm off-center. This off-centering takes into accounts the movement of the drop by air pressure when closing the second end of the capillary tube.
4. We rotate the capillary tube by 180° and we attach it again to the support.
5. We fill 2 mm of grease in the piston and insert it into the second end of the capillary tube.
6. The air pressure centers the sample perfectly inside the capillary tube, and a small part of the grease will fall out.

Typical NMR experiments in the resistive magnet require the preparation of 40 to 50 samples, thus the importance of this sample positioning procedure.

3.3 Temporal field stability of resistive magnets

In an NMR experiment, the external magnetic field B_0 determines the resonance frequency f_0 at the nucleus, and NMR excitation and detection operate at this frequency for the "on-resonant" case. However, resistive high-field magnets have limited field stability: variations of B_0 generate variations of the resonant frequency leading to different "off-resonant" cases. Therefore, the temporal stability of the magnetic field is an important requirement for an NMR experiment. There are two well-known types of temporal instability

1. Drift refers to long-term variations in the magnetic field over time, typically $> 10^2$ s.
2. Fluctuations refer to short-term variations in the magnetic field over time: range 10^{-3} - 1 s, i.e., 1 Hz - 1 kHz.

In this part of the chapter, we present the time dependence and size of these fluctuations during NMR experiments in resistive magnets. Later in this chapter, we will discuss how these fluctuations affect the NMR T_1 experiments.

3.3.1 Origin of magnetic field drift and fluctuations

Temporal instabilities of B_0 originate from a variety of sources. The main contributions are variations in the temperature of the magnet and the ripple in the power supply, causing drift and fluctuations of the resistive magnet, respectively [33].

The LNCMI resistive magnet is water-cooled by a two-loop circuit. The first, closed-loop circuit cools the magnet directly with distilled water, and the thermalization of the first circuit takes 10 to 15 minutes. The heat is then extracted through a heat-exchanger by a second circuit that uses the water from the nearby river. This process causes very small variations (10-50 ppm) of the magnetic field on long timescales. In our case, the drift of the magnet has a negligible impact on the NMR experiment due to the fact that the relaxation times T_1 and T_2 of the samples studied are shorter than the observed drift. During the NMR experiments, we always corrected these drifts by adjusting the spectrometer frequency.

The noise spectrum of the current flowing through the magnet is due to the design and construction of the power supplies, which induces short-term variations of the magnetic field that can't be corrected during the NMR experiment [33, 34].

3.3.2 Characterization of field fluctuations of resistive magnets

We quantified the size of fluctuations encountered during the NMR experiments in the resistive magnet by performing stability measurements during 30 minutes at a nominal magnetic field of 24 T corresponding to a resonance frequency of $f_0 = 1020$ MHz. During that time we recorded 2300 ^{1}H NMR FIDs. We used a rapidly relaxing sample of H_2O with added $GdCl_3$ ($c = 60$ mMol/l), where T_1 is of the order of a few ms to minimize the time interval τ_{wait} between two successive FIDs and to maximize the number of data points collected.

Figure 3.8 (top figure) shows the fluctuations of the resistive magnet as a function of the average field of each measurement. A linear drift term was subtracted. The fluctuations were calculated using the first-moment equation (2.10) from chapter 2. We can clearly see that most of the off-resonant frequencies are found to be within the range of $\Delta f/\langle f_0\rangle = \pm 50$ ppm.

The histogram of these fluctuations is shown in the figure 3.8 (bottom figure), which we have fitted using a Gaussian function

$$I\left(\frac{\Delta f}{\langle f_0\rangle}\right) = A\exp\left(-\frac{1}{2}\left(\frac{\Delta f}{\langle f_0\rangle}\frac{1}{\sigma}\right)^2\right), \tag{3.23}$$

where A represents the area, and σ is the standard deviation. We derive the full width at half maximum FWHM $= \sigma \cdot 2\sqrt{2ln(2)}$.

Based on the histogram, it's evident that about 20% of the cases are on-resonant within a window of ± 5 ppm. The standard deviation of the histogram is σ =19 ppm. From this we deduce the value of the full width at half-maximum FWHM $= 46$ ppm. These values are valid at 24 T.

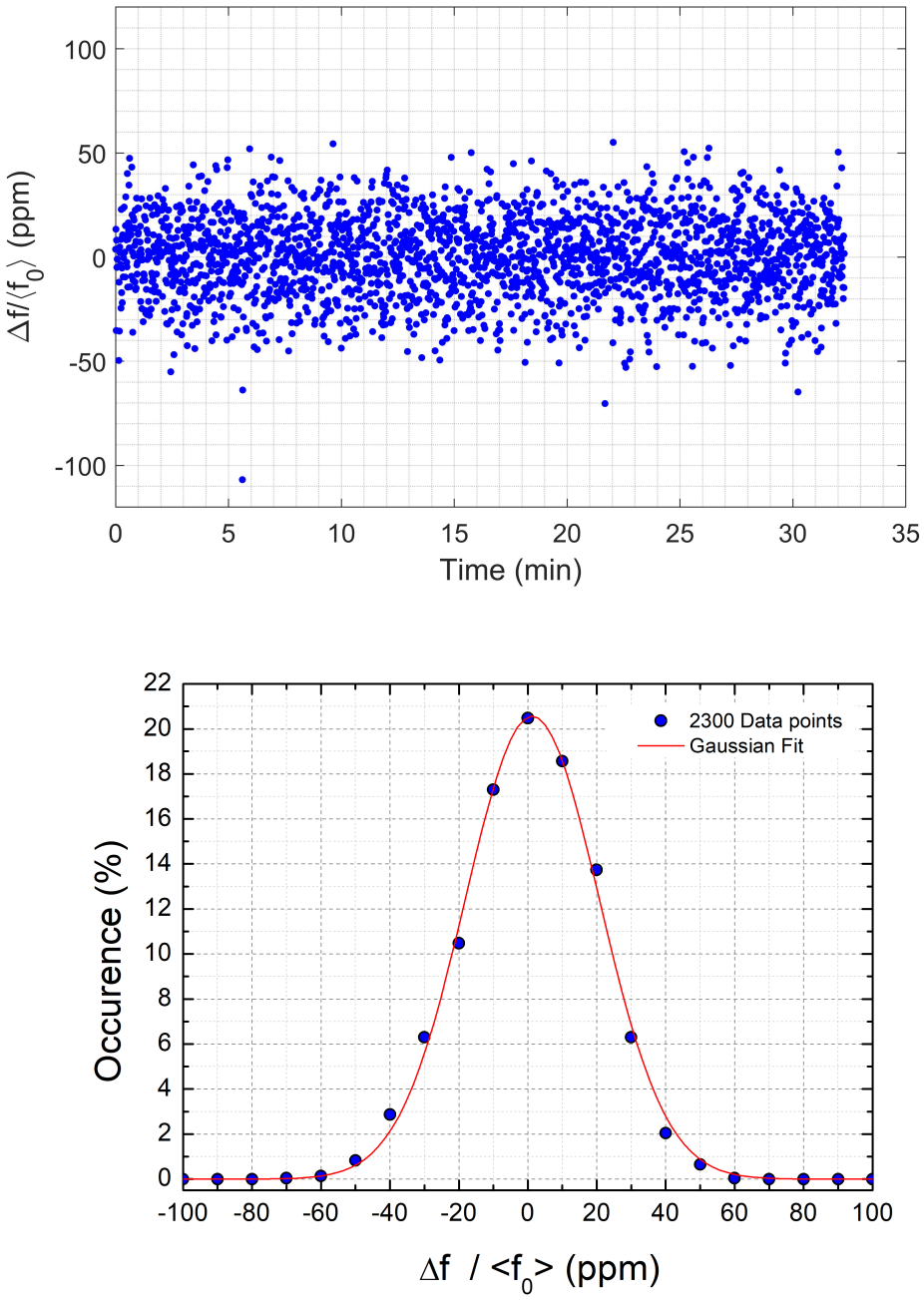

Figure 3.8: Top: Fluctuations in ppm as a function of the average field of each measurement, recorded during 30 *minutes (*2300 *measurements). A linear drift was subtracted. Bottom: Histogram of the fluctuations recorded during* 30 *minutes (*2300 *measurements).*

3.4 Hardware for high field NMR in resistive magnets

In this section we will present the NMR hardware needed to perform an NMR experiment in resistive magnets. An NMR spectrometer is composed of the following elements

- ◇ A magnet that produces an intense, homogeneous and stable magnetic field at the desired field value B_0.
- ◇ A probe with a radio frequency coil used to excite and detect the NMR signal.
- ◇ A frequency synthesizer and radio-frequency amplifier to produce short and intense pulses.
- ◇ A sensitive radio frequency receiver to capture and amplify the NMR signal.
- ◇ A pulse program to produce pulse sequences.
- ◇ A computer to control and process the data.

The NMR spectrometer consists of separate electronic components that fall into three categories: the first provides the excitation of the spins present in the sample, the second detects the NMR signal generated by the sample after a pulse sequence, and the third one serves for both excitation and detection. Figure 3.9 illustrates the general schematic of the NMR spectrometer employed for the NMR experiments in the resistive magnets. The red dashed line in the figure separates the excitation from the detection components.

The operating frequency range depends on the nucleus of interest and the desired magnetic field range. In our case, we study protons ^{1}H in a field range between 20 T and 33 T, corresponding to Larmor frequencies between 800 MHz and 1400 MHz.

This means that most of the NMR hardware components in the figure 3.9, such as the synthesiser, power amplifier, NMR duplexer, probe and preamplifier, must operate in this frequency range $800 - 1400$ MHz.

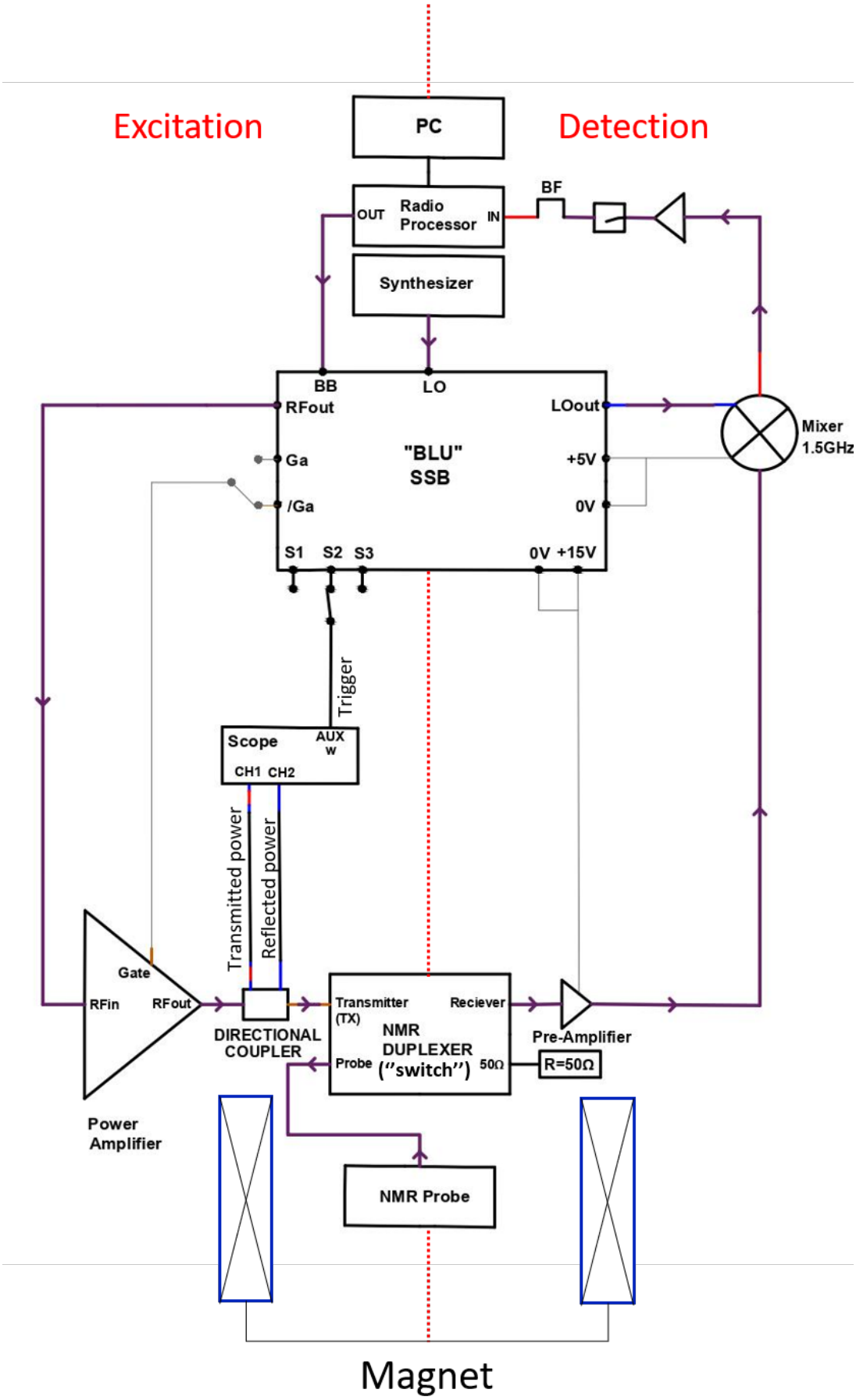

Figure 3.9: Schematic of the NMR spectrometer. The red dash line in the middle of the figure separate the excitation phase (left) from the detection phase (right).

3.4.1 NMR excitation and detection process

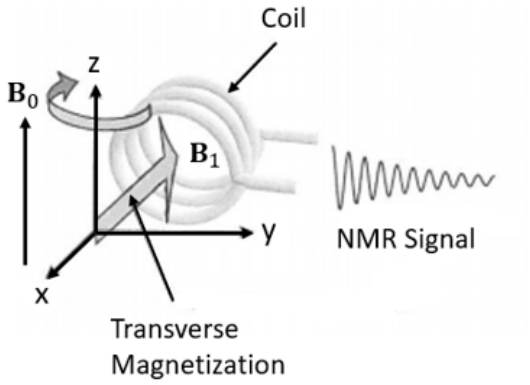

Figure 3.10: Representation of the excitation and detection coil adapted from [10]

In an NMR experiment, the precession of the magnetization vector in the transverse plane is detected after the excitation by a radio-frequency field $\boldsymbol{B}_1(t)$ near the Larmor frequency f_0. For this purpose we need to set up a radio frequency circuit, which contains a coil that is wound around the sample. In our case, the excitation and the detection coil are the same. The axis of the coil must be in the (x,y) plane perpendicular to the static field $\boldsymbol{B}_0(\boldsymbol{r})$ as shown in figure 3.10. In addition, the coil has to be positioned in a way that the sample is well centered with respect to the magnetic field profile of the magnet.

This coil has a solenoidal geometry, it is driven by an RF synthesizer and designed to generate a homogeneous RF magnetic field over the sample region and within the frequency range of the nuclei of interest. A current passing through this solenoidal coil creates a magnetic field along the axis of the coil $\boldsymbol{B}_1(\boldsymbol{r})$. We recall the equation (3.5) of Biot-Savart law, which describes the total field $\boldsymbol{B}_1(\boldsymbol{r})$ due to a closed circuit at a given observation point $\boldsymbol{r}$ as

$$\boldsymbol{B}_1(\boldsymbol{r}) = \frac{\mu_0}{4\pi} \int\int\int_V \frac{\boldsymbol{J}(\boldsymbol{r'}) \times (\boldsymbol{r} - \boldsymbol{r'})}{|\boldsymbol{r} - \boldsymbol{r'}|^3}\, d^3r', \tag{3.24}$$

$\boldsymbol{J}(\boldsymbol{r'})$ is the current density of the solenoid element located at $\boldsymbol{r'}$.

The user controls the pulse length to obtain the desired pulse angle, which requires calibration through a nutation experiment. The output of the RF source is in the order of a few mW. Therefore, we use an RF amplifier to generate pulses of kW needed to induce short and intense pulses. The probe is inserted into the bore of the magnet to position the sample at the point of the maximum field $\boldsymbol{B}_0(\boldsymbol{r})$.

When the radio frequency pulse has terminated, the precessing nuclear magnetization generates a rotating magnetic field. Through Maxwell's equations, a changing magnetic field is associated with an electric field. An induction voltage is induced in the detection coil, which after various manipulations by the radio frequency electronics in the spectrometer, results in a voltage signal.

The switching from the excitation to the detection is done by a "duplexer" that separates the high-power excitation signal transmitted to the probe from the weak NMR signal induced after the pulse (see figure 3.9).

The duplexer includes filters and switching components that selectively route signals to the appropriate path while ensuring minimal interference.

The NMR signal from the probe is very small (of the order of μV), so it needs to be amplified to a higher voltage level. The NMR signal is to be stored in the computer memory, therefore it is necessary to convert it into digital form through an analog-to-digital converter (ADC).

3.4.2 NMR excitation and detection coil: signal-to-noise ratio

The core element of an NMR probe is the excitation and detection coil, and all the other parts of the probe must fit together to ensure that it works. Generally, the efficiency of a probe for a target nucleus at a given magnetic field is measured by its sensitivity. This latter is based on the signal-to-noise ratio (S:N) induced in the coil after a 90° pulse. There are various methods used to estimate the sensitivity [35, 36], however, here we focus only on the principle of reciprocity.

The principle of reciprocity

The principle of reciprocity allows us to determine the electromotive force (emf) induced in the coil by the precession magnetization after a 90° pulse. It states that the strength of the emf ξ_i of a voxel V_i is proportional to its magnetization M_i and the magnetic field $b_{1,i}$ produced by a unit current in the coil

$$\xi_i = -(d/dt)(b_{1,i} \cdot M_i). \tag{3.25}$$

The emf ξ across a sample of volume V_s is the integral sum of the emf induced over the voxels V_i

$$\xi = -\int_{\text{sample}} (d/dt)(\boldsymbol{b}_{1,i} \cdot M_i) dV_s. \tag{3.26}$$

For small samples, where $\boldsymbol{b}_1(\boldsymbol{r})$ is nearly constant over the volume of the sample V_s, the calculation of equation 3.26 gives

$$\xi = K\omega_0 b_1 M_{eq} V_s \cos(\omega_0 t), \tag{3.27}$$

where K is an inhomogeneity factor, V_s is the sample volume, and M_{eq} the equilibrium magnetization.

Using the expression (1.7) for M_{eq}, one obtains

$$\xi = K V_s b_1 \cos(\omega_0 t) \frac{n\gamma\hbar^2 I(I+1)\omega_0^2}{3k_B T_s}. \tag{3.28}$$

The signal induced by the emf ξ in the coil is directly proportional to the square of the Larmor frequency ω_0.

The noise

The noise originates from the resistance of the coil and can be expressed by the following equation

$$V_N = \sqrt{4kT_c \Delta f R}, \tag{3.29}$$

where T_c is the coil temperature, Δf the bandwidth of the receiver, and R is the resistance of the coil. Two things to note from the equation (3.29)

1. Cooling the coil will reduce the noise.

2. Minimizing losses of the coil will reduce the noise.

However, for the fields used in NMR experiments (above 5 MHz), the "skin effect" and the "proximity effect" are introduced, which increase the coil losses, and therefore R. The skin effect limits the flow of current to a certain depth of the conductor

$$\delta = \sqrt{\frac{2}{\omega_0 \mu_r \sigma}}, \tag{3.30}$$

where δ is the skin depth, μ_r and σ are the permeability of the wire and the conductivity of the conductor respectively. The equation (3.30) shows that skin depth decreases at higher frequencies and with higher conductivity materials. The result is that the current will be more concentrated near the conductor's surface. The skin effect affects the resistance of the coil qualitatively by incresing it (resistance inversely proportional to δ).

The proximity effect occurs when alternating current flows through nearby conductors. These currents interact with one another causing a non-uniform current distribution within the conductors. As a result, the area over which the current flows is reduced and thus the coil resistance is increased by a factor ζ. The proximity factor ζ depends on the separation of the windings between the conductors of the coil, the spacing between them, the resonance frequency , and the electrical conductivity and permeability of the conductive materials. [37, 38].

One can find more details on "skin effect" and "proximity effect" in the references [38, 39]. In presence of the "skin effect" and the "proximity effect", the resistance R of the coil can be written

$$R = \frac{l}{p} \zeta \sqrt{\frac{\mu_r \omega_0 \rho}{2}}, \tag{3.31}$$

where p the circumference, l the length of the conductor, ρ is the resistivity of the conductor that depends on its temperature T_c, and ζ the proximity factor of about 3 [37]. This equation (3.31) shows that reduced skin effect losses, stray capacitance and inductance (proximity effect) contribute to a lower resistance R.

These latter depends on the size and shape of the NMR coil (l and p), and is proportional to the square-root of frequency ω_0 (the applied magnetic field). The resistance R of a coil is proportional to the quality factor Q of the coil that can be easily measured by a network analyser.

The signal-to-noise ratio

The signal-to-noise ratio ψ_{rms} using this method of calculations is obtained by combining the equations (3.28), (3.29), and (3.31)

$$\psi_{\text{rms}} = \frac{K b_1 V_s n \gamma \hbar^2 I(I+1)}{7.12 k T_s} \left(\frac{p}{F k T_c l \zeta \Delta f} \right)^{\frac{1}{2}} \frac{\omega_0^{\frac{7}{4}}}{(\mu \mu_0 \rho)^{\frac{1}{4}}}. \tag{3.32}$$

Equation (3.32) shows that the SNR depends on:

1. Coil geometry and its temperature (l, p, KB_1, ρ and T_c).
2. Sample volume V_s.
3. Quality of the amplifier F

An interesting point to note from equation (3.32) that the Larmor frequency dependence of the sensitivity is to the power of $7/4$, which is only slightly smaller than the power of 2 of equation (3.28).

3.5 Modeling and characterization of the GHz NMR probe

The probe is the centerpiece of NMR spectrometers, fulfilling two vital functions in transmitting and receiving radio-frequency (RF) signals to and from the sample under investigation. It serves in the excitation phase to generate the RF magnetic field near the resonance frequency of the target nuclei, denoted $\boldsymbol{B}_1(\boldsymbol{r})$, required to excite the nuclear spins in the sample, and then to detect the resulting NMR signal induced by the precession of the magnetization $\boldsymbol{M}(t)$ after the excitation.

3.5.1 The radio frequency resonance circuit

To ensure efficient transmission of radio-frequency power to the probe during the excitation phase and to maximize the signal-to-noise ratio in the induced NMR spectrum, the resulting impedance of the probe must be tuned to the desired resonance frequency f_0, and matched to the impedance of the connected coaxial cable (transmission line), which is equal to $Z_0 = 50\ \Omega$ [40].

However, the excitation and detection coil does not fulfill these conditions on its own. Therefore, we have to add other elements like variable capacitors and inductors. These elements form a radio-frequency (RF) circuit.

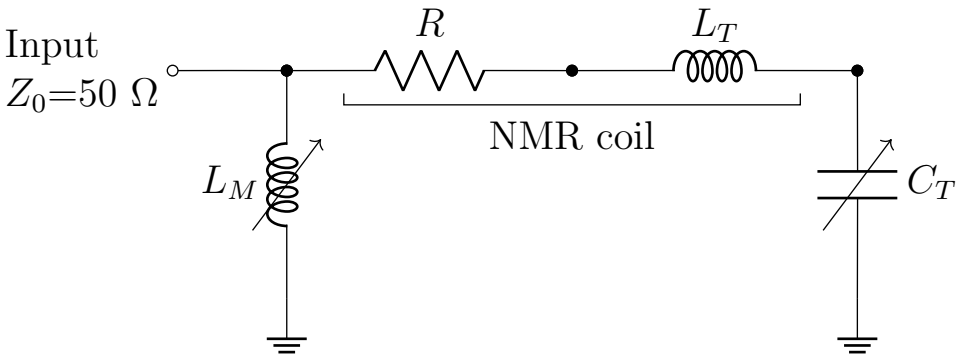

Figure 3.11: Probe circuit.

For the probe used in the resistive magnet NMR experiments, the RF circuit contains

1. A variable capacitor mounted in series with the NMR excitation and detection coil to tune the circuit to the desired resonance frequency f_0.

2. A variable inductor mounted in parallel to the circuit to match the circuit to $Z_0 = 50\ \Omega$.

The circuit required for excitation and detection is shown on the figure 3.11. Analytical calculations lead to the values of C_t and L_m, for which the total impedance Z_0 of the RF circuit is equal to $50\ \Omega$. The impedance of the branch through which the NMR coil current flows corresponds to the impedance of an RLC circuit (Z_{RLC}) and the impedance of the branch through which the "matching" current flows is simply the impedance of the matching coil (Z_m). Z_{RLC} and Z_m are mounted in parallel. The total impedance Z is given by

$$Z = \left(\frac{1}{Z_m} + \frac{1}{Z_{\text{RLC}}}\right)^{-1} = \left(\frac{1}{i\omega_0 L_m} + \frac{1}{R + i\omega_0 L_t + \frac{1}{i\omega_0 C_t}}\right)^{-1}. \tag{3.33}$$

The resonance condition is $Z = Z_0$, where $Z_0 = 50\ \Omega$ and real. Separating Z into real and imaginary parts, and using the resonance condition gives

$$\frac{R^2 + \left(\omega_0 L_t - \frac{1}{\omega_0 C_t}\right)^2}{R} = Z_0, \tag{3.34}$$

$$\frac{R^2 + \left(\omega_0 L_t - \frac{1}{\omega_0 C_t}\right)^2}{\frac{1}{\omega_0 C_t} - \omega_0 L_t} - \omega_0 L_m = 0. \tag{3.35}$$

Using these two equations, we can obtain the analytical form of C_t and L_m as functions of Z_0, ω_0, R and L_t

$$C_t = \frac{1}{\omega_0^2 L_t + \omega_0\sqrt{R(Z_0 - R)}}, \tag{3.36}$$

and

$$L_m = \frac{Z_0}{\omega_0}\sqrt{\frac{R}{Z_0 - R}} = \frac{Z_0}{\omega_0}\sqrt{\frac{R}{Z_0}}\sqrt{\frac{1}{1 - \frac{R}{Z_0}}}. \tag{3.37}$$

For small R, we find a simplified resonance condition

$$\omega_0 \approx \frac{1}{\sqrt{L_t C_t}}. \tag{3.38}$$

L_m is proportional to $\sqrt{R}/\omega_0$.

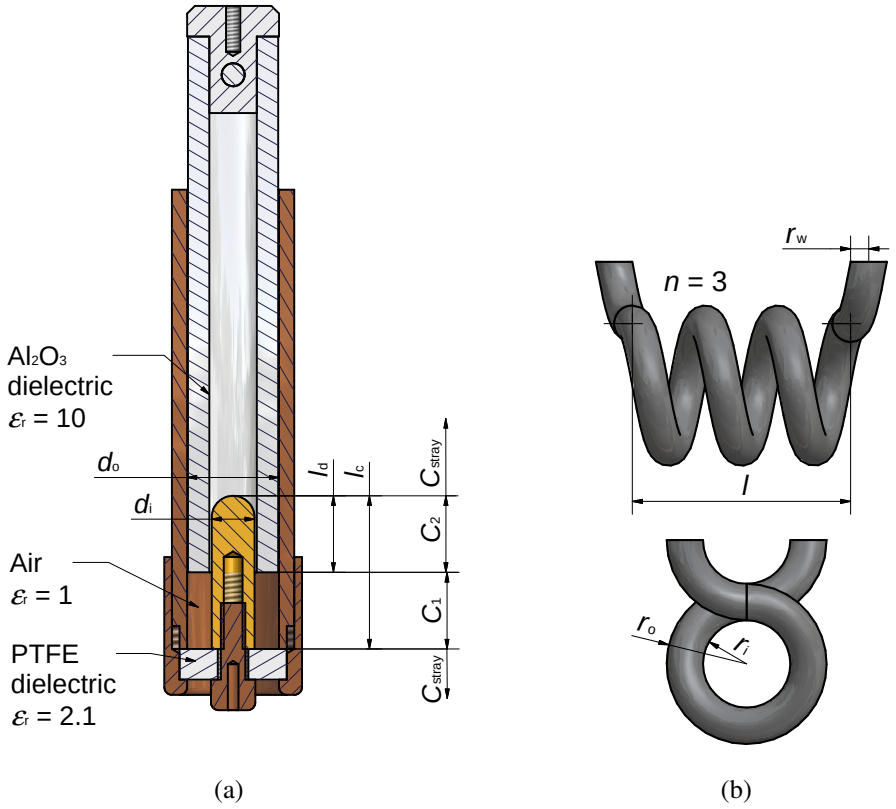

Figure 3.12: (a): Tuning capacitor C_t configuration with its relevant parameters. (b): Example of an NMR coil with its relevant parameters.

The variable tuning capacitor C_t used in our configuration is designed to be coaxial, as shown in figure 3.12 (a). A dielectric Al_2O_3 tube can be inserted in between the two concentric copper conductors. This configuration allows to change the length l_d of the dielectric Al_2O_3 inside the coaxial capacitor by sliding it in or out, thus varying the capacitance C_t.

C_1 and C_2 are connected in parallel as shown in figure 3.12 (a). For a first estimation of C_t, we neglect the effect of the stray capacitances C_{stray}

$$C_t = \underbrace{\frac{2\pi\epsilon_0(l_c - l_d)}{\ln(d_o/d_i)}}_{C_1} + \underbrace{\frac{2\pi\epsilon_0\epsilon_r(l_d)}{\ln(d_o/d_i)}}_{C_2} = \frac{2\pi\epsilon_0}{\ln(d_o/d_i)}\left(l_c + (\epsilon_r - 1)l_d\right), \tag{3.39}$$

where ϵ_0 is the permittivity of free space, ϵ_r the permittivity of the dielectric Al_2O_3, d_o and d_i are respectively the outer and the inner diameter of the dielectric, and l_c length of the capacitor inner part (copper). The length of the dielectric varies within the capacitor between $0 \leq l_d \leq l_c$.

For an RF coil of a few millimetres shown in figure 3.12 (b), the inductance taken from [41] is expressed as follows

$$L_t = \frac{4(nr)^2(1 - \frac{0.2}{n})}{l + 1.2r^{0.9}}, \tag{3.40}$$

where n is the number of turns, l is the coil length, and r is equal to

$$r = r_i + 0.2r_w \tag{3.41}$$

with r_i is the inner radius of the coil and r_w is the wire radius.

3.5.2 Quality factor of the NMR resonance circuit

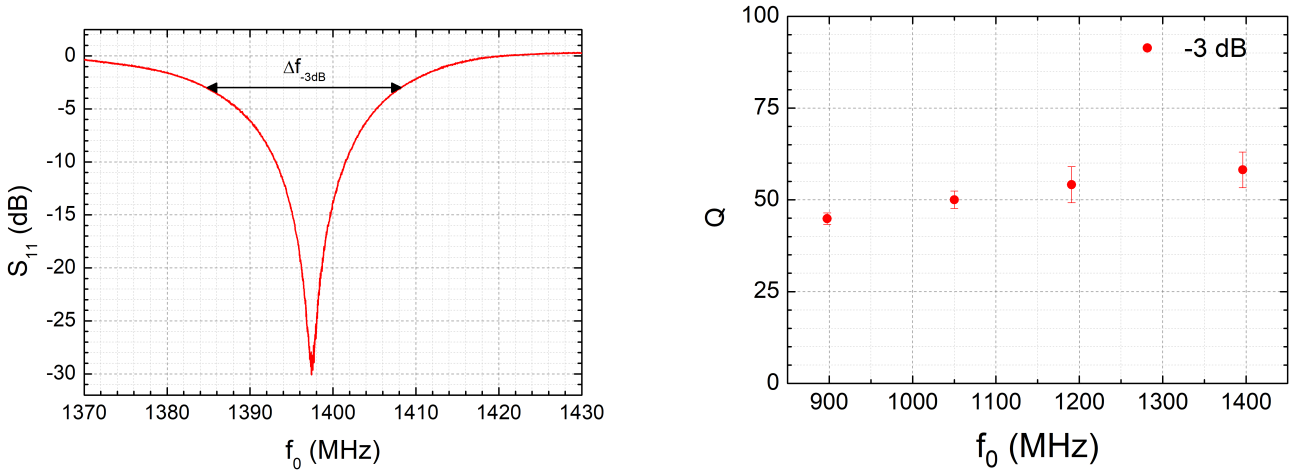

(a) (b)

Figure 3.13: (a): Example of the reflected power of the high-field NMR probe at the resonance frequency $f_0 = 1397$ MHz. (b): Quality factors at the resonance frequencies used in the high-field NMR experiments.

With the help of a network analyzer we tune the RF circuit to the desired resonance frequency f_0 and match it to $Z_0 = 50\ \Omega$. It measures the reflected power S_{11} of the RF circuit expressed in dB units

$$S_{11} = 10 \log_{10} \left(\frac{(Z - Z_0)(Z - Z_0)^*}{(Z + Z_0)(Z + Z_0)^*} \right), \tag{3.42}$$

where $Z = Z_{\text{real}} + Z_{\text{Imag}}$ is the total impedance of the probe circuit, so $(Z - Z_0)^*$ and $(Z + Z_0)^*$ are the complex conjugate of $(Z - Z_0)$ and $(Z + Z_0)$ respectively.

We tune and match the circuit in such a way that the minimum of the reflected power falls on the desired resonance frequency f_0. Figure 3.13 (a) shows an example of the reflected power of the probe circuit at the resonance frequency $f_0 = 1397$ MHz.

We define the Q factor of the circuit from the reflected power curves, defined as the ratio of the resonance frequency f_0 over $\Delta f_{-3\text{dB}}$ the response at -3 dB (shown in figure 3.13 (a))

$$Q = \frac{f_0}{\Delta f_{-3\text{dB}}}. \tag{3.43}$$

The probe is highly sensitive to signals near f_0. Figure 3.13 (b) shows the frequency dependence of the Q quality factor, an almost constant value (≈ 50), indicating the same NMR conditions at all frequencies.

3.5.3 Design of an NMR probe

There are numerous papers and books available on probe design and construction [11, 41–43]. Therefore, this section will only focus on the design and set-up of our NMR probe used for high-field experiments (figure 3.14) that require several technical factors to be considered.

This section is divided into two parts: the first concentrates on the major constraints encountered during the construction of the probe, related to the design of the RF circuit and the optimization of the probe's sensitivity, and the second concerns the control of the sample environment (temperature, positioning and probe materials).

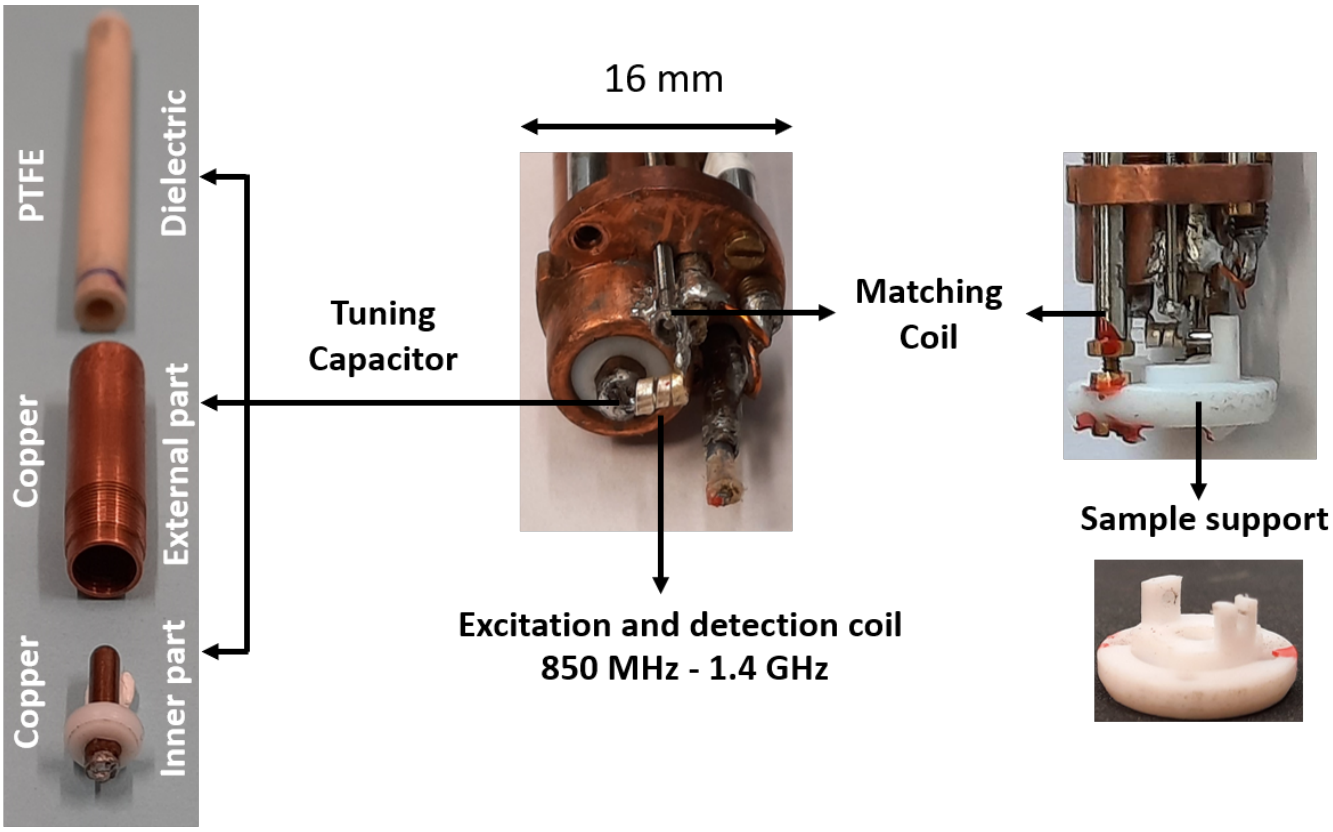

Figure 3.14: Scheme of broadband tuning probe. Left: Tuning capacitor; Center: Excitation and detection coil; Right top: Matching coil; Right bottom: Sample support. Details can be found in text.

Major constraints for probe design

1. Magnetic field inhomogeneity

   As shown before, a sample size of ≈ 1 mm^3 is used to minimize the inhomogeneity of the external field $\boldsymbol{B}_0(\boldsymbol{r})$. The solenoidal coil dimensions have to be adapted to this size in order to obtain the highest (S:N) ratio (see table 3.16).

   Moreover, to achieve the most homogeneous fields $\boldsymbol{B}_0$ and $\boldsymbol{B}_1$ across the sample volume V_s, it's best to position the sample at the center of the coil, which will be centered inside the resistive magnet.

   To facilitate that, we have designed a sample holder that can center the NMR capillary tube containing the sample within the coil and hence inside the magnet as shown in figure 3.15. Figure 3.14 shows the sample holder, which was manufactured at the LNCMI workshop.

   We estimate that off-center positioning of the sample can occur in the longitudinal coil direction with a margin of ± 0.25 mm relative to the center of the coil during the manual insertion process.

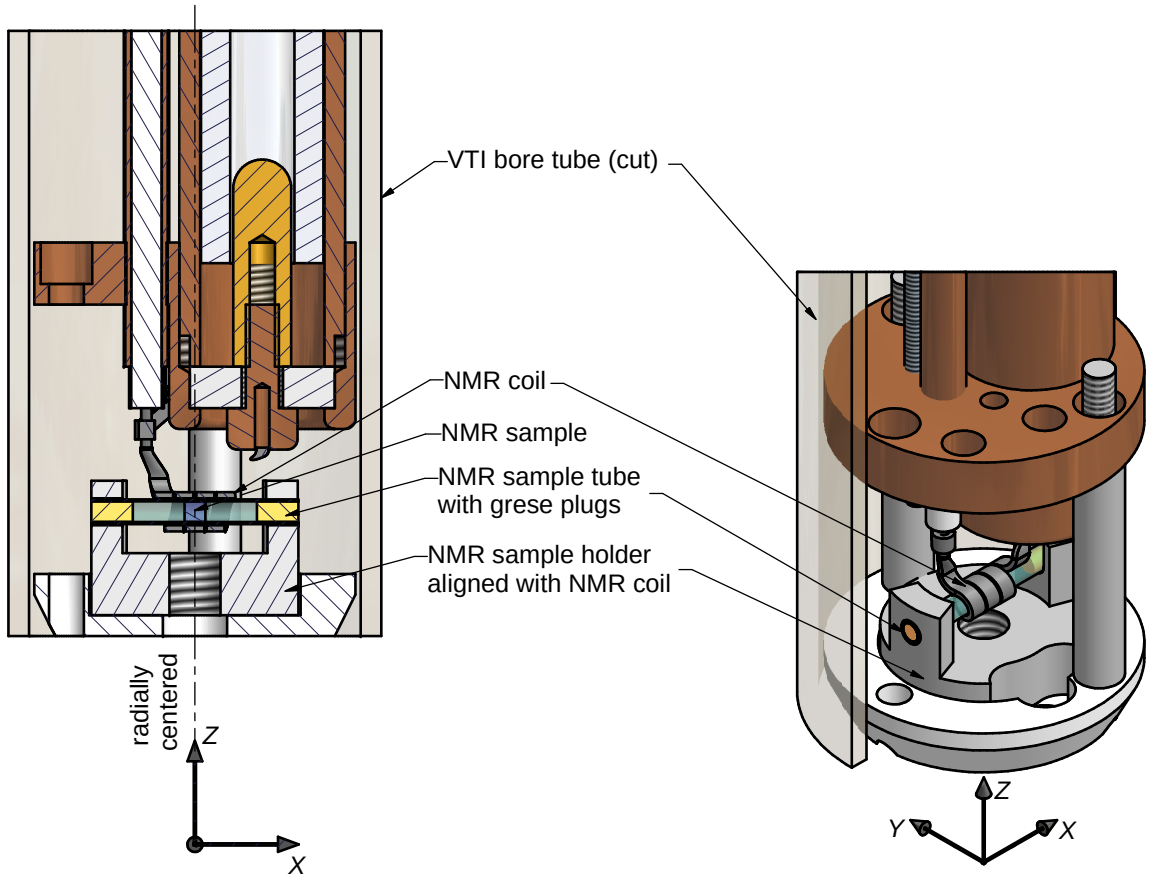

Figure 3.15: 3D view of the NMR broadband tuning probe showing the sample positioning inside the NMR excitation and detection coil.

2. Magnetic field range, nuclei of interest, and Larmor frequency

   The field of our interest for NMR experiments with resistive magnets ranges from 20 T to 33 T, corresponding to frequencies of 800 MHz to 1400 MHz for ^{1}H NMR ($\gamma = 2\pi \times 42.57$ MHz/T).

   Therefore, our liquid state ^{1}H NMR broadband tuning probe has to operate at this frequency range. The solutions of the resonance equations (3.36) and (3.37) provide solutions for C_t and L_m at a given ω_0. For ω_0 in the GHz range, we need

   (a) Small inductors L_t of the NMR coil in the nH range. Our coil uses a flat rectangular wire and has the following parameters

Property	Value
Length of Coil	3.0 mm
Number of Turns	3.0
Internal Coil Diameter	1.35 mm
External Coil Diameter	1.9 mm
Wire width	0.9 mm
Air gap	0.1 mm
Inductance	9.0 nH

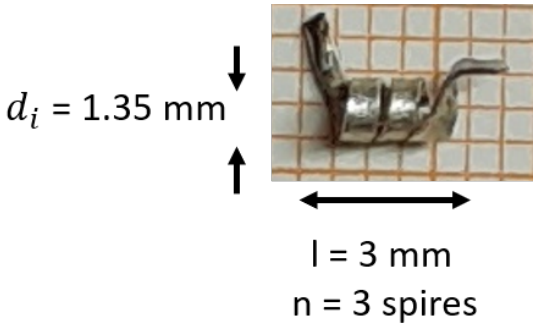

Figure 3.16: Left: Table of the excitation and detection coil L_t properties for high field induction. Right: The real excitation and detection coil L_t served to perform ^{1}H NMR experiments in the resistive magnet (for the 850 - 1400 MHz frequency range).

   Equations (3.40) and (3.41) provides an inductance of 9 nH using the parameters of the table 3.16 ($r_i = 0.95$ mm and $r_w = 0.45$ mm).

   (b) Small capacitors C_t for the tuning capacitor in the pF range. The capacitor of the probe (that part of figure 3.12 (a) and figure 3.14) has the following dimensions

Property	Value
l_d	0.0 $\rightarrow$ 9.5 mm
l_c	9.5 mm
d_i	2.7 mm
d_o	6.0 mm
ϵ_r	10.0
C_t	0.6 $\rightarrow$ 6.6 pF

Table 3.3: Tuning capacitor C_t properties.

   For the upper limit of C_t, where the dielectric is fully inside the coaxial capacitor ($l_d = l_c$), equation (3.39) provides a capacitance of 6.6 pF. For the lower limit of C_t, where the dielectric is fully outside the coaxial capacitor ($l_d = 0$), equation (3.39) provides a capacitance of 0.6 pF. Please note that this calculation is based on a simplified model and that the effective capacitance may vary depending on the size of the stray capacitance C_{stray}.

(c) Small values of L_m in the nH range. In our case L_m is a single turn coil of $d = 1$ mm mounted along the z-axis near the coaxial cable. A threaded metallic rod that enters into the coil allows an adjustment of the value of L_m.

(d) A compact design to avoid stray capacitance and inductances that reduce the sensitivity and the tuning range. In our case C_t, L_m and L_t are located within a sphere of 15 mm diameter.

Minor constraints for probe design

1. Sample temperature

   Some probe designs can incorporate a temperature control system, such as a cryogenic or heating system, to maintain the sample at a particular temperature. In our case, the experiments were carried out at room temperature. We, therefore, used a continuous flow of nitrogen to regulate and stabilize the temperature at $298 \pm 2K$.

2. Probe materials

   All the probe components are strictly composed of non-magnetic materials. Another important point to note is to avoid materials that contain the ^{1}H nucleus during the probe construction to minimize the background signals.

3.6 NMR spin dynamics in inhomogeneous static and radio frequency fields

In this section, we present the simulation of the radio-frequency properties of the NMR coil and its interaction with the nuclear spins during the excitation pulse. For this purpose we used a finite element simulation (COMSOL Multiphysics 6.1) and special Matlab scripts.

3.6.1 Finite element simulation of NMR coil

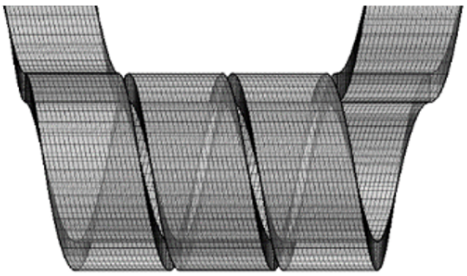

Figure 3.17: Mesh mapped method used by COMSOL Multiphysics 6.1 for the NMR coil simulation L_t.

COMSOL Multiphysics 6.1 combines the finite element method and numerical integration to solve the electromagnetic equations, to calculate the coil characteristics and the magnetic field distribution over the voxels V_i, providing insight into the coil's behavior and performance.

The simulation process involves defining the coil geometry (figure 3.16) and its material properties (copper), specifying the boundary conditions and electrical inputs, and selecting the appropriate physics modules and solvers.

We used the AC/DC module, the coil material was set to copper, and the coil was designed as a single conductor carrying a unit current. In addition, we used a fine mesh for the geometry, as shown in the figure 3.17. This method aims to align mesh elements on complex shapes such as coils and ensures that the mesh uniformly follows its geometry.

The aim of the finite element simulation was to

1. Calculate the relevant parameters of the excitation coil, such as the inductance L_t and the resistance R and the unit current magnetic field at its center $b_{1,0}$. Table 3.4 shows the results. We note that the inductance agrees well with the approximate formula (3.40) and (3.41).

Input	**Output**		
Current (A)	Inductance (nH)	Resistance (mΩ)	Field at the coil center $b_{1,0}$ (mT/A)
1.0	9.0	1.5	1.1

Table 3.4: The relevant coil parameters extracted from the COMSOL simulation.

2. Simulate the spatial profile and distribution of $\boldsymbol{B}_1(\boldsymbol{r})$ in the coil, and in particular in the sample region. The sample's coverage region is indicated with a blue cylinder in figure 3.18 and will be the only region of interest in our subsequent discussions. The coordinate system of the sample coverage area is given by
$$\frac{-l}{2} \leq x \leq \frac{l}{2}, \quad \frac{-d}{2} \leq y \leq \frac{d}{2}, \quad \frac{-d}{2} \leq z \leq \frac{d}{2} \tag{3.44}$$
where we use cylindrical samples with a diameter of $d = 1$ mm and lengths ranging from $l = 1$ to 2 mm. The voxel size was equal to $0.01 \times 0.01 \times 0.01$ mm^3.

The current density distribution is uniform across the coil's cross section at the entry points. This unit current generates an almost homogeneous magnetic field $\boldsymbol{B}_1(\boldsymbol{r})$ across the axis of the coil, particularly in the region near its center $B_{1,0}$.

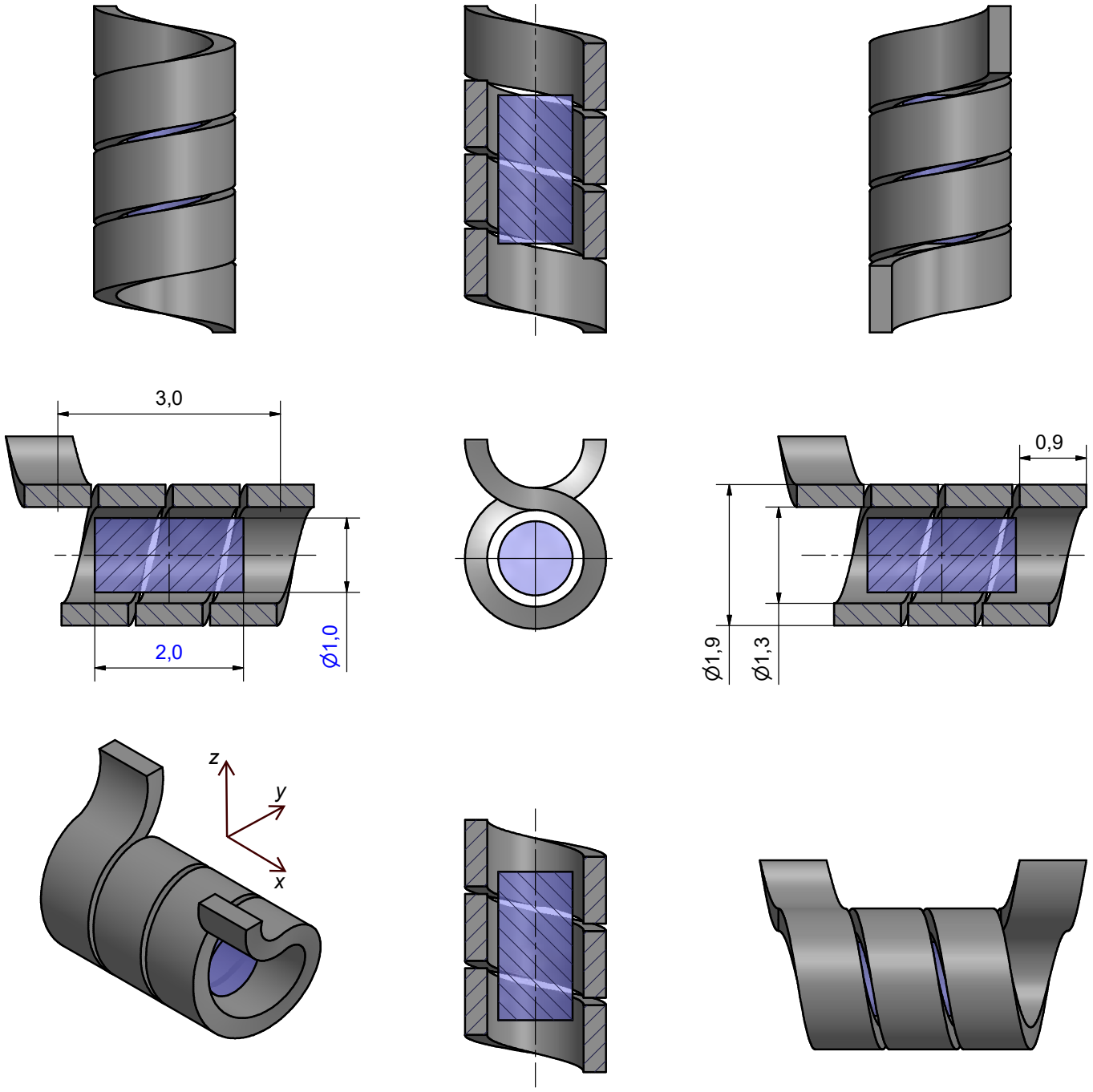

Figure 3.18: 3D representation of the NMR excitation and detection coil simulated by COMSOL in different planes such as (z,x), (z,y) and (x,y). The blue square shows the sample positioning region ($\frac{-l}{2} \leq x \leq \frac{l}{2}$, $\frac{-d}{2} \leq y \leq \frac{d}{2}$, $\frac{-d}{2} \leq z \leq \frac{d}{2}$).

To investigate the impact of local variations $\boldsymbol{B}_1(\boldsymbol{r})$ on NMR excitation in individual voxels V_i of the sample, we adopted the following assumptions:

1. To simplify the analysis, we disregard the proximity and skin effect on the distribution of $\boldsymbol{B}_1(\boldsymbol{r})$ by applying a DC current to the coil.
2. We only consider the NMR coil. All the effects of other probe elements (tuning capacitor and matching coil) that can modify the field distribution are disregarded.
3. The longitudinal component $\boldsymbol{B}_{1,z}$ was neglected since it does not contribute to the excitation of the magnetization, as discussed previously in the NMR theory chapter.
4. The transverse magnetic field $\boldsymbol{B}_1(\boldsymbol{r})$ within each voxel V_i was normalized by the field at the center of the coil $\boldsymbol{B}_{1,0}$.

The simulations show that the DC current density is uniform across the wire sections. Along the axis of the coil, the field is almost parabolic, which generates a homogeneous region near the center.

The relative variations in the magnetic field across the sample are visualized in three selected planes: (z, x), (z, y), and (x, y), as depicted in figure 3.19 (a), (b), and (c) respectively. In all three cross-section plots, it is evident that the field distribution is dependent on the proximity of the voxels to the wire. This proximity increases the relative field strength within the voxel or decreases it between two adjacent wires.

In the (z,y) plane, the field appears to be the most homogeneous compared with the other planes, where it varies within a range of $\pm 3\%$. However, these variations are more pronounced in the (y,x) and (z,x) planes, with a maximum deviation of -20 % observed at $x = \pm 1$ mm equivalent to $l = 2$ mm. In these planes, similar field profiles are obtained, where the only visible difference is the position of the wire relative to the voxels V_i. We can therefore say that the field profiles in the different planes reproduce the geometry of the coil. Moreover, the field gradients are almost symmetric for a well-centered sample.

For $l = 1$ mm and $d = 1$ mm, we can conclude that the magnetic field $\boldsymbol{B}_1$ is almost constant across the voxels V_i, since the variations do not exceed ± 3 % in the (z,y) plane, and ± 5 % in the (z,x) and (y,x) planes. As shown in figure 3.19, when the length l of the sample is greater than 1.5 mm (corresponding to $x > 0.75$ mm), the changes in magnetic field $\boldsymbol{B}_1$ become more noticeable, with a decrease of 20 % at $x = \pm 1$ mm ($l = 2$ mm).

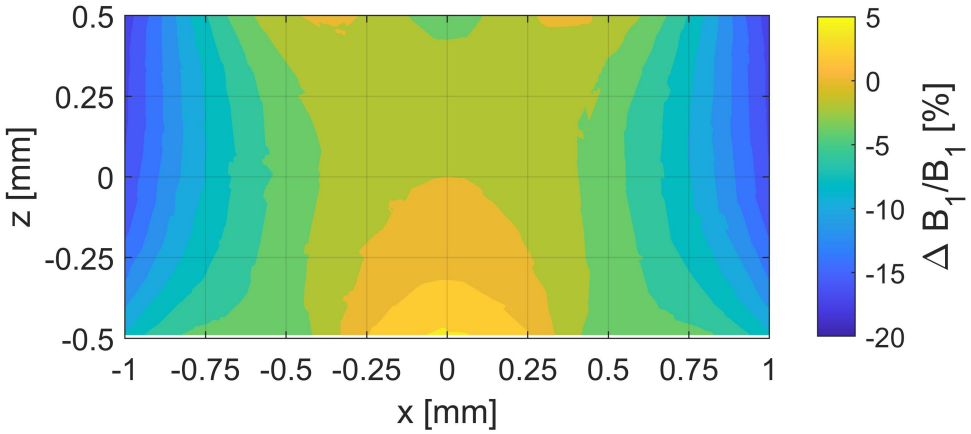

(a)

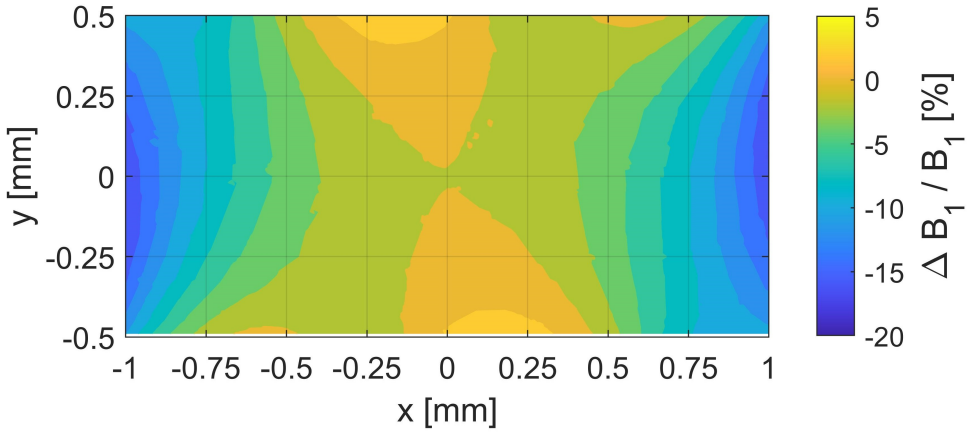

(b)

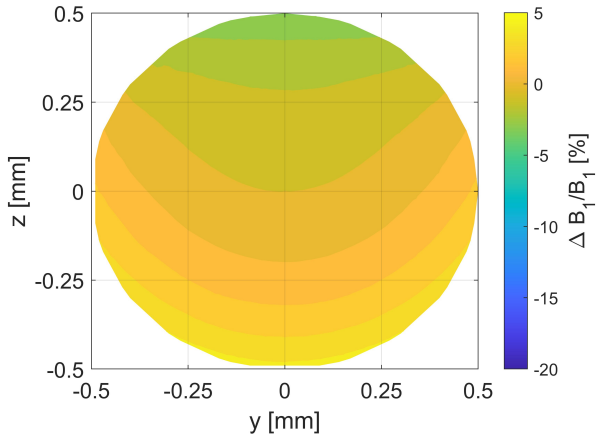

(c)

Figure 3.19: The relative field distribution $\Delta B_1/B_1$ expressed in % over the sample in the three main planes (a) : (z,x) , (b) : (x,y) , (c) : (z,y).

3.6.2 Simulation of the NMR spin dynamics

In this part, we present the results of Matlab simulations for the nuclear spin dynamics in inhomogeneous B_1 and B_0 fields. For this purpose, we solve the equations of motion of a nuclear spin ensemble described in chapter 1 using field profiles at the resistive magnet (section 3.1.2) and the NMR coil (previous part)). This provides access to the average values and the distribution of the longitudinal magnetization M_z and the transverse magnetization $M_\perp$.

This data allow to

1. Simulate the nutation experiments to show the deviation of the effective pulse angle sensed by the sample from the nominal pulse angle applied at the center of the coil.

2. Study the influence of fields $\boldsymbol{B}_0(\boldsymbol{r})$ and $\boldsymbol{B}_1(\boldsymbol{r})$ inhomogeneities on the distribution of the magnetization $\boldsymbol{M}(\boldsymbol{r})$ across the sample.

In the script, we used the two field profiles, $\boldsymbol{B}_0(\boldsymbol{r})$ and $\boldsymbol{B}_1(\boldsymbol{r})$, while using the voxel-based NMR approach described in chapter 1. They were normalized with respect to the center of the coil, which we regard as being the same as the center of the resistive magnet. The whole simulation assumes that the central point ($\boldsymbol{r} = \boldsymbol{0}$) satisfies a resonance condition and that all the other voxels deviate from this condition, with

$$\boldsymbol{\omega}_1(\boldsymbol{r}) = \omega_1(\boldsymbol{r} = \boldsymbol{0})\boldsymbol{\omega}_{1,n}(\boldsymbol{r}) \qquad \text{in the (x,y) plane,} \tag{3.45}$$

and

$$\boldsymbol{\Delta\omega}(\boldsymbol{r}) = \omega_0(\boldsymbol{r} = \boldsymbol{0})\boldsymbol{\Delta\omega}_n(\boldsymbol{r}) \qquad \text{along the z-axis.} \tag{3.46}$$

We note that $\boldsymbol{r}$ is the distance vector corresponding to a 3D vector in Cartesian coordinates (x,y,z) and that the size of each voxel is $0.01 \times 0.01 \times 0.01$ mm^3. We derive then the normalized effective field $\omega_{eff,n}(\boldsymbol{r})$ from equations 3.45, 3.46, and 1.25 (from chapter 1)

$$\omega_{eff,n}(\boldsymbol{r}) = \omega_{1,n}(\boldsymbol{r})\sqrt{1 + \left(\frac{\omega_0(\boldsymbol{r} = \boldsymbol{0})}{\omega_1(\boldsymbol{r} = \boldsymbol{0})}\frac{\Delta\omega_n(\boldsymbol{r})}{\omega_{1,n}(\boldsymbol{r})}\right)^2}, \tag{3.47}$$

where $\boldsymbol{\omega}_{1,n}(\boldsymbol{r})$, $\boldsymbol{\omega}_{0,n}(\boldsymbol{r})$, and $\boldsymbol{\Delta\omega}_n(\boldsymbol{r})$ are the normalized spatial vectors. $\omega_1(\boldsymbol{r} = \boldsymbol{0})$ and $\omega(\boldsymbol{r} = \boldsymbol{0})$ are taken from the experimental values: $\omega_1(\boldsymbol{r} = \boldsymbol{0})$ is the pulse strength extracted at each field from nutation experiment (see chapter 1.3 section 1.3.3) and $\omega_0(\boldsymbol{r} = \boldsymbol{0}) = 2\pi f_0$ is the corresponding resonance frequency. $\omega_0(\boldsymbol{r} = \boldsymbol{0})$ and $\omega_1(\boldsymbol{r} = \boldsymbol{0})$ which were used in our following model are summarized in the table 3.5.

$\omega_0/2\pi$ [MHz]	$\omega_1/2\pi$ [kHz]	ω_0/ω_1
820	93	8800
1020	96	10600
1200	84	14200
1400	60	23300

Table 3.5: Experimental parameters of the resistive magnet experiment for ω_0 and ω_1.

Equation (3.47) allows to estimate the contributions of $\boldsymbol{B}_1(\boldsymbol{r})$ and $\boldsymbol{B}_0(\boldsymbol{r})$ inhomogeneities. We can deduce from figures 3.19 and figure 3.3 and table 3.5

$$1 - |\omega_{1,n}(\boldsymbol{r})| < (5-20) \times 10^{-2}, \tag{3.48}$$

$$|\Delta\omega_n(\boldsymbol{r})| < (2.5-10) \times 10^{-6}, \tag{3.49}$$

$$\frac{\omega_0}{\omega_1} < 2.33 \times 10^4. \tag{3.50}$$

The above equations gives

$$\left(\frac{\omega_0(\boldsymbol{r}=\boldsymbol{0})}{\omega_1(\boldsymbol{r}=\boldsymbol{0})}\frac{\Delta\omega_n(\boldsymbol{r})}{\omega_{1,n}(\boldsymbol{r})}\right)^2 = \left(\left(2.33\times10^4\right)\left(\frac{(2.5-10)\times10^{-6}}{1\pm(5-20)\times10^{-2}}\right)\right)^2 \leq 0.04 \tag{3.51}$$

which leads to

$$\sqrt{1+\left(\frac{\omega_0(\boldsymbol{r}=\boldsymbol{0})}{\omega_1(\boldsymbol{r}=\boldsymbol{0})}\frac{\Delta\omega_n(\boldsymbol{r})}{\omega_{1,n}(\boldsymbol{r})}\right)^2} \approx 1. \tag{3.52}$$

Inserting the equation (3.52) back into the equation (3.47)

$$\omega_{eff,n}(\boldsymbol{r}) \approx \omega_{1,n}(\boldsymbol{r}). \tag{3.53}$$

This estimation clearly shows that $\omega_{eff,n}(\boldsymbol{r})$ is only affected by the inhomogeneities of $\boldsymbol{B}_1(\boldsymbol{r})$.

The excitation pulse distribution $\beta(\boldsymbol{r})$ was calculated with respect to the nominal angle β_{nom} applied at the center of the coil ($\boldsymbol{r}=\boldsymbol{0}$)

$$\beta(\boldsymbol{r}) = \beta_{nom}\omega_{eff,n}(\boldsymbol{r}) \tag{3.54}$$

In addition, we recall the equation (1.28) from chapter 1 to show the magnetization vector $\boldsymbol{M}(\boldsymbol{r})$ created at each voxel after an excitation pulse $\beta(\boldsymbol{r})$ where $M_i(0) = M_{eq}\boldsymbol{e}_z$ is the initial condition common to all voxels

$$\boldsymbol{M}(\boldsymbol{r},t) \rightarrow M_{eq}\begin{pmatrix} -\sin(\phi)\sin(\beta)+\cos(\theta)\sin(\theta)\cos^2(\phi)\left(\cos(\beta)-1\right) \\ \cos(\theta)\cos(\phi)\sin(\phi)\left(1-\cos(\beta)\right)-\sin(\theta)\cos(\phi)\sin(\beta) \\ \cos^2(\theta)\cos^2(\phi)+\cos^2(\theta)\sin^2(\phi)\cos(\beta)+\sin^2(\theta)\cos(\beta) \end{pmatrix} \tag{3.55}$$

where $\phi(\boldsymbol{r})$ and $\theta(\boldsymbol{r})$ are also spatially dependent. Note that we apply $-$x pulses in the simulation, so that the magnetization M ends up in the y direction after a 90° pulse. The average magnetization over the sample is given by equation (1.31) from chapter 1

$$\boldsymbol{M} = \sum_{V_i} \boldsymbol{M}_i(\boldsymbol{r},t).$$

$$\boldsymbol{M}_\perp = \sum_{V_i} \left(M_{x,i}(\boldsymbol{r},t)\cdot\boldsymbol{e}_x + M_{y,i}(\boldsymbol{r},t)\cdot\boldsymbol{e}_y\right).$$

$$\boldsymbol{M}_z = \sum_{V_i} M_{z,i}(\boldsymbol{r},t)\cdot\boldsymbol{e}_z.$$

We define an effective pulse angle β_{eff} such that the net magnetization of the nuclear spins fulfills the following conditions:

1. An effective angle of 90° requires $\boldsymbol{M}_z = 0$
2. An effective angle of 180° requires $\boldsymbol{M}_\perp$ at a minimum value.

3.6.3 Results and discussion of NMR spin dynamics in inhomogeneous static and RF fields

In the following section we will analyse the average transverse $\boldsymbol{M}_{\perp}$ and longitudinal magnetization $\boldsymbol{M}_{z}$ as well the distribution after applying effective $\beta_{eff} = 90°$ and $\beta_{eff} = 180°$ pulse angles for different sample length $l = 1, 1.5$ and 2 mm.

Average magnetization

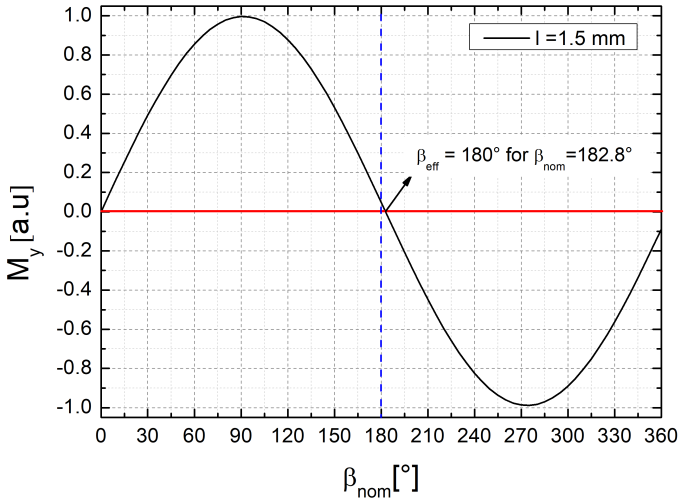

Figure 3.20: Simulated nutation experiment for a 1.5 *millimeter sample at* 1020 *MHz taking into account both field profiles.*

The effective pulse angles β_{eff} for each sample length were found by simulating a nutation experiment i.e., varying β_{nom} from zero to $360°$ and by calculating the average y-magnetization M_y. $\beta_{eff,180}$ is extracted for the nominal pulse angle β_{nom} where $M_y = 0$. This also gives the value of $\beta_{eff,90}$ which is half the value of $\beta_{eff,180}$.

The figure 3.20 shows an example of a simulated nutation experiment for a 1.5 millimeter sample at 1020 MHz. At $\beta_{nom} = 180°$, we still notice a finite magnetization M_y. It indicates that the strength of the effective pulse is weaker than the nominal pulse applied at the center of the coil. We attribute this effect to field inhomogeneity of mainly $\boldsymbol{B}_1(\boldsymbol{r})$ that prevent the full inversion of the net magnetization. As a consequence, to achieve the desired inversion, we need to apply longer pulses at the center of the coil, i.e., $\beta_{nom} = 182.8°$. This effect increases with the length of the sample, as shown in the tables (3.6) and (3.7).

To explore the behavior of the magnetization in more depth, we plot in figure 3.21 the nutation experiment for different sample lengths in a polar plot to see the evolution of both the magnitude and the phase of the transverse magnetization during the nutation experiment. The transverse magnetization during a nutation experiment shows an ellipsoidal trajectory that is broadening with sample length. These plots provide evidence that the phase exhibits two preferred directions, one at $90°$ and another near $270°$, for $\beta_{nom} < 180°$ and $\beta_{nom} > 180°$.

Moreover, the transition between these two preferential directions is smoother for the larger samples, whereas the 1 mm sample shows almost a sharp transition. The offset between the two directions is approximately $180°$ (see figure 3.22). We find that for increasing sample lengths, there is a noticeable rotation of the phase towards smaller angles, and hence the offset between the preferred directions becomes smaller than $180°$ (see figure 3.21 (a) (c) and (e)). The phase rotation is also associated with a reduction in the amplitude of the magnetization $M_\perp$.

In addition, we note from figure 3.21 (a), (c), and (e) that the transverse magnetization almost follows the theoretically expected value for an effective $90°$ pulse for all sample lengths. However, an effective pulse of $180°$ (given in table 3.6) does not result in a complete inversion of net magnetization as expected from the theoretical curve, where according to the polar diagrams 3.21 (b), (d), and (e), an amount of the transverse magnetization $M_\perp$ remains. This effect increases with the sample length, and represents 0.6, 3.4 and 7.4% respectively for 1, 1.5 and 2 mm sample.

Figure 3.22 (a), (b), (c), and (d) illustrate the evolution of $M_\perp$, M_z, and the phase $\phi_\perp$ using β_{nom} as trajectory variable. This observation is consistent with the fact that the field distribution becomes more inhomogeneous for larger samples, which leads to a bigger distribution of the pulse angles $\beta(\boldsymbol{r})$ over the voxels V_i, and prevents the total inversion of the net magnetization, even if we apply longer pulses to the center of the coil. We remark that the deviation from the theoretical curve starts to appear from $\beta_{eff} > 90°$ and increases with the nominal angle applied at the center of the coil, which also explains that the magnetization does not return to the equilibrium state after a $360°$ pulse.

Sample length [mm]	$\beta_{nom,90}$ [°]	$M_\perp$ [%]	$\phi_\perp$ [°]	M_z [%]
1	90.2	100.0	90.0	0.00
1.5	91.4	99.9	89.5	0.00
2	93.3	99.6	89.0	0.00

Table 3.6: Nominal pulse angles extracted from the nutation curves for different sample lengths needed to induce $\beta_{eff} = 90°$. The average value of both components of the relative magnetization $M_\perp$ and M_z over the voxels after the application of $\beta_{eff} = 90°$. $\phi_\perp$ represents the phase of $M_\perp$.

Sample length [mm]	$\beta_{nom,180}$ [°]	$M_\perp$ [%]	$\phi_\perp$ [°]	M_z [%]
1	180.4	0.6	182.7	99.9
1.5	182.8	3.4	180.3	99.8
2	186.6	7.4	178.3	99.5

Table 3.7: Nominal pulse angles extracted from the nutation curves for different sample lengths needed to induce $\beta_{eff} = 180°$. The average value of both components of the relative magnetization $M_\perp$ and M_z over the voxels after the application of $\beta_{eff} = 180°$. $\phi_\perp$ represents the phase of $M_\perp$.

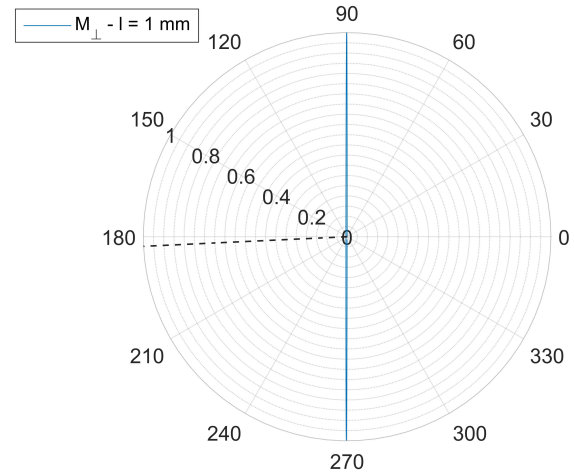

(a)

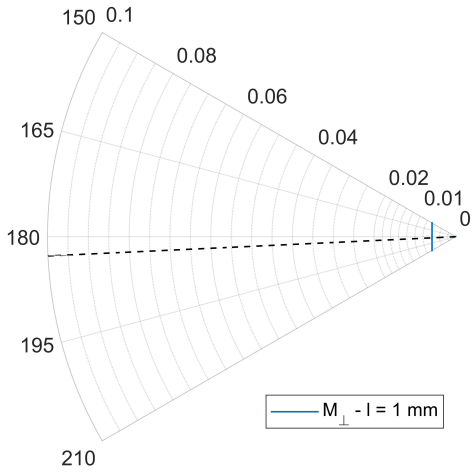

(b)

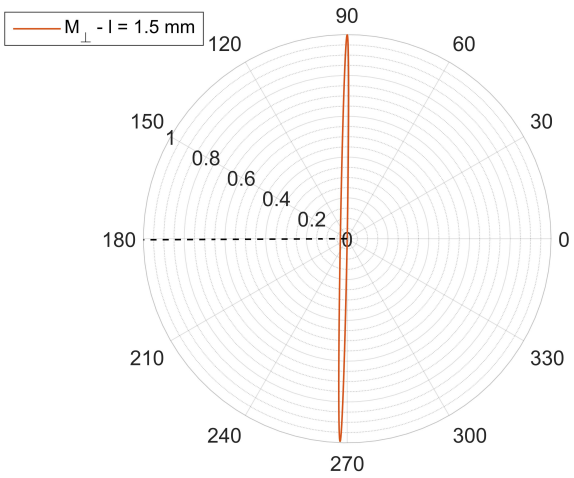

(c)

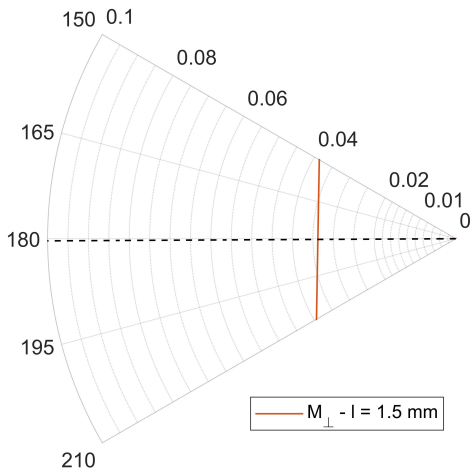

(d)

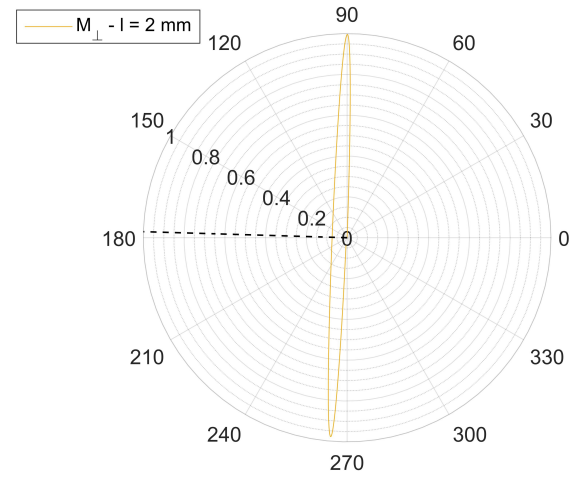

(e)

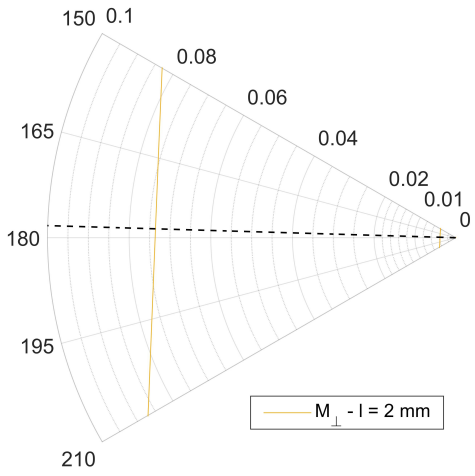

(f)

Figure 3.21: (a), (c), and (e): $\boldsymbol{M}_\perp$ evolution during a nutation experiment for 1, 1.5, *and* 2 *millimeters sample Lengths. (b), (d), and (f): A zoom on $\boldsymbol{M}_\perp$ for phases closer to the effective* 180° *pulse respectively for* 1, 1.5, *and* 2 *millimeters sample lengths. The dashed lines represents the phase of the averaged $\boldsymbol{M}_\perp$ remaining after an effective* 180° *pulse.*

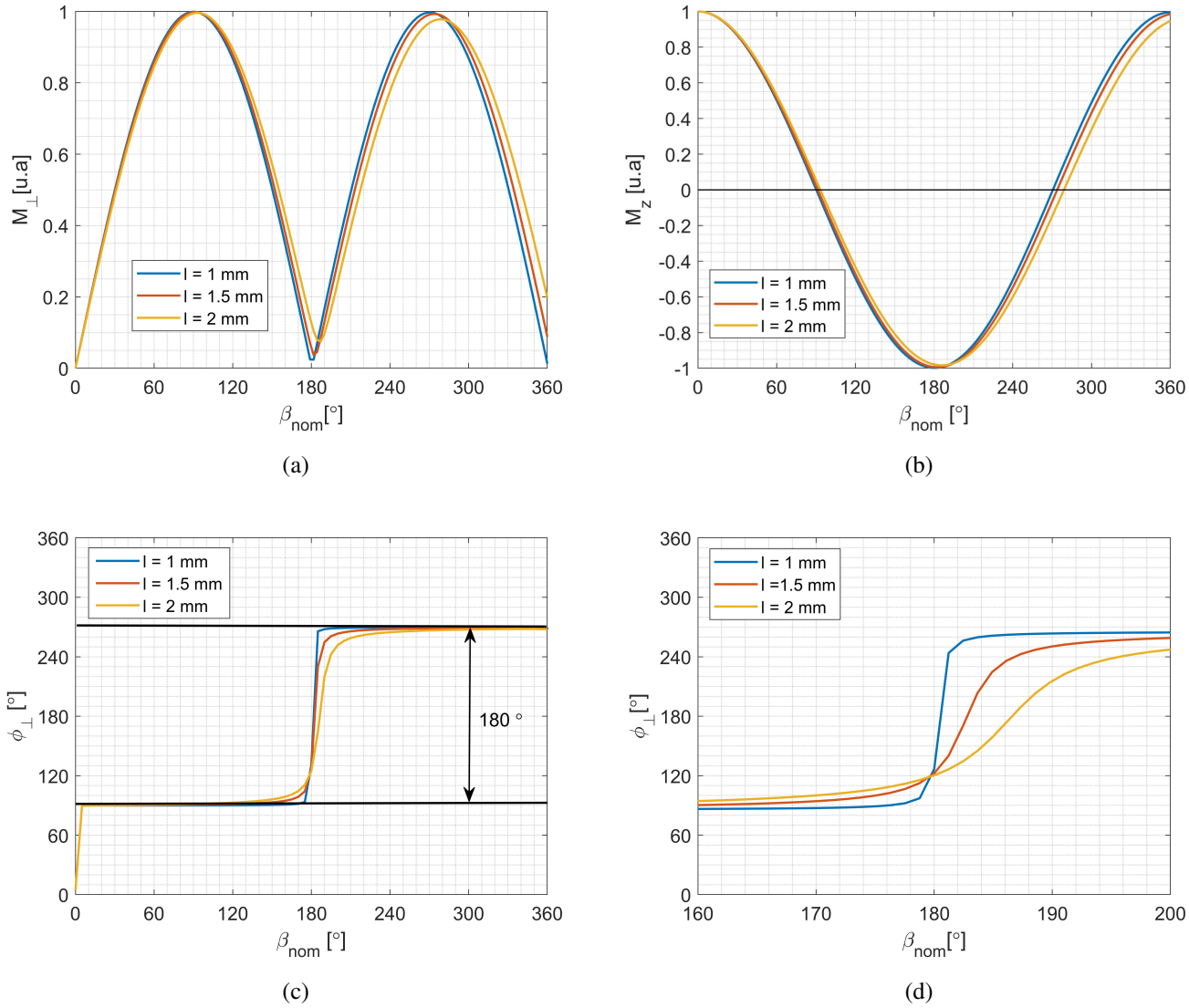

Figure 3.22: (a): Evolution of $\boldsymbol{M}_\perp$ during a nutation experiment; (b):Evolution of $\boldsymbol{M}_z$ during a nutation experiment; (c): Evolution of the phase during the nutation experiment for 1, 1.5 *and* 2 *millimeters samples respectively; and (d): Zoom on the evolution of the phase* $\phi_\perp$ *for* β_{nom} *between* 160° *and* 200°.

Magnetization distribution

Once the corresponding $\beta_{eff} = 90°$ and $\beta_{eff} = 180°$ effective pulses are determined, we simulate for these two cases their spatial distribution of $\boldsymbol{M}_{\perp}$ and $\boldsymbol{M}_{z}$ using the equation (3.55).

After the application of the desired effective pulse, the voxels magnetization $\boldsymbol{M}_{i}$ are distributed into different directions due to fields inhomogeneities of $\boldsymbol{B}_1(\boldsymbol{r})$ and $\boldsymbol{B}_0(\boldsymbol{r})$. Consequently, each spatial distribution of voxels V_i gives rise to a global magnetization $\boldsymbol{M}$ in a particular orientation ($\boldsymbol{M}_{\perp} \rightarrow \phi$, $\boldsymbol{M}_{z} \rightarrow \theta$).

In this section, we show the histograms of the transverse and longitudinal magnetization vectors accordingly to the different orientations ϕ and θ normalized by the total number of voxels V_i. β_{eff} that were used in this simulation are summarized in the table 3.6.

$\frac{\pi}{2}$ Pulse case

Figure 3.23 shows distributions for a $\frac{\pi}{2}$ pulse case, we find that:

1. Most of the transverse magnetization $\boldsymbol{M}_{\perp}(\boldsymbol{r})$ over the voxels points into the same direction for a sample length of 1 mm at $\phi = 90°$. The line shape of the distribution for this case is close to a Lorentzian one. However, for $l > 1$ mm, the $\boldsymbol{M}_{\perp}(\boldsymbol{r})$ distribution deviates from the Lorentzian shape, where the line splits into two preferred directions.

   For $l = 1.5$ mm, the transverse magnetization $\boldsymbol{M}_{\perp}(\boldsymbol{r})$ over the voxels is mainly oriented towards the directions $89°$ and $91°$ respectively, where the $89°$ direction is dominant. As for $l = 2$ mm, the two preferred directions are $88°$ and $90°$ respectively, where both directions have almost the same distribution of $\boldsymbol{M}_{\perp}(\boldsymbol{r})$.

2. Most of the longitudinal magnetization $\boldsymbol{M}_{z}$ along the voxels points into two opposite direction with different probabilities. This gives a zero average z-magnetization M_z deduced from the histograms.

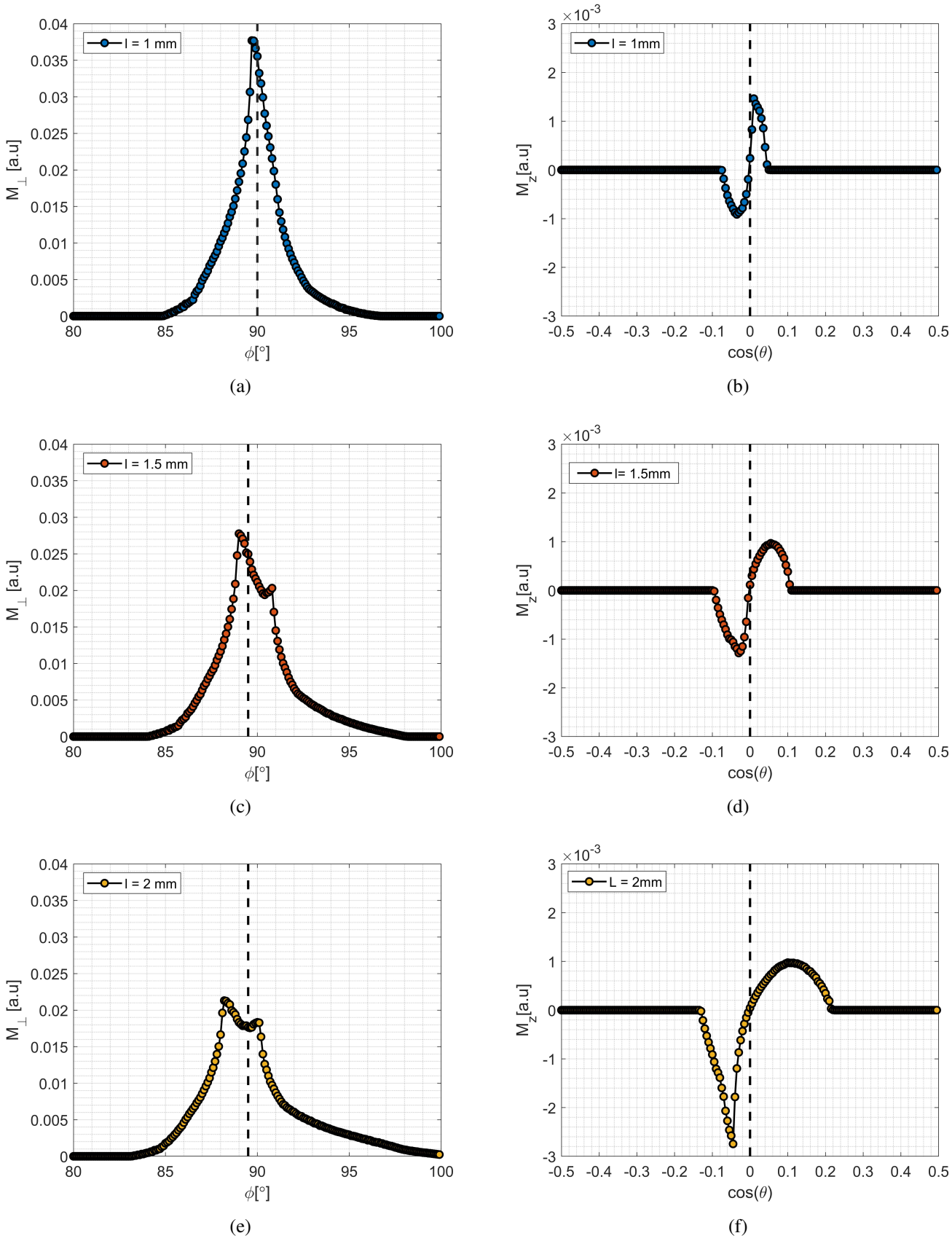

Figure 3.23: Magnetization distribution over the different directions ($\boldsymbol{M}_\perp \rightarrow \phi$, $\boldsymbol{M}_z \rightarrow \theta$) for three sample lengths, $l = 1$, 1.5 and 2 mm after the application of an effective $90°$ pulse. The dashed lines denote the average value of the transverse $M_\perp$ and longitudinal M_z magnetization.

π Pulse case

Figure 3.24 shows the same distributions after an effective π pulse. For this case, we observe:

1. Contrary to the $90°$ pulse case, the transverse magnetization $\boldsymbol{M}_{\perp}(\boldsymbol{r})$ distribution is spread throughout various directions for the 1 mm length sample. However, for $l > 1$ mm, the spread of the transverse magnetization vector becomes less homogeneous, and a preferred direction occurs at $128°$. The alignment along this direction is more pronounced for the 2 mm sample and a second preferable direction becomes visible at $270°$. This leads to a non-zero average transverse magnetization of 3.6 and $8\ \%$ respectively for $l = 1.5$ and 2 mm. For $l > 1$ mm, this shows that imperfect $180°$ pulse starts to occur, where the expected value of $\boldsymbol{M}_{\perp}$ deviates from the theoretical one, i.e., $\boldsymbol{M}_{\perp} = 0$.

2. Most of the longitudinal magnetization $\boldsymbol{M}_z$ over the voxels points into the same direction at $\phi = 180°$ ($\cos(\theta) = -1$) for a sample length of 1 and 1.5 mm. However, the occupation of $\boldsymbol{M}_z$ in this direction decreases with the sample size, where the distribution of $\boldsymbol{M}_z$ becomes larger as seen for $l = 1.5$ mm in figure 3.24 (d), which give rise to the transverse magnetization $\boldsymbol{M}_{\perp}$.

   For $l = 2$ mm, most of $\boldsymbol{M}_z$ is pointing in a different direction than $180°$ as shown in the figure 3.24 (f). Therefore, we can deduce that $\boldsymbol{M}_z$ is no longer inverted after an effective π pulse, which explains the non-zero average transverse magnetization $M_{\perp}$ ($8\ \%$).

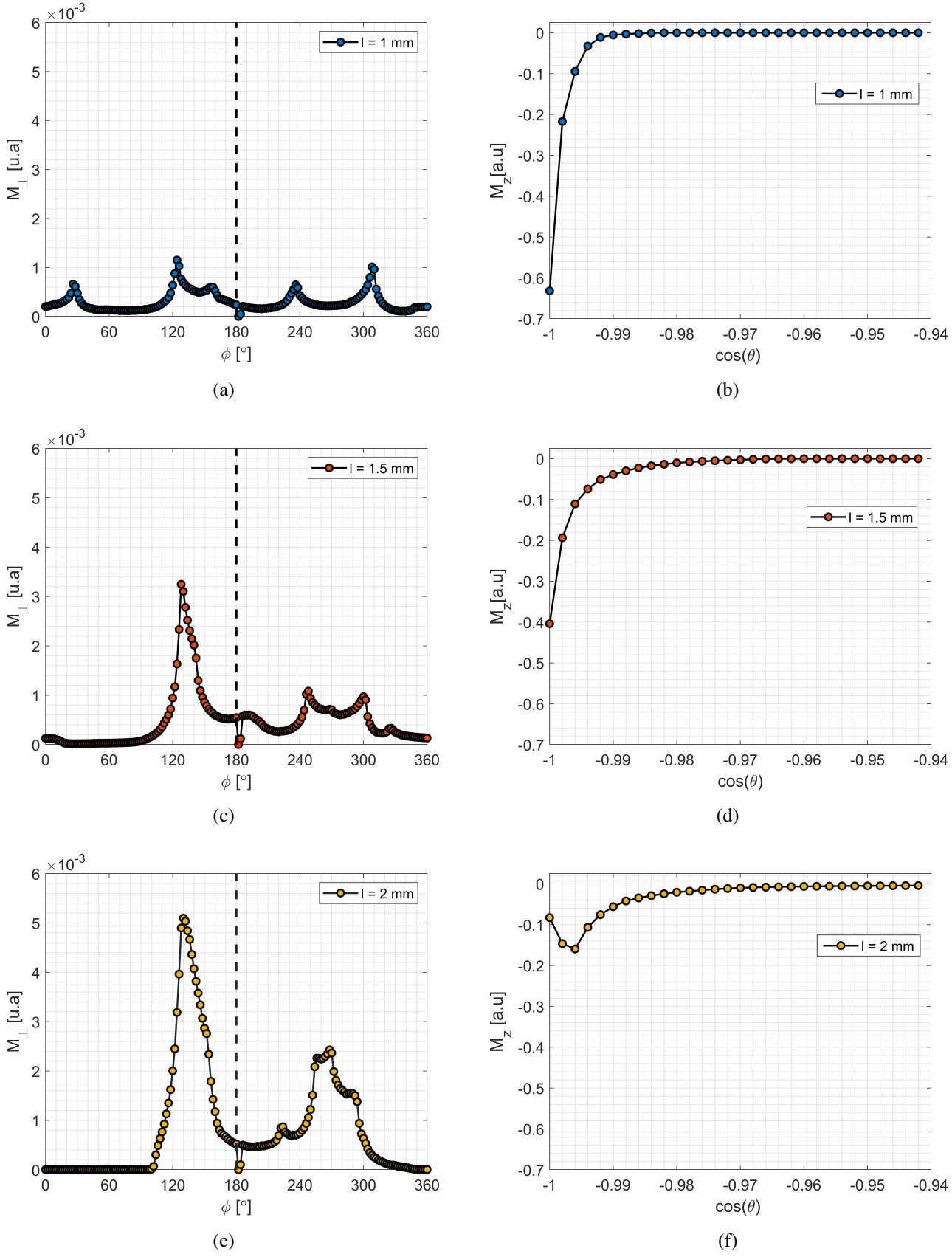

Figure 3.24: Magnetization distribution over the different directions ($\boldsymbol{M}_\perp \rightarrow \phi$, $\boldsymbol{M}_z \rightarrow \theta$) for three sample lengths, $l = 1$, 1.5, and 2 mm after the application of an effective $180°$ pulse. The dashed lines denote the average value of the transverse magnetization $M_\perp$ that remains after an effective $180°$ pulse.

3.6.4 Conclusion

We conclude here that the coil we used for high-field NMR is sufficiently homogeneous for sample lengths up to 1.5 mm, since we can obtain an effective pulse of $90°$ and that the deviation from total inversion of the net magnetization after an effective pulse of $180°$ is less than 5%. Imperfect pulses become more significant for a sample length of 2 mm (7.4%).

Thus, a model that does not take into account inhomogeneities of $\boldsymbol{B}_1(\boldsymbol{r})$ and $\boldsymbol{B}_0(\boldsymbol{r})$ describes the spin dynamics with a sufficient precision.

3.7 NMR spin dynamics in fluctuating static field B_0

In this part of the chapter, we quantify the size of fluctuations encountered during the NMR experiments in the resistive magnet by performing stability measurements after the application of $\frac{\pi}{2}$ and π nominal pulses. The aim of these measurements was to study the influence of the fluctuations on the T_1 experiment.

To simplify the data analysis, we used the classical NMR approach, in which we focused only on the net magnetization of the sample. In addition, we assumed that the sample behaves as a single voxel, ignoring spatial variations of $\boldsymbol{B}_0$ and $\boldsymbol{B}_1$. Since $\boldsymbol{B}_0$ is always set along the z-axis, the equilibrium state of the magnetization will be $M_0 = M_{eq}\boldsymbol{e}_z$.

After the application of an NMR pulse at the spectrometer frequency f_{rf}, the transverse magnetization will be detected. According to the theory detailed in chapter 1, the relation between the magnetization and the off-resonant cases produced by the fluctuations of the resistive magnet is given in frequency units by the equation 1.29

$$\frac{M(t)}{M_{eq}} = \begin{pmatrix} \frac{\Delta f \cdot f_1}{\Delta f^2 + f_1^2}(\cos\left(\sqrt{1+\left(\frac{\Delta f}{f_1}\right)^2}\beta_{nom}\right) - 1) \\ \frac{\Delta f}{\sqrt{\Delta f^2 + f_1^2}}\sin\left(\sqrt{1+\left(\frac{\Delta f}{f_1}\right)^2}\beta_{nom}\right) \\ \frac{1}{\Delta f^2 + f_1^2}(\Delta f^2 + f_1^2\cos\left(\sqrt{1+\left(\frac{\Delta f}{f_1}\right)^2}\beta_{nom}\right)) \end{pmatrix} \tag{3.56}$$

where x is replaced by $\frac{\Delta f}{f_1}$ and $\beta_{nom} = 2\pi f_1 t_p$ the pulse angle(t_p is the pulse length).

We deduce from this equation the transverse magnetization $M_\perp$

$$M_\perp = \sqrt{M_x^2 + M_y^2} = \sqrt{1 - M_z^2} \tag{3.57}$$

Experimental section

We performed ^{1}H liquid state NMR experiments at a constant magnetic field of 24 T corresponding to a resonance frequency of $f_0 = 1020$ MHz with a 1 mm sample length of H_2O + $GdCl_3$ (c = 60 mMol/l). These measurements aimed to quantify and investigate the influence of the different "off-resonant" scenarios on NMR experiments in the resistive magnet. In addition, a preliminary nutation experiment was carried out to determine the pulse lengths of $\frac{\pi}{2}$ and π pulses using the same sample of H_2O + $GdCl_3$. The pulse lengths and the excitation field strengths that were deduced from the nutation experiment are presented in the table 3.8. Large data sets for single-scan measurements at room temperature were collected (2500 measurements for the $\frac{\pi}{2}$ pulse and 200 measurements for the π pulse) to cover a wide range of "off-resonant" situations.

Frequency [MHz]	$\frac{\pi}{2}$ pulse length [μs]	π pulse length [μs]	$f_1(\frac{\pi}{2})$ [kHz]	$f_1(\pi)$ [kHz]
1020	2.4	5.2	104	99.5

Table 3.8: Parameters extracted from nutation experiments.

Results and discussion

Figure 3.25 presents selected spectra for the $\pi/2$ and π NMR pulses for the same liquid sample H_2O + $GdCl_3$ as a function of the resonance position at the Larmor frequency f_0. Their intensities were normalized by the maximum of the NMR spectrum at the resonance frequency of the $\pi/2$ pulse (blue spectrum figure 3.25 (Top)). They have a finite width and an asymmetric shape indicating that there is an asymmetric distribution of Larmor frequency over the spins due to the inhomogeneity of $\boldsymbol{B}_0$. The line shape of the $\pi/2$ pulse spectra is frequency-independent, however, for nearly on-resonant π pulses, we observe that the line shape is different from the others, and the asymmetry has shifted to the left side.

In addition, we present by the red dashed curves the simulated evolution of the magnetization in the vicinity of non-resonant frequencies ($\Delta f \neq 0$) considering perfect $\pi/2$ and π pulses. The parameters presented in the table 3.8 were used for these simulations respectively for $\pi/2$ and π pulse. The magnetization was normalized by its value at the equilibrium state M_{eq}.

According to equation (2.10) in chapter 2, the intensity of the NMR signal is proportional to the amplitude of the magnetization. Therefore, from a qualitative point of view, intensities of the spectra follow the theoretical magnetization curves (red dashed curves in figure 3.25 (Top) and (Bottom)) for NMR pulses of $\pi/2$ and π really well. To confirm the theoretical approach, we decided to extract the transverse magnetization $M_\perp = M_0$ and the off-resonant position $\Delta f = M_1$ for each spectrum consecutively using the moment equations (2.10) from chapter 2. After that, we fitted the evolution of the magnetization as a function of these different off-resonance positions using the equations (3.56) and (3.57) described earlier.

The fit provided us with the strength f_1 and length t_p of the pulse, as well as the equilibrium state magnetization M_{eq}. The latter value was used for normalization, and the pulse angle was deduced by the equation $\beta_{nom} = 2\pi f_1 t_p$. The results of these calculations and fits are discussed separately for the $\pi/2$ and π NMR pulse:

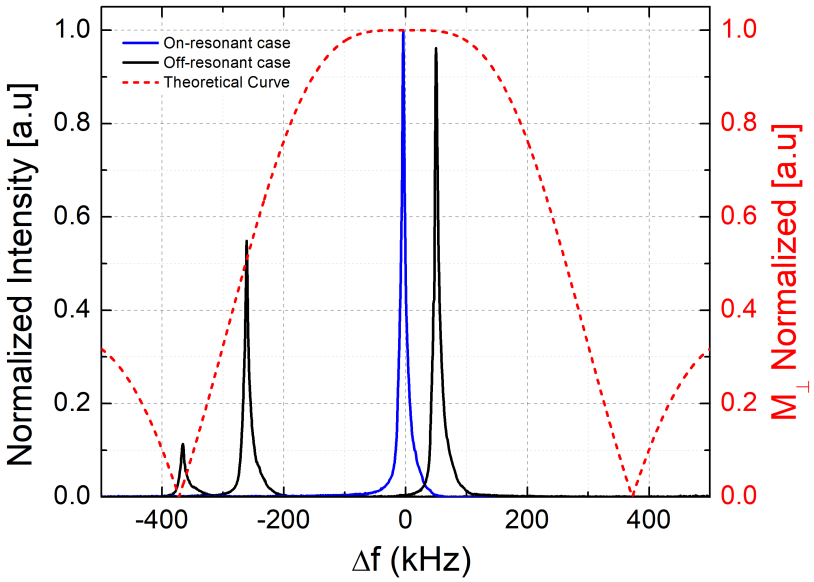

(a)

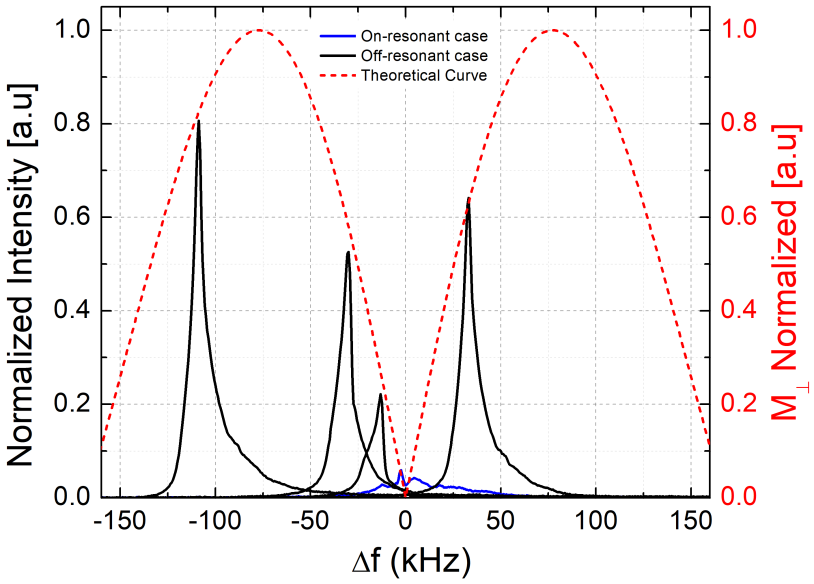

(b)

Figure 3.25: Impact of the fluctuating field on the magnitude of the NMR signal for the same liquid sample H_2O + $GdCl_3$ with the Larmor frequency $f_0 = 1020$ MHz after the application of $\pi/2$ (Top) and π (Bottom) NMR pulses. The dotted red curves represent the theoretical simulation of $M_\perp$ respectively for $\beta_{nom} = \pi/2$ and $\beta_{nom} = \pi$ pulses. In both figures we used the same normalization value.

Detailed analysis of $\pi/2$ pulses

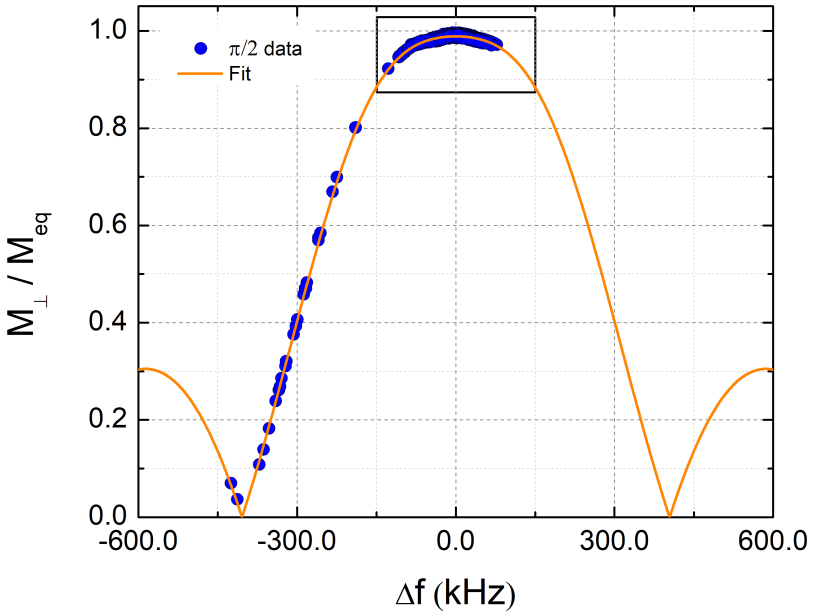

(a)

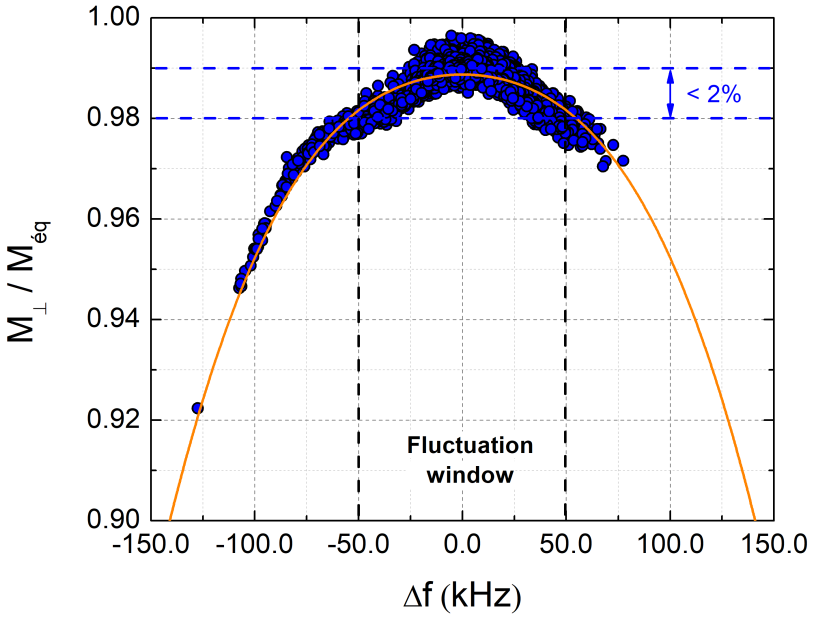

(b)

Figure 3.26: Transverse magnetization $M_\perp$ measured after $\pi/2$ pulse for different off-resonant cases. The transverse magnetization $M_\perp = M_0$ and the off-resonant position $\Delta f = M_1$ for each spectrum were calculated using the moments equations (2.10) from chapter 2. The black line represents the theoretical dependence of the transverse magnetization with the off-resonant position. The bottom figure shows a zoom on $M_\perp$ for Δf closer to the resonant cases.

After a $\pi/2$ pulse, the magnetization ends up along the transverse plane $M_\perp$. As $M_\perp$ lies on the detection axis in the rotation frame, the intensity of $M_\perp$ is the highest for $\Delta f = 0$, as shown in figure 3.25. However, this latter decreases for $|\Delta f| > 0$ due to the appearance of the magnetization along the z-axis, which reduces the NMR signal.

In figure 3.26, we see a reduction of the transverse magnetization with the off-resonant frequencies. The most encountered cases are for $|\Delta f| < 50$ kHz, where the amplitude of the magnetization decreased by less than 2%. In this region of frequencies, the data scatter around the theoretical curve, defining the accuracy of our $M_\perp$ calculations and their error bars. For $|\Delta f| > 50$ kHz, the magnetization becomes more sensitive to the off-resonant frequency.

We remark that the maximum amplitude of the fitted curve reaches $\approx 99\%$ of the M_{eq} value. This is due to the imperfection of the radio frequency pulses. The parameters extracted from the fit, lead to the calculation of β_{nom}, which shows a deviation of $9°$ from the desired pulse angle ($90°$).

M_{eq}	f_1 (kHz)	t_p [μs]	β_{nom} [°]
38.05	94	2.4	81

Detailed analysis of π pulses

After a π pulse, we invert the magnetization to the z-axis. Therefore, the NMR signal is zero since there is no finite transverse component of the magnetization available to induce such a signal. When an off-resonance case is present, a transverse component of the magnetization begins to appear, and an NMR signal becomes visible.

In figure 3.27, we see the effect of an off-resonance case on the magnetization after a π pulse. Contrary to the $\pi/2$ pulse, the magnetization here increases with $|\Delta f|$, where the transverse magnetization is observable mainly for the off-resonant frequency. For $|\Delta f| < 50$ kHz, the deviation from the resonant frequency increases the magnetization by a factor of 10 (from 0.1 to 1). This confirms that the π pulse is more sensitive to the variation of Δf than the $\pi/2$ pulse.

Furthermore, the experimental points are shifted by -10 kHz with respect to the theoretical curve. A possible reason for this shift is that the signal-to-noise ratio becomes lower, which affects the sensitivity of the calculation of the exact values of $M_\perp = M_0$ and $\Delta f = M_1$. Another important factor that may be responsible for this shift could be the asymmetric shape of the NMR spectra that changes near the on-resonant frequency.

We also observe, at the resonance frequency, that the magnetization has not been completely inverted. This is due to the imperfection of the radio frequency pulses. The fitted parameters show the deviation of $7°$ from the desired pulse angle ($180°$). Moreover for $|\Delta f| = 75$ kHz, the π pulse is behaving as $\pi/2$ pulse at the resonance frequency.

M_{eq}	f_1 (kHz)	t_p [μs]	β_{nom} [°]
35.76	97	5.02	173

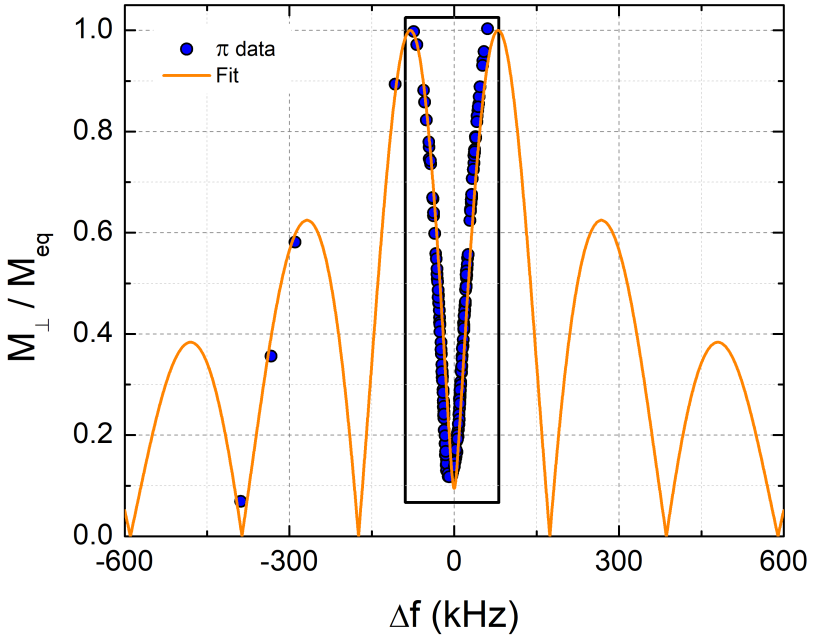

(a)

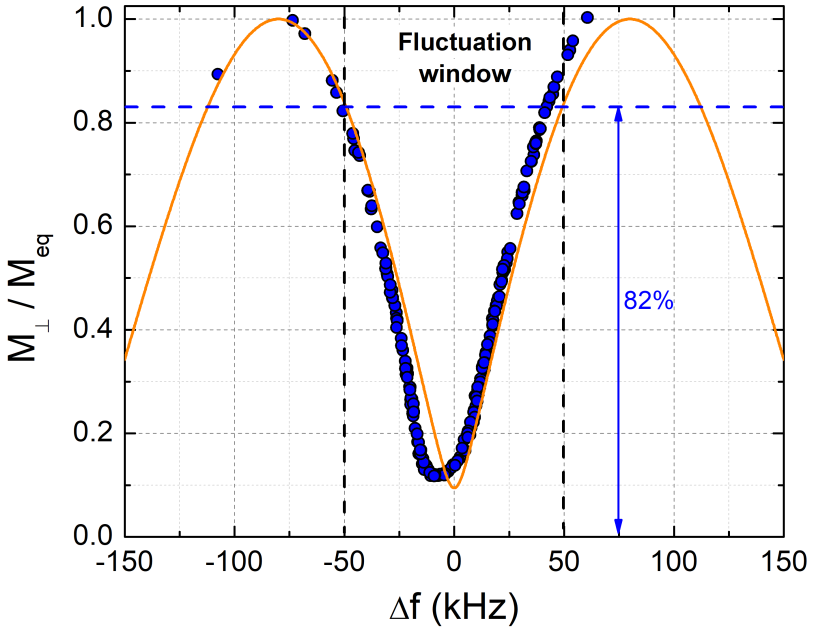

(b)

Figure 3.27: Transverse magnetization $M_\perp$ measured after π pulse for different off-resonant cases. The description of this figure follows the caption of figure 3.26.

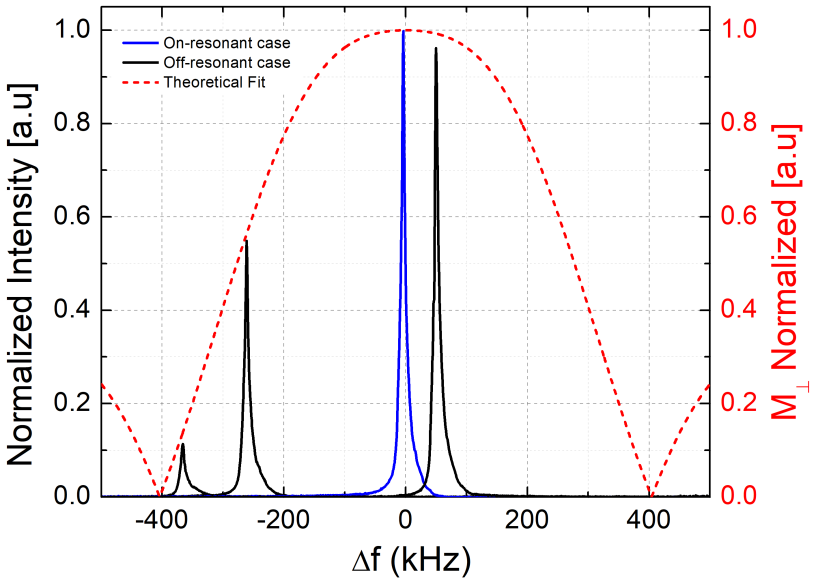

(a)

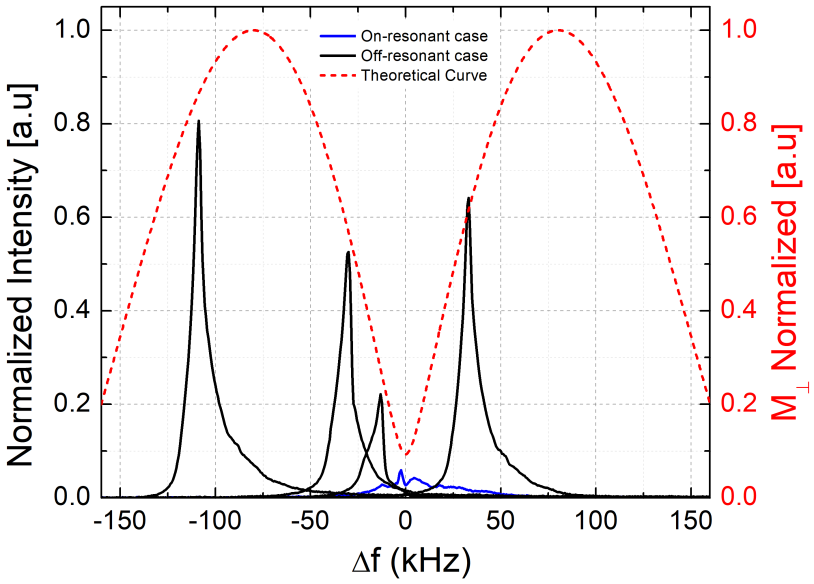

(b)

Figure 3.28: Fit of the impact of the fluctuating field on the magnitude of the NMR signal for the same liquid sample H_2O + $GdCl_3$, where the Larmor frequency $f_0 = 1024,977$ MHz after the application of $\pi/2$ (Top) and π (Bottom) NMR pulses. The dashed red curves represent the fitted curves respectively for $\beta_{nom} = 173°$ pulses.

In figure 3.28, the intensity of the spectra follows the fitted curves respectively at the deduced NMR pulse angles (81° and 173°).

3.7.1 Influence of fluctuation on T_1 measurements

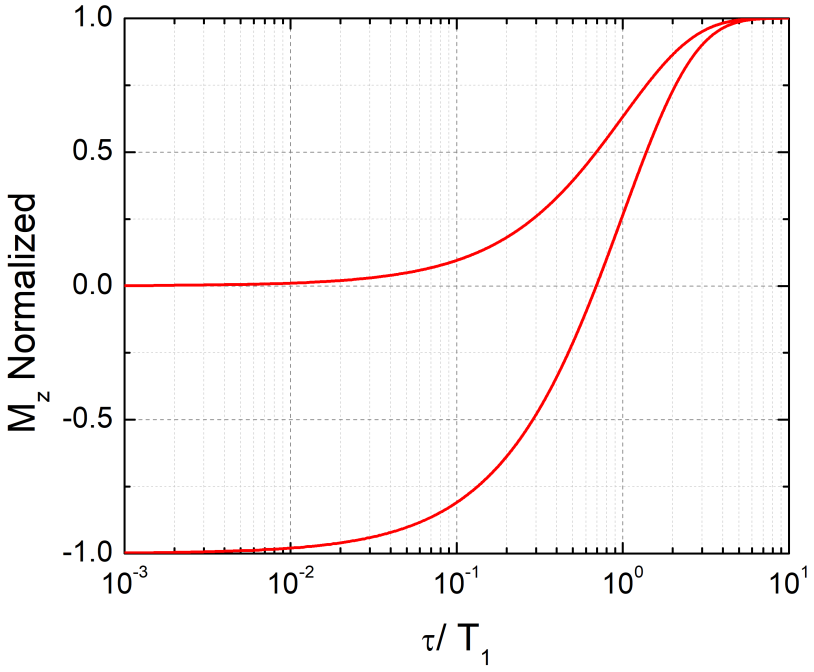

Figure 3.29: Impact of the fluctuating field on the T_1 measurements

In the previous section, we discussed the influence of the fluctuations on the transverse magnetization $M_\perp$ magnitude for $\pi/2$ and π pulses. In this section, we discuss the influence of the fluctuations on the measurements of T_1 in the case of an inversion recovery sequence (more details on this pulse sequence are given in chapter 1.3). This sequence consists of two radio-frequency pulses (the first pulse in the sequence is a π pulse and the second one is a $\pi/2$ pulse) separated by an interval time τ_i.

The histogram of the fluctuations of the resistive magnet (figure 3.8 in section 3.3.2) reveals that most of the off-resonant cases (> 68 %) are for $|\Delta f|/f_0 < 50$ ppm, i.e., $|\Delta f| < 50$ kHz for $f_0 = 1020$ MHz. In this region of $|\Delta f|$, the transverse magnetization $M_\perp$ magnitude is roughly constant for the $\pi/2$ pulse but increases dramatically as a function of $|\Delta f|$ for the π pulse. Therefore, we can say that the fluctuations clearly affect the T_1 measurements. Thus, in this section we will focus on the influence of the first radio-frequency pulse on the T_1 measurements (we will always consider that $\pi/2$ pulse is performed exactly at the Larmor frequency).

Moreover, to illustrate this phenomenon, two extreme cases are shown in Figure 3.29. In the first case, we consider that the magnetic field is time stable, thus the magnetization is perfectly inverted after the application of the first radio frequency pulse (π pulse). In this case, the longitudinal magnetization obeys the following evolution law

$$\frac{M_z(\tau_i)}{M_{eq}} = 1 - C\exp\left(\frac{-\tau_i}{T_1}\right) \tag{3.58}$$

C represents the inversion rate of the radio frequency pulses, and the value $C = 2$ is used for this perfect inversion recovery sequence. In the second case, we consider that the π pulse is no longer inverting the magnetization but is behaving as a $\pi/2$ pulse due to the fluctuations of the magnetic field for all values of τ_i. This behavior affects the evolution law of longitudinal magnetization. Thereby, C is equal to 1 instead of 2 in this case.

In reality, we cannot predict the fluctuation of the magnetic field, so the detected longitudinal magnetization for the different intervals of τ_i will be scattering between these two curves presented in figure 3.29.

The solution is to use the saturation recovery pulse sequence involving only $\pi/2$ pulses, where C becomes 1 in equation (3.58).

Chapter 4: Theory of paramagnetic relaxation enhancement (PRE)

Paramagnetic relaxation enhancement (PRE) is the increase of the nuclear spin relaxation of a nucleus in a solvent (here ^{1}H in H_2O) induced by magnetic interactions with unpaired electron spins. PRE is nowadays an important research area due to its application in magnetic resonance imaging (MRI) [44]. There, PRE affects the image contrast, and the compounds generating PRE are called MRI contrast agents (CA). They are chemical compounds that contain paramagnetic ions. Hence the origin of the term "paramagnetic relaxation enhancement".

Amongst others, PRE is explored in the field of MRI and NMR spectroscopy for the development of new CAs and for the determination of the structure of bio-molecule , respectively. The efficiency of a CA in a given magnetic field is quantitatively measured by their NMR relaxivities r_i, which are equal to the longitudinal (R_1) or transverse (R_2) NMR relaxation rates divided by the CA concentration c [45, 46].

PRE depends on the electronic properties of paramagnetic ions, as well as other dynamic and structural characteristics such as the number of bound water molecules, their rate of exchange with the bulk, size, clustering, aggregation, as well as tumbling, diffusional and rotational correlation times. In this chapter, we will discuss the principle elements of PRE theory restricted to the lanthanide ions. More details can be found in [1].

4.1 Nuclear spin relaxation mechanisms

For an in-depth understanding of how the presence of a paramagnetic complex in solution alters the relaxation rate of a nucleus in a solvent, we introduce the main PRE mechanisms. Although numerous mechanisms exist, two principal ones generally dominate for spin-half nuclei: (1) Dipolar interaction and (2) Curie spin contribution. We note that the general theory contains an additional contact term, which is neglected in the case of lanthanides [47].

4.1.1 Nuclear spin relaxation by dipolar interaction

In the simplest case, the paramagnetic ion from the contrast agent has a magnetic moment μ_S related to its spin S, which generates its own magnetic field called magnetic dipolar field or local field. When the nuclear magnetic moment μ_I of spin I is within the dipolar field created by S and located at a distance r, they will interact as represented in figure 4.1. In our case, the dipolar interaction is established by the interaction between an electronic magnetic moment of the paramagnetic ion and a nuclear magnetic moment of the ^{1}H nuclei in the water molecule H_2O. The absolute value of the magnetic moment of the free electron μ_S is about three orders of magnitude bigger than that of the proton μ_I.

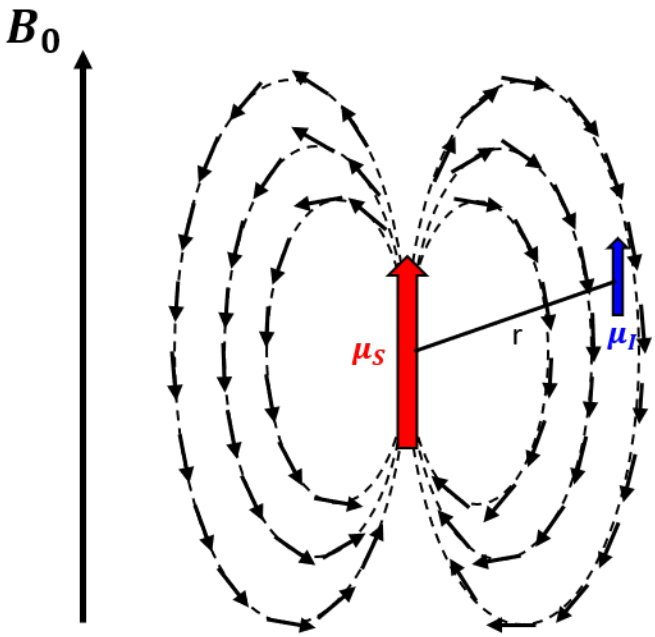

Figure 4.1: Interaction between nuclear magnetic moments μ_I with a dipolar field generated by an electron spin μ_S.

The Hamiltonian $\mathcal{H}$ describing this interaction, in a static magnetic field B_0 along the z-axis is given by

$$\mathcal{H} = g_e \mu_B \boldsymbol{S} \cdot \boldsymbol{B}_0 - \hbar \gamma_I \boldsymbol{I} \cdot \boldsymbol{B}_0 + \mathcal{H}_{DD}(t). \tag{4.1}$$

This Hamiltonian (4.1) consists of three terms. The first two terms, are time-independent, representing the Zeeman interactions for the electron (first term) and for the nucleus (second term) separately. The third term, $\mathcal{H}_{DD}(t)$, represents the dipolar interaction induced between the two spins (I and S). Unlike the first two terms, the dipolar interaction is time-dependent due to various molecular motions and can be expressed as

$$\mathcal{H}_{DD}(t) = \frac{\mu_0}{4\pi} \hbar^2 \gamma_I \gamma_S \left(\frac{3(\boldsymbol{I} \cdot \boldsymbol{r})(\boldsymbol{S} \cdot \boldsymbol{r})}{r^5} - \frac{\boldsymbol{I} \cdot \boldsymbol{S}}{r^3} \right) \tag{4.2}$$

It depends on the distance between the magnetic moments (the interaction falls off as r^{-3}) and therefore on the concentration of the paramagnetic ions in the compound, the gyromagnetic ratios of the spins (γ_I and γ_S), and the orientation of the vector $\boldsymbol{r}$ joining both magnetic moments.

For the simplest case $S = 1/2$ and $I = 1/2$, the Hamiltonian has the energy level scheme shown in figure 4.2. If one adds these small local fields $\boldsymbol{B}_{dd}$ to the large static field $\boldsymbol{B}_0$, we obtain a total field that fluctuates in direction and magnitude [48], which causes PRE of the spin-lattice T_1 and spin-spin T_2 relaxation.

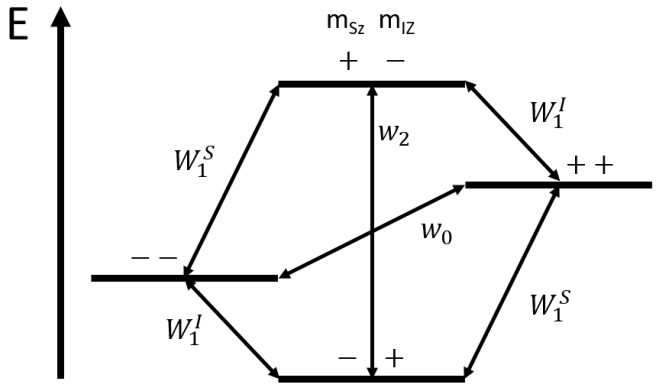

Figure 4.2: Energy levels, transition frequencies and probabilities per unit time (W_0, W_1^I, W_1^S, and W_2) in a S-I dipolar coupling system of spin $1/2$ for $\gamma_S < 0$ and $\gamma_I > 0$. The figure is adapted from [49], and details can be found in text.

The dipolar Hamiltonian can be transcribed as a function of quantum operators [50]

$$\mathcal{H}_{DD}(t) = k(A + B + C + D + E + F), \tag{4.3}$$

where

$$k = \frac{\mu_0}{4\pi r^3}\hbar^2\gamma_I\gamma_S$$

$$A = (1 - 3\cos^2(\theta))I_zS_z$$

$$B = -\frac{1}{4}(1 - 3\cos^2(\theta))(I_+S_- + I_-S_+)$$

$$C = -\frac{3}{2}\sin(\theta)\cos(\theta)\exp(-i\phi)(I_zS_+ + I_+S_z)$$

$$D = -\frac{3}{2}\sin(\theta)\cos(\theta)\exp(i\phi)(I_zS_- + I_-S_z)$$

$$E = -\frac{3}{4}\sin^2(\theta)\exp(-2i\phi)(I_+S_+)$$

$$F = -\frac{3}{4}\sin^2(\theta)\exp(2i\phi)(I_-S_-),$$

with θ and ϕ are the polar coordinates of the distance vector $\boldsymbol{r}$. All the above terms A -F are composed of time-dependent random functions of the relative positions of the interacting spins $f(t) = F\left(\theta(t), \phi(t)\right)$ and the quantum operators I_z, S_z, $I_\pm$, and $S_\pm$ acting on the spin states.

The various operators A - F make contributions which are qualitatively different to the dipolar Hamiltonian. The fluctuating magnetic field produced by one spin at the location of the other spin may induce spin transition on the other center, and thus provide a relaxation pathway [10]. The transition probability per unit time W_{ij} for a coupled system $S-I$ between two defined states $|m_i\rangle$ and $|m_j\rangle$ is given by the following equation

$$W_{ij} = \frac{1}{\hbar^2}\left|\int_{-t}^{t}\overline{\langle m_j|H_{DD}(0)|m_i\rangle\,\langle m_i|H_{DD}(t')|m_j\rangle}\exp\left(-i\omega_{ij}t'\right)\,dt'\right|, \tag{4.4}$$

where $\omega_{ij} = (E_i - E_j)/\hbar$. In our case, the dipolar Hamiltonian $H_{DD}(t')$ fluctuations are random and fast, which makes the transition induced W_{ij} independent of time. The eigenstates of the $S - I$ coupling

can be obtained by the product of the individual states defined by the values of m_{S_z} and m_{I_z}. In the product, the first component represents the state of S_z, while the second component represents the state of I_z $\left(|m_{S_z}\rangle|m_{I_z}\rangle = |m_{S_z}m_{I_z}\rangle\right)$.

In addition, there are four possible eigenstates linked to the values of m_{I_z} and m_{S_z}, resulting in four types of transitions shown in figure 4.2 with corresponding probabilities

$$W_0 = \frac{1}{\hbar^2}\left|\int_{-t}^{t} \overline{\langle - - |H_{DD}(0)| + +\rangle \langle + + |H_{DD}(t')| - -\rangle} \exp\left(-i(\omega_I - \omega_S)t'\right)\ dt'\right| \tag{4.5}$$

$$W_1^I = \frac{1}{\hbar^2}\left|\int_{-t}^{t} \overline{\langle - + |H_{DD}(0)| - -\rangle \langle - - |H_{DD}(t')| - +\rangle} \exp\left(-i\omega_I t'\right)\ dt'\right| \tag{4.6}$$

$$W_1^S = \frac{1}{\hbar^2}\left|\int_{-t}^{t} \overline{\langle + - |H_{DD}(0)| - -\rangle \langle - - |H_{DD}(t')| + -\rangle} \exp\left(-i\omega_S t'\right)\ dt'\right| \tag{4.7}$$

$$W_2 = \frac{1}{\hbar^2}\left|\int_{-t}^{t} \overline{\langle + - |H_{DD}(0)| - +\rangle \langle - + |H_{DD}(t')| + -\rangle} \exp\left(-i(\omega_I + \omega_S)t'\right)\ dt'\right|, \tag{4.8}$$

where the frequencies of transitions are: (1) ω_I proton spin changes and electron spin remains; (2) $\omega_I + \omega_S$ proton and electron spins increase or decrease their energy; and (3) $\omega_I - \omega_S$ proton spin increases and electron spin decrease or the opposite. This gives

$$W_i^{I,S} = \frac{k^2}{\hbar^2} a_i^{I,S} \int_{-t}^{t} \langle f(0) f^*(t')\rangle \exp\left(-i\omega_i t'\right)\ dt', \tag{4.9}$$

where k is the interaction strength, $a_i^{I,S}$ is the transition matrix element that depends on the spin operators, and the last term (the integral) is the Fourier transformation of the correlation function that will be described in section 4.1.2.

In our case, we are interested in nuclear spin relaxation, i.e., equations (4.5), (4.6), and (4.8). The dipolar contribution to the nuclear relaxation rates $R_{1,2}$ can be expressed according to the probabilities of the transitions $R_{1,2} = \sum W_i^{I,S}$.

4.1.2 Correlation function and spectral density

In order to obtain a model for the correlation function, we assume that the dipolar field $B_{dd}(t)$ fluctuates with the following properties:

1. The fluctuating fields have zero average over a long time for a single spin: $< B_{dd}(t) > = 0$
2. The mean square of the fluctuating field is: $< B_{dd}^2(t) > \neq 0$
3. The autocorrelation function of the field is a stationary random function that stays invariant under a change in the origin of time. It describes how rapidly the field fluctuates and is expressed as

$$G(\tau) = \langle B_{dd}(0) B_{dd}(\tau)\rangle, \tag{4.10}$$

where we define a correlation time τ_c by the condition that $G(\tau) \to 0$ for $|\tau| >> \tau_c$. We assume that the autocorrelation function is symmetric and even. This gives

$$G(\tau) = G(-\tau), \tag{4.11}$$

and

$$G(0) = \left\langle B_{dd}^2(0) \right\rangle \geq 0. \tag{4.12}$$

For a molecule modeled as a rigid sphere subjected to Brownian motion (molecular motions that are random), the autocorrelation function $G(\tau)$ can be described as an exponential decay

$$G(\tau) = G(0)^2 \exp\left(-\frac{|\tau|}{\tau_c}\right) = G(0)^2 g(\tau), \tag{4.13}$$

where $g(\tau)$ is the reduced correlation function.

4. The spectral density is defined as the Fourier transform of the autocorrelation function $G(\tau)$

$$J(\omega, \tau_c) = \int_{-\infty}^{\infty} G(\tau) \exp(-i\omega\tau)\, d\tau \tag{4.14}$$

$$J(\omega, \tau_c) = G(0)^2 \frac{\tau_c}{1 + \omega^2 \tau_c^2}. \tag{4.15}$$

In the case of dipolar interaction, using equation (4.9)

$$J(\omega, \tau_c) = \langle f(0) \rangle^2 \frac{\tau_c}{1 + \omega^2 \tau_c^2}, \tag{4.16}$$

where $\langle f(0) \rangle^2$ is a constant representing the square average over the molecular rotation, i.e., $\theta + \phi$. ω represents the frequency of the nuclear transitions: ω_I, $\omega_I + \omega_S$, and $\omega_I - \omega_S$.

For the discussion on the dependence of spectral densities on $\omega = 2\pi f$ or τ_c vary, we assume here and in the following that the spectral density is

$$J(\omega, \tau_c) = \frac{\tau_c}{1 + \omega^2 \tau_c^2}. \tag{4.17}$$

First, we show in figure 4.3 (a) the plot of spectral density function $J(f)$ as a function of frequency f in the logarithmic scale for fixed τ_c values. For $\omega << \tau_c$ the spectral densities $J(f)$ takes the form of a constant function

$$J(\omega) = J(0) = \tau_c, \tag{4.18}$$

With τ_c representing the correlation time of a real fluctuation mode of the molecule. When ω approaches the value of τ_c^{-1}, the spectral density decays $J(\omega)$ to zero with a power law ω^{-2}. Consequently, for the longest correlation time $\tau_c = 1$ μs, the intensity of the spectral density is the highest, but the decay towards zero is much faster than for the other two curves as shown in the figure 4.3 (a). An inflection point at $\omega = \tau_c^{-1}$ occurs, known as the dispersion value where the spectral densities reach their initial half-value $J(0)$.

Second, we show in figure 4.3 (b) the plot of spectral density function $J(\tau_c)$ as a function of correlation time τ_c in the logarithmic scale for fixed $\omega = 2\pi f$ values. The spectral densities $J(\tau_c)$ are of the peak function type and reach their maximum value at the inflection point $\omega = \tau_c^{-1}$.

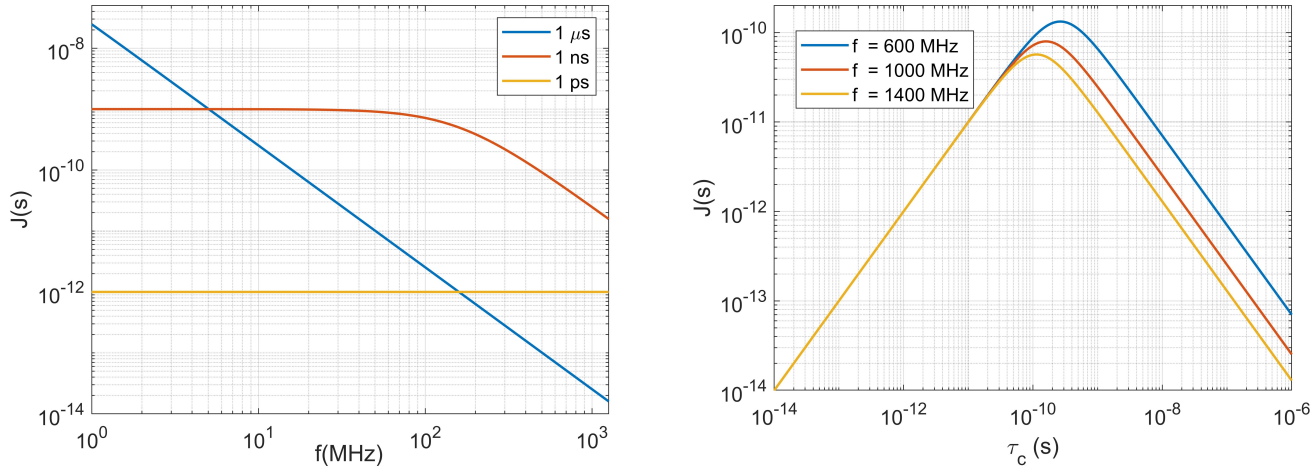

(a) (b)

Figure 4.3: (a): Spectral density function $J(f, \tau_c)$ as a function of frequency in the logarithmic scale simulated for fixed correlation times $\tau_c = 1$ μs, 1 ns, and 1 ps. (b): Spectral density function $J(f, \tau_c)$ as a function of correlation times in the logarithmic scale simulated for fixed frequencies $f = 600$, 1000, and 1400 MHz.

4.1.3 Curie spin contribution

In the previous discussion of dipolar interaction, we neglected the slight population difference between electron spin levels according to the Boltzmann distribution. This difference accounts for the time-averaged magnetic moment of the molecule, which is related to the time-averaged electronic spin S_c, also known as Curie spin [51].

The alignment of paramagnetic ions increases with the field and is inversely proportional to the temperature through Curie's law. S_c is given by

$$S_c = JB_J(x), \tag{4.19}$$

where J is the total electron spin and $B_J(x)$ represents the Brillouin function

$$B_J(x) = \frac{J + \frac{1}{2}}{J} \coth\left(\frac{\left(J + \frac{1}{2}\right) x}{J}\right) - \frac{1}{2J} \coth\left(\frac{x}{2J}\right) \tag{4.20}$$

with

$$x = \frac{J\hbar\gamma_S B_0}{kT}. \tag{4.21}$$

The interaction of the nuclear spins with S_c provides the so-called Curie spin contribution.

4.1.4 Correlation times relevant for PRE

Molecular dynamics responsible for nuclear spin relaxation are directly linked to the presence of unpaired electrons, as seen in sections 4.1.1 and 4.1.3. The molecular dynamics occurring in solution associated by their corresponding correlation times are shown in figure 4.4:

1. Chemical exchange (figure 4.4 (a)):

There are paramagnetic compounds with water-binding sites. The water molecules located at these sites form the so-called inner sphere. There is a chemical exchange with the free water molecules of the solvent, the outer sphere, with a characteristic correlation time τ_M.

2. Molecular rotation (figure 4.4 (b)):

   The paramagnetic compounds containing the water-binding sites rotate with a correlation time τ_R. The rotational correlation time τ_R for a rigid sphere of radius a in a medium having viscosity η can be derived using the Debye diffusion equation. By employing spherical harmonics, we can predict the rotational correlation time of a rigid sphere [49]

$$\tau_R = \frac{4\pi\eta a^3}{3k_BT} = \frac{\eta M}{dN_Ak_BT}, \tag{4.22}$$

   where η is the viscosity of the solvent used, 9:1 D_2O:H_2O, expressed in (kg·s^{-1}·m^{-1}), a is the radius of the molecule assumed as spherical, d represents the density of the molecule (kg·m^{-3}) taken usually equal to 10^3, $N_A = 6,022 \cdot 10^{23}$ is Avogadro's constant, M is the molecular weight of the molecule, k_B Boltzman constant, and T is the temperature of the solution (room temperature).

   This formula shows that τ_R depends on the molecule's size M and the solvent's viscosity η, and increases with them.

3. Electron spin relaxation (figure 4.4 (c)):

   τ_S is the correlation time of the electron spin relaxation. The longitudinal and transverse electronic relaxation rates $R_{S,i} = \tau_S^{-1}$ ($i = 1, 2$) can be expressed by the following equations [52]

$$R_{S,1} = \frac{2\Delta_t^2}{50}\left(4S(S+1)-3\right)\left(\frac{\tau_v}{1+\omega_S^2\tau_v^2} + \frac{4\tau_v}{1+4\omega_S^2\tau_v^2}\right) \tag{4.23}$$

$$R_{S,2} = \frac{\Delta_t^2}{50}\left(4S(S+1)-3\right)\left(3\tau_v + \frac{5\tau_v}{1+\omega_S^2\tau_v^2} + \frac{2\tau_v}{1+4\omega_S^2\tau_v^2}\right) \tag{4.24}$$

   where τ_v represents the correlation time for the instantaneous distortions of the paramagnetic ion and Δ_t^2 is the mean squared fluctuations of the zero field splitting (ZFS).

   Electron spin relaxation has the same form as nuclear spin relaxation and is thus generally field-dependent.

4. Diffusion process:

   The diffusion process refers to the random motion of molecules, which then leads to net flow from an area of higher concentration to a lower concentration. This provides the tendency of molecules to distribute themselves uniformly in a system.

   The diffusional correlation time τ_D can be derived from the Einstein-Stokes equation by considering the characteristic time for a diffusing molecule to cover a distance of its own size. The diffusional correlation time τ_D is given by [53]

$$\tau_D = \frac{a^2}{D}, \tag{4.25}$$

   where D is the relative diffusion constant, which is inversely proportional to the size of the molecules involved in the difussional process (paramagnetic compound and water molecules) and the viscosity of the solvent (9:1 D_2O:H_2O), and a is the closest distance that determines the diffusional correlation time τ_D.

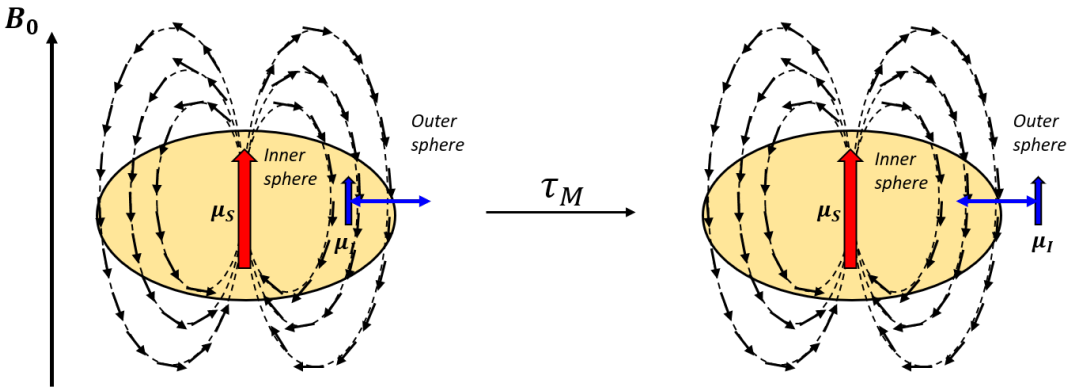

(a)

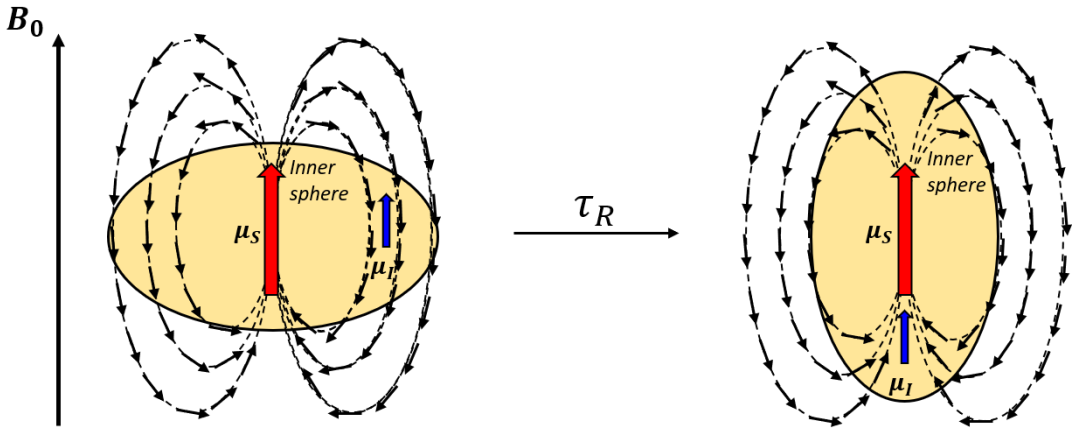

(b)

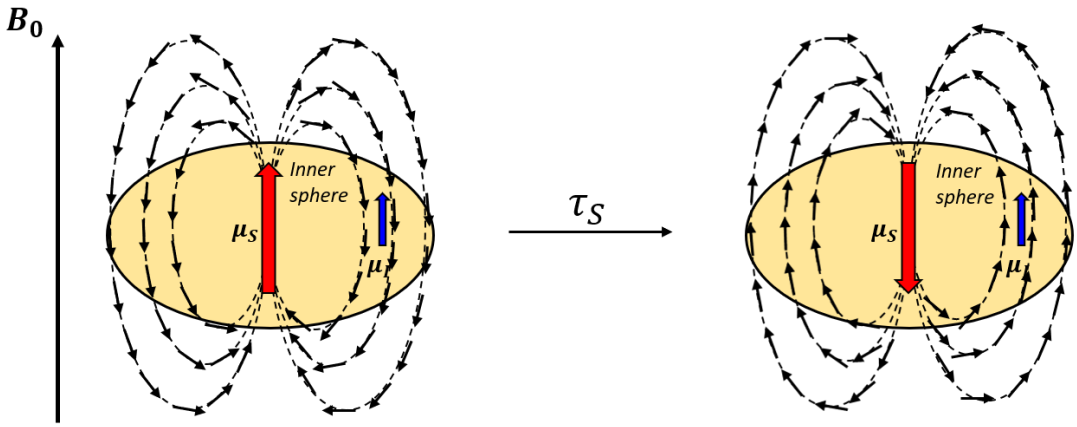

(c)

Figure 4.4: Processes that make the dipolar Hamiltonian time dependent and causes nuclear relaxation (a): chemical exchange with correlation time τ_M ; (b): molecular rotation with correlation time τ_R ; (c): electron spin relaxation with correlation time τ_S . The inner sphere represents the nuclear magnetic moments (here$\mu_{I,1}$) directly coordinated to the electron spin μ_S in the contrast agent complex, which exchanges position with the nuclear magnetic moment $\mu_{I,2}$ from the solvent. The outer sphere represents the nuclear magnetic moments (here$\mu_{I,2}$) from outside the complex or the solvent. This figure is adapted from [49].

All of these correlation times can modulate the dipolar interaction, hence causing nuclear relaxation. They all contributes to the decay of the correlation function. In the model used here, we consider that these movements are independent of one another, then the correlation function decays accordingly

$$\exp\left(-\frac{t}{\tau_R}\right)\exp\left(-\frac{t}{\tau_M}\right)\exp\left(-\frac{t}{\tau_S}\right) = \exp\left(-(\tau_R^{-1}+\tau_M^{-1}+\tau_S^{-1})t\right) \tag{4.26}$$

The overall correlation time of the dipolar coupling τ_c^{-1}, therefore, is given by

$$\tau_c^{-1} = \tau_R^{-1} + \tau_M^{-1} + \tau_S^{-1}. \tag{4.27}$$

However, only τ_R and τ_M can modulate the Curie-spin contribution, which can also cause nuclear relaxation. Therefore, the overall correlation time of the Curie-spin contribution is such that

$$\tau_{cc}^{-1} = \tau_R^{-1} + \tau_M^{-1}. \tag{4.28}$$

Most often, for both dipolar and Curie-spin contribution only one of the correlation times (τ_R, τ_M, or τ_S) dominates. This depends mainly on the electronic properties of the paramagnetic ion and on the structural properties of the contrast agent. Typical ranges of rotational τ_R, chemical exchange τ_M, and electronic τ_S correlation times are shown in the figure 4.5, that is adapted from [49].

In addition, the dipolar and Curie spin contributions can be modulated by the diffusion process τ_D.

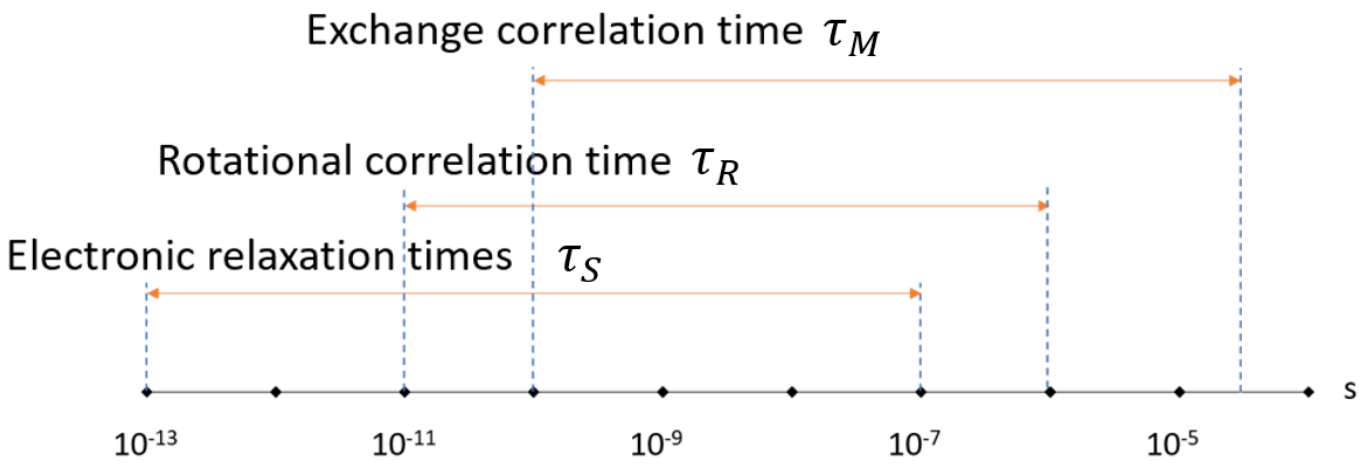

Figure 4.5: Typical ranges of rotational τ_R, chemical exchange τ_M, and electronic τ_S correlation times [49].

4.2 Quantitative expressions of PRE

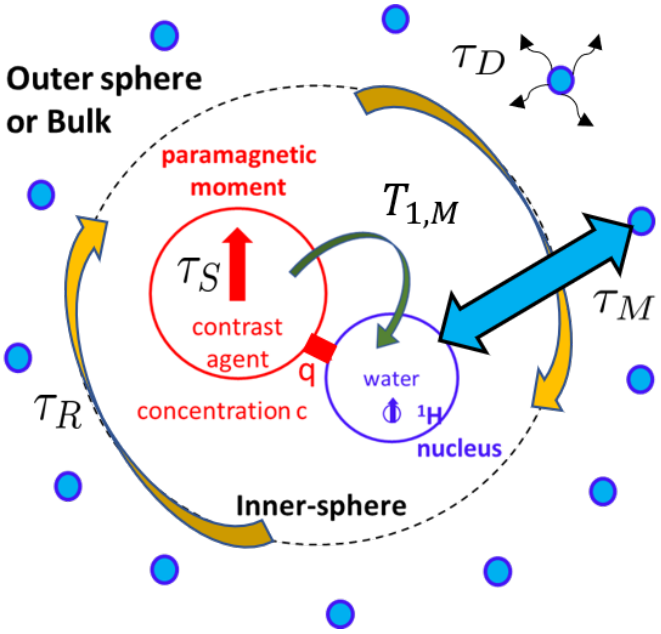

Figure 4.6: Representation of inner and outer sphere contributions. Details can be found in text.

We first present the common characteristics of longitudinal and transverse relaxation rates R_i ($i = 1, 2$).

The relaxation rate enhancement caused by the paramagnetic compound of a given concentration c can be written as

$$R_i = r_i.c = R_{i,\text{solution}} - R_{i,\text{solvent}}, \tag{4.29}$$

where $R_{i,\text{solution}}$ and $R_{i,\text{solvent}}$ are the relaxation rates of the solution and the solvent (9:1 D_2O:H_2O), respectively, and r_i is the relaxivity.

R_i can be separated in two-sub terms: (1) $R_{i,is}$ inner-sphere relaxation; and (2) $R_{i,os}$ outer-sphere relaxation

$$R_i = R_{i,is} + R_{i,os}. \tag{4.30}$$

Both inner and outer-sphere relaxation are shown in figure 4.6. The inner-sphere refers to water molecules directly coordinated to the paramagnetic center known as the first coordination sphere, which exchanges with bulk water molecules. The characteristic correlation time is given by τ_M. $T_{1,M}$ is the relaxation rate of the nuclei in that first coordination sphere. However, the outer-sphere or bulk refers to water molecules from outside the complex (from solvent), which diffuse (τ_D) around the paramagnetic center [54].

The inner and outer-sphere relaxation are driven by the dipolar and Curie-spin contributions. However, the electronic properties of the paramagnetic ion and the structural properties of the contrast agent will determine which contribution will dominate, and at which range of fields.

4.2.1 Longitudinal relaxation rate R_1

Here, we will separate the longitudinal relaxation rate from the transverse one. The notation used in this thesis is that of references [6, 55].

Inner sphere contribution $R_{1,is}$

The inner sphere contribution to PRE is based on the Solomon-Bloembergen-Morgan (SBM) equations [56–58]. It depends on: the molar fraction (paramagnetic ion complex/solvent) f , the number of water molecules in the first coordination sphere of the complex q, the residence time of the coordinated water molecules exchanging with the bulk τ_M, and the relaxation rate of the bound nuclei $T_{1,M}^{-1}$.

$$R_{i,is} = fq\frac{1}{T_{1,M} + \tau_M}, \tag{4.31}$$

As a result, R_1 has a linear dependence on the concentration f. Therefore, it is convenient to define the relaxivity r_i ($i = 1, 2$) as the relaxation rate over the concentration of the whole paramagnetic complex.

Moreover, $T_{1,M}$ is linked to the magnetic moment of the paramagnetic ion and its dynamics. In the absence of exchange process ($\tau_M = \infty$), the inner sphere contribution $R_{1,is}$ equals zero. However, in our case i.e., in the presence of fast exchange ($\tau_M \ll T_{1,M}$), the inner sphere contribution is proportional to the relaxation rates of the coordinated nucleus $T_{1,M}$. $R_{1,M} = T_{1,M}^{-1}$ contains the dipolar $R_{1,is}^{DD}$ and Curie spin $R_{1,is}^{C}$ contributions to the relaxation of the inner sphere, expressed as the sum of the two

$$R_{1,M} = R_{1,is}^{DD} + R_{1,is}^{CS}, \tag{4.32}$$

We recall that the dipolar contribution on the longitudinal relaxation rate R_1 is proportional to the sum of the transition probabilities ($W_0 + W_1^I + W_2$) given in equations (4.5), (4.6) , and (4.8). The dipolar contribution to the inner-sphere relaxation can be written as

$$R_{1,is}^{DD} = \frac{2}{15}\left(\frac{\mu_0}{4\pi}\right)^2 \gamma_I^2 \mu_B^2 g_j^2 J(J+1)\frac{1}{r^6}\left(3J(\omega_I, \tau_c) + 6J(\omega_I + \omega_S, \tau_c) + J(\omega_I - \omega_S, \tau_c)\right), \tag{4.33}$$

The last three terms in the parentheses are the spectral densities of the transition probabilities. Given that $\omega_S >> \omega_I$, this equation can be simplified to

$$R_{1,is}^{DD} = \frac{2}{15}\left(\frac{\mu_0}{4\pi}\right)^2 \gamma_I^2 \mu_B^2 g_j^2 J(J+1)\frac{1}{r^6}\left(3J(\omega_I, \tau_c) + 7J(\omega_S, \tau_c)\right), \tag{4.34}$$

where γ_I is the nuclear gyromagnetic ratio, μ_B the Bohr magneton, g_j is the Landé factor, and J represents the total electronic spin. In analogy to equation (4.17), the spectral densities $J(\omega_I, \tau_c)$ and $J(\omega_S, \tau_c)$ are given by

$$J(\omega_I, \tau_c) = \frac{\tau_{c1}}{1 + \omega_I^2 \tau_{c1}^2} \qquad \text{and} \qquad J(\omega_S, \tau_c) = \frac{\tau_{c2}}{1 + \omega_S^2 \tau_{c2}^2}. \tag{4.35}$$

We reproduce from equation (4.27), τ_c the correlation time of the inner-sphere dipolar coupling

$$\tau_{c1,2}^{-1} = \tau_R^{-1} + \tau_M^{-1} + \tau_{S1,2}^{-1}. \tag{4.36}$$

The spectral densities are proportional to τ_c^{-1}, therefore, the shortest correlation time between rotational, chemichal exchange and electronic relaxation time dominates $J(\omega, \tau_c)$.

For the lanthanide ions Dy(III), Er(III), and Ho(III) : τ_R ranges between 10^{-11} s for small molecules and 10^{-6} s for large molecules, τ_M ranges between 10^{-10} - 10^{-5} s, and τ_S is of the order of 10^{-13} s (very short) [59]. Since the correlation times of Dy(III), Er(III), and Ho(III) are in the same range, the dipolar contribution to the inner-sphere relaxation will be of the same order of magnitude. This later is modulated by the electronic relaxation $\tau_c^{-1} \approx \tau_S^{-1}$.

However, for Gd(III), τ_S varies between 10^{-8} and 10^{-9} s [59] with τ_R and τ_M being in the same range of values as the lanthanide ions Dy(III), Er(III), and Ho(III). In this case the dipolar contribution to the inner-sphere relaxation is modulated by $\tau_c^{-1} \approx \tau_R^{-1}$.

We should note here that some correlation times can be field-dependent, such as the electronic relaxation time τ_S of the paramagnetic ion , and others are field-independent, such as the rotational correlation time τ_R of the molecule. For Dy(III), Er(III), and Ho(III), the value of τ_S is independent of the magnetic field [60], while for Gd, it is dependent [60, 61]. Hence the importance of these spectral density curves in figures 4.3 (a) and (b). Moreover, the electron relaxation times of lanthanide ions in solution are not largely affected by temperature.

Another important factor in the dipolar contribution is the distance between the paramagnetic ion and the observed nucleus denoted as r, because this contribution decreases inversely with the sixth power r^{-6}. There is an implicit field dependence of the dipolar contribution, which is reflected in the spectral densities through the proton and electron frequencies ω_I and ω_S respectively.

The Curie-spin contribution $R_{1,is}^{CS}$ depends only on the transition probability $2W_1^I$, represented by the Larmor frequency ω_I and is given by

$$R_{1,is}^{CS} = \frac{2}{5}\left(\frac{\mu_0}{4\pi}\right)^2 \gamma_I^2 B_0^2 \mu_B^4 g_j^4 J^2(J+1)^2 \frac{1}{r^6}\frac{1}{(3k_BT)^2} 3J(\omega_I, \tau_{cc}), \tag{4.37}$$

where

$$J(\omega_I, \tau_{cc}) = \frac{\tau_{cc}}{1+\omega_I^2\tau_{cc}^2}. \tag{4.38}$$

B_0 is the applied magnetic field, k_B is the Boltzmann constant, T the temperature. From equation (4.28), we reproduce the correlation time of the inner-sphere Curie spin contribution:

$$\tau_{cc}^{-1} = \tau_R^{-1} + \tau_M^{-1}. \tag{4.39}$$

The Curie spin contribution is characterized by its dependence on the square of the applied magnetic field B_0^2 and becomes more noticeable at high fields. The Curie-spin correlation time depends only on the molecular rotation and the chemical exchange. For small complexes containing Dy(III), Ho(III), and Er(III) as paramagnetic ions, the Curie spin contribution will be modulated by τ_R^{-1}. Regarding Gd, the Curie-spin contribution can be neglected. Curie spin relaxation becomes significant when the dipolar contribution is modulated by the electronic relaxation times τ_S, which is the case for Dy(III), Ho(III), and Er(III) lanthanide ions. Similar to the dipolar interaction, the Curie-spin contribution decreases inversely with the sixth power of the distance, r^{-6}. Moreover, Curie-spin contribution is temperature-dependent.

Outer sphere contribution $R_{1,os}$

The outer sphere contribution is again the sum of the dipolar $R_{1,is}^{DD}$ and Curie $R_{1,is}^{C}$ terms, as well as the diffusion processes terms contribute. The dipolar contribution in the outer sphere relaxation is

$$R_{1,os}^{DD} = \frac{C_{DD}}{aD}\left(6\left(J(J+1) - S_c \coth\left(\frac{\chi}{2J}\right) - S_c^2\right) J_o(\omega_I, \tau_S, \tau_D) + 7\coth\left(\frac{\chi}{2J}\right) S_c J_o(\omega_S, \tau_S, \tau_D)\right), \tag{4.40}$$

where

$$C_{DD} = \frac{16\pi}{135}\left(\frac{\mu_0}{4\pi}\right)^2 \gamma_I^2 \mu_B^2 g_j^2 N_a c, \tag{4.41}$$

$$\chi = \frac{JB_0\mu_B g_j}{kT}, \tag{4.42}$$

where c is the molar concentration of the paramagnetic ion, S_c is the time average electronic spin known as "Curie" spin [62, 63]. This latter is field dependent [63].

The spectral densities of the dipolar contribution of the outer-sphere relaxation J_o depends on the diffusional correlation time τ_D given in the equation (4.25) and on the electronic relaxation time τ_S at the frequencies ω_I and ω_S, respectively [64].

The Curie contribution in the outer sphere relaxation is

$$R_{1,os}^{C} = \frac{C_C}{aD} S_C^2 J^A(\omega_I, \tau_D). \tag{4.43}$$

with

$$C_C = \frac{32\pi}{45}\left(\frac{\mu_0}{4\pi}\right)^2 \gamma_I^2 \mu_B^2 g_j^2 N_a c. \tag{4.44}$$

The outer-sphere contribution shows an explicit field dependance (equations (4.40) and (4.43)) through the time average electronic spin S_c. Various studies showed that at low fields for Dy(III)-compounds (< 400 MHz) the dipolar outer-sphere term is modulated by τ_S, and is the dominant contribution, whereas at high fields (> 700 MHz) the Curie outer-sphere term modulated by τ_D starts to be the dominant term [6, 55]. Analogously to Dy(III), for the Ho(III) and Er(III) compounds it is predicted that they behave similarly, due to similar correlation times values.

4.3 Experimental access to PRE

Longitudinal and transverse relaxation rate studies offer experimental access to PRE. For NMR relaxation measurements, we dissolve an amount of a paramagnetic compound in a solution, typically water H_2O or D_2O:H_2O mixtures.

The measured longitudinal R_1 and transverse R_2 relaxation rate are normalized by the concentration c of the paramagnetic compound and the relaxivities are extracted according to the equation (4.29)

$$r_i = \frac{R_i}{c} \quad \text{with} \quad i = 1, 2. \tag{4.45}$$

Since the contributions to PRE are field dependent, the relaxivity is very often measured from very low to very high magnetic fields. This technique is known as nuclear magnetic relaxation dispersion (NMRD).

NMRD involves various type of NMR instruments:

1. Fast field cycling.
2. Permanent magnets.
3. Superconducting magnets.
4. Resistive magnets.

In this context of PRE induced by lanthanide compounds, there is a strong interest in using the highest magnetic fields beyond the limit of today's superconducting magnets. This is the motivation for the PRE studies presented in this thesis.

Chapter 5: PRE studies of paramagnetic polyoxometalates compounds (PM-POMs)

In NMR, PRE up to the highest magnetic fields is an important research area due to the current trend for ultra-high-field MRI. However, the relaxivity of conventional PRE compounds (contrast agents) containing Gd(III) ions, generally decreases with magnetic field strength, resulting in a reduction of efficiency [1, 5, 6, 65, 66]. For this reason, alternative materials with high relaxivity up to the highest fields are needed for future MRI applications. This requires the development of appropriate contrast agents and a better understanding of the PRE mechanism.

In this context, lanthanide ions other than Gd have recently attracted widespread interest due to their interesting magnetic properties, particularly their high magnetic moments and short electronic relaxation times, making Curie spin relaxation the dominant contributor to water relaxivity in complexes containing lanthanide ions [47, 55, 67, 68].

In addition, the magnetic susceptibility tensor caused by the 4f orbitals of lanthanide ions can be either prolate (axially elongated) as found in Er(III), or oblate (axially compressed) as found in Dy(III) [68–70]. As a result of this anisotropic distribution of lanthanide ions, a Larmor frequency difference occurs between the lanthanide-coordinated and the bulk water molecules in the ground state. This latter is proportional to the external magnetic field [71] and strongly influences both paramagnetic NMR effects of solutions containing lanthanide complexes, the shifts [72], and the relaxation properties of the neighboring nuclei [73].

Consequently, the search for efficient PRE Ln-compounds at high magnetic fields requires the synthesis of complexes incorporating lanthanide ions such as Dy(III) and Er(III) and the investigation of their PRE properties. In this perspective, one of the approaches we took was to synthesize ultrahigh-spin polyoxometalates (POM)-based heterometallic clusters and measure their nuclear magnetic relaxation dispersion (NMRD) in aqueous solutions [4, 5]. POMs, as clusters of anionic metal oxides, possess numerous properties that make them suitable for applications in different fields such as magnetism, optics, imaging, and medicine, as well as interesting electrochemical properties [74–79]. These POM clusters are viewed as an inorganic analogue of the well known contrast agent porphyrins. The use of lanthanide-based POM nanocomposites as host assemblies for potential MRI contrast agents has also been investigated by other groups [80–82].

The studies presented in this chapter are an extension of previous work carried out by the LNCMI and KIT teams [2–4, 6]. In this work, PRE of water ^{1}H NMR has been investigated over a wide range of frequencies, for aqueous solutions of three Ln-POM compounds: (1) $[Dy^{III}(H_2O)_4GeW_{11}O_{39}]^{5-}$(Dy-$W_{11}$); (2) $[Er^{III}(H_2O)_3GeW_{11}O_{39}]^{5-}$(Er-$W_{11}$); and (3) $[Er^{III}(H_2O)(CH_3COO)(P_2W_{17}O_{61})_2]^{16-}$ (Er_2-W_{34}) from 20 to 1400 MHz.

The results that will be presented in this chapter were published in reference [5], and indicate that the three investigated POM complexes (Dy-W_{11}), (Er-W_{11}), and (Er_2-W_{34}) are indeed potential candidates for contrast agents, especially at high magnetic fields.

5.1 Structural and magnetic properties of PM-POM compounds

Three compounds were synthesized at Kalsruhe Institute of Technology (KIT) and investigated in these PRE studies:

- $[Dy(H_2O)_4\ GeW_{11}O_{39}]^{5-}$ (Dy-W_{11}),
- $[Er(H_2O)_3GeW_{11}O_{39}]^{5-}$ (Er-W_{11}),
- $[(Er(H_2O)(CH_3COO)(P_2W_{17}O_{61}))_2]^{16-}$ (Er_2-W_{34}).

Dy-W_{11}, Er-W_{11}, and Er_2-W_{34} were synthesized by the KIT chemistry group following literature methods and characterized by FTIR spectroscopy [83, 84].

In this section, we will describe the structural properties of the Ln-POM clusters and their magnetic properties relevant to the PRE studies.

5.1.1 Structure of Ln-W_{11} and Er_2-W_{34} POM clusters

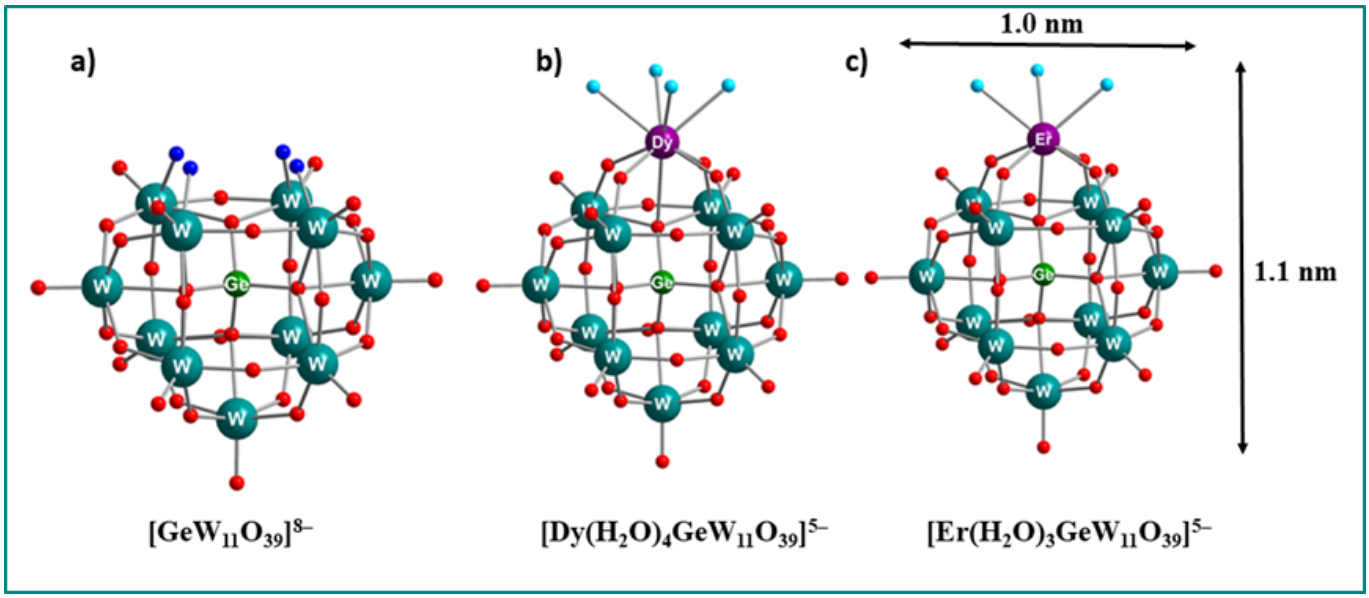

Figure 5.1: Ball-and-stick representation of detailed structure and size of: (a) Keggin POM ligand - (b) and (c) for Ln-W_{11} with Ln = Dy and Er taken from [5]. Color scheme: The red stands for the oxygen atoms, the turquoise stands for the water molecules bound to the lanthanide ions in violet, and the dark blue stands for the four oxo ligands that coordinate to Ln metal ions.

Ln-W_{11} clusters are mono-lanthanide substituted Keggin-type POMs that contain one mono-lacunary Keggin [α-$GeW_{11}O_{39}$]$^{8}-$ subunit and one lanthanide metal ion, which in our case is either dysprosium Dy or erbium Er. This occupies the position that has been formed by loss of a W-O_t group from the plenary [α-$GeW_{12}O_{40}$]$^{4}-$ anion, which consists of GeO_4 tetrahedron surrounded by four vertex sharing W_3O_{13} triads as shown in the figure A.1 (a).

Figure A.1 (b) and (c) shows respectively the structure of the Ln-POM: Dy-W_{11} and Er-W_{11}. They share the same structure, the only difference being the number q of coordinated water molecules in the first coordination sphere to the lanthanide ion. Er(III) is coordinated to three terminal water molecules due to the smaller ionic radius compared to Dy(III) ion, which possesses four terminal water molecules. This will have a direct impact on the inner-sphere contribution to the nuclear relaxation.

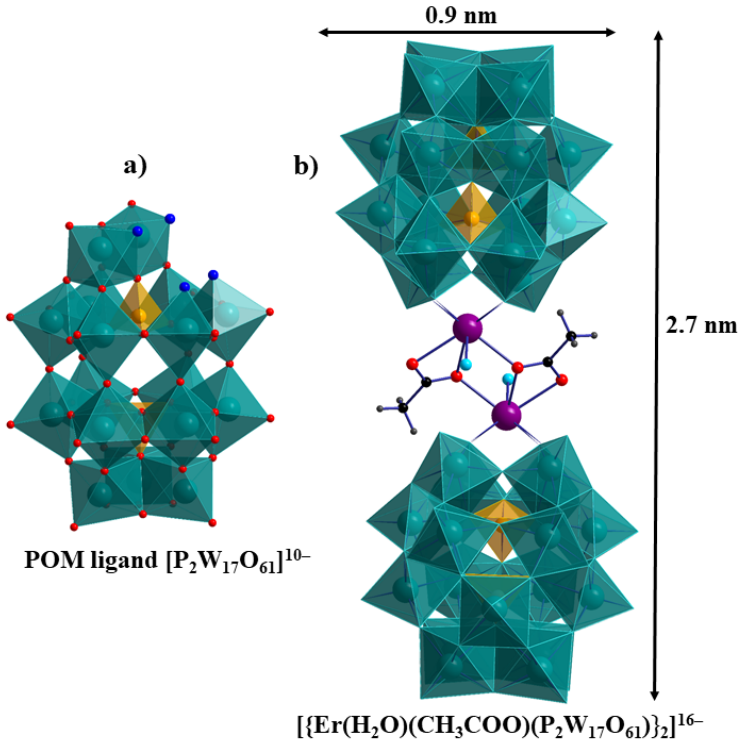

Figure 5.2: Combined polyhedral/ball-and-stick representation of detailed structure and size of: (a) Wells-Dawson POM ligand and (b) Er-W_{34}. Color scheme: The red stands for the oxygen atoms, the aqua stands for the water molecules bound to the Er ion in violet, the dark blue stands for the four oxo ligands that coordinate with the lanthanide metal ions, the teal stands for WO_6 octahedra, the yellow stands for PO_4 tetrahedra, the black stands for carbon, and the grey stands for hydrogen.

Er_2-W_{34} cluster is an Er-substituted Wells-Dawson-type POM that is composed of a binuclear Er(III) core [$(Er(H_2O)(CH_3COO))_2$]$^{4+}$ sandwiched between two mono-lacunary Wells-Dawson units [$P_2W_{17}O_{61}$]$^{10-}$ as shown in figure 5.2 (a). Each Er(III) in these units takes up the mono-lacunary site of [$P_2W_{17}O_{61}$]$^{10-}$ and is coordinated to the four available oxygen atoms, whereas the two $ErP_2W_{17}O_{61}$ units are connected by acetate groups. Each Er(III) ion is eight-coordinated with square antiprismatic geometry. Hence, every Er(III) ion in these units is coordinated by four oxygen atoms of the POM ligand, two oxygen atoms from the acetate ligand, one oxygen atom from the other acetate ligand, and one water molecule. Figure 5.2 (b) shows the final structure of the Er_2W_{34} cluster.

5.1.2 Properties of POM clusters relevant for PRE studies

As seen in the previous chapter 4 on the PRE theory, the relaxivity r_i depends on the (1) magnetic properties of the paramagnetic ion (S, L, g, μ_{eff}); (2) the structural parameters of the PM-POM compound: the number of coordinated water molecules in the first coordination sphere q , the distance of PM ion r for inner and outer sphere water molecules, the distance of closest approach of diffusing water molecules a, the molecular weight M, and the viscosity η of the solvent (9:1 D_2O : H_2O) which enters in different process as rotation and diffusion; (3) the dynamic parameters of the molecules related to the correlation times τ_r, τ_M, and τ_D; and (4) electronic properties of the paramagnetic ion τ_S (here we consider $\tau_S = \tau_{S1} = \tau_{S2}$).

These parameters contribute collectively to the paramagnetic relaxation enhancement of the relaxivity and determine the efficiency of a molecule as a potential contrast agent. The relevant properties for PRE studies of the investigated Ln-POM clusters are summarized in the tables 5.1 and 5.2, where τ_R was determined using the equation (4.22) and τ_S values are taken from the reference [49]. Moreover, in these compounds spin orbital coupling dominates.

Compounds	Ln(III)	Dy-W_{11}	Er-W_{11}	Er_2-W_{34}
Magnetic Properties	S	5/2	3/2	$2 \times 3/2$
	L	5	6	2×6
	J	15/2	15/2	$2 \times 15/2$
	g	4/3	6/5	
	μ_{eff} [μ_B]	10.6	9.6	
	Anisotropy of Ln(III)	oblate	prolate	prolate
Structural Parameters	q	4	3	2
	M [10^{-3} kg.mol^{-1}]	2953	2940	8815
	Molecular size (Height [nm] $\times$ width [nm])	1.1×1	1.1×1	2.7×0.9
Electronic Parameters	τ_S [10^{-13} s]	4 - 10	3 - 8	3 - 8
Dynamic Parameters	τ_R [10^{-9} s]	1.2	1.2	3.6

Table 5.1: Relevant properties of Lanthanide-POM compounds for PRE studies, which includes: (1) magnetic properties of non-interacting Dy(III) and Er(III) ions with $\mu_{eff} = g_j\sqrt{J(J+1)}$; (2) the structural parameters of the lanthanide-POM compounds with M the molecular weight and q the number of the number of coordinated water molecules in the first coordination sphere; and (3) the dynamic and electronic parameters related to the dominant correlation times.

Viscosity at 25° C	H_2O	D_2O	9:1 D_2O:H_2O
η [10^{-4} Kg.s^{-1}.m^{-1}]	8.94	10.08	9.9

Table 5.2: Viscosity of the solvent 9:1 D_2O:H_2O at room temperature according to [85].

5.1.3 Stability studies of Er_2-W_{34} in solution

Before exploring the PRE properties of the POMs, its important to validate their structural integrity in solution.

Since the previously reported mass spectrometric (MS) studies on a dilute solution of Er_2-W_{34} have shown the fragmentation of the POM in the gas phase, the chemistry team at KIT decided to investigate their solution phase behavior [83]. Three techniques were used for the stability studies on Er_2W_{34}: (1) Dynamic Light Scattering (DLS); (2) Fourier Transform Infrared Spectroscopy (FTIR); and (3) Xylenol Orange test.

Dynamic light scattering (DLS) is a technique that measures the size of a given molecule (hydrodynamic diameter). The hydrodynamic diameter of Er_2W_{34} was measured at selected pH values. The obtained data suggest that, unless the pH of the particle is acidified (pH < 4.7), the dimeric structure of Er_2W_{34} is preserved in water.

Fourier Transform Infrared Spectroscopy (FTIR) is an analytical technique used to identify the chemical compounds based on their absorption or emission of infrared radiation. FTIR was performed on dried Er_2W_{34} sample, that was obtained by evaporating the aqueous solvent. The FTIR spectra of the recovered Er_2W_{34} show the expected absorption bands attributed to the pristine POM. The two spectra perfectly match each other and no wavenumber shifts are observed indicating the stability of the Er_2W_{34} in solution.

Xylenol Orange test: This test detects the presence of free metal ions and free ligands in a given Ln-complex solution, where it undergoes a color change from orange to violet in case of the presence of free lanthanide ions [86]. No color change was observed on the addition of 30 μl Xylenol Orange to the Er_2W_{34} solution (pH $= 5.6$), which was used for NMR relaxivity studies. This indicates that the Er(III) ion does not leach out into the solution.

All the above-performed experiments confirmed the structural integrity of the Er_2W_{34} complex in solution. More details on the performed experiments can be found in the article of reference [5].

5.2 Experimental section

For this PRE study, several types of magnets were used to cover the desired Larmor frequency range of ^{1}H NMR from 20 up to 1400 MHz, for aqueous solutions for the Ln-POM clusters Dy-W_{11}, Er-W_{11}, and Er_2W_{34}. This included both NMR facilities at KIT and LNCMI. The former uses commercial Bruker NMR spectrometers, mainly for frequencies below 400 MHz, while the latter uses a non-standard NMR in the resistive magnet for frequencies above 800 MHz. All measurements were carried out at room temperature 298 ± 2K.

For this PRE studies, pure crystals of PM-POMs were dissolved in $9{:}1$ D_2O: H_2O solvent and five sets of concentrations c, 0, 0.2, 0.4, 0.6, 0.8 and 1 mMol/l, of the complex were prepared at KIT by Aiswarya Venu, a chemist PhD student. Note that c represents the concentration of the POM complex rather than the lanthanide ion. Initially, Aiswarya measured the field dependence of relaxivities at frequencies below 800 MHz using the NMR facility in Karlsruhe. Subsequently, the samples were transported to the LNCMI site in Grenoble.

The investigated PM-POM cluster solutions remained clear after the NMR measurements had been per-

formed. All the compounds showed mono-exponential relaxation curves that do not change when the solution is stored for a long period (several weeks). This confirms that the cluster is stable in solution and that no phase separation occurs.

At Grenoble, Steffen Krämer (my co-director), Aiswarya Venu, and I performed the relaxivity measurements for the frequencies above 800 MHz. A combined analysis of the field dependence of the relaxivities was done by both the KIT and LNCMI teams.

5.2.1 ^{1}H NMR above 800 MHz at LNCMI resistive magnet

Sample preparation

In the initial stage of the experiment, capillaries having inner diameter of 1 mm were filled manually with a sample volume corresponding to $l = 1 - 1.5$ mm, using the method described in section 3.2.2 of chapter 3. A total of 46 samples were prepared by this method, $2 - 3$ samples per concentration for each compound.

Sample positioning in the center of the resistive magnet

After the sample preparation, we transferred the NMR spectrometer to the M9 site of the resistive magnets. The resistive magnet control program displays the location of the magnet center. On the basis of this value, we calculated an approximately vertical position for the probe. We inserted the probe into the magnet bore to the calculated vertical position. First, we set the static magnetic field to 21 T and tuned the probe to the ^{1}H resonant frequency f_0. A water-based reference sample containing a high concentration of $GdCl_3$ ($c = 60$ mMol/l), hence short T_1, was used to center the probe inside the resistive magnet to its optimal position. To this end, the NMR signal was recorded using the FID pulse sequence and the vertical position of the probe was varied with a 0.5 mm step. The optimal position was taken to be the one where the NMR signal had the narrowest width.

Pulse program parameter calibration

In the next step, keeping the same water-based reference sample, we find the $\frac{\pi}{2}$ and the π pulse lengths presented in table 5.3 by performing a nutation experiment (section 1.3.3 of chapter 1) at each magnetic field.

We then proceeded to the characterization of the samples synthesized by KIT. A single scan inversion-recovery sequence was applied in the T_1 experiments. The Matlab program described previously in the thesis (chapter 2) was used to make the necessary corrections to the NMR spectrum and to extract the T_1 relaxation time immediately after each measurement. We repeated each T_1 experiment several times before moving on to the next one in order to improve signal quality. For each concentration, the relaxation time T_1 was subsequently measured at the corresponding frequencies: 870 MHz (20.4 T), 1050 MHz (24.7 T), 1200 MHz (28.2 T), and 1400 MHz (33 T). To check that there had been no phase separation in the sample during the experiments, we returned to the first magnetic field (20.4 T), and we performed an additional measurement of T_1 to ensure that the relaxation time T_1 remained unchanged.

We removed the probe and changed the sample to the next concentration following the same procedure. Once all the concentrations for one compound were measured, we move on to the next one.

Due to the limited availability of the resistive magnet, the T_1 experiments were performed only for certain concentrations 0.2, 0.6, and 1 mMol/l. Moreover, due to the resistive magnet fluctuations, we were not able to perform the T_2 experiments for all three compounds.

Frequency [MHz]	$\frac{\pi}{2}$ pulse length [μs]	Power [dBm]	Power [W]
870	2.4	43.8	23.9
1050	2.6	44.1	25.7
1200	3.0	44	25.1
1400	4.0	42.5	17.7

Table 5.3: $\frac{\pi}{2}$ and the π pulse lengths found by nutation experiment at the interesting fields. The power was determined from the values of the oscilloscope using a 40 dB decoupler.

5.3 Results and discussion

Based on the PRE theory explained in the previous chapter, the relaxation rates R_i $(i = 1, 2)$ exhibit a linear dependence as a function of the complex concentration c at a given field. Therefore, before performing field dependence measurements, we check at a selected field that the linear dependence of R_i $(i = 1, 2)$ on concentration is confirmed. Another relevant point is that the offset of this linear dependence must always be equal to the relaxation rate R_i $(i = 1, 2)$ of the pure solvent (9:1 D_2O: H_2O), i.e., at $c = 0$ mMol/l. Hence the importance of measuring the solvent (9:1 D_2O:H_2O) relaxation rates R_i $(i = 1, 2)$ at all the fields of interest. If these two conditions are not satisfied, the PRE studies of the compound become more complicated and beyond the standard PRE model.

An example of such a compound is shown in the appendix section A.1, where we can clearly see that the offsets in the figure A.2 turned out to be different from the relaxation rates of the used solvent (9:1 D_2O:H_2O). Moreover, its PRE properties evolve with time.

The error bars on R_1 of the resistive magnet measurement are shown in the table (5.4). For all fields, the T_1 measurements are repeated up to 6-7 times. The error bars represent the relative error between the maximum and minimum values of R_1 expressed in percentage.

Figure 5.3 shows an example of the measured longitudinal relaxation rate R_1 of the Er-W_{11} POM cluster at different fields, where a linear dependence is observed as expected for a homogeneous solution. Note that the concentration in this figure is the entire Er-W_{11} complex rather than the Er-ion. The offset in the figure at $c = 0$ mMol/l represents the relaxation rate of the pure solvent (9:1 D_2O:H_2O), which is weakly field dependent. At a given field, the slope of the linear fits provides then, the relaxivity r_i $(i = 1, 2)$.

We can see from the figure that the relaxivity r_1 is increasing with the field. Similar behavior was observed for the Dy-W_{11} and Er_2-W_{34} clusters concerning the linear dependence of $R_i(c)$ $(i = 1, 2)$. Table 6.5 shows the relative error of r_1 expressed in $\%$ in the resistive magnet when using the inversion recovery (IR) pulse sequence for T_1 experiments.

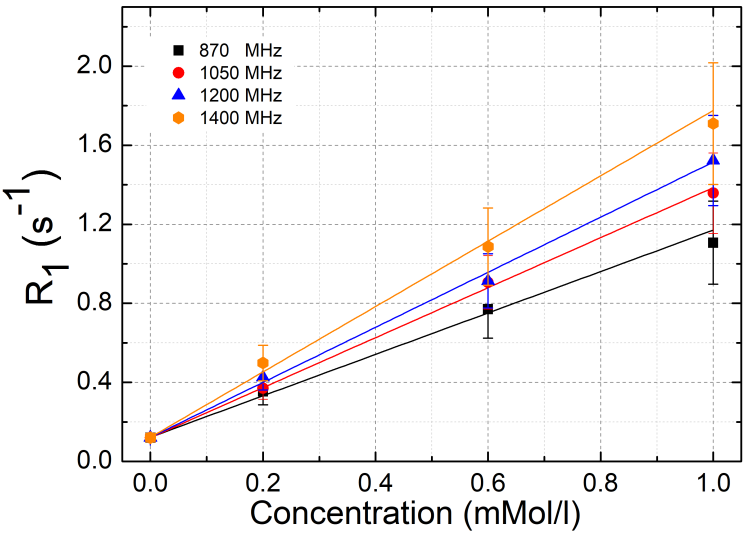

Figure 5.3: Example of longitudinal relaxation rates R_1 of ^1H NMR of an aqueous (9:1 D_2O : H_2O) solution of Er-W_{11} as a function of concentration and at different fields that was measured in the resistive magnet, with the corresponding linear fits. The slope of the fits provides the relaxivity r_1.

Frequency [MHz]	R_1 error [%]
870	19
1050	15
1200	15
1400	18

Table 5.4: Relative error of the longitudinal relaxation R_1 measurements on the resistive magnet using the inversion recovery (IR) pulse sequence for $c = 1$ mMol/l. For all fields, the T_1 measurements are repeated up to 6-7 times. The error bars represent the relative error between the maximum and minimum values of R_1.

5.3.1 Longitudinal relaxivity r_1

The extracted relaxivities (slopes) for all three clusters with respect to the field strength, are shown in figure 5.4. For all Ln-POM clusters, the relaxivity r_1 monotonically increases with the magnetic field. Among them, Er_2-W_{34} shows the highest r_1. Next, we will split the relaxivity discussion into two distinct categories: (1) Dy-W_{11} in conjunction with Er-W_{11} clusters with a similar structure but distinguished by their respective lanthanide ion and number of exchangeable water molecules q. (2) Er-W_{11} in conjunction with Er_2-W_{34} sharing the same lanthanide ion but two completely different POM complexes.

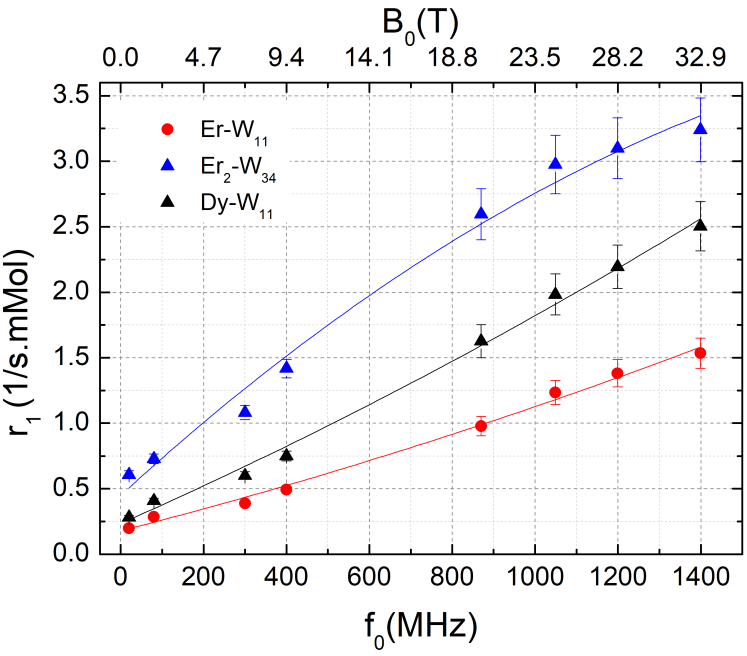

Figure 5.4: Longitudinal relaxivity r_1 data of ^1H of water with POM clusters (Dy-W_{11}, Er-W_{11}, and Er_2-W_{34}) as a function of Larmor frequency f_0, i.e., magnetic field. r_1 data up to 400 MHz were measured using the KIT facilities on commercial superconducting and permanent NMR magnets. For the frequency range 800 up to 1400 MHz, relaxivity studies were performed on the LNCMI resistive magnets. The solid lines are second-order polynomial fit that serves only as a guide to the eye lines.

Dy-W_{11} and Er-W_{11}

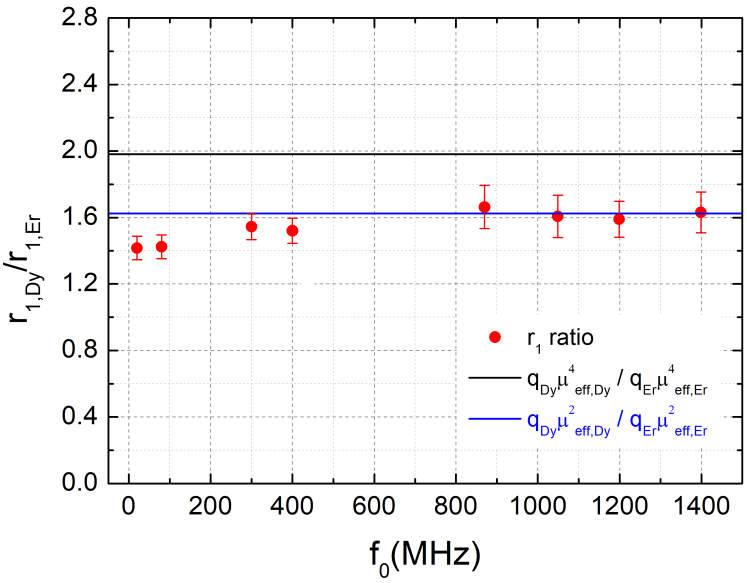

Figure 5.5: Longitudinal relaxivity ratio $r_{1,Dy}/r_{1,Er}$ between the two POM clusters Dy-W_{11} and Er-W_{11} as a function of Larmor frequemcy, i.e., magnetic field. The black line gives the calculated value of $q_{Dy}\mu^4_{eff,Dy}/q_{Er}\mu^4_{eff,Er}$ which is related to the Curie contribution. The blue line gives the calculated value of $q_{Dy}\mu^2_{eff,Dy}/q_{Er}\mu^2_{eff,Er}$ which is related to the dipolar contribution.

In a first approximation, for both Dy-W_{11} and Er-W_{11} POM clusters, the r_1 linearly increase with the applied magnetic field.

In table 5.1, we can see that both Dy-W_{11} and Er-W_{11} have very similar electronic and dynamic parameters. A notable difference between this two compounds is in the magnetic properties the lanthanide ion, where the magnetic moment of Dy(III) (10.6) is higher than the one of Er(III) (9.6). This leads to a higher r_1 of Dy-W_{11} compared with Er-W_{11}, which supports the influence of electron spin of the paramagnetic ion on PRE, since, in these POM clusters, only one lanthanide ion (Dy(III) and Er(III)) is incorporated within same diamagnetic keggin $[GeW_{11}O_{39}]^{8-}$ POM unit.

Despite having a similar structure, we note that the number of exchangeable water molecules for Dy-W_{11} ($q = 4$) is higher than for Er-W_{11} ($q = 3$). Assuming fast exchange ($\tau_M << T_{1,M}$), r_1 becomes proportional to water binding sites q and to the residence time of water molecules. Consequently, the difference in number of water q also contributes to the higher longitudinal relaxivity r_1 of Dy-W_{11} compared to Er-W_{11}.

Figure 5.1 clearly shows that Dy(III) and Er(III) have similar NMRD profiles. For this reason, we plot the relaxivity ratio between the two compounds $r_{1,Dy}/r_{1,Er}$ in figure 5.5 and compare it qualitatively with

$$\frac{q_{Dy}\mu^2_{eff,Dy}}{q_{Er}\mu^2_{eff,Er}},$$

and

$$\frac{q_{Dy}\mu^4_{eff,Dy}}{q_{Er}\mu^4_{eff,Er}}. \tag{5.1}$$

In the figure 5.5, the data scatter in the range of $q_{Dy}\mu^2_{eff,Dy}/q_{Er}\mu^2_{eff,Er}$ ratio, which means that the dipolar contribution is dominant in these compounds.

Other relevant properties that certainly contribute to the difference in relaxivities of Dy-W_{11} and Er-W_{11} are the ionic radii of Dy(III) and Er(III), their magnetic anisotropy being oblate for Dy(III) and prolate for Er(III) [73].

Er-W_{11} and Er_2-W_{34}

Er_2-W_{34} shows the highest relaxivity r_1, more than doubled values compared to Er-W_{11}. This ratio is enhanced towards lower frequencies. At higher frequencies, Er_2-W_{34} shows a deviation from a linear slope. Several factors need to be considered to explain the difference in r_1 between Er_2-W_{34} and Er-W_{11}.

First, the magnetic moment of Er_2-W_{34} is twice as high as Er-W_{11} which increases the relaxivity. However, for a more detailed quantitative modeling, further information is required on the couplings and correlations between the two Er(III) ions sandwiched between two mono-lacunary Wells-Dawson units $[P_2W_{17}O_{61}]^{10-}$. Second, the chemical structure of Er_2-W_{34} limits the exchange of water with the paramagnetic Er(III) ion, since only one of the eight coordination sites of each Er(III) is bounded to a single water molecule, which reduces the PRE. Third, the molecular weight of Er_2-W_{34} is larger compared to Er-W_{11} (see table 5.1), causing lower tumbling rates and a different diffusion behavior which may explain the relative increase of r_1 at low fields and the leveling-off at highest fields.

However, with the presented data set, our model is qualitative at the current state but makes the observed PRE behavior plausible. More systematic studies of other Ln_2-W_{34} complexes are needed to identify and

quantify the microscopic mechanisms responsible for the observed PRE behavior in these highly complex systems.

5.3.2 Transverse relaxivity r_2

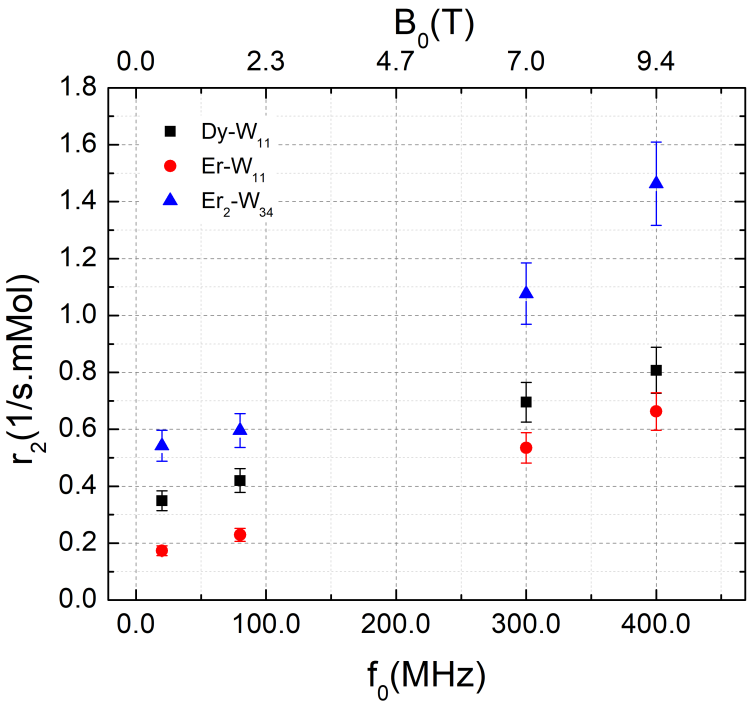

Figure 5.6: Transverse relaxivity r_2 data of ^1H of water with POM clusters (Dy-W_{11}, Er-W_{11}, and Er_2-W_{34}) as a function of Larmor frequency f_0, i.e., magnetic field. r_2 data up to 400 MHz were measured using the KIT facility on commercial superconducting and NMR permanent magnets.

Both transverse and longitudinal relaxivity are equally important for MRI contrast agents. The transverse relaxivities r_2 of POMs clusters Dy-W_{11}, Er-W_{11}, and Er_2W_{34} up to 400 MHz are presented in figure 5.6 and show also an approximately linear field dependence due to PRE. For Er_2-W_{34} a deviation from the linear slope occurs above 300 MHz, probably due to a Curie-contribution due to the large size of the molecule. This behavior is consistent with an increasing Curie-spin contribution to the transverse relaxivity r_2. This term has a quadratic field dependence and becomes enhanced for large molecules and at high magnetic fields [47, 62, 63].

The higher transverse relaxivity r_2 of Dy-W_{11} compared to Er-W_{11} can be correlated with the effective magnetic moment μ_{eff} of the lanthanide ion since r_2 is proportional to the square of the magnetic moment of the paramagnetic center. The magnetic moment of Dy(III) is higher ($\mu_{eff} = 10.6$) than that of Er(III), which has $\mu_{eff} = 9.6$. The comparison of the transverse relaxivity data of Er-W_{11} with Er_2-W_{34} indicates that the PRE-induced r_2 also depends on the number of paramagnetic centers in the molecule.

5.4 Conclusion

The effectiveness of MRI contrast agents can be evaluated by measuring the relaxivity of water protons (^{1}H). Paramagnetic systems with higher relaxivities often improve the image contrast. PRE studies were performed over a large range of Larmor frequencies (20 up to 1400 MHz) for aqueous solutions for the Ln-POM clusters Dy-W_{11}, Er-W_{11}, and Er_2W_{34}.

The r_1 and r_2 values are the fitted slopes of $R_1(c)$ and $R_2(c)$ as a function of the entire POM cluster concentration, respectively. We compared the PRE behavior of the three compounds.

These PRE studies revealed that all three compounds are potential MRI contrast agents at intermediate and high magnetic fields due to their very short electronic relaxation times τ_S compared to their Gd(III) analogs. The total magnetic moments and the number of exchangeable water molecules with the paramagnetic ion seem to be the key to the development of efficient contrast agents for future high-field MRI application.

More systematic studies on other Ln_2-W_{34} are needed to quantify the different factors responsible for the observed PRE behavior in these highly complex systems.

Chapter 6: PRE studies of Ln(III) aqua ions

The study of paramagnetic relaxation enhancement (PRE) has attracted interest since the early days of NMR [87], in particular regarding the aqueous solutions of lanthanide ions (Ln(III) aqua ions) with total spin $J > 0$ [61,67]. Except for Gd, these lanthanide ions have short electronic relaxation times. This allows the Curie spin contribution to the PRE to be observed at high fields, making these ions suitable for specific applications.

Previous studies on lanthanide aqua ions of Dy(III), Ho(III), and Er(III) up to 600 MHz showed that the Curie spin contribution becomes observable at fields above 100 MHz [67]. A large set of data for frequencies below 100 MHz has consistently shown almost field independent relaxivities for these ions. This means that the dipolar relaxation dominates at lower fields than 100 MHz and that the short electronic relaxation times modulate this contribution. Furthermore, the weak field dependance indicates that the electronic relaxation time is independent of the magnetic field. For gadolinium (Gd), the relaxivity data exhibit a dispersion step between 1 and 20 MHz, beyond which the relaxivity decreases to reach a plateau [61, 88].

In our study, PRE of water ^{1}H NMR has been investigated for aqueous solutions of $LnCl_3$ salts with Ln $\in \{$Gd, Dy, Ho, and Er$\}$ over a wide range of frequencies from 20 up to 1400 MHz. The measurements at very high fields are of particular interest since almost no experimental PRE data for single lanthanide ion solutions are available above 600 MHz. It is essential to discern whether the plateau observed in Gd relaxivity persists at higher fields, and how Curie spin relaxation evolves for the three lanthanide Dy(III), Ho(III), and Er(III) ions.

These compounds have similar molecular weights and hence similar rotational correlation times τ_R. PRE data obtained from this study will help in PRE modeling. Moreover, it will provide important information in the form of known parameters and their numerical values for modeling of PRE of more complex compounds.

Another important open issue is, whether the limited field homogeneity and temporal stability of the resistive magnet discussed in chapter 3 has an influence on r_i ($i = 1, 2$). Therefore, we used two state-of-the-art Bruker superconducting magnets at 800 and 950 MHz to compare the $r_{1,2}$ data from these magnets with those obtained from the resistive magnet measurements. This helps us to better understand possible systematic errors caused by the resistive magnet. This is very important for the future usage of resistive magnets for PRE dispersion studies at very high magnetic fields.

6.1 Experimental section

To better understand the role of the Ln(III) aqua ions in PRE, we investigated the relaxivity behavior of various $LnCl_3$ salts with Ln $\in$ {Gd, Dy, Ho, and Er}. Each $LnCl_3$ has been dissolved in aqueous solutions of 9:1 D_2O: H_2O. For each $LnCl_3$ compound, we prepared a series of concentrations $c = 10$, 5, 2, 1, 0.5, and 0.2 mMol/l. The main point to note here is that *all* samples of $LnCl_3$ (Ln $\in$ {Gd, Dy, Ho, and Er}) for *all* the concentrations ($c = 10$, 5, 2, 1, 0.5, and 0.2 mMol/l) studied in the permanent, superconducting, and resistive magnets were *identical*. In total, we prepared 25 samples including the solvent.

This study covered a wide range of frequencies where we used three distinct types of magnets:

1. Permanent magnets operating at 20 and 80 MHz frequencies at the Karlsruhe Institute of Technology (KIT).

2. Superconducting commercial Bruker magnets located at different facilities:

   (a) 200, 300, and 400 MHz magnets at the Karlsruhe Institute of Technology (KIT) in Karlsruhe, Germany.

   (b) 600 and 950 MHz magnets at the IBS Institute in Grenoble, France.

   (c) An 800 MHz magnet at Bruker's own facility in Ettlingen, Germany.

3. Resistive magnet at the LNCMI in Grenoble, for NMR experiments in the 800 to 1400 MHz frequency range.

6.1.1 Preparation of lanthanide-based chloride salts samples

An important step in the experimental part is the preparation of the samples. In order to ensure the most accurate concentration possible, which is a critical parameter for obtaining good relaxivity r_i ($i = 1, 2$) data. For each compound, we first prepared a 10 mMol/l solution, in the following called the stock solution. The lower concentrations were then obtained by dilution

For the sample preparation, the following instruments were used

- Balance METTLER TOLEDO with a 0.01 mg precision.
- Little graduated beaker for stock solution preparation.
- 25 ml pipette for solvent (9:1 D_2O:H_2O) preparation.
- 1 ml Eppendorf tube for the preparation of the diluted concentration solution.
- Tube holder.
- 100-1000 μl Eppendorf pipettes.

– Wilmad sample tubes of 5.0 mm outer diameter (OD) NMR tubes (for Larmor frequencies < 600 MHz). Bruker sample tubes of 1.7 mm outer diameter (OD) NMR tubes (for Larmor frequencies 600, 800, and 950 MHz). Capillary tubes of 1.2 mm outer diameter (OD) for the NMR experiments in the resistive magnets at Larmor frequencies > 800 MHz.

Photos of these materials are shown in the Appendix section A.2.

For the preparation of the 10 mMol/l stock solution and its dilution, the following procedure was applied:

1. The 9:1 D_2O:H_2O solvent was prepared using a 25 ml pipette with an accuracy of ± 0.5 ml, where 90 % of the total volume was filled by D_2O and 10 % by H_2O.

2. We aim to have the same volume V_{ref} for each concentration.

   (a) Dilution calculations were performed using the formulas:

   $$c_{start}.V_1 = c_{final}.V_{ref} \tag{6.1}$$

   $$V_1 = \frac{c_{final}.V_{ref}}{c_{start}}, \quad \text{and} \quad V_2 = V_{ref} - V_1 \tag{6.2}$$

   Where c_{start} is the highest concentration in the dilution set (10 mMol/l) i.e., the stock solution. V_1 represent the amount of volume taken from the stock solution. V_2 is the volume of the solvent added to obtain the desired concentration c_{final}. The error calculation on the concentration is detailed in the Appendix section A.2.2.

   (b) Then we prepare a stock solution with the highest concentration in the dilution set. The volume of the stock solution V_{stock} should be equal to or greater than the sum of V_1 calculated in the previous step.

   (c) The amount m_0 of $LnCl_3$ used to prepare the stock solution is defined by the equation (6.3):

   $$m_0 = c_{start}.M.V_{stock} \tag{6.3}$$

   Where M is equal to the molar mass of the whole ($LnCl_3 + 6H_2O$) complex. The molar mass of the atoms is shown in table A.1 and the calculated molar mass of the $LnCl_3$ samples and their weights are reported in table A.2 and table 3.38.

   (d) m_0 of the $LnCl_3$ were then dissolved in V_{stock} of 9:1 D_2O:H_2O to make the required stock solution.

   (e) V_1 and V_2 values were extracted using the $100 - 1000$ μl Eppendorf single-channel pipette, and the dilution proceeded. The accuracy and precision of this micropipette is listed in the table A.3, where the total error reflects the sum of the systematic error and the random error (2σ). The error calculation on the concentration is described in the Appendix section A.2.2.

3. We transferred the samples to Wilmad NMR sample tubes with an outer diameter of 5.0 mm. In addition, we stored the samples in these 5 mm tubes, where some portions were transferred later on to 3 mm, 1.7 mm tubes and 1 mm capillary tubes depending on the conditions required for the NMR experiment.

This ensures that all experiments were performed on the same set of samples.

6.1.2 NMR instruments below 1 GHz using Bruker NMR spectrometers

The experimental details for the employed commercial Bruker NMR spectrometers (frequency range between 20 and 950 MHz) are summarized in the table 6.1 and will be discussed in the next upcoming paragraphs.

Facility	KIT					IBS	Bruker	IBS
Frequency [MHz]	20	80	200	300	400	600	800	950
Magnetic field [T]	0.5	1.9	4.7	7.0	9.4	14.1	18.8	22.3
Type of Magnet	Permanent		Superconducting					
Spectrometer type	Minispec	Fourier	ASCEND^{TM}					
Sample tube OD [mm]	5					1.7		
Spectrometer software	Minispec	TOPSPIN 3+4						
Processing software	Origin	Spin dynamics				Python	Spin dynamics	Python
T_1 parameters								
T_1 sequence	PSR	IR			PSR	IR		
Number of scans	4							
Exp dimension	2D							
Number of 2D data points	16							
T_2 parameters								
T_2 sequence	CPMG (1)	CPMG (2)						
Number of scans	4					8		
Exp dimension	1D	2D						
Number of 2D data points	-	16						

Table 6.1: Experimental details for the employed commercial Bruker NMR spectrometers. PSR is Progressive saturation recovery pulse sequence and IR is Inversion recovery pulse sequence. Both methods are detailed in chapter 1.

Time domain NMR (TD-NMR) Bruker instruments at 20 MHz

The 20 MHz spectrometer is a TD-NMR spectrometer of the Bruker Minispec series. T_1 was measured by a progressive saturation recovery (PSR) pulse sequence (see Chapter 1 Section 1.3.4). As the magnet at 20 MHz is inhomogeneous, the T_2 was extracted from the transverse magnetization decay of a Carr-Purcell-Meiboom-Gill multi-echo sequence (1D CPMG), which suppresses the spin diffusion contribution to the T_2 [2,3]. All the data processing was done in the time domain. Data treatment was performed using Origin.

Frequency domain NMR Bruker instruments up to 950 MHz

The 80 MHz NMR spectrometer is a Benchtop NMR spectrometer of the Bruker Fourier series.

The 200, 300, 400, 600, 800, and 950 MHz spectrometers are of the Bruker ASCEND^{TM} series.

All NMR spectrometers feature auto-tuning and active z-gradient shiming. Data was acquired using Bruker's TOPSPIN VERSION $3 + 4$ software for all the spectrometers. For further data processing, the phase corrected spectra was stored in 2D data files. For analysis of T_1 and T_2, we used the spin dynamics software (Bruker software) that enables the user to choose the size of the integration window for the moment equations (Chapter 2, Section 2.1.2) to determine the magnetization values, except for the 600 and 950 MHz spectrometers. For these, an in-house Python script of the IBS NMR team was provided, in which the magnetization was determined by finding the maximum value in the NMR spectrum [89].

T_1 was measured by multi-scan inversion recovery pulse sequence (IR), except for the 400 MHz spectrometer where we used the saturation recovery sequence (SR). T_2 was obtained by a multi-scan 2D CPMG echo sequence (see Chapter 1, Section 1.3.5).

6.1.3 Experimental protocol and optimization of T_1 and T_2 experiments

Optimization of T_1 and T_2 experiments

We perform the first measurements of T_i ($i = 1, 2$) on the highest concentration sample for each compound. The reason is that it has the shortest T_1 and T_2 values. Then, it becomes easy to predict the range of T_i ($i = 1, 2$) for the other concentrations since: (1) The dependence of the relaxation rate R_i ($i = 1, 2$) on the concentration is linear according to the PRE theory; (2) Solvent relaxation rates are very small and depend only slightly on the field.

This allows to: (1) Optimize the T_1 measurements by using the appropriate timetable as described in section 1.3.4 of the chapter 1; (2) Optimize the T_2 measurements by choosing the echo time τ_e so that the last time interval $\tau_{i,max} = 5T_2$ (see section 1.3.5 of the chapter 1).

Previous PRE studies on $LnCl_3$ compounds give an insight into their relaxivity values r_i ($i = 1, 2$) at 400 MHz [67]. Therefore, T_i ($i = 1, 2$) were measured first on the 400 MHz NMR spectrometer at KIT. For T_1, the saturation recovery pulse sequence was used to avoid waiting for $5T_1$ between two consecutive time intervals τ_n, so the optimization of T_1 takes less time when compared to an inversion recovery pulse sequence. The timetable consists of 16 time intervals equidistant in the logarithmic scale. Taking the value of T_1 from the reference [67], we adapt the timetable so the last time interval $\tau_n >> 5T_1$, where we set the

base of the logarithm to $k = 2$. A new value of T_1 is obtained after the first measurement. The timetable is adapted accordingly, and the base of the logarithm is modified to $k = 1.3$.

For T_2 we used a 2D CPMG pulse sequence. We assumed as a first approximation that $T_1 = T_2$. The echo time τ_e was chosen so that the last time interval $\tau_{i,max} = 5T_2$. After we extract the first experimental value of T_2, we repeat the experiment by adapting the echo time τ_e accordingly to the experimental value.

However, at fields higher than 600 MHz, no experimental data on the PRE behavior of $LnCl_3$ samples exist. In this case, we extrapolated the relaxivity curves r_i ($i = 1.2$) for $LnCl_3$ samples (Ln $\in$ Dy, Ho, and Er) using a fourth-order polynomial to get an idea of how the relaxation times T_i ($i = 1.2$) might evolve with the field. For $GdCl_3$ samples, we assumed a constant relaxivity as a function of the field.

Experimental protocol

The experimental protocol was the following:

1. 25 samples were prepared according to the dilution protocol.
2. The following procedure was adapted for the NMR experiment:
   (a) Check whether the sample in the tube is at the nominal center. For this purpose Bruker provides a calibrated ruler.
   (b) Insert the probe using sample loading system.
   (c) Tune and match the RF circuit to the desired resonant frequency f_0.
   (d) Lock the field using the 2D signal of the solvent (9:1 D_2O: H_2O) as a reference to correct any magnet drift at the desired frequency.
   (e) The magnet was shimmed using a procedure provided by Bruker.
   (f) The pulses were calibrated through an auto-calibration process.
   (g) The T_1 and T_2 measurements were performed. For the pulse sequences used for these T_i ($i = 1, 2$) experiments at each field, see table 6.1. The optimization of the T_i ($i = 1, 2$) pulse sequences will be discussed in the next paragraph.
   (h) The T_1 and T_2 analyses were performed immediately after each measurement. Magnetization was calculated using the zero moment equation with integral limits assigned to both ends of the NMR signal.
   (i) Once the relaxation times had been measured, we removed the probe, and the sample was changed. After each sample change, the circuit was re-tuned to the resonant frequency f_0, and the same procedure was followed for characterization.
3. Once all the concentrations of a sample are measured on the different NMR spectrometers, we moved on to the next $LnCl_3$ sample.
4. The relaxation rates R_1 = 1/T_1 and R_2=1/T_2 were deduced from the curves fitted according to a saturation, recovery or a mono-exponential decay.
5. During the entire experiment period the temperature was recorded and found at 298$\pm$2 K.

The same procedure was applied to the 20 MHz, except for locking, and shimming, which are not available on this NMR spectrometer.

6.1.4 Radiation damping at very high fields above 400 MHz

Radiation damping is a phenomenon that can occur in NMR experiments. It originates from the precessing magnetization M_0 of the sample that interacts with the radio-frequency circuit of the NMR probe [90–93]. This generates an additional decay with a time constant

$$\tau_r = \frac{1}{2\pi\eta M_0 Q\gamma_I}, \tag{6.4}$$

where M_0 is the magnetization of the sample ($\propto n\omega_0\gamma^2$, n density of the nucleus), η the filling factor of the probe ($\propto V_S/V_c$), and Q the quality factor of the probe. Therefore, radiation damping becomes stronger when high abundant nuclei (like ^{1}H) are measured at high magnetic fields using high-Q probes (cryoprobe). In addition, radiation damping becomes stronger in homogeneous magnets (T_2^* very long).

In order to effectively check the presence of radiation damping at a magnetic field, we need a reference sample, which has long relaxation times T_1 and T_2. For this reason, we used the pure solvent 9:1 D_2O:H_2O as the reference sample, where we expect small and slightly field dependent relaxation rate R_i ($i = 1, 2$) in the absence of radiation damping (see figure 6.3).

Figure 6.1 shows the results of the T_1 preliminary experiments of the solvent measured on the 600 MHz Bruker spectrometer at IBS. For this experiment, we transferred a small quantity of the same solvent sample 9:1 D_2O:H_2O (200 μl) that had been measured on other NMR spectrometers into a 3 mm outer diameter (OD) sample tube.

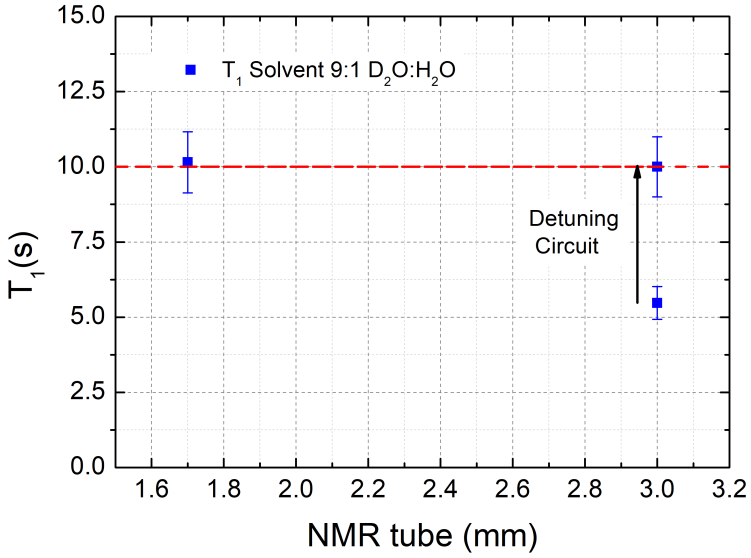

Figure 6.1: Longitudinal relaxation time T_1 of ^{1}H NMR as a function of the employed NMR sample tube using different methods to check the radiation damping effect.

The expected value of R_1 the relaxation rate of the solvent at 600 MHz is indicated in the figure by the red dotted line (about 10 s for T_1). The first measurements were performed for a well-tuned circuit at the corresponding ^{1}H Larmor frequency 600 MHz. However, the resulting T_1 was two times below its expected value, indicating the presence of the radiation damping effect. In this case, we can act on three factors to eliminate radiation damping effect:

1. Using diluted samples. This was the reason for employing 9:1 D_2O: H_2O as a solvent instead of pure water H_2O to decrease the number of ^{1}H protons in the samples and thus decrease magnetization M_0.

2. We detune the RF circuit away from the resonance frequency, which decreases the probe quality factor Q (see figure 6.2).

3. We reduce the sample volume, which decreases both the filling factor η and the magnetization M_0 (number of protons).

Both solutions were confirmed to be effective as the obtained T_1 values matched the expected values as shown in figure 6.1. Moreover, we opted for the second solution to maintain optimal pulse conditions, where we reduced the sample volume by switching to 1.7 mm NMR sample tubes.

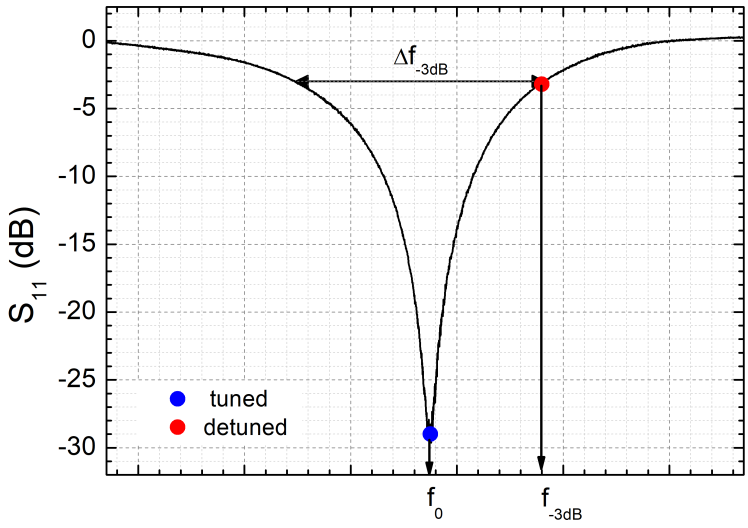

Figure 6.2: Circuit detuning method used to avoid radiation damping.

The table 6.2 summarizes the sample volumes used for each experiment at different frequencies with different (OD) sample tubes, where the last row of the table provides the numbers for the resistive magnet. Therefore, switching from 5 mm to 1.7 mm (OD) sample tubes, the filling factor η ($\propto V_S/V_c$) is reduced by a factor of 10, preventing radiation damping at high fields in commercial Bruker NMR spectrometers. Figure 6.3 shows the field dependency of the solvent 9:1 D_2O:H_2O relaxation rates.

The relaxation times T_i ($i = 1, 2$) of $LnCl_3$ samples are shorter than that of the solvent. Therefore, the radiation damping cannot affect the T_i measurements of these compounds when using 1.7 mm sample tubes. Similar preliminary experiment on radiation damping were performed on the 800 and 950 MHz spectrometers. No radiation damping was observed when using 1.7 mm sample tubes at these fields.

As for the resistive magnet, there was no need to perform this preliminary experiment on radiation damping since (1) The magnetic field is very inhomogeneous $T_2^* = 1.5$ ms, therefore M_0 decays very fast ; (2) The Q factor of the probes used in commercial Bruker NMR spectrometers are 10 to 100 times higher compared to the resistive magnet probe; (3) We already use small samples of 1 to 1.5 μl in the resistive magnet for homogeneity reasons.

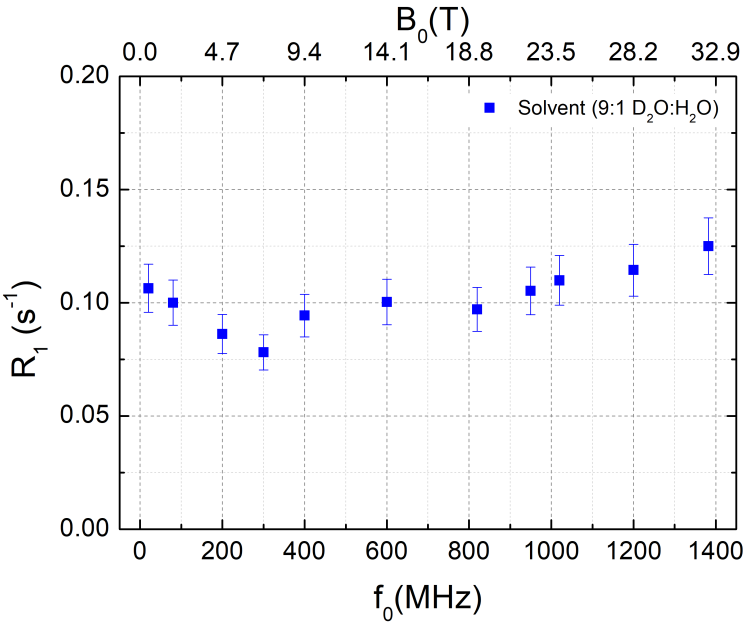

Figure 6.3: Field dependence of the solvent 9:1 D_2O:H_2O longitudinal relaxation rate R_1.

Sample tube (OD)	Inner diameter (ID)	h	V_S	$V_S/V_{5\text{mm}}$
5 mm (<400 MHz)	4.2 mm	1 cm	125 μl	1
3 mm (600 MHz)	2.4 mm	1 cm	50 μl	0.4
1.7 mm (600, 800, 950 MHz)	1.3 mm	1 cm	12.5 μl	0.1
1.2 mm (800→1400 MHz)	1 mm	1-1.5 mm	1-1.5 μl	0.01

Table 6.2: Sample volumes V_S needed for an active height h when using different NMR spectrometers. The ratio V_S/V_{5mm} is proportional to the filling factor η in the commercial Bruker NMR spectrometers. The last row in the table provides the numbers for the resistive magnet.

6.1.5 NMR instruments above 800 MHz at LNCMI resistive magnets

For ^{1}H NMR performed at the LNCMI's resistive magnet for the 800 to 1400 MHz frequency range, the instruments and methods used are extensively discussed in chapters 2 and 3. The only change is that we used a single-scan progressive saturation recovery sequence for the T_1 experiments instead of the inversion recovery sequence employed in the previous PRE study. The reason for this modification in the pulse sequence is to avoid the impact of π pulses on the T_1 experiment since they are more sensitive to the fluctuation of the resistive magnet than the $\pi/2$ pulses (seen in more details in chapter 3). However, this modification cannot be applied to the T_2 measurements, where there's a need for a train of π refocusing pulses to remove the decoherence of the spins induced by the inhomogeneity of the magnetic field B_0. For the T_2 measurements we used the same method as on the 20 MHz time domain NMR (TD-NMR) Bruker instruments (CPMG (1D)).

6.2 Properties of Ln(III) aqua ions relevant for PRE studies

The relevant properties for PRE studies of the investigated Ln(III) aqua ions are summarized in the table 6.3. The last column of the table lists the references from which the parameters are taken. The inner sphere radius r_{IS} and the number of the coordinated water molecules q are adapted from the previous PRE studies on aqua-lanthanide ions [67]. The radius of the outer sphere r_{OS} must always be greater than the radius of the inner sphere r_{IS}. The viscosity of the solvent η at room temperature is given in the table 6.4.

Compounds	Ln(III)	$Gd(H_2O)_q$	$Dy(H_2O)_q$	$Ho(H_2O)_q$	$Er(H_2O)_q$	Ref
Magnetic Properties	S	7/2	5/2	2	3/2	
	L	0	5	6	6	
	J	7/2	15/2	8	15/2	
	g	7/2	4/3	5/4	6/5	
	μ_{eff} [μ_B]	13.9	10.6	10.6	9.6	
	Anisotropy	none	oblate	oblate	prolate	
Structural Parameters	q	9	8	8	8	[67]
	M [10^{-3} kg.mol^{-1}]	371.72	376.97	379.4	381.73	
Electronic Parameters	τ_S [10^{-13} s]	10^4 -10^5	4 - 10	4 - 10	3 - 8	[49]
Inner-sphere radius	r_{IS} [10^{-10} m]	≈3.1	≈3.1	≈3.1	≈3.1	[67]
Outer-sphere radius	r_{OS} [10^{-10} m]	> r_{IS}	> r_{IS}	> r_{IS}	> r_{IS}	

Table 6.3: Relevant properties of Ln(III) aqua ions for PRE studies, which includes: (1) magnetic properties of non-interacting Gd(III), Dy(III), Ho(III) and Er(III) ions with $\mu_{eff} = g_j\sqrt{J(J+1)}$; (2) their structural parameters with M the molecular weight and q the number of the number of coordinated water molecules in the first coordination sphere; (3) the electronic parameters of the Ln(III) aqua ions; and (4) the inner and outer sphere radius. The last column of the table lists the references from which the parameters are taken.

Solvent	H_2O	D_2O	9:1 D_2O:H_2O
Viscosity η [10^{-4} Kg.s^{-1}.m^{-1}]	8.94	10.08	9.9
Diffusion constant D^{298} [10^{-9} m^{2}s^{-1}]	2.62	2.62	2.62

Table 6.4: Viscosity and diffusion constant of the solvent 9:1 D_2O:H_2O at room temperature respectively according to [94] and [85].

6.3 Results and discussion

For all Ln(III) aqua compounds, we measured longitudinal and transverse relaxation rates as a function of concentration and extracted the relaxivities r_i $(i = 1, 2)$ from the slope of the $R_i(c)$ $(i = 1, 2)$ plot. Due to the limited availability of the resistive magnet, the relaxivity measurements r_i $(i = 1, 2)$ were performed only for certain concentrations 1, 5, and 10 mMol/l as well as for the pure solvent ($c = 0$ mMol/l).

All longitudinal and most of the transverse relaxation curves were found mono-exponential. All the Ln(III) aqua compounds showed a linear dependence of the relaxation rates R_i $(i = 1, 2)$ as a function of the concentration at all fields. We will separate in the following the longitudinal relaxivity from the transverse one.

6.3.1 Longitudinal relaxivity

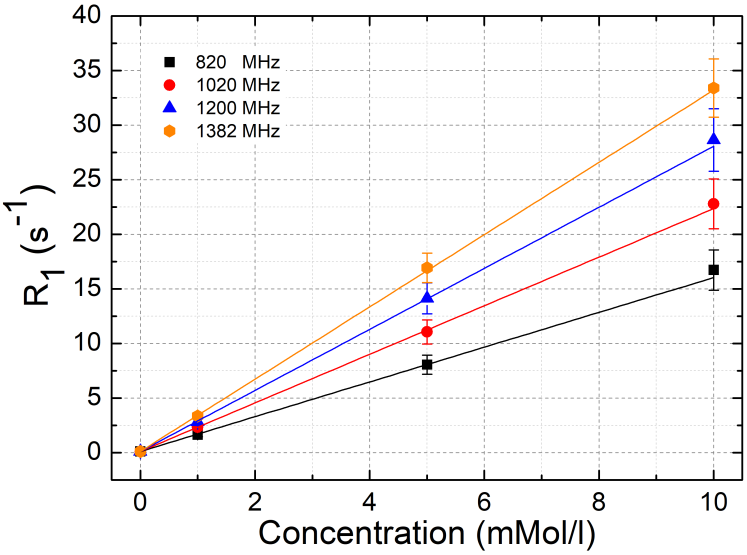

Figure 6.4: Example of longitudinal relaxation rates R_1 of ^1H NMR of an aqueous (9:1 D_2O : H_2O) solution of $ErCl_3$ linear dependance with concentration at different fields that was measured in the resistive magnets, and their corresponding linear fits. The slope of the fits provides the relaxivity r_1.

Figure 6.4 shows an example of the linear dependence of the longitudinal relaxation rates R_1 of the Er(III) aqua compound with the concentration at various fields measured in the resistive magnet, as expected for a homogenous solution. We recall that the offset in the figure at $c = 0$ mMol/l represents the relaxation rate of the pure solvent (9:1 D_2O: H_2O).

Frequency [MHz]	R_1 error (PSR)[%]	R_1 error (IR)[%]
820	11	19
1020	10	15
1200	10	15
1400	8	18

Table 6.5: Relative error of the longitudinal relaxation R_1 measurements on the resistive magnet using the progressive saturation recovery (PSR) pulse sequence. The last column represents the relative error of the longitudinal relaxation R_1 measurements on the resistive magnet obtained in the last PRE studies on PM-POM using inversion recovery (IR)pulse sequence. For all fields, the T_1 measurements are repeated up to 6-7 times. The error values represent the relative error between the maximum and minimum values of R_1.

Table 6.5 shows the relative error of r_1 expressed in percentage in the resistive magnet when using the progressive saturation recovery (PSR) pulse sequence for T_1 measurements. They are 1.5 to 2 times smaller than the relative error when using the inversion recovery pulse sequence for the T_1 measurements (see table 6.5).

The extracted r_1 slopes for all the Ln(III) (Ln $\in$ {Gd, Dy, Ho, Er}) compounds with respect to the field strength, are shown in figure 6.5 (semi logarithmic representation) and figure 6.6 (logarithmic representation). r_1 of Dy(III), Ho(III), and Er(III) increases monotonically with the field, whereas it is roughly field independent for the Gd(III). This latter is scattering between 12 and 15 s^{-1}·mMol^{-1}·l within the error bars of the experiments. Among the investigated lanthanide ions, Gd(III) shows the highest relaxivity r_1 at all fields.

Table 6.3 shows that Dy(III), Ho(III), and Er(III) exhibit short electronic relaxation times compared to the Gd(III), which has 4 to 5 orders of magnitude longer τ_S. In addition, for the three lanthanide ions Dy(III), Ho(III), and Er(III), as $\tau_S << \tau_R$, the Curie spin contribution is expected to dominate over the dipolar contribution in the PRE at high fields, as long as $\omega_I^2 \tau_R^2 << 1$. In this case, the Curie spin, which depends on the square of the external magnetic field becomes more significant and results in an increase in r_1. However, this is not the case for Gd(III), where the PRE is expected to be dominated by the dipolar relaxation. Therefore, in the following we will separate the discussion of Dy(III), Ho(III), and Er(III) compounds from that of Gd(III). For the aqua ions case, the outer sphere contribution to relaxivity is less than 10%, and therefore it is often neglected [61, 95]. However, we tried to include this contribution in our model.

Figure 6.5 that the relaxivity values of Dy(III) are the highest for the frequencies below 800 MHz, where Ho(III)and Er(III) have comparable r_1 values. Above this frequency, r_1 of both lanthanide ions Dy(III) and Ho(III) becomes relatively equal and higher than Er(III). Taking the data from table 6.3, the effective magnetic moments of Dy(III) and Ho(III) are equal (10.6 μ_B), and higher than the one of Er(III), which leads to a higher r_1, since these compounds have comparable structural, dynamic, and electronic properties. Other factors such as the magnetic anisotropies are oblate for Dy(III) and Ho(III), and is prolate for Er(III) can account for the difference of the observed relaxivities [73]. Despite that $q = 8$ is listed to be equal for all the three lanthanide ions, this parameter remains under debate in the modeling of PRE as stated in reference [67].

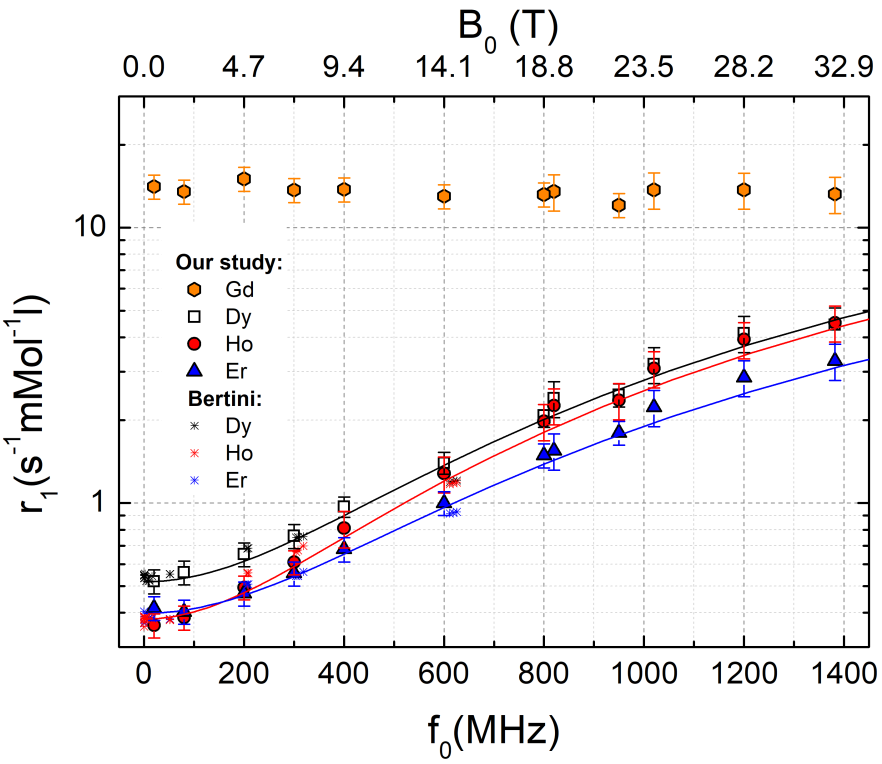

Figure 6.5: Longitudinal relaxivity r_1 data of ^1H of water with $LnCl_3$ compounds with Ln ϵ Gd, Dy, Ho, Er as a function of Larmor frequemcy, i.e., magnetic field. The r_1 data up to 400 MHz were measured using KIT facility on commercial Bruker NMR superconducting magnets, the data at 600 MHz and 950 MHz were measured using IBS facility, and 800 MHz using Bruker facility. r_1 data was measured for Larmor frequencies of 820 MHz, 1020 MHz, 1200 MHz, and 1400 MHz using the LNCMI resistive magnet. The star symbols represent previous PRE studies performed on $LnCl_3$ compounds taken from the reference [67]. The solid lines are the best fitting results using equations 4 and 5. The initial parameters that were used for finding the best fit are given in tables 6.3 and 6.4. The results of the fits are shown in table (6.6).

Although both Dy(III) and Ho(III) have equal effective moments ($\mu_{eff} = 10.6\mu_B$) with axially elongated magnetic anisotropies, the dispersion of Ho(III) is larger than that of Dy(III). This can be attributed to the distinct spacing of electronic energy levels in Dy(III) and Ho(III), which is influenced by their different total angular momentum quantum numbers J (Ho is integer and Dy is half integer). These differences lead to varying electronic relaxation times between the two lanthanide ions, resulting in different nuclear magnetic resonance dispersion (NMRD) profiles.

To discuss all the data related to r_1, including previous studies on $LnCl_3$ from reference [67] ranging from 0.01 to 600 MHz and new data ranging from 20 to 1400 MHz, it is better to use a logarithmic scale for the plot. We first note that the r_1 data are consistent with previous PRE studies. Figure 6.6 shows that the relaxivity data for Dy(III), Ho(III), and Er(III) have a constant value below 200 MHz, indicating that the dipolar contribution is the determining factor for r_1 in this frequency range. Electronic relaxation times, τ_S, modulating dipolar relaxation can be determined by modeling r_1 in the frequency range below 200 MHz. As mentioned, Curie spin becomes the dominant relaxation mechanism for PRE above 200 MHz, surpassing dipolar relaxation.

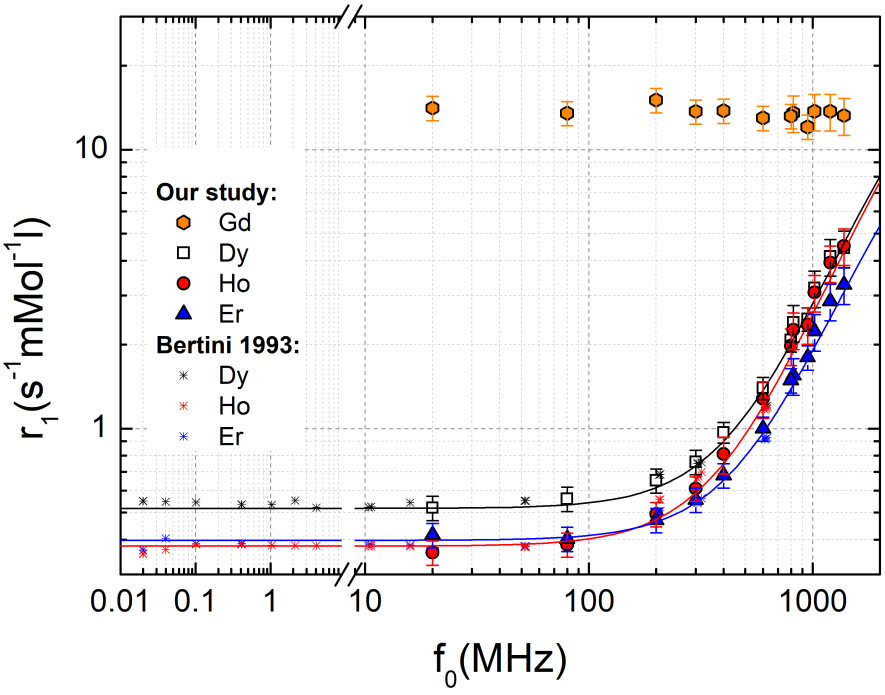

Figure 6.6: The description of this figure follows the caption of figure 6.5.

In a further step we tried to model our data using a Matlab script [96]. The data for Dy(III), Ho(III), and Er(III) were modeled using the equations (4.31), (4.34) and (4.37) for inner-sphere relaxation, and equations (4.40) and (4.43) for the outer-sphere relaxation taken from chapter 4. The initial parameters are based on a previous low-field PRE studies on these compounds in reference [67].

We fixed for the fit the number of coordinated water molecules to $q = 8$ for all three lanthanide ions, used fast chemical exchange $\tau_M = 3.9 \times 10^{-8}$ s as shown by previous ^{17}O NMR studies [97, 98], the magnetic properties of free Ln(III) ions from table 6.3, the average inner sphere radius to $r_{IS} = 3.1 \times 10^{-10}$ s, the closest outer sphere distance $r_{OS} = 4 \times 10^{-10}$, and the temperature $T = 298$ K. For the diffusion process we took relative diffusion constant of pure water at room temperature $D^{298} = 2.62 \times 10^{-9}$ m^{2}s^{-1} [94].

Two parameters, τ_S and τ_R, were extracted from the fitting that are summarized in table 6.6. The extracted values of τ_S and τ_R are slightly shorter than those reported in the previous work on lanthanide aqua ions [67]. This result could be due to the insertion of the outer sphere relaxation into the fit model of the $LnCl_3$ relaxivity data, unlike Bertini's study, where this contribution was neglected [67]. In this PRE study the outer sphere relaxation is reported to be less than 15%. For Dy(III), Ho(III), and Er(III) the correlation times have the following order τ_S<τ_R<τ_M.

In the case of Gd(III), the correlation time that modulates dipolar relaxation is the same as the one modulating Curie spin relaxation mechanisms. This is because the electronic relaxation time (τ_S) is longer in this case (10^{-8}). The NMRD profile remains flat over a wide range of frequencies, from 20 to 1400 MHz. This indicates that dipolar relaxation is the primary contributor to relaxation, and Curie spin relaxation is minimal for Gd(III). Additionally, there is no decrease in r_1 observed at high fields, ensuring that the condition of $\omega_I^2\tau_c^2 << 1$ is still valid for Gd(III). This suggests that τ_R modulates the dipolar contribution in Gd(III) and is smaller than $<< 10^{-9}$ s, as the first estimations shown in table 6.3 indicated. For Gd(III) aqua-ion, the correlation times follow this order: τ_R<τ_M<τ_S.

Ln(III) aqua	τ_S [ps]	τ_R [ps]	τ_M [ns]	q	r_{IS} [Å]	r_{OS} [Å]
Dy	0.3 [0.39]	50 [63]	39	8	3.1	4.0
Ho	0.21 [0.27]	45 [65]	39	8	3.1	4.0
Er	0.28 [0.31]	50 [61]	39	8	3.1	4.0

Table 6.6: Table of fitted and fixed parameters used in the PRE modeling of Dy(III), Ho(III), and Er(III) relaxivity data. The electronic correlation time τ_S and rotational correlation time τ_R are the parameters fitted from the relaxivity data, the values in brackets are the results of previous PRE studies [67]. The parameters that were fixed and their corresponding values are the correlation time of chemical exchange τ_M, the number of coordinated water molecules in the inner sphere q, and the inner and outer sphere radius. More details can be found in text.

In figure 6.5, there exists a small step between the r_1 data acquired from the resistive magnet and the data obtained from the superconducting magnet at comparable fields (800 and 950 MHz). This could be due to a systematic error caused by temperature, which needs further investigation. In order to estimate this error, we measured r_1 and r_2 as a function of the temperature on the 950 MHz NMR spectrometer as shown in figure 6.7. It shows the deviation of the relaxation rate in percentage from that measured at room temperature for the $HoCl_3$ of the $c = 10$ mMol sample. We can clearly see that the relaxation rate decreases linearly with temperature with a reduction of $2.4\ \%$ per degree. Same linear dependence (reduction of $2.4\ \%$ per degree) was observed for all the $LnCl_3$ compounds.

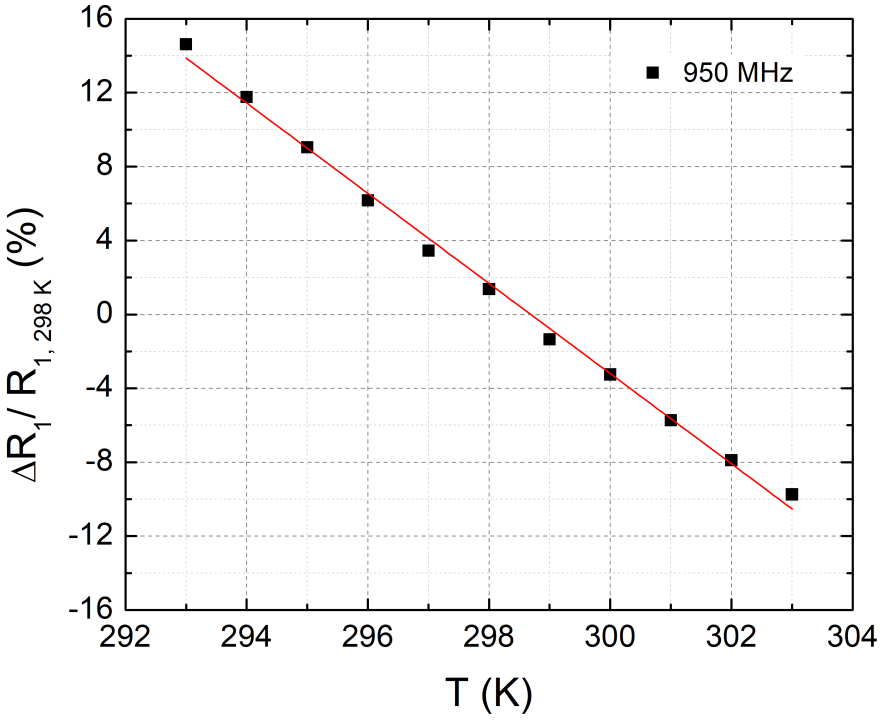

Figure 6.7: Deviation of the relaxation rate in percentage from that measured at room temperature expressed in $\%$ $\Delta R_1 = R_{1,T} - R_{1,298K}/R_{1,298K}$ of ^1H NMR of an aqueous solution (9:1 D_2O: H_2O) of $HoCl_3$ for a concentration $c = 10$ mMol as a function of temperature. The experiments were measured on the 950 MHz NMR spectrometer. Similar behavior was observed for all the $LnCl_3$ compounds. The relaxation rate decreases linearly with temperature with a reduction of $2.4\ \%$ per degree for all compounds.

6.3.2 Transverse relaxivity

The extracted r_2 slopes for all the $LnCl_3$ (Ln $\in$ {Gd, Dy, Ho, Er}) compounds with respect to the field strength, are shown in figure 6.8 (semi logarithmic representation). We observe a discontinuity in the r_2 data between measurements taken in superconducting and resistive magnets for the Dy(III), Ho(III), and Er(III) aqua ions. On the other hand, the r_2 data for Gd(III) are reasonably aligned with the superconducting data.

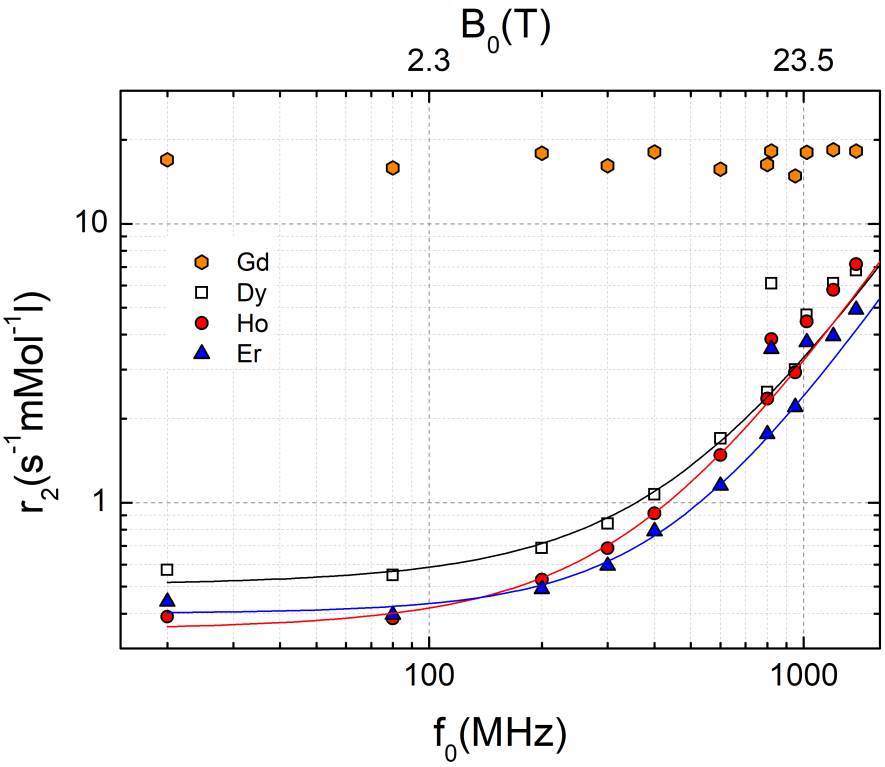

Figure 6.8: Transverse relaxivity r_2 data of ^1H of water with $LnCl_3$ compounds with Ln ϵ Gd, Dy, Ho, Er as a function of Larmor frequemcy, i.e., magnetic field. The r_1 data up to 400 MHz were measured using KIT facilities on commercial Bruker NMR superconducting magnets, the data at 600 MHz and 950 MHz were measured using IBS facilities, and 800 MHz using Bruker facilities. r_1 data was measured for Larmor frequencies of 820 MHz, 1020 MHz, 1200 MHz, and 1400 MHz using the LNCMI resistive magnet. The star symbols represent the previous PRE studies performed on the $LnCl_3$ compounds taken from the reference [67]. The solid lines are second-order polynomial fit that serves only as a guide to the eye lines. More details are found in text.

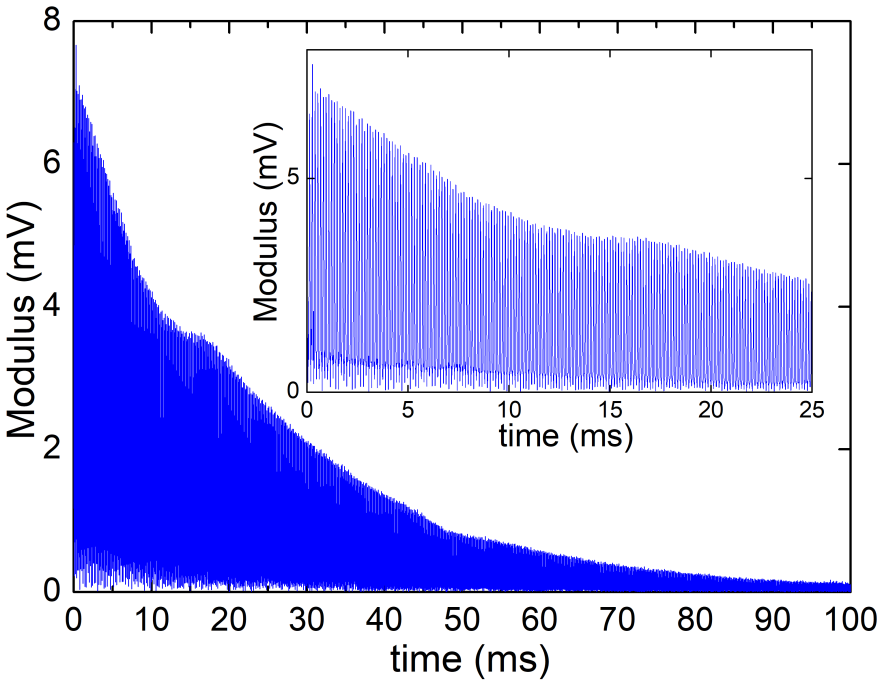

Figure 6.9: CPMG (1D) experiment of ^1H NMR of an aqueous solution (9:1 D_2O: H_2O) of $DyCl_3$ for a concentration $c = 10$ mMol performed at the Larmor frequency $f_0 = 820$ MHz.

For Dy(III), Ho(III) and Er(III), we were not able to measure T_2, except for the highest concentrations ($c = 10$ mMol/l). Thus, the extracted r_2 values for these compounds represents the value of R_2 normalized by $c = 10$ mMol/l, assuming the linear dependence, which was always observed in superconducting magnets.

However, even at high concentrations the R_2 were sometimes found non-monoexponential. An example of the CPMG (1D) experiment for $DyCl_3$ ($c = 10$ mMol/l) at 820 MHz is shown in figure 6.9. It shows a deviation from the expected mono-exponential decay after a CPMG pulse sequence. The most likely explanation for the observed result arises due to the fluctuations in the resistive magnets.

The use of π pulses in the CPMG pulse is necessary to eliminate the spin decoherence induced by magnetic field inhomogeneity and fluctuations but is extremely sensitive off-resonant effects, as we explained in detail in chapter 3. This causes systematic errors on the extracted T_2 value. A similar behavior was seen in the relaxation curves of Ho(III) and Er(III). However, at higher fields, T_2 of the studied samples becomes shorter, and this effect gradually becomes weaker, leading to improved T_2 fits. We confirmed this hypothesis with the $GdCl_3$ sample (shortest T_2 values), where we observed mono-exponential decay relaxation curves at all fields (see figure 1.12 taken at 32.9 T).

We propose two ways for overcoming field fluctuations in the future so that T_2 may be measured for long relaxing samples:

- As the relaxation rate R_2 has a linear dependence on concentration, an increase in concentration will lead to a proportional reduction in T_2. This solution works only for high soluble samples such as the investigated $LnCl_3$.
- We can use more powerful amplifiers, i.e., stronger pulses (higher ω_1) to compensate for the off-resonance frequencies Δf encountered due to the field fluctuations in the resistive magnet. This

solution can extend the range of measurable T_2 relaxation times in the resistive magnet.

- Further investigations on the origin of the observed effect on the T_2 measurements may allow a better understanding of how the fluctuations interact with the nuclear magnetization of the samples during the CPMG sequence. Results of such experiments should provide important information for the design of an active correction system to reduce the field fluctuations.

Therefore, for now, we suggest that the highest achievable concentration for a given compound in aqueous solution (9:1 D_2O : H_2O) be used with a more powerful amplifier until we understand how the fluctuations interact with the T_2 of the sample.

In the following, for Dy(III), Ho(III), and Er(III), we will remove their r_2 data obtained in the resistive magnet for further discussion as shown in figure 6.10 (logarithmic representation). As for r_1, for Dy(III), Ho(III), and Er(III), the Curie spin relaxation also dominates the transverse relaxivity r_2. Therefore, the interpretation of r_2 is the same as r_1. r_2 values were slightly higher than r_1. Using the same parameters as for r_1, the model didn't fit the r_2 data set. The solid lines in the figure 6.10 serves only as a guide to the eye lines. Figure 6.11 shows that the ratio r_2/r_1 is roughly constant with field.

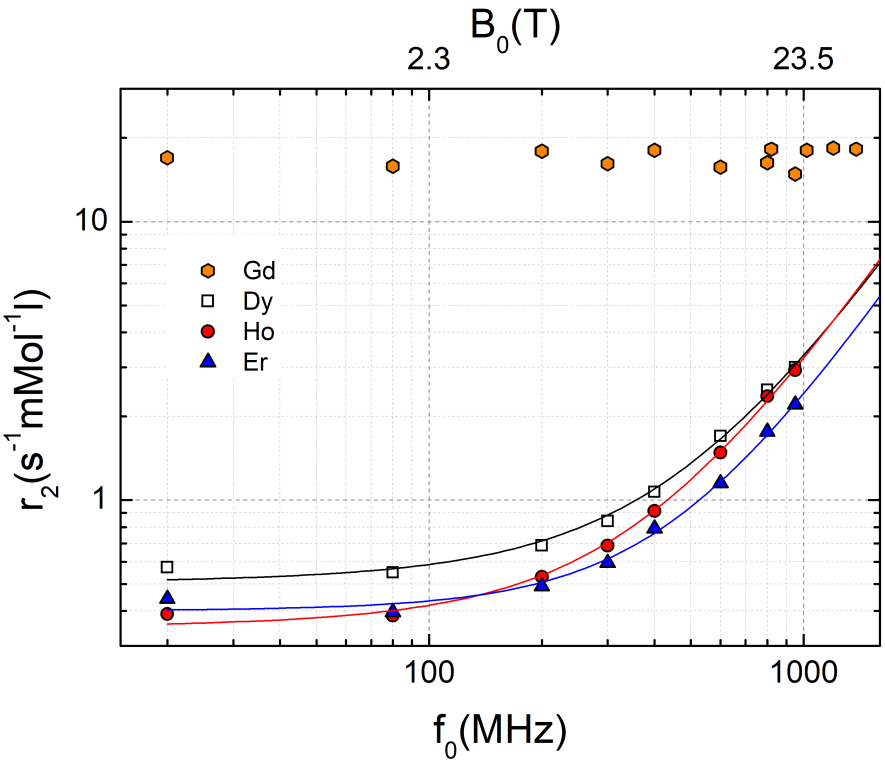

Figure 6.10: The description of this figure follows the caption of figure 6.8.

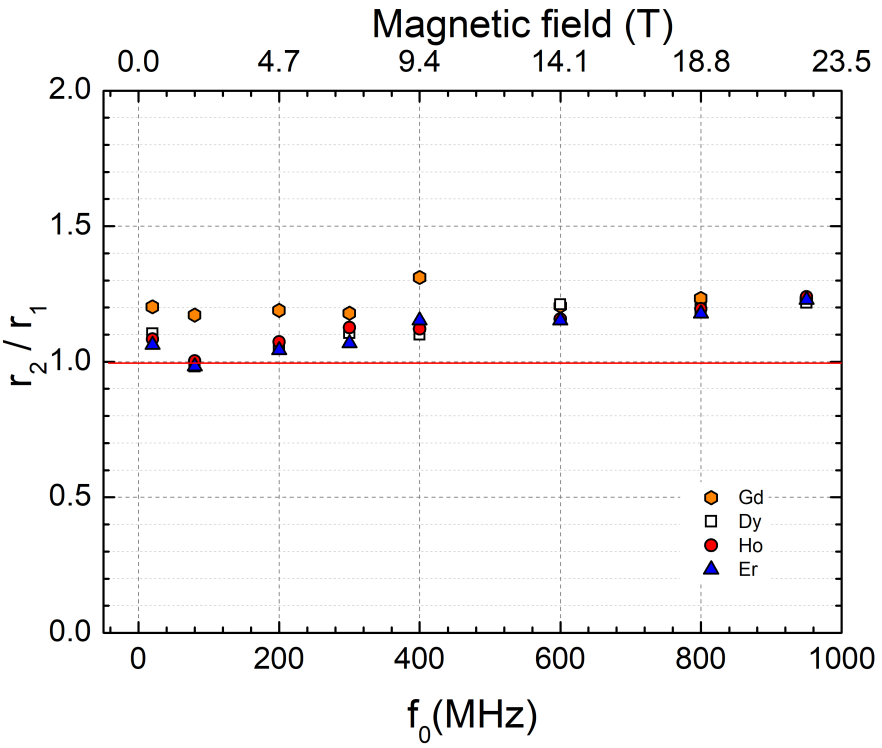

Figure 6.11: Ratio of r_2/r_1 data as a function of field. The red line is the low field limit or fast exchange.

6.4 Conclusion

PRE studies were performed over a large range of Larmor frequencies (20 up to 1400 MHz) for aqueous solutions of the $LnCl_3$ salts Ln $\in$ {Gd, Dy, Ho, Er}. The r_1 and r_2 values are the fitted slopes of $R_1(c)$ and $R_2(c)$ as a function of the entire $LnCl_3$ concentration, respectively. We compared the PRE behavior of the four lanthanide ions. r_1 and r_2 of all the compounds showed similar behaviors across the whole frequency range. For Gd(III), the NMRD profile is flat, which can be explained by the long electronic relaxation time τ_S, which results in the dipolar contribution dominating the Curie spin relaxation at all fields. On the other hand, Dy(III), Ho(III), and Er(III) have short electronic relaxation time τ_S, resulting in an increase of the relaxivities r_i $(i = 1, 2)$ with field due to Curie spin relaxation that depends on the square of the magnetic fields. The inner sphere relaxation is the main contributor to PRE in the lanthanide aqua ions, where the outer sphere relaxation is less than 15%.

In this PRE study, we modeled the relaxivity data set, which showed consistency with previous studies on lanthanide aqua ions at frequencies below 600 MHz [67]. They were useful as initial parameters for the fitting of the relaxivity data set. However, for the r_2 data, the model didn't work when using the deduced parameters τ_S and τ_R deduced from the fitted r_1 curves of Dy(III), Ho(III), and Er(III) ions. The obtained results of r_1 confirmed the model used but this was not the case for r_2 data. Further investigations are needed in order to better understand the results of the transverse relaxivity.

For high field measurements above 600 MHz, the radiation damping effect in commercial NMR spectrometers using superconducting magnets was quantitatively discussed, where we focused on reducing the sample volume by a factor of 10 to avoid this effect.

In addition, instead of using inversion recovery as in the previous PRE studies, we opted for progressive saturation recovery as a pulse sequence (PSR) for the T_1 measurements in resistive magnets. By this decision, we avoided the use of the π pulses that are sensitive to the fluctuations and led to a lower relative error on T_1 (1.5 to 2 times) than when using the inversion recovery pulse sequence for the T_1 measurements.

We also showed in this PRE study the importance of temperature control for the lanthanide ions exhibiting Curie spin relaxation. This latter is sensitive to temperature which can lead to systematic errors in the relaxivity data.

The results of r_2 showed the limitation of the resistive magnet in measuring long T_2 due to the presence of fluctuations. We provide solutions that can help for future PRE studies concerning T_2 measurements such as using more concentrated samples and more powerful amplifiers to improve the NMR pulse conditions. We highlight the importance of studying the fluctuations of the resistive magnet, which can lead to a better understanding of its interaction with samples having long T_2's.

In summary, the use of a tailored NMR approach with the resistive magnet has been shown to enable relaxivity studies on upcoming contrast agents, as demonstrated by this benchmark PRE study on Ln(III) aqua samples.

General conclusion and perspectives

Paramagnetic Relaxation Enhancement (PRE) in nuclear magnetic resonance (NMR) is an important research area, particularly with the increasing use of high magnetic fields in magnetic resonance imaging (MRI) applications. This trend towards future high-field MRI applications requires the development of new, effective contrast agents due to the reduced relaxivity of conventional PRE compounds based on Gd(III) at high fields. Additionally, the availability of resistive magnets at the LNCMI laboratory in Grenoble opens the way for PRE studies up to 33 T (1.4 GHz) and beyond. This is above current limit of superconducting magnets, which stands at 28.2 T (1.2 GHz). However, the limited field quality of resistive magnets, field inhomogeneity and fluctuations generate off-resonance effects that make NMR experiments a technical challenge. For this reason, during this thesis, we extensively worked on the developments of NMR instrumentation and methods to overcome these limitations that enable PRE studies in resistive magnets. Furthermore, we applied them in two experimental PRE studies.

Therefore, the thesis consists of two main parts. The first part focused on the developments that make high-field PRE studies with resistive magnets feasible, even though their field quality is limited compared to superconducting magnets. The second part, included two PRE studies on lanthanide-based compounds over a wide range of frequencies, from 20 to 1.4 GHz. For this reason, the conclusion will be divided into two distinct parts: instrumentation methods and scientific application.

NMR instrumentation and methods

The impacts of off-resonance effects in NMR excitation and detection produced by field inhomogeneity and fluctuations of the resistive magnets have been extensively explored in this work, both from theoretical (see Chapter 1) and experimental (see Chapter 3) perspectives. Field inhomogeneity and fluctuations influence NMR pulse conditions and NMR spectra. This makes NMR experiments a technical challenge. The theory revealed that the inversion pulse (π-pulse) is more sensitive to the off-resonance effect than saturation pulse ($\pi/2$-pulse). Different solutions were adapted to reduce the impact of field inhomogeneity and fluctuations on the relaxation experiments.

NMR in inhomogeneous static and radio-frequency fields

To ensure a homogeneous static magnetic field over the sample, the optimum sample size should be between 1-1.5 mm in length and with a diameter of 1 mm equivalent to a volume of 1-1.5 μl and well centered in the magnet. For the filling process of the sample in the capillary tubes of inner/outer 1/1.2 mm diameter and a length of 10 mm, a new tool was constructed to overcome the filling problems like the air pressure when sealing the tubes and handling small amounts of grease. Using this method, we kept the line width of the NMR spectrum below 15 ppm (Chapter 3).

To ensure a homogeneous radio-frequency field over the sample, simulations by both COMSOL Multiphysics 6.1 and special special Matlab scripts have demonstrated that the excitation coil produces a homo-

geneous on-resonant field for both $\pi/2$ and π pulses for sample lengths up to 1.5 mm. Imperfect pulses become more significant for sample lengths of 2 mm for the case of π pulses.

NMR in fluctuating fields

During the detection of the NMR signal, magnet fluctuations generate a frequency offset and unwanted echoes in the baseline, which perturbs the data treatment of the NMR experiments. For this reason, a non-standard collective data processing method has been developed, that is adapted to the field fluctuations of resistive magnets. The Matlab routine focuses on special methods for correcting the baseline and frequency offset of the NMR spectrum. These methods allow us to obtain a well-phased NMR spectrum and improve the signal-to-noise ratio for calculating NMR intensities, line positions, and line width (see Chapter 2).

During the excitation phase, it was found that the inversion pulses are strongly perturbed by the fluctuations of the resistive magnets at LNCMI. The analysis of the impact of fluctuations on T_1 experiments led to the use of the progressive saturation recovery pulse sequence, which uses saturation pulses exclusively, contrary to the previously used inversion recovery pulse sequence. By this decision, we avoided the use of the inversion pulses, which led to a lower relative error on the extracted T_1 (1.5 to 2 times) compared to the inversion recovery pulse that have been used in previous PRE studies on PM-POM compounds.

However, the issue of measuring T_2 on high fields was not resolved for samples with long T_2 values due to the necessity of using inversion pulses in the CPMG pulse sequence. For this problem we suggest several solutions that could lead in the future to resolve the effect of fluctuations on the T_2 measurements:(1) The use of higher concentration for highly soluble samples (shortening of T_2 value); (2) Improve the NMR pulse conditions by using more powerful amplifiers to better compensate the off-resonant effects; and (3) Reduce the fluctuations of the magnets by an active correction system. For this more investigations are needed to understand the interaction of the fluctuations with the nuclear magnetic moments of the samples during the CPMG sequence.

Finally, it was found that a precise temperature measurement and control is necessary for PRE in resistive magnets. Due to their narrow bore sizes, special instrumentation needs to be developed.

PRE studies of lanthanide compounds

Two PRE studies on lanthanide based compounds were performed over a large range of Larmor frequencies from 20 MHz up to 1.4 GHz. These studies were performed using three distinct types of magnets: (1) Permanent magnets for frequencies below 100 MHz; (2) superconducting magnets for the frequency range between 200 and 950 MHz; and (3) resistive magnets for the frequency range between 800 MHz and 1.4 GHz. They were carried out using NMR facilities in Germany (KIT) < 400 MHz and France (LNCMI) > 800 MHz. For the second study we also used superconducting magnets at Bruker (800 MHz) and IBS (600 MHz and 950 MHz). The studies at 800 and 950 MHz overlapped with the resistive magnets and allowed the identification of potential systematic errors induced by resistive magnets. We were able to identify the effect of the fluctuations on r_2 and a precise temperature control, as described in the instrumentation section.

The first PRE study was on three new paramagneic lanthanide containing polyoxometalates (PM-POMs) compounds synthesized by the colleagues at KIT. All three PM-POM clusters shows an increase of relaxivities with field, which indicated that the Curie spin contribution dominates over the dipolar contribution in the relaxation mechanisms leading to PRE. This is attributed to the fact that both lanthanide ions Dy(III) and

Er(III) have short electronic relaxation times. More systematic studies on other PM-POM complexes are needed to quantify the different factors responsible for the observed PRE behavior in these highly complex systems.

The second PRE study was on aqua lanthanide ions of $LnCl_3$ salts in solution with Ln $\in$ {Gd, Dy, Ho, Er} that are extensively investigated since the early days of NMR. However, almost no data were available for frequencies above 600 MHz. In our study we obtained longitudinal and transverse relaxivities over a frequency range from 20 MHz to 1400 MHz. Our r_1 results are consistent with previous work and we were able to model the longitudinal relaxivity r_1 with standard PRE models. PRE of Gd(III) shows a field independent NMRD profile, whereas the other three lanthanide ions Dy(III), Ho(III), and Er(III) show a strong increase at high fields due to the Curie spin contribution. Different electronic relaxation times of the free lanthanide ions are the source of the two different behaviors observed in the PRE study. The Curie spin contribution is more significant for lanthanide ions with short electronic spin relaxation times. The outer sphere relaxation is less than 15% for the aqua-ions.

The field dependence of the transverse relaxivity r_2 follows the longitudinal one with an almost constant r_2/r_1 ratio of 1.15. However, the modeling of the data does not yet quantitatively explain our data, which requires further investigation.

In conclusion, the work presented in this thesis proofs that the developed NMR instruments and methods allow PRE studies up to the highest magnetic fields with good precision. The obtained data sets are expected to contribute to a better understanding of this phenomena in view of high field applications.

Chapter A: Appendix

A.1 Deviation from standard PRE behavior in Gd_8PW_9 compounds

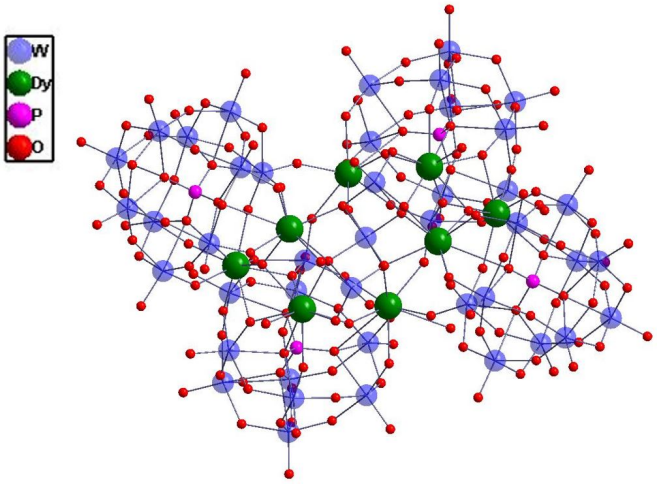

Figure A.1: Ball-and-stick representation of detailed structure of Dy_8-PW_9. Color scheme: The red stands for the oxygen atoms, the pink stands for the phosphorus, the green stands for the lanthanide ion dysprosium, and the blue stands for the tungsten.

During my thesis, we also attempted to study the PRE of another series of PM-POM clusters Ln_8PW_9 with Ln ϵ {Gd, Dy, Ho, Er}. However, we discontinued the study of these Ln_8PW_9 compounds due to a non-linear relationship between relaxation rates (R_i) and concentration observed during initial measurements on the 300 MHz spectrometer.

As an example, I present in figure A.2 the results of these studies obtained for Gd_8PW_9 at Bruker ASCEND^{TM} 300 MHz spectrometer as a function of different sets of concentrations at various dates after their preparation as indicated in the legend. A linear dependence with an offset was observed for concentrations above 0.2 mMol/l. However, the offsets turned out to be different from the relaxation rates of the solvent (red points). At lower concentrations (0.02, 0.05, and 0.1 mMol/l), a deviation from the linear slope is apparent, where the relaxation rates approach the values of the solvent. According to the theory, the dependence should be linear and independent of sample aging. These results are inconsistent with the theory. One possible explanation could be that due to the temporal instability of Gd_8PW_9 composition. This will need further studies. The molecular structure of a PM-POM cluster Ln_8PW_9 (here Ln = Dy) is shown in figure A.1.

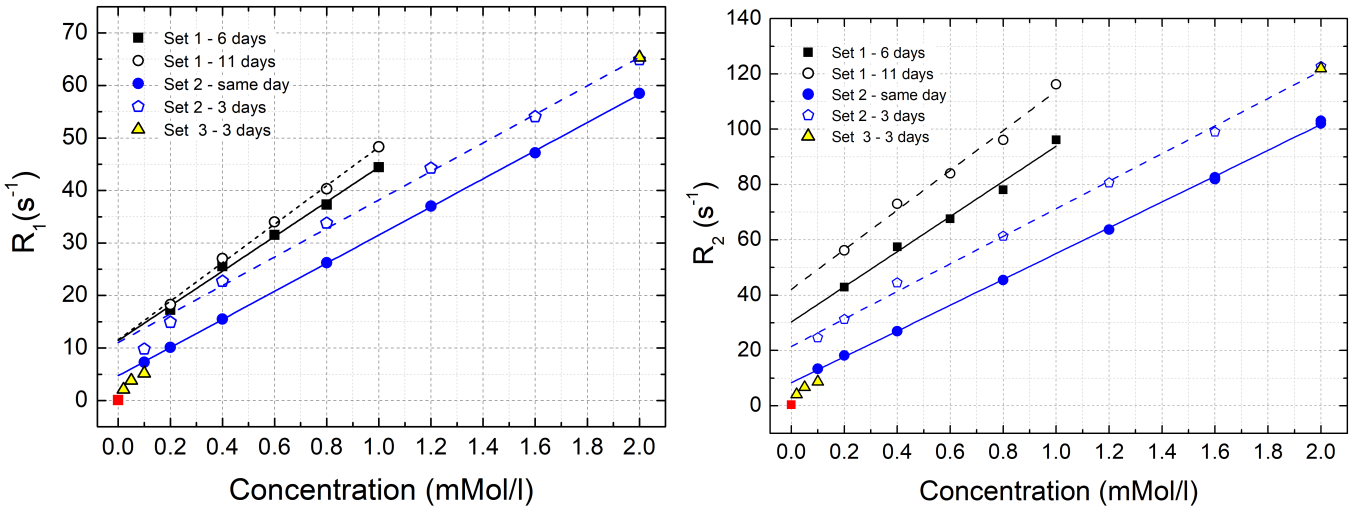

(a) (b)

Figure A.2: Relaxation rates R_1 and R_2 for Gd_8PW_9 at 300 MHz as a function of three sets of concentrations. The symbols show experimental R_i $(i = 1, 2)$ values obtained for the three measured sets. The red square symbol represents the R_i $(i = 1, 2)$ of the 9:1 D_2O/H_2O solvent. The delays between preparation and experiment are indicated in the legend. R_1 results are shown in the left figure. R_2 results are shown in the right figure. The lines are linear fits to the data without R_i $(i = 1, 2)$ value at $c = 0$. Both $R_1(c)$ and $R_2(c)$ differ from the expected behavior and the results depend on the delays between preparation and experiment. Details are discussed in the text.

A.2 Sample preparation and dilution process

A.2.1 Photos of sample dilution materials

(a)

(b)

(c)

(d)

Figure A.3: Sample preparation materials: (a)Balance (b) 25 ml pipette for solvent (9:1 D_2O/H_2O) preparation (c) 100-1000 µl, 20-200 µl, and 1-10 µl Eppendorf pipettes (d) 1 ml Eppendorf tube for the preparation of the diluted concentration solution.

A.2.2 Error calculation of the concentrations

To calculate the error bars on the concentrations obtained by the dilution process, we must first calculate the error bar of the stock solution concentration. The concentration can be expressed:

$$c_{start} = \frac{m}{M.V_{stock}}, \tag{A.1}$$

with $m = m_0 \pm \Delta m$, where m_0 is the measured weight of $LnCl_3$ (Ln ϵ {Gd, Dy, Ho, Er}) and $\Delta m = 0.01$ mg the precision of the balance. M is the molar mass of the sample.
$V_{stock} = V_{stock} + \Delta V_{stock}$, V_{stock} is the stock solution volume and $\Delta V_{stock} = n.\Delta V_{100-1000\mu l}$, where $n = 5$ is the number of times the $1000\mu l$ pipettes was used and $\Delta V_{100-1000\mu l} = 10\mu l$ the $1000\mu l$ pipette error (table A.3).
The error of the stock solution concentration is:

$$\begin{aligned} dc_{start}(m, V) &= \left|\frac{dc_{start}}{dm}\right| dm + \left|\frac{dc_{start}}{dV}\right| dV \\ \Delta c_{start} &= \left|\frac{\delta c}{\delta m}\right| \Delta m + \left|\frac{\delta c}{\delta V}\right| \Delta V_{stock} \\ &= \frac{\Delta m}{M.V_{stock}} + \frac{m.\Delta V_{stock}}{M.V_{stock}^2} \\ \Delta c_{start} &= \frac{1}{M.V_{stock}} \left(\Delta m + \frac{m.\Delta V_{stock}}{V_{stock}}\right). \end{aligned} \tag{A.2}$$

The dilution error calculation is derived from the equation 6.2:

$$c_{final} = \frac{c_{start}.V_1}{V_1 + V_2}, \tag{A.3}$$

with $c_{start} = c_{stock} \pm \Delta c_{start}$
$V_1 = V_1 \pm \Delta V_1$, V_1 is the amount of volume needed to be taken from the stock solution and ΔV_1 is the sum of pipettes total error used to extract V_1 (table A.3).
$V_2 = V_2 \pm \Delta V_2$, V_2 is the amount of volume needed to be taken from the solvent and ΔV_2 is the sum of pipettes total error used to extract V_2 (table A.3).
The error of the final concentration obtained after the dilution process is:

$$\begin{aligned} dc_{final}(c_{start}, V_1, V_2) &= \left|\frac{dc_{final}}{dc_{start}}\right| dc_{start} + \left|\frac{dc_{final}}{dV_1}\right| dV_1 + \left|\frac{dc_{final}}{dV_2}\right| dV_2 \\ \Delta c_{final} &= \left|\frac{\delta c_{final}}{\delta c_{start}}\right| \Delta c_{start} + \left|\frac{\delta c_{final}}{\delta V_1}\right| \Delta V_1 + \left|\frac{\delta c_{final}}{\delta V_1}\right| \Delta V_2 \\ &= \frac{V_1}{V_1 + V_2}.\Delta c_{start} + \left|\frac{c_{start}.(V_1 + V_2) - c_{start}.V_1}{(V_1 + V_2)^2}\right| \Delta V_1 + \frac{c_{start}.V_1}{(V_1 + V_2)^2}.\Delta V_2 \\ &= \frac{V_1}{V_1 + V_2}.\Delta c_{start} + \frac{c_{start}.V_2}{(V_1 + V_2)^2}.\Delta V_1 + \frac{c_{start}.V_1}{(V_1 + V_2)^2}.\Delta V_2 \\ \Delta c_{final} &= \frac{V_1}{V_1 + V_2}.\Delta c_{start} + \frac{c_{start}}{(V_1 + V_2)^2} \left(V_2.\Delta V_1 + V_1.\Delta V_2\right). \end{aligned} \tag{A.4}$$

The error on the concentrations for the different samples are represented in the table A.4.

A.2.3 Tables

Molar mass	Value [g/mol]
M(Gd)	157.25
M(Dy)	162.5
M(Ho)	164.93
M(Er)	167.26
M(Cl)	35.45
M(H)	1.0079
M(O)	16

Table A.1: Atomic Molar mass values

Sample ($LnCl_3$ + $6H_2O$)	M [g/mol]	m_0 [mg]
$GdCl_3$	371.72	18.58
$DyCl_3$	376.97	18.85
$HoCl_3$	379.4	18.97
$ErCl_3$	381.73	19.08

Table A.2: Molar Mass and weight of $LnCl_3$ + $6H_2O$ complexes needed for preparation a V_{stock} = 5ml of C_{start} = 10 mMol/l stock solution

Pipette eppendorf	Volume [μl]	Total Error [μl]
100-1000 μl	100	4.2
	200	4.9
	300	5.6
	400	6.3
	500	7
	600	7.6
	700	8.2
	800	8.8
	900	9.4
	1000	10

Table A.3: Eppendorf pipette total error on volume

Sample	c_{final} [mMol/L]	Δc_{final} 10^{-4}.[mMol/L]	Δc_{start} 10^{-4}.[mMol/L]	ΔV_{stock} 10^{-3}.[ml]	ΔV_1 10^{-3}.[ml]	ΔV_2 10^{-3}.[ml]
$LnCl_3$	10	1.05	1.05	50	10	0
	5	700	1.05	50	7	7
	2	560	1.05	50	4.9	8.8
	1	262	1.05	50	5.6	28.2
	0.5	71	1.05	50	7	7
	0.2	57	1.05	50	4.9	8.8

Table A.4: Table of the dilution error bars

Bibliography

[1] I. Bertini, C. Luchinat, G. Parigi and E. Ravera. *NMR of Paramagnetic Molecules*. Elsevier Science, 2017.

[2] J. R. Machado, A. Baniodeh, A. K. Powell, B. Luy, S. Krämer and G. Guthausen. *Nuclear Magnetic Resonance Relaxivities: Investigations of Ultrahigh-Spin Lanthanide Clusters from 10 MHz to 1.4 GHz*, ChemPhysChem **15**, 3608 (2014). doi:10.1002/cphc.201402318.

[3] G. Guthausen, J. R. Machado, B. Luy, A. Baniodeh, A. K. Powell, S. Krämer, F. Ranzinger, M. P. Herrling, S. Lackner and H. Horn. *Characterisation and application of ultra-high spin clusters as magnetic resonance relaxation agents*, Dalton Transactions **44**, 5032 (2015). doi:10.1039/c4dt02916j.

[4] M. Ibrahim, S. Krämer, N. Schork and G. Guthausen. *Polyoxometalate-based high-spin cluster systems: a NMR relaxivity study up to 1.4 GHz/33 T*, Dalton Transactions **48**, 15597 (2019). doi:10.1039/c9dt02052g.

[5] A. C. Venu, R. N. Din, T. Rudszuck, P. Picchetti, P. Chakraborty, A. K. Powell, S. Krämer, G. Guthausen and M. Ibrahim. *NMR Relaxivities of Paramagnetic Lanthanide-Containing Polyoxometalates*, Molecules **26**, 7481 (2021). doi:10.3390/molecules26247481.

[6] N. Schork, M. Ibrahim, A. Baksi, S. Krämer, A. K. Powell and G. Guthausen. *NMR Relaxivities of Paramagnetic, Ultra-High Spin Heterometallic Clusters within Polyoxometalate Matrix as a Function of Solvent and Metal Ion*, ChemPhysChem **23** (2022). doi:10.1002/cphc.202200215.

[7] A. Abragam. *The principles of nuclear magnetism*. Oxford university press, 1961.

[8] M. H. Levitt. *Composite pulses*, Progress in Nuclear Magnetic Resonance Spectroscopy **18**, 61 (1986). doi:10.1016/0079-6565(86)80005-X.

[9] J. Keeler. *Understanding NMR spectroscopy*. Wiley, 2nd edition, 2010.

[10] M. H. Levitt. *Spin dynamics: basics of nuclear magnetic resonance*. Wiley, 2nd edition, 2008.

[11] E. Fukushima. *Experimental pulse NMR: a nuts and bolts approach*. CRC Press, 2018.

[12] K. C. Brown. *Essential mathematics for NMR and MRI Spectroscopists*. Royal Society of Chemistry, 2016.

[13] F. Bloch, W. W. Hansen and M. Packard. *The Nuclear Induction Experiment*, Physical Review **70**, 474 (1946). doi:10.1103/physrev.70.474.

[14] F. Bloch. *Nuclear Induction*, Physical Review **70**, 460 (1946). doi:10.1103/physrev.70.460.

[15] J. Keeler. *Understanding NMR spectroscopy*, chapter IV, pp. 61–63. Wiley, 2010.

[16] R. Freeman and H. D. W. Hill. *Fourier Transform Study of NMR Spin–Lattice Relaxation by "Progressive Saturation"*, The Journal of Chemical Physics **54**, 3367 (1971). doi:10.1063/1.1675352.

[17] V. F. Mitrović, E. E. Sigmund and W. P. Halperin. *Progressive saturation NMR relaxation*, Physical Review B **64**, 024520 (2001). doi:10.1103/physrevb.64.024520.

[18] H. Wang, M. Zhao, J. L. Ackerman and Y. Song. *Saturation-inversion-recovery: A method for T1 measurement*, Journal of Magnetic Resonance **274**, 137 (2017). doi:10.1016/j.jmr.2016.11.015.

[19] H. Y. Carr and E. M. Purcell. *Effects of Diffusion on Free Precession in Nuclear Magnetic Resonance Experiments*, Physical Review **94**, 630 (1954). doi:10.1103/physrev.94.630.

[20] S. Meiboom and D. Gill. *Modified Spin-Echo Method for Measuring Nuclear Relaxation Times*, Review of scientific instruments **29**, 688 (1958). doi:10.1063/1.1716296.

[21] E. Fukushima. *Experimental pulse NMR: a nuts and bolts approach*, chapter II, pp. 60–76. CRC Press, 2018.

[22] M. Buess and G. Petersen. *Acoustic ringing effects in pulsed nuclear magnetic resonance probes*, Review of Scientific Instruments **49**, 1151 (1978). doi:10.1063/1.1135538.

[23] E. Fukushima and S. Roeder. *Spurious ringing in pulse NMR*, Journal of Magnetic Resonance (1969) **33**, 199 (1979). doi:10.1016/0022-2364(79)90203-8.

[24] K. Roth. *A simple resolution enhancement technique: Delayed fourier transformation*, Journal of Magnetic Resonance (1969) **38**, 65 (1980). doi:10.1016/0022-2364(80)90177-8.

[25] F. Debray, J. Dumas, C. Trophime and N. Vidal. *DC High Field Magnets at the LNCMI*, IEEE Transactions on Applied Superconductivity **22**, 4301804 (2012). doi:10.1109/tasc.2012.2183109.

[26] F. Debray and P. Frings. *State of the art and developments of high field magnets at the "Laboratoire National des Champs Magnétiques Intenses"*, Comptes Rendus Physique **14**, 2 (2013). doi:10.1016/j.crhy.2012.11.002.

[27] K. Paillot, F. Debray, C. Grandclement, S. Kramer, C. Trophime and B. Vincent. *Energy Efficiency of Resistive High Field Magnets: Aspects of Magnet Technology, Power Supply Operation and Field Quality*, IEEE Transactions on Applied Superconductivity **32**, 1 (2022). doi:10.1109/tasc.2022.3151568.

[28] P. Wikus, W. Frantz, R. Kümmerle and P. Vonlanthen. *Commercial gigahertz-class NMR magnets*, Superconductor Science and Technology **35**, 033001 (2022). doi:10.1088/1361-6668/ac4951.

[29] Y. Yanagisawa, M. Hamada, K. Hashi and H. Maeda. *Review of recent developments in ultra-high field (UHF) NMR magnets in the Asia region*, Superconductor Science and Technology **35**, 044006 (2022). doi:10.1088/1361-6668/ac5644.

[30] P. van Bentum, J. Maan, J. van Os and A. Kentgens. *Strategies for solid-state NMR in high-field Bitter and hybrid magnets*, Chemical Physics Letters **376**, 338 (2003). doi:10.1016/s0009-2614(03)01014-5.

[31] Z. Gan, H.-T. Kwak, M. Bird, T. Cross, P. Gor'kov, W. Brey and K. Shetty. *High-field NMR using resistive and hybrid magnets*, Journal of Magnetic Resonance **191**, 135 (2008). doi:10.1016/j.jmr.2007.12.008.

[32] W. A. Anderson. *Electrical Current Shims for Correcting Magnetic Fields*, Review of Scientific Instruments **32**, 241 (1961). doi:10.1063/1.1717338.

[33] V. Soghomonian, M. Sabo, A. Powell, P. Murphy, R. Rosanske, T. A. Cross and H. J. Schneider-Muntau. *Identification and minimization of sources of temporal instabilities in high field (> 23 T) resistive magnets*, Review of Scientific Instruments **71**, 2882 (2000). doi:10.1063/1.1150707.

[34] E. Sigmund, E. Calder, G. Thomas, V. Mitrović, H. Bachman, W. Halperin, P. Kuhns and A. Reyes. *NMR Phase Noise in Bitter Magnets*, Journal of Magnetic Resonance **148**, 309 (2001). doi:10.1006/jmre.2001.2397.

[35] A. Abragam. *The principles of nuclear magnetism*, chapter III, pp. 82–84. Oxford university press, 1961.

[36] E. Fukushima. *Experimental pulse NMR: a nuts and bolts approach*, chapter VI, pp. 437–440. CRC Press, 2018.

[37] D. Hoult and R. Richards. *The signal-to-noise ratio of the nuclear magnetic resonance experiment*, Journal of Magnetic Resonance (1969) **24**, 71 (1976). doi:10.1016/0022-2364(76)90233-x.

[38] H. B. Dwight. *Proximity effect in wires and thin tubes*, Journal of the American Institute of Electrical Engineers **42**, 961 (1923). doi:10.1109/joaiee.1923.6593373.

[39] H. Wheeler. *Formulas for the Skin Effect*, Proceedings of the IRE **30**, 412 (1942). doi:10.1109/jrproc.1942.232015.

[40] D. D. Traficante. *Impedance: What it is, and why it must be matched*, Concepts in Magnetic Resonance **1**, 73 (1989). doi:10.1002/cmr.1820010205.

[41] F. D. Doty. *Probe Design and Construction*, Encyclopedia of NMR **6**, 3753 (1996). doi:10.1002/9780470034590.emrstm1000.

[42] D. D. Wheeler and M. S. Conradi. *Practical exercises for learning to construct NMR/MRI probe circuits*, Concepts in Magnetic Resonance Part A **40A**, 1 (2012). doi:10.1002/cmr.a.21221.

[43] J. Mispelter, M. Lupu and A. Briguet. *NMR probeheads for biophysical and biomedical experiments: theoretical principles and practical guidelines*. World Scientific Publishing Company, 2015.

[44] R. B. Lauffer. *Paramagnetic metal complexes as water proton relaxation agents for NMR imaging: theory and design*, Chemical Reviews **87**, 901 (1987). doi:10.1021/cr00081a003.

[45] É. Tóth, L. Helm and A. E. Merbach. *Relaxivity of MRI Contrast Agents*, Contrast agents I: magnetic resonance imaging , 61 (2002). doi:10.1007/3-540-45733-x_3.

[46] L. Helm. *Relaxivity in paramagnetic systems: Theory and mechanisms*, Progress in Nuclear Magnetic Resonance Spectroscopy **49**, 45 (2006). doi:10.1016/j.pnmrs.2006.03.003.

[47] J. Peters, J. Huskens and D. Raber. *Lanthanide induced shifts and relaxation rate enhancements*, Progress in Nuclear Magnetic Resonance Spectroscopy **28**, 283 (1996). doi:10.1016/0079-6565(95)01026-2.

[48] A. Abragam. *The principles of nuclear magnetism*, chapter VIII, pp. 278–297. Oxford university press, 1961.

[49] I. Bertini, C. Luchinat, G. Parigi and E. Ravera. *NMR of Paramagnetic Molecules*, chapter IV, pp. 77–97. Elsevier Science, 2017.

[50] A. Abragam. *The principles of nuclear magnetism*, chapter IV, pp. 97–104. Oxford university press, 1961.

[51] I. Bertini, C. Luchinat, G. Parigi and E. Ravera. *NMR of Paramagnetic Molecules*, chapter IV, pp. 95–98. Elsevier Science, 2017.

[52] I. Bertini, C. Luchinat, G. Parigi and E. Ravera. *NMR of Paramagnetic Molecules*, chapter IV, pp. 82–88. Elsevier Science, 2017.

[53] I. Bertini, C. Luchinat, G. Parigi and E. Ravera. *NMR of Paramagnetic Molecules*, chapter VI, pp. 165–168. Elsevier Science, 2017.

[54] I. Bertini, C. Luchinat, G. Parigi and E. Ravera. *NMR of Paramagnetic Molecules*, chapter VI, pp. 168–170. Elsevier Science, 2017.

[55] L. V. Elst, A. Roch, P. Gillis, S. Laurent, F. Botteman, J. W. Bulte and R. N. Muller. *Dy-DTPA derivatives as relaxation agents for very high field MRI: The beneficial effect of slow water exchange on the transverse relaxivities*, Magnetic Resonance in Medicine **47**, 1121 (2002). doi:10.1002/mrm.10163.

[56] I. Solomon. *Relaxation Processes in a System of Two Spins*, Physical Review **99**, 559 (1955). doi:10.1103/physrev.99.559.

[57] N. Bloembergen. *Proton Relaxation Times in Paramagnetic Solutions*, The Journal of Chemical Physics **27**, 572 (1957). doi:10.1063/1.1743771.

[58] N. Bloembergen and L. O. Morgan. *Proton Relaxation Times in Paramagnetic Solutions. Effects of Electron Spin Relaxation*, The Journal of Chemical Physics **34**, 842 (1961). doi:10.1063/1.1731684.

[59] I. Bertini, C. Luchinat, G. Parigi and E. Ravera. *NMR of Paramagnetic Molecules*, chapter IV, pp. 83–84. Elsevier Science, 2017.

[60] I. Bertini, C. Luchinat and Z. Xia. *Electronic relaxation of the titanium(III) hexaaqua complex detected by solvent water proton-NMRD spectroscopy*, Inorganic Chemistry **31**, 3152 (1992). doi:10.1021/ic00040a028.

[61] S. H. Koenig and M. Epstein. *Ambiguities in the interpretation of proton magnetic relaxation data in water solutions of Gd3+ ions*, The Journal of Chemical Physics **63**, 2279 (1975). doi:10.1063/1.431677.

[62] M. Gueron. *Nuclear relaxation in macromolecules by paramagnetic ions: a novel mechanism*, Journal of Magnetic Resonance (1969) **19**, 58 (1975). doi:10.1016/0022-2364(75)90029-3.

[63] P. Gillis, A. Roch and R. A. Brooks. *Corrected Equations for Susceptibility-InducedT2-Shortening*, Journal of Magnetic Resonance **137**, 402 (1999). doi:10.1006/jmre.1998.1691.

[64] L.-P. Hwang and J. H. Freed. *Dynamic effects of pair correlation functions on spin relaxation by translational diffusion in liquids*, The Journal of Chemical Physics **63**, 4017 (1975). doi:10.1063/1.431841.

[65] F. Carniato, L. Tei, M. Botta, E. Ravera, M. Fragai, G. Parigi and C. Luchinat. *1H NMR relaxometric study of chitosan-based nanogels containing mono-and bis-hydrated Gd (III) chelates: Clues for MRI probes of improved sensitivity*, ACS Applied Bio Materials **3**, 9065 (2020). doi:10.1021/acsabm.0c01295.

[66] P. M. Singer, A. V. Parambathu, T. J. P. dos Santos, Y. Liu, L. B. Alemany, G. J. Hirasaki, W. G. Chapman and D. Asthagiri. *Predicting 1 H NMR relaxation in Gd 3+-aqua using molecular dynamics simulations*, Physical Chemistry Chemical Physics **23**, 20974 (2021). doi:10.1039/d1cp03356e.

[67] I. Bertini, F. Capozzi, C. Luchinat, G. Nicastro and Z. Xia. *Water proton relaxation for some lanthanide aqua ions in solution*, The Journal of Physical Chemistry **97**, 6351 (1993). doi:10.1021/j100126a007.

[68] D. Cicolari, F. Santanni, L. Grassi, F. Brero, M. Filibian, T. Recca, P. Arosio, M. Perfetti, M. Mariani, R. Sessoli and A. Lascialfari. *Longitudinal and transverse NMR relaxivities of Ln(III)-DOTA complexes: A comprehensive investigation*, The Journal of Chemical Physics **155** (2021). doi:10.1063/5.0072185.

[69] J. D. Rinehart and J. R. Long. *Exploiting single-ion anisotropy in the design of f-element single-molecule magnets*, Chemical Science **2**, 2078 (2011). doi:10.1039/c1sc00513h.

[70] G. Pintacuda, M. John, X.-C. Su and G. Otting. *NMR Structure Determination of Protein-Ligand Complexes by Lanthanide Labeling*, Accounts of Chemical Research **40**, 206 (2007). doi:10.1021/ar050087z.

[71] M. Norek and J. A. Peters. *MRI contrast agents based on dysprosium or holmium*, Progress in Nuclear Magnetic Resonance Spectroscopy **59**, 64 (2011). doi:10.1016/j.pnmrs.2010.08.002.

[72] E. A. Suturina, K. Mason, C. F. G. C. Geraldes, I. Kuprov and D. Parker. *Beyond Bleaney's Theory: Experimental and Theoretical Analysis of Periodic Trends in Lanthanide-Induced Chemical Shift*, Angewandte Chemie **129**, 12383 (2017). doi:10.1002/ange.201706931.

[73] E. A. Suturina, K. Mason, C. F. G. C. Geraldes, N. F. Chilton, D. Parker and I. Kuprov. *Lanthanide-induced relaxation anisotropy*, Physical Chemistry Chemical Physics **20**, 17676 (2018). doi:10.1039/c8cp01332b.

[74] Y. Wu and L. Bi. *Research Progress on Catalytic Water Splitting Based on Polyoxometalate/Semiconductor Composites*, Catalysts **11**, 524 (2021). doi:10.3390/catal11040524.

[75] N. Li, J. Liu, B.-X. Dong and Y.-Q. Lan. *Polyoxometalate-Based Compounds for Photo- and Electrocatalytic Applications*, Angewandte Chemie **132**, 20963 (2020). doi:10.1002/ange.202008054.

[76] M. Ibrahim, V. Mereacre, N. Leblanc, W. Wernsdorfer, C. E. Anson and A. K. Powell. *Self-Assembly of a Giant Tetrahedral 3 d–4 f Single-Molecule Magnet within a Polyoxometalate System*, Angewandte Chemie International Edition **54**, 15574 (2015). doi:10.1002/anie.201504663.

[77] M. Ibrahim, Y. Peng, E. Moreno-Pineda, C. E. Anson, J. Schnack and A. K. Powell. *Gd3 Triangles in a Polyoxometalate Matrix: Tuning Molecular Magnetocaloric Effects in {Gd30M8} Polyoxometalate/Cluster Hybrids Through Variation of M2+*, Small Structures **2** (2021). doi:10.1002/sstr.202100052.

[78] A. V. Anyushin, A. Kondinski and T. N. Parac-Vogt. *Hybrid polyoxometalates as post-functionalization platforms: from fundamentals to emerging applications*, Chemical Society Reviews **49**, 382 (2020). doi:10.1039/c8cs00854j.

[79] K.-Y. Wang, B. S. Bassil, Z. Lin, I. Römer, S. Vanhaecht, T. N. Parac-Vogt, C. Sáenz de Pipaón, J. R. Galán-Mascarós, L. Fan, J. Cao and U. Kortz. *Ln12-Containing 60-Tungstogermanates: Synthesis, Structure, Luminescence, and Magnetic Studies*, Chemistry - A European Journal **21**, 18168 (2015). doi:10.1002/chem.201502457.

[80] J. Elistratova, B. Akhmadeev, V. Korenev, M. Sokolov, I. Nizameev, I. Ismaev, M. Kadirov, A. Sapunova, A. Voloshina, R. Amirov and A. Mustafina. *Aqueous solutions of triblock copolymers used as the media affecting the magnetic relaxation properties of gadolinium ions trapped by metal-oxide nanostructures*, Journal of Molecular Liquids **296**, 111821 (2019). doi:10.1016/j.molliq.2019.111821.

[81] S. Pizzanelli, R. Zairov, M. Sokolov, M. C. Mascherpa, B. Akhmadeev, A. Mustafina and L. Calucci. *Trapping of Gd (III) ions by keplerate polyanionic nanocapsules in water: A 1H fast field cycling NMR relaxometry study*, The Journal of Physical Chemistry C **123**, 18095 (2019). doi:10.1021/acs.jpcc.9b05044.

[82] R. F. S. Carvalho, G. A. L. Pereira, J. Rocha, M. M. C. A. Castro, C. M. Granadeiro, H. I. S. Nogueira, J. A. Peters and C. F. G. C. Geraldes. *Lanthanopolyoxometalate-Silica Core/Shell Nanoparticles as Potential MRI Contrast Agents*, European Journal of Inorganic Chemistry **2021**, 3458 (2021). doi:10.1002/ejic.202100445.

[83] M. Ibrahim, I. M. Mbomekallé, P. de Oliveira, A. Baksi, A. B. Carter, Y. Peng, T. Bergfeldt, S. Malik and C. E. Anson. *Syntheses, Crystal Structure, Electrocatalytic, and Magnetic Properties of the*

Monolanthanide-Containing Germanotungstates [Ln (H2O) n GeW11O39]5-(Ln= Dy, Er, n= 4, 3), ACS Omega **4**, 21873 (2019). doi:10.1021/acsomega.9b02846.

[84] M. Ibrahim, A. Baksi, Y. Peng, F. K. Al-Zeidaneen, I. M. Mbomekallé, P. de Oliveira and C. E. Anson. *Synthesis, characterization, electrochemistry, photoluminescence and magnetic properties of a dinuclear erbium (III)-containing monolacunary dawson-type tungstophosphate:[{Er (H2O)(CH3COO)(P2W17O61)} 2] 16-*, Molecules **25**, 4229 (2020). doi:10.3390/molecules25184229.

[85] W. N. Baker. *A New Comparison of the Viscosity of D2O with that of H2O*, The Journal of Chemical Physics **4**, 294 (1936). doi:10.1063/1.1749842.

[86] A. Barge, G. Cravotto, E. Gianolio and F. Fedeli. *How to determine free Gd and free ligand in solution of Gd chelates. A technical note*, Contrast media & molecular imaging **1**, 184 (2006). doi:10.1002/cmmi.110.

[87] N. Bloembergen, E. M. Purcell and R. V. Pound. *Relaxation effects in nuclear magnetic resonance absorption*, Physical review **73**, 679 (1948).

[88] L. Banci, I. Bertini and C. Luchinat. *1H NMRD studies of solutions of paramagnetic metal ions in ethyleneglycol*, Inorganica Chimica Acta **100**, 173 (1985). doi:10.1016/s0020-1693(00)88305-x.

[89] A. Favier. *Private comunication*, 2023.

[90] N. Bloembergen and R. V. Pound. *Radiation Damping in Magnetic Resonance Experiments*, Physical Review **95**, 8 (1954). doi:10.1103/physrev.95.8.

[91] W. S. Warren, S. L. Hammes and J. L. Bates. *Dynamics of radiation damping in nuclear magnetic resonance*, The Journal of Chemical Physics **91**, 5895 (1989). doi:10.1063/1.457458.

[92] A. Szöke and S. Meiboom. *Radiation Damping in Nuclear Magnetic Resonance*, Physical Review **113**, 585 (1959). doi:10.1103/physrev.113.585.

[93] X. an Mao, J. xin Guo and C. hui Ye. *Radiation damping effects on spin—lattice relaxation time measurements*, Chemical Physics Letters **222**, 417 (1994). doi:10.1016/0009-2614(94)00388-2.

[94] H. R. Pruppacher. *Self-Diffusion Coefficient of Supercooled Water*, The Journal of Chemical Physics **56**, 101 (1972). doi:10.1063/1.1676831.

[95] S. H. Koenig and R. D. Brown. *Field-cycling relaxometry of protein solutions and tissue: Implications for MRI*, Progress in Nuclear Magnetic Resonance Spectroscopy **22**, 487 (1990). doi:10.1016/0079-6565(90)80008-6.

[96] G. Guthausen. *Private comunication*, 2023.

[97] J. Reuben and D. Fiat. *Proton chemical shifts in aqueous solutions of the rare-earth ions as an indicator of complex formations*, Chemical Communications (London) , 729 (1967). doi:10.1039/c19670000729.

[98] J. Reuben and D. Fiat. *Nuclear Magnetic Resonance Studies of Solutions of the Rare-Earth Ions and Their Complexes. III. Oxygen-17 and Proton Shifts in Aqueous Solutions and the Nature of Aquo and Mixed Complexes*, The Journal of Chemical Physics **51**, 4909 (1969). doi:10.1063/1.1671883.

List of Figures

List of Tables